Dispersion and Dissolution of Indian Coal in Ionic Liquids: Theoretical Predictions and Experimental Validation

A thesis submitted

in partial fulfilment of the requirements

for the degree of

Doctor of Philosophy

by

Sanjukta Bhoi

Department of Chemical Engineering
Indian Institute of Technology Guwahati
June 2017

Dispersion and Dissolution of Indian Coal in Ionic Liquids: Theoretical Predictions and Experimental Validation

A thesis submitted

in partial fulfilment of the requirements

for the degree of

Doctor of Philosophy

by

Sanjukta Bhoi

Department of Chemical Engineering
Indian Institute of Technology Guwahati
June 2017

Department of Chemical Engineering
Indian Institute of Technology Guwahati

CERTIFICATE

It is certified that the work contained in this thesis entitled *"***Dispersion and Dissolution of Indian Coal in Ionic Liquids: Theoretical Predictions and Experimental Validation"**, by Sanjukta Bhoi, has been carried out under our supervision and that this work has not been submitted elsewhere for a degree.

Prof. Tamal Banerjee
Professor
Department of Chemical Engineering
Indian Institute of Technology Guwahati

Prof. Kaustubha Mohanty
Professor
Department of Chemical Engineering
Indian Institute of Technology Guwahati

Department of Chemical Engineering
Indian Institute of Technology Guwahati

STATEMENT

I hereby declare that the matter embodied in this thesis is the result of investigations carried out by me in the Department of Chemical Engineering, Indian Institute of Technology Guwahati, Assam, India under the supervision of **Dr. Tamal Banerjee** and **Dr. Kaustubha Mohanty**.

In keeping with the general practice of reporting scientific observations, due acknowledgement has been made wherever the work described is based on the findings of other investigations.

Guwahati — Sanjukta Bhoi

May 2017

ACKNOWLEDGMENT

It is my great privilege to sincerely thank several people who have supported me to complete my Doctoral Dissertation.

First and foremost, with the deepest sense of gratitude, I would like to express my sincere thanks to my supervisors **Prof. Tamal Banerjee** and **Prof. Kaustubha Mohanty**, who have been a constant source of inspiration for me. Their timely help during the crucial phases of my Ph.D. career has made it possible for me to achieve my target. My special thanks to them for their valuable guidance, encouragement, inspiration, creative, and scientific ideas which helped me to enhance my knowledge. I am also fortunate enough to have their guidelines to cultivate scientific thought. I would like to thank them for their wonderful and friendly nature that encouraged me to have many scientific discussions and also for teachings of life, for which I will remain indebted to them.

I would like to acknowledge my sincere gratitude to my doctoral committee members, **Dr. Mahuya De** and **Dr. Chandan Das**, Department of Chemical Engineering and **Dr. Pankaj Kalita**, Department of Center for Energy. Their intuitive revision of my work, valuable advice, and constructive suggestions during my research progress kept the flow of my research work in the right direction.

I am indebted to **Prof. V. S. Moholkar, Dr. Pankaj Tiwari, Dr. Chandan Das,** and **Dr. Subrata Kumar Majumder** for their research oriented teaching during my course of work. I also thank **Prof. Bishnupada Mandal**, Head, Department of Chemical Engineering for his administrative support. Furthermore, I would like to thank all the other Faculties and Staff members of the Department of Chemical Engineering for their invaluable support during my research.

I express my sincere gratitude and acknowledgment to IIT Guwahati for all the facilities that were made available to me. I am grateful to the Analytical Laboratory of the Department of Chemical Engineering and Department of Chemistry, IIT Guwahati for providing me with the necessary support for Sample Analysis using Fourier Transform Infrared (FTIR) Spectroscopy and Thermogravimetric Analyzer (TGA).

I would also like to thank the Department of Mineral Processing, CSIR-Institute of Minerals and Materials Technology, Bhubaneswar, India for sharing the Coal samples.

I wish to thank our lab seniors **Dr. Santhi Raju Pilli**, **Dr. Dharamashibhai V. Rabari**, **Dr. Krushna Prasad Shadangi** for lending their hands of support whenever needed. I thank all my lab members **Mr. Himadri Sahu**, **Mr. Anand Bharti**, **Ms. Basudhrity Banerjee**, **Mr.**

Debanjan Dey, **Mr. Ankit Bishnoi**, **Ms. Tooba Fatma**, **Mr. Jitendra Meena**, **Ms. Rima Biswas**, **Mr. Mood Mohan**, **Mr. Proloy Das**, **Mr. Sanjeev Mishra, Mr. Bikashbindu Das**, **Mr. Ranjeet Kumar Mishra**, **Mr. Pyarimohan Dehuri**, **Mr. Kulbhushan Samal**, **Mr. Debasish Kundu**, **Mr. Papu Nayak**, **Ms. Upasana Mohanta, Mr. Sarvesh Namdeo, Mrs. Madhusmita Dash, Mr. Rupesh Verma, Mr. Sounak Bera, Ms. Madonna Roy, Ms. Barasa Malakar, Mr. Sachankar Buragohain, Mr. Pranab Jyoti Sarma** and **Ms. Munmi Bhattacharyya** for providing a co-operative research environment.

My sincere thanks to IIT Guwahati friends **Ms. Lipika Kalo**, **Mrs. Sreedevi Maharana**, **Ms. Camelia Das**, **Ms. Trushna Meher,** and **Mr. Rashmi Ranjan Behera** for all the laughs, joyful moments, support and suggestions. I would also thank all of my Ph.D. batch mates **Late Ms. Cherukuri Jayalakshmi**, **Mr. Pritam Kumar Dikshit**, **Mr. Raj Kumar Das**, **Mr. Fahad M K**, **Mr. Sudarshan Konidena** and the other research scholars of Chemical Engineering Department and all my IITG friends, who have shared their thoughts and views with me.

Words of motivation and encouragement from some of my friends and relatives were only a call away. They always appreciated my efforts and outcomes of my research work. My sincere gratitude to **Mr. Bhaskar Jyoti Das**, **Mr. Jyotilal Murmu**, **Mrs. Shanti Nayak**, **Ms. Sucharita Jena, Mr. Soumya Kanta Nayak, Mrs. Chhabirani Tudu** and many more.

My whole hearted gratitude goes to my parents, **Mr. Raghumani Bhoi** and **Mrs. Kunti Bhoi,** my brother **Mr. Amit Kumar Bhoi** as well as **family members of Prof. Kaustubha Mohanty and Prof. Tamal Banerjee** whose blessings, wise advice and boundless patience kept my morale high during the course of study.

Finally, for the financial support of this research, I would sincerely like to thank the **Council of Scientific and Industrial Research (CSIR), India vides sanction letter No. 02(0093)/12/EMR-II.**

Sincerely,

Sanjukta Bhoi

Synopsis

Coal is a naturally occurring carbonaceous material which is one of the most important sources for energy production. Approximately 40% of worldwide electricity is produced from coal for power generation. In addition, gasification and liquefaction are two important processes for the gaseous and liquid fuel production, so that it can be easily transported or conveniently stored in a tank for future utilization. Coal has a complex structure and contains various heterogeneous clusters of polycyclic aromatic fused rings. It comprises various functional groups such as; phenolic, carboxylic, carbonyl, and ether which results in their spontaneous combustion. Spontaneous combustion of a coal refers to the heating of coal at high temperatures which usually results in exothermic reactions. Quite often the heat generated or the calorific value reduces due to the presence oxygen-containing functional groups. One possible way to reduce the oxygen containing functional groups is to dissolve the coal in a suitable solvent. A non-polar solvent such as toluene has limited ability to disrupt and swell the coal molecules, so as to extract the soluble materials. Some of the acceptor group solvents such as pyridine provide strong hydrogen bonding to swell the coal particles. However, they are known to fractionate a lesser amount of these hydroxyl groups.

Thus along with the conventional solvents, there is a need to explore other green solvents which may provide a better swelling ratio and also reduce the oxygen-containing functional groups to a larger extent. In such a scenario Ionic Liquids (ILs) are known to play a dominant role for coal beneficiation. In coal beneficiation, the quality of raw coal is improved by either reducing the extraneous matter or reducing the associated ash or both using solvents. IL's are known to disrupt intramolecular hydrogen bonding such as those containing –OH and –COOH groups. The beneficiated coal possessing higher surface area

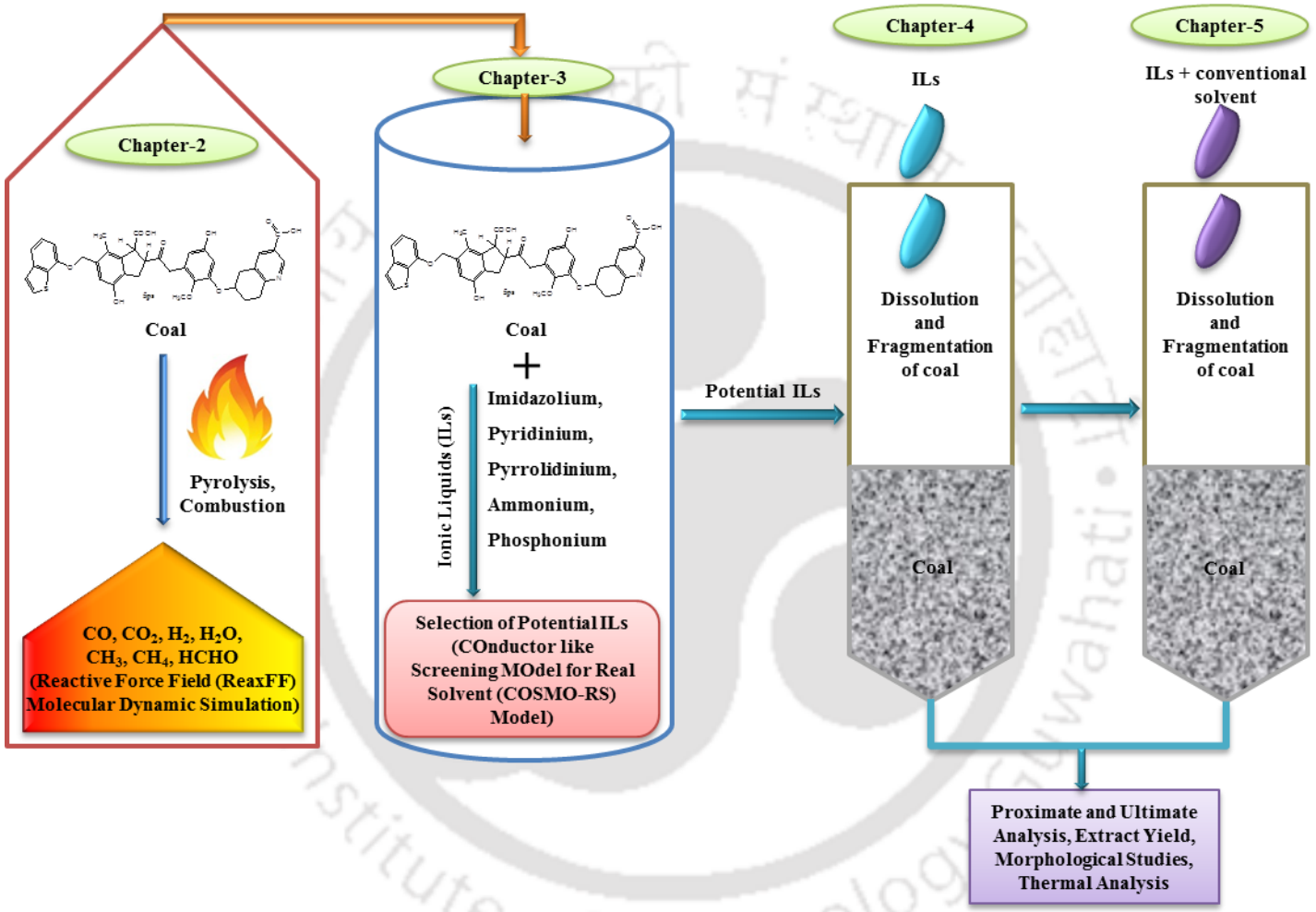

Fig. 1 Outline of the Thesis

can then be easily converted to lighter hydrocarbons such as SNG (Substitute Natural Gas), propane LPG, butane LPG, naphtha, and fuel oil. The outline of the thesis shown in Fig. 1.

Based on the outline (Fig. 1), the thesis focuses on the Coal and Ionic Liquid (ILs) interaction involving both theoretical as well as experimental studies. The initial theoretical study focuses on the RexFF reactive force field (ReaxFF) simulations for the pyrolytic and combustive phenomena of untreated coal. Thereafter potential combination of IL and coal were quantified with liquid phase activity coefficients using the Continuum Solvation Model namely COSMO-RS (COnductor like Screening MOdel for Real Solvents). The acquired combinations were then dissolved with coal samples to gain physical and chemical insights in the beneficiated coal. This includes both proximate and ultimate analysis along with other pertinent physical properties such as swelling ratio and extract yield.

Chapter 1 includes a brief introduction and a literature review on combustion and pyrolysis of raw and pretreated coal. It includes an extensive search on the dispersion and dissolution studies on Indian coal. The phenomena of fragmentation and swelling of coal using various conventional as well as green solvents are then demonstrated from literature. It also discusses the importance of computational studies for the selection of appropriate solvents toward coal beneficiation technology.

The first step was to analyse the detailed structural and kinetic insights involving the coal pyrolysis and combustion. This was performed using RexFF reactive force field MD simulation studies. **Chapter 2** discusses the combustion and pyrolysis analysis of three different ranks of coals (anthracite, bituminous and lignite) using ReaxFF simulations. A detailed reaction mechanism along with the numerous intermediates evolved during the

course of the reaction is explained. A part of this chapter is devoted to the combustion and pyrolysis study of brown coal. To examine the pyrolysis/combustion process and initiation mechanism of brown coal, a fuel lean (ϕ=2), fuel rich (ϕ=0.5), and stoichiometric (ϕ=1) condition were used in this chapter. The temperature used was kept higher (2000-4000 K) as per experimentally reported condition so as to enable chemical reaction within a computationally affordable time. Furthermore, the combustion of other ranks of coal was also studied in the same conditions namely fuel rich, fuel lean, and stoichiometric. Some important common intermediates such as formaldehyde (HCHO) generated during the simulation reaction was found to agree well with the experimental kinetic data reported in the literature. Regardless of the rank of coal, the gases CO and CO_2 were found to be predominant in nature. The formation rate of CO and CO_2 were found to be higher for lignite coal which agreed with the experimental trend as reported in the literature. In a similar manner, the fraction of CO and CO_2 was found to be higher in pyrolysis process. Further, a large number of principal intermediates such as methane, ethane, and ethylene were also generated for low to high rank (lignite, bituminous, and anthracite) coal. The pyrolysis and combustion processes were seen to be affected by temperature (2000-4000 K), primarily with respect to the formation of various intermediates (methane, ethane, and ethylene).

Chapter 3 discusses the computational methodology based on Continuum Solvation Model (CSM) such as COSMO-RS model for the potential cation + anion or IL selection. The study was initiated with *ab-initio* calculations on IL and pseudo coal using both Density Functional Theory (DFT) and COSMO-RS model. Taking the process economics and the nature of ionic liquids into account, 18 ILs having cations: imidazolium, pyridinium, pyrrolidinium, phosphonium, and ammonium were selected from the *Sigma-Aldrich*

Catalogue. A three-tier approach comprising of HOMO (Higher Occupied Molecular Orbital)-LUMO (Lower Unoccupied Molecular Orbital) energies, quantum descriptors (Electronegativity, Electrophilicity, Global hardness, Global softness); and Infinite Dilution Activity Coefficient (IDAC) by COSMO-RS model were selected to study the simultaneous interaction of coal and IL. Initially, the model was benchmarked qualitatively using the data available in the literature for coal and conventional solvents such as pyridine and N-Methylpyrrolidone (NMP). Thereafter, Gibb's Free Energy of solvation and Solid-Liquid Equilibria (SLE) predictions were performed for these 18 ILs. The IL showing the highest solubility was chosen as a potential solvent which possess the maximum ability to disrupt the hydrogen bonding of coal molecules. 1-butyl-1-methylpyrrolidinium methyl carbonate [BMPYR][CH_3CO_3] and 1-methyl-3-propylimidazolium methyl carbonate [MPIM][CH_3CO_3] were the recommended IL's on the basis of HOMO-LUMO band energy gap. A similar trend for IL-coal interactions were followed up and confirmed by the quantum descriptors and IDAC predictions.

Once the potential IL was chosen, a validation was performed by the wet beneficiation technique using the Ionic Liquids as obtained in **chapter 3**. **Chapter 4** hence comprises experimental studies on the dissolution and dispersion of coal with the potential cation and anion combination. The interaction between five different ionic liquids and four Indian coals from the mineral-rich eastern part of the country were carried out to identify its dissolution and swelling characteristics. Five ILs consisting of different cations namely: 1-butyl-3-methylimidazolium hexafluorophosphate [BMIM][PF_6], tributylmethylammonium methyl sulfate [TMA][$MeSO_4$], 1-butyl-1-methylpyrrolidinium methyl carbonate [BMPYR][CH_3CO_3], 1-butyl-4-methylpyridinium tetrafluoroborate [BMPY][BF_4], and

tributylmethylphosponium methyl sulfate [MTBP][$MeSO_4$] were selected from **Chapter 3** screening studies. Morphological studies of coal both before and after heating were carried out to determine the extent of swelling and fragmentation of coal particles. Using Fourier Transfer Infrared Spectroscopy (FTIR), the functional groups of ILs in untreated and ILs pretreated coal were identified. An overall 47.6, 55.6, and 68.1% reduction in the peak area of a hydroxyl group (phenolic and free hydroxyl radical) was observed for the ILs [BMIM][PF_6], [BMPY][BF_4], and [BMPYR][CH_3CO_3] in bituminous coal respectively. From the proximate analysis, the increase in fixed carbon content (on a weight basis) was found to be 1/3rd as compared to the raw coal. Among the ILs studied, [BMPYR][CH_3CO_3] was found to have a highest swelling ratio of 1.5. Following a similar trend, the morphological studies also concluded that the IL [BMPYR][CH_3CO_3] was the most effective in disintegrating the coal particles to micrometer size. The IL gave a total yield extraction of 27.41% (on *dry-ash-free* basis) for coal 2 (bituminous) and 35.13% (on *dry-ash-free* basis) for coal 4 (lignite).

The penultimate step was to observe the performance of mixed solvent namely IL and Pyridine. **Chapter 5** focuses on the interaction of coal with three different ionic liquids (ILs) and a mixed solvent (IL + conventional solvent) for analysing the oxidizing effect on Indian Coal. The IL's used in **Chapter 5** were 1-butyl-1-methylpyrrolidinium methyl carbonate [BMPYR][CH_3CO_3], 1-butyl-3-methylimidazolium hexafluorophosphate [BMIM][PF_6], and 1-butyl-4-methylpyridinium tetrafluoroborate [BMPY][BF_4]. They were subsequently used for dissolution studies in coal samples. The Thermogravimetric Analysis (TGA) results show that the mass loss was less for [BMPYR][CH_3CO_3] pre-treated coal as compared to coal treated with [BMPY][BF_4] and [BMIM][PF_6]. Hence the IL

[BMPYR][CH_3CO_3] has the largest ability to fractionate the more active oxygen-containing functional groups present in the coal molecules. Mass loss of mixed solvent ([BMPYR][CH_3CO_3] + pyridine) treated coal was also less as compared to IL-pretreated coal. A kinetic study was also conducted using a first order, non-isothermal kinetic method to investigate the insight into the coal structure. From the TGA scan, activation energy (E_a) and pre-exponential factor (A) were calculated. The thermal degradation study confirmed a high thermal stability (~630 ºC) for both mixed solvent and IL pre-treated coal when compared to raw coal (450 ºC). Further, the activation energy of IL pre-treated coal was also less when compared to the untreated coal.

भारतीय प्रौद्योगिकी संस्थान गुवाहाटी
Indian Institute of Technology Guwahati

Table of Contents

List of Tables

List of Figures

Nomenclature

	Abbreviations
AAD	Absolute Average Deviation
B3LYP	Becke, Three-Parameter, Lee-Yang-Parr
COSMO-RS	COnductor Like Screening MOdel For Real Solvent
COSMO-SAC	COnductor Like Screening MOdel For Segment Activity Coefficient
CHELPG	CHarges from Electrostatic Potentials using a Grid based method
DTG	Differential Thermo Gravimetry
DFT	Density Functional Theory
ES	Electrostatic
EA	Electron Affinity
HOMO	Higher Occupied Molecular Orbital
IDAC	Infinite Dilution Activity Coefficient
IP	Ionization Potential
LUMO	Lower Unoccupied Molecular Orbital
MD	Molecular Dynamic
NMP	N-Methylpyrrolidone
NPT	Fixed Number of atoms, at a constant Pressure and Temperature
NVT	Fixed Number of atoms, at fixed Volume, and Temperature
NVE	Fixed Number of atoms, fixed Volume, and a total Energy
QC	Quantum Chemical
QM	Quantum Mechanics
ReaxFF	Reactive Force Field

SCD	Screening Charge Density
SCF	Self-Consistent Field
SLE	Solid-Liquid-Equilibrium
TGA	Thermogravimetric Analysis
TZPV	Triple Zeta Valence Potential
UNIQUAC	UNIversal QUAsiChemical
UNIFAC	UNIvesral Functional Group Activity Coefficient
W	Weight of Coal Sample in kg
Z	Solute Nuclei

	Ionic Liquids Cations and Anions
[BDMIM]	1-butyl-2,3-dimethylimidazolium
[BF_4]	Tetrafluoroborate
[BMPY]	1-butyl-4-methylpyridinium
[BM_3PY]	*n*-butyl-3-methylpyridinium
[BM_4PY]	*n*-butyl-4-methylpyridinium
[BMPYR]	1-butyl-1-methylpyrrolidinium
[BYMIM]	1-benzyl-3-methyleimmidazolium
[C_2MIM]	1-methylimidazolium
[C_4MIM]	1-butyl-3-methylimidazolium
[CH_3CO_3]	Methyl carbonate
[$COOCH_3$]	Acetate
[DHXMIM]	1,3-dihydroxy-2-methylimmidazolium
[DMXIM]	1,3-dimethoxyimmidazolium
[DMXMIM]	1,3-dimethoxy-2-methylimmidazolium
[DMPIM]	1,2-dimethyl-3-propylimmidazolium

[EMIM]	1-ethyl -3-methylimmidazolium
[$EtSO_4$]	Ethyl sulphate
[HM_3PY]	*n*-hexyl-3-methylpyridinium
[$MeSO_4$]	Methyl sulphate
[MPIM]	1-methyl -3-propylimidazolium
[MPPY]	3-methyl-1-propylpyridinium
[$M_{1,4}PY$]	1,4-dimethylpyridinium
[MTBP]	Tributylmethylphosphonium
[$N(CN)_2$]	Dicyanamide
[PF_6]	Hexafluorophosphate
[Tf_2N]	Bis(trifluoromethylsulfonyl)imide
[TfO]	Trifluoromethanesulfonate
[TMA]	Tributylmethylammonium
[TOS]	Tosylate

Chapter 1

Introduction

1.1 Introduction

Coal is a naturally occurring carbonaceous material which is one of the most important sources for energy production. Approximately 40% of worldwide electricity is produced from coal for power generation. In addition, gasification and liquefaction are two important processes for the gaseous and liquid fuel production from coal. This can be easily transported and conveniently stored in a tank for the future utilization. It generally ranges from brown to black sedimentary rock composed mainly of organic or inorganic compounds [1, 2]. It has a complex structure and contains polycyclic aromatic clusters. A structural representation of a coal molecule is shown in Fig. 1.1 [3]. Coal comprises of various functional groups such as; phenolic, carboxylic, carbonyl, and ether which results in their spontaneous combustion. Due to the variation of physical and chemical properties along with composition, coal is classified by its carbon content. It is classified based on its rank such as lignite (low), sub-bituminous, bituminous, and anthracite (high). The ages of coal are directed by its carbon content or rank. Further, the elemental composition and product formation vary with coal rank. Coal rank also depends on volatile matter, fixed carbon, inherent moisture, and oxygen [4, 5]. On combustion and pyrolysis, it evolves gases such as carbon monoxide, carbon dioxide, SO_x, and NO_x.

Coal also produces a wide range of other pollutants (solid as well as gases) with the functional groups as mentioned above. For e.g. coal with higher oxygen content is expected to be more reactive towards gaseous oxygen which in turn produces a large amount of CO_2 and CO upon heating [6]. However, these studies are difficult to perform in the lab scale [1, 7] due to its higher process operating conditions. Further heating rate of coal also depends on the coal rank. For e.g. lignite will have the lowest heating value. On a similar note, the

gaseous yield of CH_4, C_2H_4, and C_2H_6 is known to be higher for low-rank coal [8-11]. The low-rank coal essentially oxidizes at high temperature, where the evolved CO and CO_2 are found to vary with temperature [6, 8-14]. The hydrogen production rate is also high for low-rank coal which in turn gives a low calorific value due to the loss of volatile components [15, 16]. Hence the quantification of these gases depends on the functional groups of the raw coal. This, in turn, results in the quality and quantity of the evolved gases. This necessitates a comprehensive insight with respect to coal structure along with adoption of coal beneficiation methodologies.

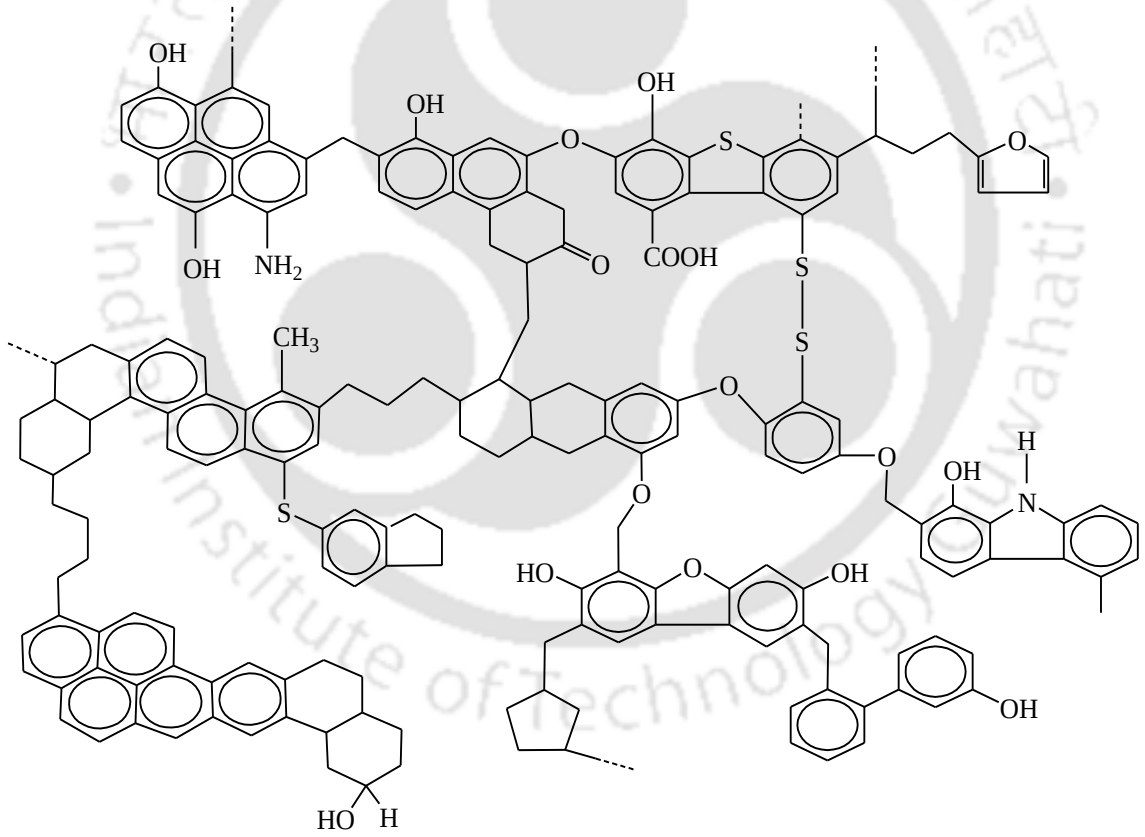

Fig. 1.1 A pseudo-coal molecular structure [3]

1.2 Combustion and Pyrolysis of Coal

Coal primarily consists of a network of aromatic and aliphatic hydrocarbons which inherently affects its physico-chemical properties along with its pyrolysis and combustion characteristics [17]. During the oxidation and pyrolysis steps processes, large numbers of hydrocarbons, alternative fuels and chemicals are produced. Rapid loss of moisture and devolatilization is known to occur during the coal combustion process. High-pressure pyrolysis of hydrocarbon decreases the volatile matter and increase the H/C and O/C ratio which is beneficial for the spontaneous heating of coal at low temperature. Pyrolysis temperature is hence one of the key parameters to describe the physical and chemical properties of the char atomic structure [17-26]. At low temperature, coal oxidation is an important source for spontaneous combustion of coal which in turn contributes to greenhouse gas emission.

In such a scenario, the reaction mechanism can provide useful information with respect to the details of the consumption of oxygen and formation of the gas and solid phase oxidation products. The solid oxidation products like aliphatic and aromatic compounds and gaseous products such as CO, CO_2, and H_2O are known to form during the reaction (Fig. 1.2) [27-32]. These gases are more pronounced for liquefaction process where the interaction of cross-linking of coal surface and solvents play a vital role [1, 17, 19-21]. Oxygen-containing functional groups are known to reduce the calorific value. One possible way to reduce the oxygen functional groups is to dissolve the coals in a suitable solvent. A non-polar solvent such as toluene has limited ability to disrupt and swell the coal molecules so as to extract the soluble materials [32, 33]. Some of the acceptor group solvents such as pyridine provide strong hydrogen bonding to swell the coal particles. However, they also

fractionate a lesser amount of these hydroxyl groups [22-26, 33]. Pseudo solvents such as pyridine and tetracyanoethylene also gave comparable results for coal fractionation. Along with the conventional solvents, there is a need to explore other green solvents which may provide a better swelling ratio and also lower the oxygen-containing functional groups. In such a scenario Ionic Liquids are known to play a dominant role for coal beneficiation.

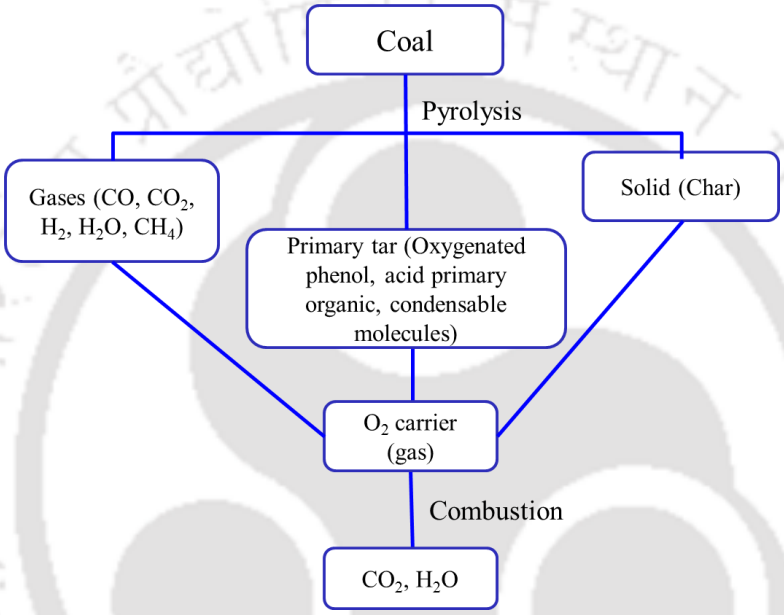

Fig. 1.2 Coal combustion and pyrolysis processes

1.3 Ionic Liquids

Ionic Liquids (IL's) are a combination of large organic cations with organic or inorganic anions having melting point below 100 ºC. IL's are chemically and thermally stable with negligible vapour pressure. Their non-volatility behavior implies lower impact within the environment. Some IL's are molten salts, but most are liquids at room temperature due to its inherent structure. It has two asymmetric ion i.e. the large organic structure of the cation and a small inorganic structure of the anion. The commonly used

cations are dialkylimmidazolium, alkylpyridinium, alkylpyrrolidinium, alkylammonium, alkyl-phosphonium with various organic and inorganic anions such as ([BF_4], [PF_6], [NTf_2], [CH_3COO], Br, Cl. These are shown in Fig. 1.3 and Fig. 1.4 [28, 29].

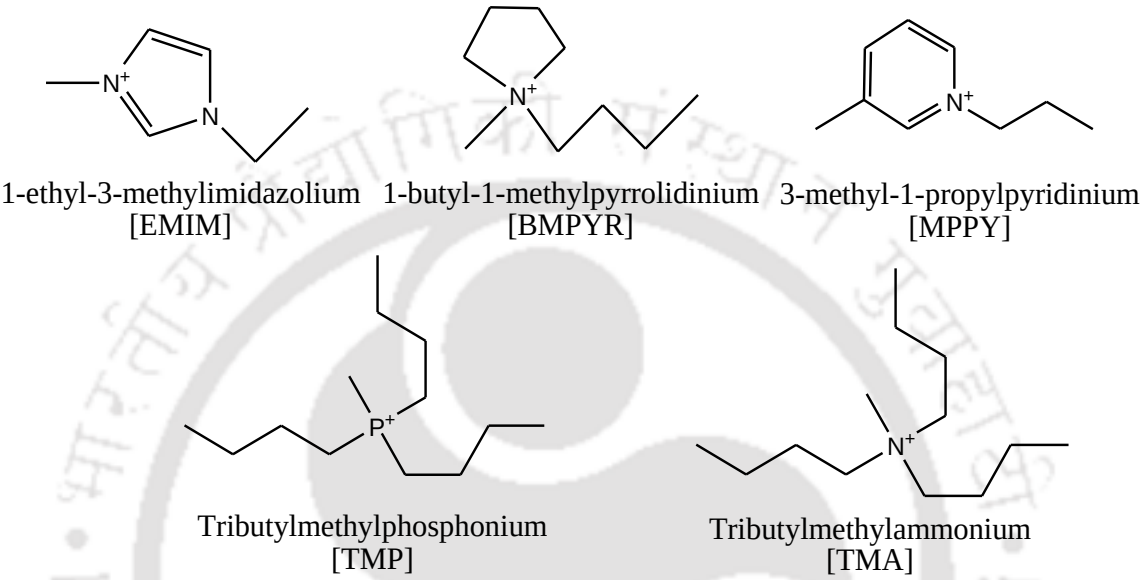

Fig. 1.3 List of commonly used cations

The selection of solvent is a tricky one as it needs to disrupt the intramolecular hydrogen bonding within the coal. With the disruption of intramolecular hydrogen bonding, –OH and –COOH groups gets dissolved in the IL's phase leading to higher calorific value. A coal with a higher surface area easily converts to light hydrocarbons such as SNG (Substitute Natural Gas), propane LPG, butane LPG, naphtha, and fuel oil [34, 35]. Till date, previous work has reported heterocyclic molecular orbital calculation studies with IL [29, 30]. In a recent work, it was observed that the alkyl ether chains (smaller oxygen numbers) of IL tends to control the molecular sizes of the hydrocarbon products obtained after coal liquefaction [34, 35]. ILs have been found to have excellent ability to disrupt intermolecular

interactions in Powder River Basin (PRB) and Illinois No. 6 coal by the fragmentation of coal network [36]. In their work, [EMIM][Cl] was used to fragment, and disperse coal, due to an excellent contact between ILs and coal.

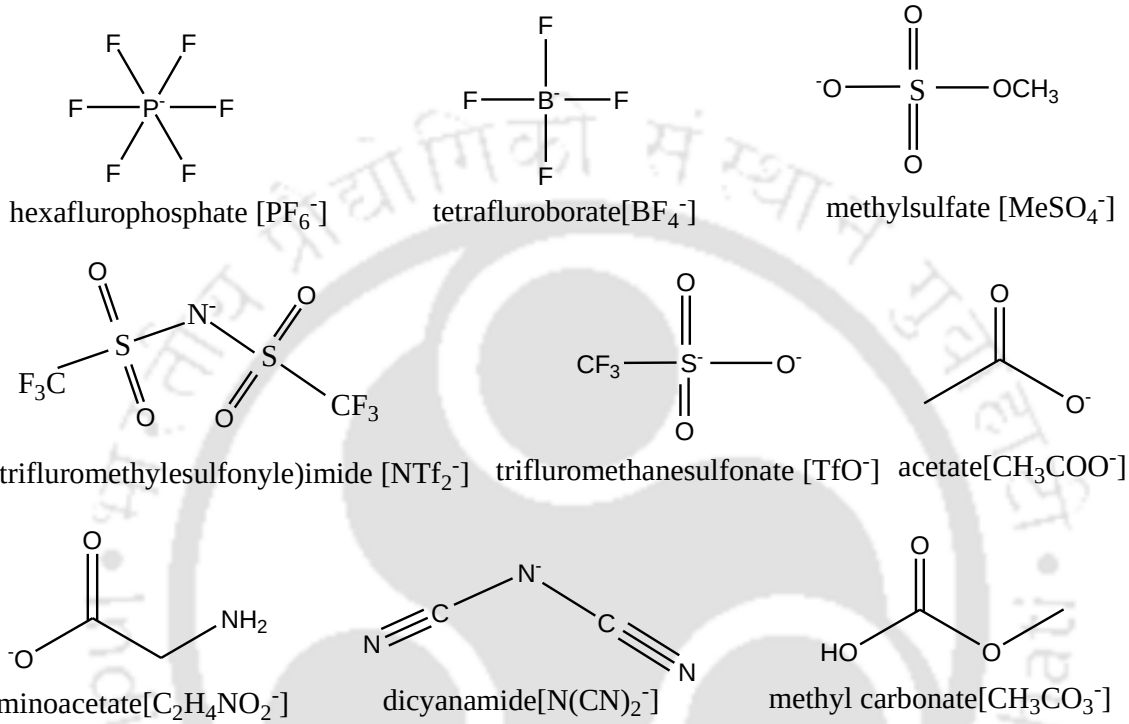

Fig. 1.4 List of commonly used anions

1.4 Extractability and Swelling Properties of Coal

Metallurgical coke consists of both ash and sulfur which in turn are linearly dependent on the coal used for production. Most of the Indian coals contain high ash with low sulfur. The extent of solvent swelling and solubility of coal is of practical importance for its processing, especially for coke oven batteries or plants. The nature of coal/solvent interactions and their effect on swelling and solubility provides important insights into the physical and chemical structure of coal. In conventional processing, steps such as

hydrogenation and hydrogenolysis within coal liquefaction are limited until coal particles have been fragmented or solubilized into smaller particles so as to allow a more intimate contact with catalysts for post-processing operations [2, 7].

For the fragmentation and solubilisation of coal, catalysts and coal are allowed to interact with each other [37-39] which results in the breakdown of covalent linkages and help in the subsequent formation of radicals. In a low and medium rank coal, a large amount of ionic clusters are formed due to the presence of carboxylate group. The subsequent ion/coal interactions thus play an important role for coal cohesion [40, 41]. Solvents such as pyridine, methanol, tetralin, N-methylpyrrolidinone (NMP) form strong hydrogen bonds with coal particles. They tend to swell coal particles and dissolve a significant portion to form very fine coal particles which increase the surface area. Raw coals are usually extracted at room temperature by mixing with a suitable solvent. The extracts obtained are fractionated with solvent and with increasing solubility and infusibility, the swelling properties of the coal tend to rise. The swelling ratio of the raw coal is inherently less than that of the extracted coal [42-46]. Coals such as upper Freeport coals are fractionated and the residue is then mixed with solvents. This helps in the formation of complexes with cation [47]. Coals were also found to fractionate at a micrometer-size with molybdenum disulfide (MoS_2) as a catalyst [33, 36, 48, 49].

One of the main drawback of conventional solvents are its low solubility and toxicity. Hence the focus has shifted on green solvents such as Ionic Liquids (ILs) [50]. Kim et al. [34] reported that with IL + catalyst mixtures an increased amount of lighter hydrocarbons were present and the rate of conversion of coal to hydrocarbons gave a marked improvement [34]. Cummings et al. [51] also observed a similar trend by pretreating coal

particles in ILs: [Emim][DCA] and [Bmim][Cl]. Among the studied IL's, [Bmim][Cl] gave a significant change of size in coal structure due to the large discrepancy in size of cation and anion [51].

1.5 Objectives

Based on the above studies, insights into the coal and IL interaction is beneficial for both coal liquefaction and benificiation. It helps in increasing the heating value as well as reducing the particle size. Therefore the following objectives are defined to provide a logical conclusion to the present thesis:

1. *Combustion and pyrolysis studies* of three different rank coals using Reactive Force Field Molecular Dynamic (ReaxFF MD) Simulation. This is required so as to understand the reaction mechanism for coal fragmentation.
2. *Identification of the best IL* based on Quantum Chemical Approach, primarily using the Higher Occupied Molecular Orbital (HOMO)-Lower Unoccupied Molecular Orbital (LUMO) approach; so as to quantify the secondary interactions.
3. *Initiate a pseudo-coal structure* and obtain its Solid-Liquid Equilibria using COnductor like Screening MOdel for Real Solvent (COSMO-RS) for the coal component (Solid) in IL (Liquid) phase.
4. *Conduct Experimental studies* as to validate the results obtained in (1) and (2) with pure IL's
5. *Observe the effect of IL* and a mixed solvent (IL + conventional solvent) on coal oxidation by thermal analysis.

1.6 Structure of Thesis

The thesis is organized into the following chapters:

Chapter 2 describes the combustion and pyrolysis analysis of three different coals using Reactive Force Field (ReaxFF) MD simulation studies. In this chapter, we investigate the reactive products using the ReaxFF force field for three different ranks (low to high) coals namely lignite, bituminous, and anthracite. The combustion process is explained in three different conditions such as fuel rich, stoichiometric and fuel lean. Similarly, pyrolysis is also conducted in three different densities. Thereafter combustion and pyrolysis processes is compared with available experimental results.

Chapter 3 discusses the computational methodology like Continuum Solvation Model (CSM) for the IL selection in the case of coal fragmentation. The choice of IL is quite cumbersome owing to its infinite cation and anion combination. Initially benchmarking studies are reported for data available in the literature for coal and solvents. Thereafter, a HOMO-LUMO interaction study coupled with Gibb's free energy of solvation and SLE predictions using COSMO-RS methodology were used for the selection of IL. IL's showing the highest solubility was chosen as potential solvent for the coal dissolution.

Chapter 4 includes experimental studies on the dissolution and dispersion of coal in selected IL's from chapter 3. The interactions between five IL's and four Indian coals were carried out to identify its dissolution and swelling characteristics. Five ILs consisting of different cations namely: 1-butyl-3-methylimidazolium hexafluorophosphate [BMIM][PF_6], 1-butyl-1-methylpyrrolidinium methyl carbonate [BMPYR][CH_3CO_3], 1-butyl-4-methylpyridinium tetrafluoroborate [BMPY][BF_4], tributylmethylphosphonium methylsulfate [MTBP][$MeSO_4$]

and tributylmethylammonium methylsulfate [TMA][$MeSO_4$] were chosen for the dissolution study. Morphological studies prior and post thermal treatment of the coal were recorded so as to determine the extent of swelling and fragmentation of coal particles. For the confirmation of the microscopic observation of coal structure, Fourier Transfer Infrared Spectroscopy (FTIR) analysis was also conducted for the study of species containing oxygen functional groups. The concluding section then discusses the solvent swelling and extractions studies with IL and coal.

Chapter 5 explains the effect of IL on coal oxidation by thermogravimetric analysis. The IL's selected in this work were 1-butyl-3-methylimidazolium hexafluorophosphate [BMIM][PF_6], 1-butyl-1-methylpyrrolidinium methyl carbonate [BMPYR][CH_3CO_3], and 1-butyl-4-methylpyridinium tetrafluoroborate [BMPY][BF_4]. They were subsequently used for dissolution studies in coal samples. Thermal analysis of raw coal and IL-pretreated coal were then conducted using Thermogravimetric Analyzer (TGA).

Chapter 6 summarizes the key results obtained from the present studies and also the future scope for coal beneficiation using IL's.

References

[1] World Coal Association, Annual Energy Report, 2011.

[2] D. W. Krevelen, Coal--typology, physics, chemistry, constitution, Elsevier Science1993.

[3] Coal, Wikipedia, The Free Encyclopedia., Wikipedia, 2014.

[4] N. Vasilakos, Advances in coal chemistry, (1988).

[5] A. A. Agroskin, Chemistry and technology of coal, Program for Scientific Translations [published for the US Department of the Interior and the National Science Foundation]1966.

[6] R. Kaji, Y. Hishinuma, Y. Nakamura, Low temperature oxidation of coals: Effects of pore structure and coal composition, Fuel, 64 (1985) 297-302.

[7] A. Küçük, Y. Kadıoğlu, M. Gülaboğlu, A study of spontaneous combustion characteristics of a Turkish lignite: particle size, moisture of coal, humidity of air, Combustion and Flame, 133 (2003) 255-261.

[8] S. R. Dhaneswar, S. V. Pisupati, Oxy-fuel combustion: The effect of coal rank and the role of char-CO_2 reaction, Fuel Processing Technology, 102 (2012) 156-165.

[9] C. Moon, Y. Sung, S. Ahn, T. Kim, G. Choi, D. Kim, Thermochemical and combustion behaviors of coals of different ranks and their blends for pulverized-coal combustion, Applied Thermal Engineering, 54 (2013) 111-119.

[10] Y. Chen, S. Mori, W.-P. Pan, Estimating the combustibility of various coals by TG-DTA, Energy and Fuels, 9 (1995) 71-74.

[11] S. Bhaskaran, A. Ganesh, S. Mahajani, P. Aghalayam, R. Sapru, D. Mathur, Comparison between two types of Indian coals for the feasibility of Underground Coal Gasification through laboratory scale experiments, Fuel, 113 (2013) 837-843.

[12] I. Adánez-Rubio, A. Abad, P. Gayán, L. F. De Diego, F. García-Labiano, J. Adánez, Performance of CLOU process in the combustion of different types of coal with CO_2 capture, International Journal of Greenhouse Gas Control, 12 (2013) 430-440.

[13] K. Baris, S. Kizgut, V. Didari, Low-temperature oxidation of some Turkish coals, Fuel, 93 (2012) 423-432.

[14] K. Baris, H. Aydin, V. Didari, Statistical modeling of the effect of rank, temperature, and particle size on low-temperature oxidation of Turkish coals, Combustion Science and Technology, 183 (2010) 105-121.

[15] K. Stańczyk, N. Howaniec, A. Smoliński, J. Świądrowski, K. Kapusta, M. Wiatowski, J. Grabowski, J. Rogut, Gasification of lignite and hard coal with air and oxygen enriched air in a pilot scale ex situ reactor for underground gasification, Fuel, 90 (2011) 1953-1962.

[16] T. Mendiara, F. García-Labiano, P. Gayan, A. Abad, L. de Diego, J. Adanez, Evaluation of the use of different coals in Chemical Looping Combustion using a bauxite waste as oxygen carrier, Fuel, 106 (2013) 814-826.

[17] N. Yoshizawa, K. Maruyama, T. Yamashita, A. Akimoto, Dependence of microscopic structure and swelling property of DTF chars upon heat-treatment temperature, Fuel, 85 (2006) 2064-2070.

[18] J. Yu, J. A. Lucas, T. F. Wall, Formation of the structure of chars during devolatilization of pulverized coal and its thermoproperties: A review, Progress in Energy and Combustion Science, 33 (2007) 135-170.

[19] D. Zeng, T. H. Fletcher, Effects of pressure on coal pyrolysis and char morphology, Energy and Fuels, 19 (2005) 1828-1838.

[20] L. Lu, V. Sahajwalla, D. Harris, Characteristics of chars prepared from various pulverized coals at different temperatures using drop-tube furnace, Energy and Fuels, 14 (2000) 869-876.

[21] J. P. Mathews, A. L. Chaffee, The molecular representations of coal–A review, Fuel, 96 (2012) 1-14.

[22] V. Kříž, Z. Brožová, Co-pyrolysis of coal/waste polymers mixtures, Acta Geodynamica et Geomaterialia, 4 (2007) 146.

[23] S. S. Tamhankar, J. T. Sears, Coal pyrolysis at high temperatures and pressures, Fuel, 63 (1984) 1230-1235.

[24] Y. Yun, G.-B. Lee, Effects of pressure in coal pyrolysis observed by high pressure TGA, Korean Journal of Chemical Engineering, 16 (1999) 798-803.

[25] O. Herbinet, P.-M. Marquaire, F. Battin-Leclerc, R. Fournet, Thermal decomposition of n-dodecane: Experiments and kinetic modeling, Journal of Analytical and Applied Pyrolysis, 78 (2007) 419-429.

[26] A. Arisoy, F. Akgün, Modelling of spontaneous combustion of coal with moisture content included, Fuel, 73 (1994) 281-286.

[27] H. Wang, B. Z. Dlugogorski, E. M. Kennedy, Coal oxidation at low temperatures: oxygen consumption, oxidation products, reaction mechanism and kinetic modelling, Progress in Energy and Combustion Science, 29 (2003) 487-513.

[28] H. Weingärtner, Understanding ionic liquids at the molecular level: Facts, problems, and controversies, Angewandte Chemie International Edition, 47 (2008) 654-670.

[29] N. V. Plechkova, K. R. Seddon, Applications of ionic liquids in the chemical industry, Chemical Society Reviews, 37 (2008) 123-150.

[30] G.-S. Liu, S. Niksa, Coal conversion submodels for design applications at elevated pressures. Part II. Char gasification, Progress in Energy and Combustion Science, 30 (2004) 679-717.

[31] J. Abichandani, C. Deradourian, R. Gannon, D. Stickler, J. Woodroffe, K. Neoh, Pressure effects on steam pyrolysis of coal, Fuel Processing Technology, 18 (1988) 133-146.

[32] C. Hu, S. Jiang, Z. Wu, M. Miao, Influence of ionic liquids on the species and content of coal functional group, Electronic Journal of Geotechnical Engineering, 19 (2014) 1365-1375.

[33] P. Painter, R. Cetiner, N. Pulati, M. Sobkowiak, J. Mathews, Dispersion of liquefaction catalysts in coal using ionic liquids, Energy and Fuels, 24 (2010) 3086-3092.

[34] J. W. Kim, D. Kim, C. S. Ra, G. B. Han, N.-K. Park, T. J. Lee, M. Kang, Synthesis of ionic liquids based on alkylimidazolium salts and their coal dissolution and dispersion properties, Journal of Industrial and Engineering Chemistry, 20 (2014) 372-378.

[35] W. Lan-yun, J. Shu-guang, X. Yong-liang, Z. Wei-qing, K. Li-wen, W. Zheng-yan, C. Ting-xiang, Effect of imidazolium based ionic liquids on coal exothermic oxidation by thermal analysis experiments, Procedia Engineering, 26 (2011) 647-651.

[36] P. Painter, N. Pulati, R. Cetiner, M. Sobkowiak, G. Mitchell, J. Mathews, Dissolution and dispersion of coal in ionic liquids, Energy and Fuels, 24 (2010) 1848-1853.

[37] F. Derbyshire, Role of catalysis in coal liquefaction research and development, Energy and Fuels, 3 (1989) 273-277.

[38] M. W. Haenel, J. Narangerel, U. B. Richter, A. Rufińska, The first liquefaction of high-rank bituminous coals by preceding hydrogenation with homogeneous borane or iodine catalysts, Angewandte Chemie International Edition, 45 (2006) 1061-1066.

[39] I. Mochida, K. Takeshita, Coal Liquefaction Fundamentals, by D. Duayne Whitehurst, ACS Symposium Series, 1980, pp. 259.

[40] P. Opaprakasit, A. W. Scaroni, P. C. Painter, Ionomer-like structures and π-cation interactions in Argonne Premium coals, Energy and Fuels, 16 (2002) 543-551.

[41] P. Painter, P. Opaprakasit, A. Scaroni, Ionomers and the structure of coal, Energy and Fuels, 14 (2000) 1115-1118.

[42] M. Iino, T. Takanohashi, S. Obara, H. Tsueta, Y. Sanokawa, Characterization of the extracts and residues from CS_2-N-methyl-2-pyrrolidinone mixed solvent extraction, Fuel, 68 (1989) 1588-1593.

[43] M. Iino, T. Takanohashi, H. Ohsuga, K. Toda, Extraction of coals with CS_2-N-methyl-2-pyrrolidinone mixed solvent at room temperature: Effect of coal rank and synergism of the mixed solvent, Fuel, 67 (1988) 1639-1647.

[44] M. Fujiwara, H. Ohsuga, T. Takanohashi, M. Iino, Swelling of the extracts and residues from carbon disulfide-N-methyl-2-pyrrolidinone mixed solvent extraction, Energy and Fuels, 6 (1992) 859-862.

[45] T. Ishizuka, T. Takanohashi, O. Ito, Effects of additives and oxygen on extraction yield with CS_2-NMP mixed solvent for argonne premium coal samples, Fuel, 72 (1993) 579-580.

[46] T. Takanohashi, M. Iino, M. Nishioka, Investigation of associated structure of Upper Freeport coal by solvent swelling, Energy and Fuels, 9 (1995) 788-793.

[47] T. Takanohashi, T. Kudo, M. Iino, Coal gels formed by coal-solvent interactions, Energy and Fuels, 12 (1998) 470-475.

[48] G. S. F. Tianbo, L. Yunyi, Application of ionic liquid [BMIm]BF_4 in swelling pretreatment of Shenhua coal [J], Coal Conversion, 2 (2010) 008.

[49] L. R. Radovic, P. L. Walker, R. G. Jenkins, Importance of catalyst dispersion in the gasification of lignite chars, Journal of Catalysis, 82 (1983) 382-394.

[50] H. K. A. H. Jadhav, Short oligo (ethylene glycol) functionalized imidazolium dicationic room temperature ionic liquids: Synthesis, properties, and catalytic activity in azidation, Chemical Engineering Journal 264 (2012) 200–202.

[51] J. Cummings, K. Shah, R. Atkin, B. Moghtaderi, Physicochemical interactions of ionic liquids with coal; the viability of ionic liquids for pre-treatments in coal liquefaction, Fuel, 143 (2015) 244-252.

Chapter 2

Combustion and Pyrolysis Studies using Reactive Force Field Simulations (ReaxFF)

2.1 Introduction

One of the major problems encountered by coke oven batteries has been the continuous deterioration in the quality of coal resulting in coke with high ash content and poor strength. This has contributed to the phenomenal increase in the demand of coke in blast furnaces in developing countries. Coke having both ash and sulphur content are linearly dependent on the rank of the coal used. Thus an important objective for studying coal combustion and pyrolysis is to evaluate the fixed carbon in the fuel portion of coke or coal. The higher the fixed carbon, the higher the thermal value of coke and the lower the environmental impact. While combustion of coal is primarily used for power generation, its use is also manifested in other domains such as material construction, town gas, and iron and steel industry. Similarly, coal pyrolysis contributes multiple products such as gas, liquid, and char. The gas, liquid, and char produced from the coal can further be used as fuel oil, chemical feedstock, boiler feedstock, and as a raw material for iron. It also plays a vital role in the production of liquid fuels and chemicals. However, an increase in coal utilization results in greenhouse gas emissions from fossil fuel-fired power generation. The greenhouse gas emissions primarily CO and CO_2 thus need to be quantified first and then reduced by improving efficiency in gasification process [1-4].

Therefore, to understand the combustion phenomena, the chemical kinetics and thermodynamic models are important aspects [5]. Hence it is very essential to study the combustion phenomena even though the detailed structural model of coal or char is complicated and complex [6]. Recently a complex structure of coal and char was described by experimental and atomistic simulation [6-8]. This work has opened pathways in understanding the combustion and pyrolysis phenomena of coal which otherwise was impossible few years ago. This chapter thus attempts to study the

combustion and pyrolysis studies of three different ranks (low to high) coals namely lignite, bituminous, and anthracite using the ReaxFF reactive force field (ReaxFF) [9] molecular dynamic (MD) simulation. The ReaxFF MD simulation is accurately close to quantum mechanics (QM) as well as experimental results [10-12]. Further, ReaxFF MD system is known to be 10^6 times faster than the methods of quantum mechanics (QM) and 100 times faster than that of typically used by semi-empirical methods [9].

ReaxFF [9] has been developed with force fields [8, 13-20] for large scale systems to describe the bond order, bond distance, and bond dissociation energy for the total atomic structure. A common advantage for both MD and ReaxFF is that the force field parameters are easily obtained from QC (Quantum Chemical) calculations which are computationally affordable. Keeping the above advantages in mind, ReaxFF was used in this chapter to predict the reaction mechanism for the coal having varying rank such as lignite, bituminous, and anthracite. All the ReaxFF simulations were implemented in ADF suite of programs [21]. The intermediate products formed or evolved from the reaction were also analysed. Thereafter comparison of combustion behaviour for all the three coals was done with available experimental data.

2.2 ReaxFF Reactive Force Field

ReaxFF [9] is based on the covalent formalism [22] and the bond order principle which relates the bond energy to bond lengths, valence angles, and torsion angle [23]. It was developed for bond dissociation and formation to efficiently simulate molecular dynamics of large-scale chemical systems containing more than a thousand atoms. The force field parameters are derived from the quantum mechanics (QM) and are then directly applied to the system. ReaxFF combines quantum mechanics (QM) and classical mechanics models. It is based on the empirically determined interatomic potential where

the potential energy of the system is described by different energies of the system (equation (2.1)) [9, 24].

Thus ReaxFF is a bond order dependent force field where the bond orders are calculated from the interatomic distances which are updated at every iteration during reactive MD-simulation. The total energy of the system is thus the sum of partial non-bonded and covalent interaction energy (equation (2.1)) [9]. It should be noted that one of the differences between ReaxFF and classical MD lies in the fact that the charges are required to be computed for every time step. Like classical MD, it also has a bonded and a non-bonded potential form of energy. In such a strategy, a bond order correction is a one-step correction term to organise the 2-body bond order term. This implies removal of unphysical weak bond orders for fully coordinated atoms. Further to account for the over coordination and under-coordination of valence atoms, correction based on bond orders are used. Similarly, the non-bonded van der Waals energy and Coulomb energy terms derived from the partial charges are also computed. The total energy of the system is then the sum of the partial energy distribution terms, which are described by equation (2.1) [9],

$$E_{system} = E_{bond} + E_{over} + E_{under} + E_{val} + E_{pen} + E_{tors} + E_{conj} + E_{vdWaals} + E_{Coulomb} \qquad (2.1)$$

where E_{system} is the potential energy (kcal/mol) of the system which describes the interaction between the atoms of the systems. E_{bond} represents the bond energy due to the interatomic distance between a pair of atoms. It calculates the bond order between the interatomic distances, which is given by equation (2.2) [9],

$$E_{bond} = -D_e^{\sigma}.BO_{ij}^{\sigma}.\exp\left[p_{be,1}\left(1-\left(BO_{ij}^{\sigma}\right)^{p_{be,2}}\right)\right] - D_e^{\pi}.BO_{ij}^{\pi} - D_e^{\pi\pi}.BO_{ij}^{\pi\pi} \qquad (2.2)$$

$BO_{ij}^{'}$ is the bond order between a pair of atoms which is obtained directly from the interatomic distances. For e.g. if a pair of atoms like carbon-hydrogen or hydrogen-hydrogen is observed, then σ-bond is accounted; while for carbon-carbon, a bond order of three results in one sigma and two π-bonds. $p_{be,1}$, $p_{be,2}$ D_e^{π} and $D_e^{\pi\pi}$ are force field parameters. Hence the total bond order is given by:

$$BO_{ij}^{'} = BO_{ij}^{\sigma} + BO_{ij}^{\pi} + BO_{ij}^{\pi\pi} = \exp\left[p_{bo,1}\cdot\left(\frac{r_{ij}}{r_o^{\sigma}}\right)^{p_{bo,2}}\right] + \exp\left[p_{bo,3}\cdot\left(\frac{r_{ij}}{r_o^{\pi}}\right)^{p_{bo,4}}\right] + \exp\left[p_{bo,5}\cdot\left(\frac{r_{ij}}{r_o^{\pi\pi}}\right)^{p_{bo,6}}\right] \quad (2.3)$$

Here the first, second, and third exponential terms indicate the bond orders due to a single (σ), double (π), and triple (double π) bond order contributions respectively. Each bonding parameter p and bond radii r_o have been parameterized such that atomic distances and bond strength agrees with quantum mechanically predicted values for the same species with distance r_{ij} apart.

E_{over} and E_{under} represents over- and under- coordinated energy, respectively. After the correction of the original bond order, a degree of over coordination with respect to its valency may occur. To prevent this physical phenomenon where non-valence electrons get drawn into bonding, ReaxFF penalizes it in the form of E_{over} which is given below:

$$E_{over} = p_{over}.\Delta_i.\left(\frac{1}{1+\exp(\lambda_6.\Delta_i)}\right) \quad (2.4)$$

where $\Delta_i^{'} = \sum_{j=1}^{nbond} BO_{ij}^{'} - Val_i$ is the degree of deviation for the sum of the uncorrected bond orders around an atomic centre from its valency Val_i. In a similar manner, the under-coordination term is represented as below:

$$E_{under} = -p_{under} \cdot \frac{1-\exp(\lambda_7.\Delta_i)}{1+\exp(-\lambda_8.\Delta_i)} . f_6\left(BO_{ij,\pi}, \Delta_j\right) \tag{2.5}$$

where $f_6\left(BO_{ij,\pi}, \Delta_j\right) = \dfrac{1}{1+\lambda_9.\exp\left(\lambda_{10}.\sum_{j=1}^{neighbors(i)} \Delta_j.BO_{ij,\pi}\right)}$

Other terms, including E_{val} for valence angle *i-j-k*, (*i*, *j*, *k* are location for three atoms) is given below in equation (2.6).

$$E_{val} = f_7(BO_{ij}).f_7(BO_{jk}).f_8(\Delta_j)\left(k_a - k_a \exp\left[-k_b\left(\Theta_0 - \Theta_{ijk}\right)^2\right]\right) \tag{2.6}$$

where $f_7(BO_{ij}) = 1-\exp(-\lambda_{11}.BO_{ij}^{\lambda_{12}})$

$$f_8(\Delta_j) = \frac{2+\exp\left(-\lambda_{13}.\Delta_j\right)}{1+\exp\left(-\lambda_{13}.\Delta_j\right)+\exp\left(p_{v,1}.\Delta_j\right)}\left[\lambda_{14} - (\lambda_{14}-1).\frac{2+\exp\left(\lambda_{15}.\Delta_j\right)}{1+\exp\left(\lambda_{15}.\Delta_j\right)+\exp\left(-p_{v,2}.\Delta_j\right)}\right]$$

BO_{ij}, BO_{jk} are the bond orders for each of the two bonds connecting the three atoms within an angle. k_a and k_b are the harmonic force constants that determine the depth and width of the angular potential, Θ_0 is the equilibrium angle and Θ_{ijk} is the valence angle. Thus, if one of the two bonds in the angle break, the valence angle energy disappears smoothly. The energy contribution from the valence angle term goes to zero as the bond orders in the valence angle goes to zero.

To stabilize the system with two double bonds sharing an atom in a valence angle, one additional term i.e. penalty energy E_{pen} used is given by:

$$E_{pen} = \lambda_{19} \cdot f_9\left(\Delta_j\right) \cdot \exp\left[-\lambda_{20}\left(BO_{ij} - 2\right)^2\right] \cdot \exp\left[-\lambda_{20}\left(BO_{jk} - 2\right)^2\right] \tag{2.7}$$

where $f_9\left(\Delta_j\right)=\dfrac{2+\exp\left[-\lambda_{21}\Delta_j\right]}{1+\exp\left[-\lambda_{21}\Delta_j\right]+\exp\left[\lambda_{22}\Delta_j\right]}$

E_{tors} (Equation (2.8)) represents the torsion energy i.e. the position where bond order tends to zero and is greater than one.

$$\begin{aligned}E_{tor} &= f_{10}(BO_{ij},BO_{jk},BO_{kl})\sin\Theta_{ijk}\sin\Theta_{jkl}[\frac{1}{2}V_1\left(1+\cos\omega_{ijkl}\right)\\&+\frac{1}{2}V_2\exp\left[p_{tor1}\left(BO_{jk}-1+f_{11}\left(\Delta_j,\Delta_k\right)\right)^2\right]\left(1-\cos 2\omega_{ijkl}\right)\\&+\frac{1}{2}V_3\left(1+\cos 3\omega_{ijkl}\right)]\end{aligned} \qquad (2.8)$$

where $f_{10}(BO_{ij},BO_{jk},BO_{kl})=\left(1-\exp[-\lambda_{23}BO_{ij}]\right)\left(1-\exp[-\lambda_{23}BO_{jk}]\right)\left(1-\exp[-\lambda_{23}BO_{kl}]\right)$

$$f_{11}\left(\Delta_j,\Delta_k\right)=\frac{2+\exp\left[-\lambda_{24}.\left(\Delta_j+\Delta_k\right)\right]}{1+\exp\left[-\lambda_{24}.\left(\Delta_j+\Delta_k\right)\right]+\exp\left[-\lambda_{25}.\left(\Delta_j+\Delta_k\right)\right]}$$

This contribution smoothly disappears when one of the bonds in the torsion angle breaks or the valence angle approaches π. The torsion angle is denoted as ω_{ijkl} ,

E_{conj} is denoted as conjugate effect of the molecular energy, especially for the aromatic molecules where successive bond have bond order values of 1.5. The conjugate energy is given by:

$$E_{conj}=f_{12}\left(BO_{ij},BO_{jk},BO_{kl}\right).\lambda_{26}.\left[1+\left(\cos^2\omega_{ijkl}-1\right).\sin\Theta_{ijk}.\sin\Theta_{jkl}\right] \qquad (2.9)$$

where $f_{12}\left(BO_{ij},BO_{jk},BO_{kl}\right)=\exp\left[-\lambda_{27}.\left(BO_{ij}-1\frac{1}{2}\right)^2\right].\exp\left[-\lambda_{27}.\left(BO_{jk}-1\frac{1}{2}\right)^2\right].\exp\left[-\lambda_{27}.\left(BO_{kl}-1\frac{1}{2}\right)^2\right]$

We now focus on the two penultimate terms contributing to the non-bonded interaction, namely $E_{vdWaals}$ which is the non-bonded van der Waals interaction. This term avoids

excessive high repulsion between bonded atoms or atoms sharing a valence angle. The van der Waals interaction energy is given below:

$$E_{vdWaals} = D_{ij}.\left\{\exp\left[\alpha_{ij}\left(1-\frac{f_{13}(r_{ij})}{r_{vdW}}\right)\right]-2.\exp\left[\frac{1}{2}.\alpha_{ij}.\left(1-\frac{f_{13}(r_{ij})}{r_{vdW}}\right)\right]\right\} \qquad (2.10)$$

where $f_{13}(r_{ij}) = \left[r_{ij}^{\lambda_{29}} + \left(\frac{1}{\lambda_{\omega}}\right)^{\lambda_{28}}\right]^{1/\lambda_{28}}$ and α_{ij}, r_{vdW} are van der Waals parameters.

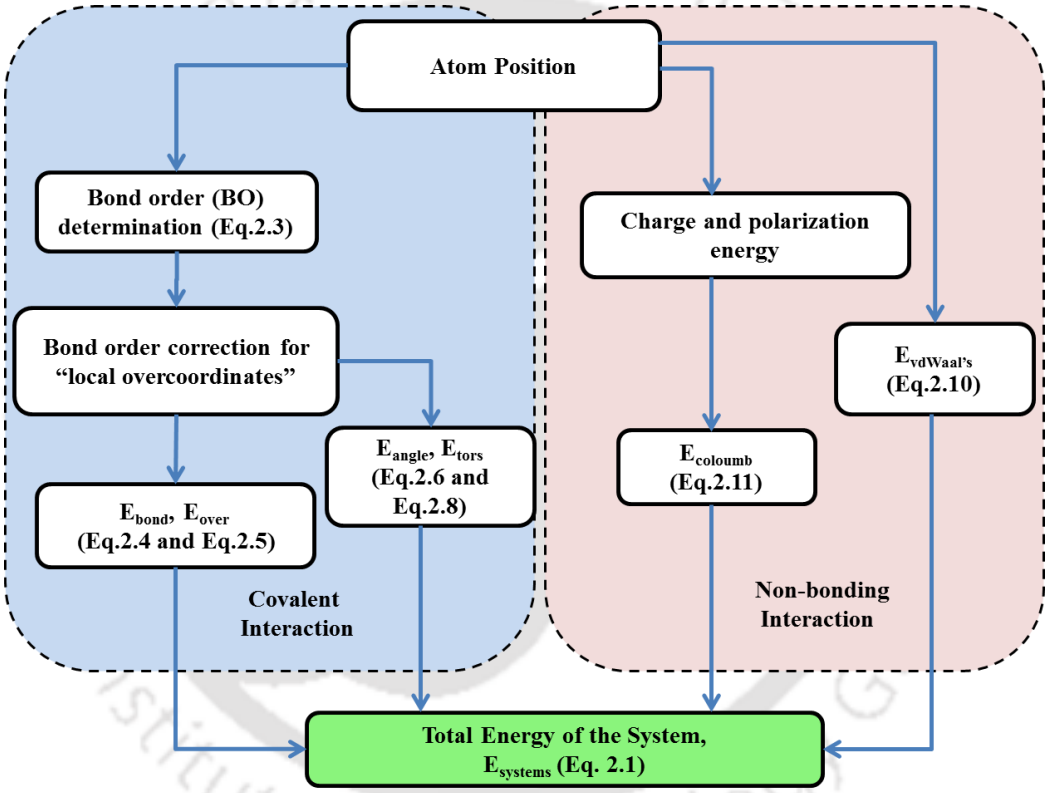

Fig. 2.1 Overview of total energy of the system in ReaxFF reactive force field [24]

$E_{Coulomb}$ represents Coulomb interaction between all atom pairs. A shielded Coulomb potential is used as adjustment for orbitals overlapping between close distances atoms.

$$E_{Coulomb} = C.\frac{q_i.q_j}{\left\{r_{ij}^3 + \left(1/\gamma_{ij}\right)^3\right\}^{1/3}} \quad (q_i,\ q_j \text{ are atomic charges}) \qquad (2.11)$$

where γ_{ij} represents the shielded Coulomb potential which can be optimized to reproduce the charge equilibration orbital overlap correction.

Thus in summary ReaxFF provides a relationship between the bond order/bond distance and bond order/bond energy for the dissociation and formation of chemical bond during the MD-simulation. A flow chart for ReaxFF is summarized in Fig. 2.1.

2.3 Computational Details

The simulation of the systems studied here should accurately model the coal systems with elastic bonds exhibiting translational, rotational, torsional, and vibrational motion. As a rule of thumb, this requires a time step of an order of magnitude smaller than the shortest vibrational motion of C-H and O-H bond for the coal molecules. This comes out to be approximately 0.1-0.25 fs. A smaller time step is preferred with ReaxFF as the charges and bond orders are allowed to change at every time step. In reactive molecular dynamics, covalent bonds of reactant molecules involve breaking of old bonds and formation of new bonds [25]. A 1 fs time step will be quite large and newly formed bonds will have huge vibration. Thus the simulation will be unstable; hence a time step of 0.1 to 0.25 fs is usually used. In the simulation of non-reactive systems (classical MD) we usually give a minimum time step of 1 fs unless we are dealing with proteins [9, 13, 14].

For high-temperature (~3000 K) simulations, a time step of 0.1 fs allows a proficient coverage of the phase space and collisions. This helps the reaction to come about smoothly. This has been usually the case for Ammonia-Borane decomposition which was studied earlier [11]. In ReaxFF, we always maintain a balance between computational accuracy and computational time. The higher temperature is only given to the system to increase the velocity of molecules and thus to enhance the probability of

faster collision. As mentioned previously, it is used to reduce the bond length to a user-defined value (or default value of program itself). This step creates a huge amount of energy which needs to be dissipated. To dissipate this energy, if the system, as well as thermostat temperature, is kept low, huge computational time will be required to control the set temperature. To optimize this time of computing, the simulation is run at an elevated temperature. This makes dissipation of heat consume lesser amount of time [9, 11]. Keeping all this in mind, ReaxFF reactive simulation was adopted to study the pyrolysis and combustion of brown coal.

2.3.1 Pyrolysis Process

The structures of the three different types of coal are taken from literature [26-29] and are given in Fig. 2.2. Eighteen anthracite coal molecules, 45 bituminous coal molecules, and 16 lignite coal molecules were randomly placed in a periodic box of 60×60×60 Å, 56×56×56 Å, and 44×44×44 Å with densities having 0.08 g/cm^3, 0.1 g/cm^3, and 0.2 g/cm^3 respectively. The varying numbers of coal molecules were taken so as to make the number of atoms equal in each case. This allows a uniform comparison for anthracite, bituminous, and lignite coal properties. The C/H/O/N/S/B force field was used to study the ReaxFF reactive simulation [11, 15, 30].

Initially, the system was minimized at a lower temperature of 10 K in a NVE ensemble. The energy minimization was conducted for 10 ps with a time step of 0.25 fs to optimize the intermolecular interaction and prepare the structure of coal for longer simulation. The C−O and O−H bond parameters were switched off during the equilibration simulations to prevent reaction occurrence. The process is a non-reactive process in which simply the overlap of the assembly of atoms (if any) are detected and subsequently corrected. After minimization, they are equilibrated in NVT ensemble for 5

ps with a time step of 0.25 fs. The temperature of the equilibrated system was raised up to 4000 K at a rate of 20 K/ps. The atomic position, velocity, and acceleration were saved at 3000, 3500, and 4000 K respectively.

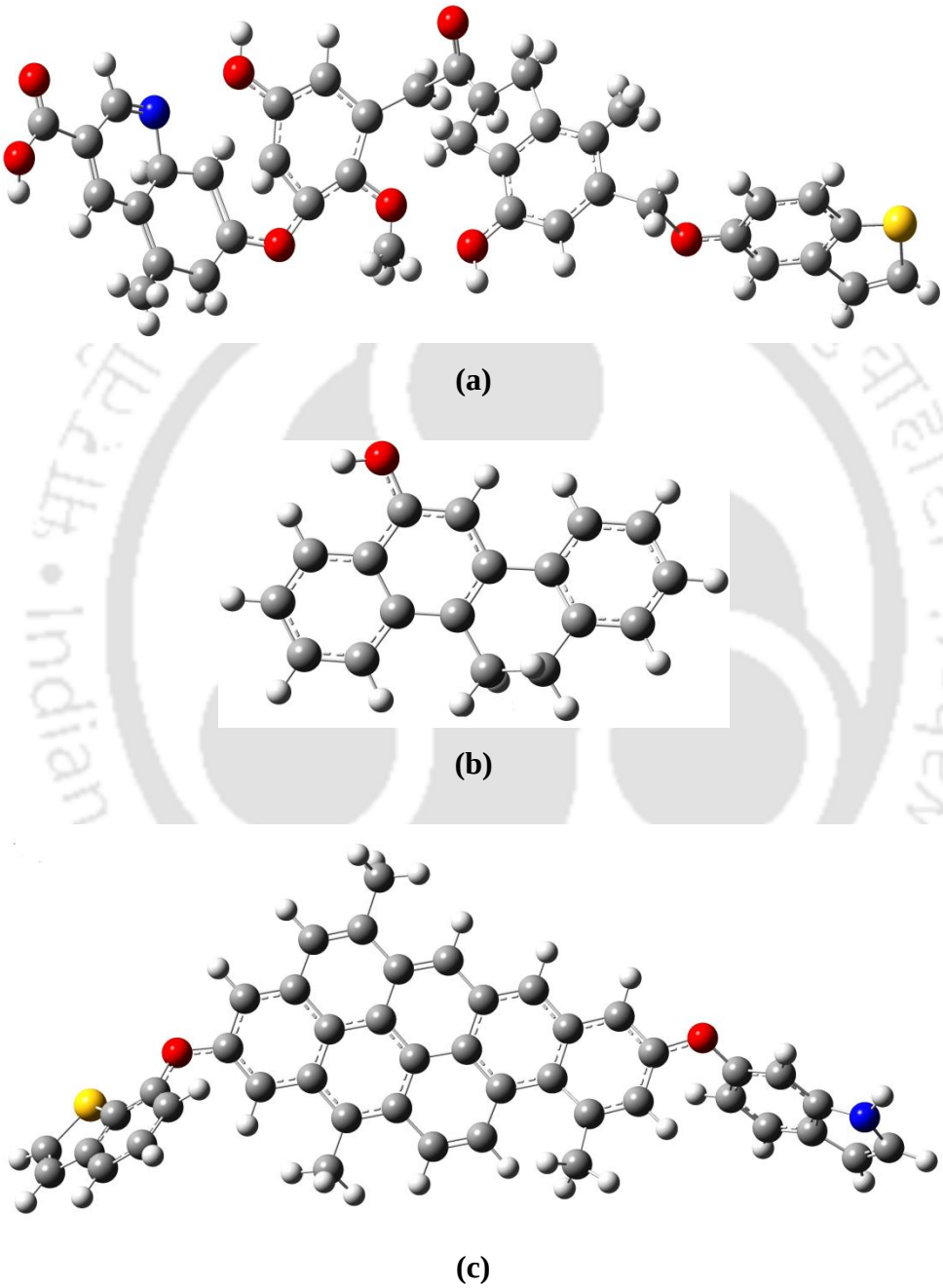

(a)

(b)

(c)

Fig. 2.2 Structure of (a) lignite ($C_{39}H_{35}O_{10}NS$) (b) bituminous ($C_{18}H_{14}O$) and (c) anthracite coals ($C_{45}H_{29}O_2NS$) (Colour represents the different atoms such as yellow: Sulphur, blue: Nitrogen, grey: Carbon, red: Oxygen, white: Hydrogen atoms respectively [26-29])

This heating rate would eventually not affect the reaction mechanism, but only alter the time at which the reactant begins to decompose. Using Berendsen thermostat, the temperature was controlled with a damping constant of 100 fs. A 0.25 fs time step along with a total time of 200 ps was used to study the pyrolysis process. The total time (200 ps) and time step (0.25 fs) were chosen from previous work [17-19, 30], where the thermal decomposition occurred at a small time. This also gives reasonable descriptions for the oxidation reaction of hydrocarbon [15]. For the analysis of the intermediates and products formed during the MD simulation, a 0.3 bond order cut-off was used for the identification of the molecular species [12].

2.3.2 Combustion Process

For the combustion process, systems were created at densities of 0.08 g/cm^3, 0.1 g/cm^3, and 0.2 g/cm^3 respectively. Here the systems comprise of (a) 14 anthracite coal molecules, (b) 35 bituminous coal molecules, and (c) 12 lignite coal molecules, placed in periodic boxes of dimension 93×93×93 Å, 79×79×79 Å, and 69×69×69 Å respectively. In each case, three combustion criteria namely with 250, 500, and 1000 numbers of O_2 molecules were adopted so as to achieve an equivalence ratio (ϕ) of 0.5, 1.008, and 2.0 respectively. This is also referred as fuel lean, stoichiometric, and fuel rich combustion respectively. The equivalence ratio (ϕ) is expressed as;

$$Equivalent\ ratio\ (\phi) = \frac{Fuel\ (coal)}{Oxygen} \tag{2.12}$$

The system was minimized at a lower temperature of 10 K using NVE-MD (fixed number of atoms (N), fixed volume (V), and a total energy (E)) ensemble simulation for all the coal molecules. The system was subsequently equilibrated in a NVT ensemble for 5 ps at a time step of 0.25 fs. Thereafter, production run was performed at the same ensemble similar to pyrolysis process at a temperature range of 2000-4000 K for 200 ps

[30]. Using Berendsen thermostat, the temperature was controlled at a damping constant of 100 fs and 0.25 fs time step. To analyse the intermediates and the products, a 0.3 bond order cut-off was used. Fig. 2.3 shows the flow chart for details ReaxFF MD-simulation process.

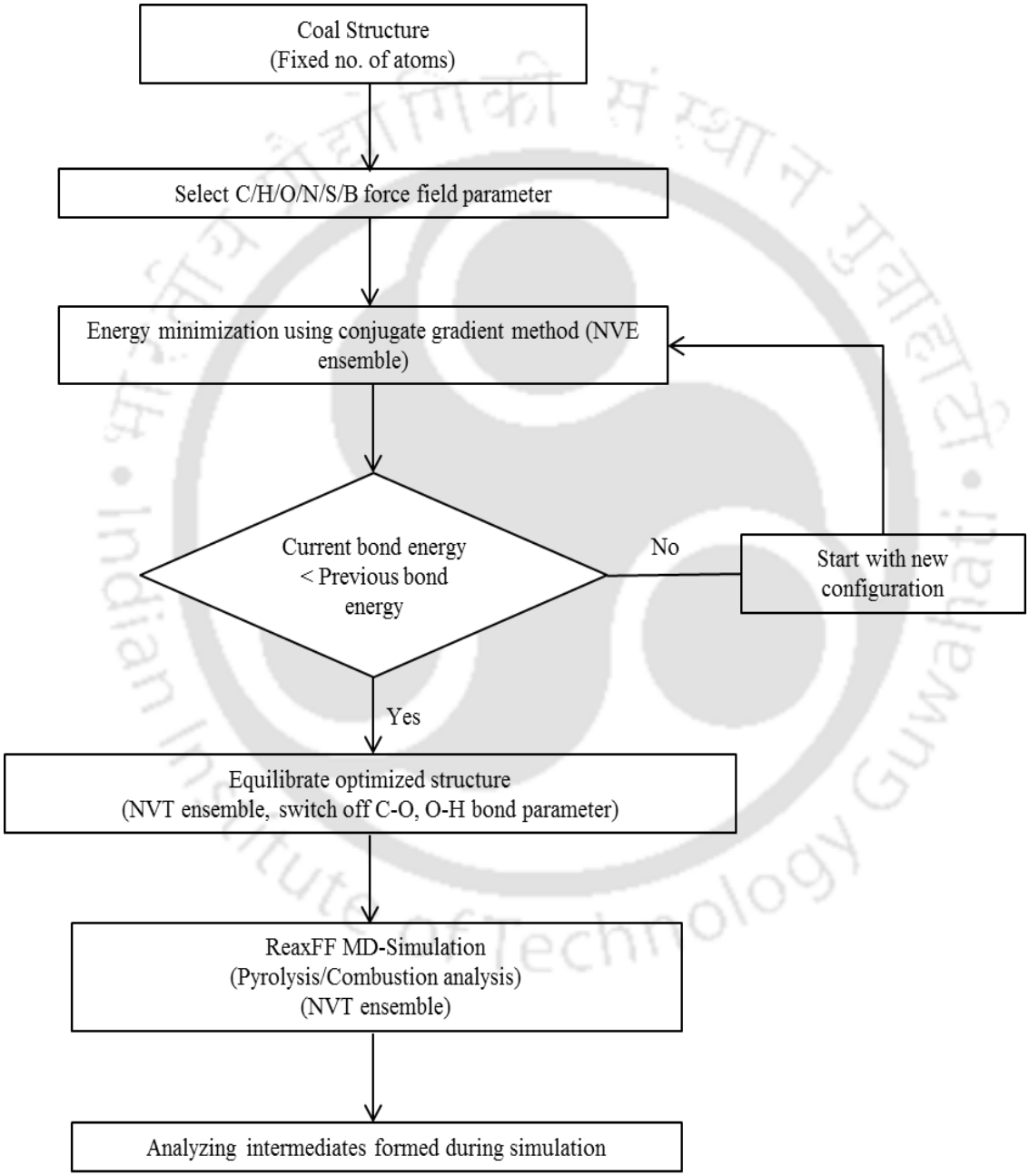

Fig. 2.3 Flow Chart of the Combustion and Pyrolysis of coal

2.4 Results and Discussions

We shall now use ReaxFF simulations for two sets of coal namely (a) brown coal (section 2.4.1) and (b) anthracite, bituminous and brown coal (section 2.4.2). The combustion and pyrolysis characteristics along with a comparison with experimental data are also presented and compared in section 2.4.2 for effective benchmarking.

2.4.1 Pyrolysis and Combustion Analysis of Brown Coal

2.4.1.1 Product Analysis during Combustion Process

To analyse the combustion environment and temperature effect on the product distribution, a series of ReaxFF combustion simulation have been carried out at different conditions like fuel lean (ϕ=0.5), fuel rich (ϕ=2), and stoichiometric (ϕ=1) composition at temperature range of 2000-4000 K. Thermal decomposition and direct oxidation by different ratio of oxygen provides the detailed information of the major products. Fig. 2.4 shows that the evolution of gaseous products (CO_2, CO, H_2O, H_2) formed in the initial stage with oxygen at different equivalent ratio for constant temperatures. From Fig. 2.4 we can observe that in the case of fuel lean conditions the rate of product generation was greater in comparison to fuel rich condition. This is due to the higher amount of O_2 present which agrees with the experimental results [31, 32]. Due to the excess oxygen in the fuel lean combustion, the concentration of CO_2 was found to be higher than CO. In the fuel rich combustion condition, there is an incomplete conversion of CO and H_2 which is the reason around 20-25 CO molecules are present in the fuel rich combustion, whereas 80-100 CO molecules are present in the fuel lean conditions. The rate of product generation is higher in fuel lean conditions as compared to fuel rich condition. This is due to the coal combustion rate which is faster due to the higher amount of oxygen present in the fuel lean condition. The high level of oxygen present in the system

decomposes the coal molecules very easily. In the case of fuel rich condition, there would be incomplete conversion and some amount of gaseous products like CO, H_2 is left due to insufficient oxygen present in the combustion reaction. This is in agreement with the experimental observation that the concentration of CO_2 production is four times that of CO by continuous combustion of coal [2]. Oxidation of CO to CO_2 is a very slow process in the combustion reaction. Therefore, in the case of fuel lean combustion, at a longer time scale, a portion of the CO molecules oxidises to CO_2 [33]. When the brown coal is oxidized at high temperature, a large amount of CO_2 is produced. During coal combustion, small amount of H_2O and H_2 are also formed due to hydrogen content in the brown coal.

From Fig. 2.4, it was observed that the rate of O_2 decreased more rapidly at high temperature and the initiation reaction time was found to be less. The combustion reaction undergoes rapidly due to the rapid increase of temperature. CO_2 production is favoured at low temperature, whereas CO forms at higher temperature [34]. Again from Fig. 2.4, it was observed that at high temperature, CO is more stable as compared to the CO_2 formation. This also agrees with the previous experimental findings [6, 33, 35]. From Fig. 2.5, it was noticed that the numbers of oxygen molecules consumed are very rapid in the combustion reaction of brown coal with an increase in temperature. Fig. 2.6 shows the comparison of oxygen consumption for all the three cases (fuel lean, fuel rich, and stoichiometric). The oxygen consumption was the largest in the case of fuel rich combustion which was due to the small amount of oxygen present in the combustion reaction.

2.4.1.2 Effect of Temperature on Combustion Process

Fig. 2.7 shows the time distribution of potential energy with different temperature in the combustion reaction. During production run, the potential energy was decreases rapidly with increase in temperature. This is directly proportional to the oxygen consumption which suggests that the combustion of brown coal with oxygen is an exothermic reaction [35]. Fig. 2.8 shows the time evolution of potential energy in fuel lean, fuel rich, and stoichiometric combustion. Potential energy was again highest in fuel rich condition due to less number of molecules present in the combustion reaction.

2.4.1.3 Major Intermediates/Products produced during Combustion Process

In combustion of brown coal, large amount of gaseous products and important intermediates are produced during combustion reaction. Gaseous products like CO_2 and H_2O are the main components and some valuable intermediates like CH_4, C_2H_4, CH_3, and H_2CO are also produced. From Fig. 2.9, it can be seen that the number of CO_2 and H_2O molecules increased with temperature. During brown coal combustion process formaldehyde (H_2CO) molecules was found to be an important intermediate, but at high temperature the H_2CO formation is slightly unstable and decreases rapidly. Fig. 2.10 shows the main products distribution sampling at 175 ps and 250 ps. In both the cases high amount of products were formed when temperature was higher, however CO_2 was consumed at a lower rate in high temperature at 250 ps.

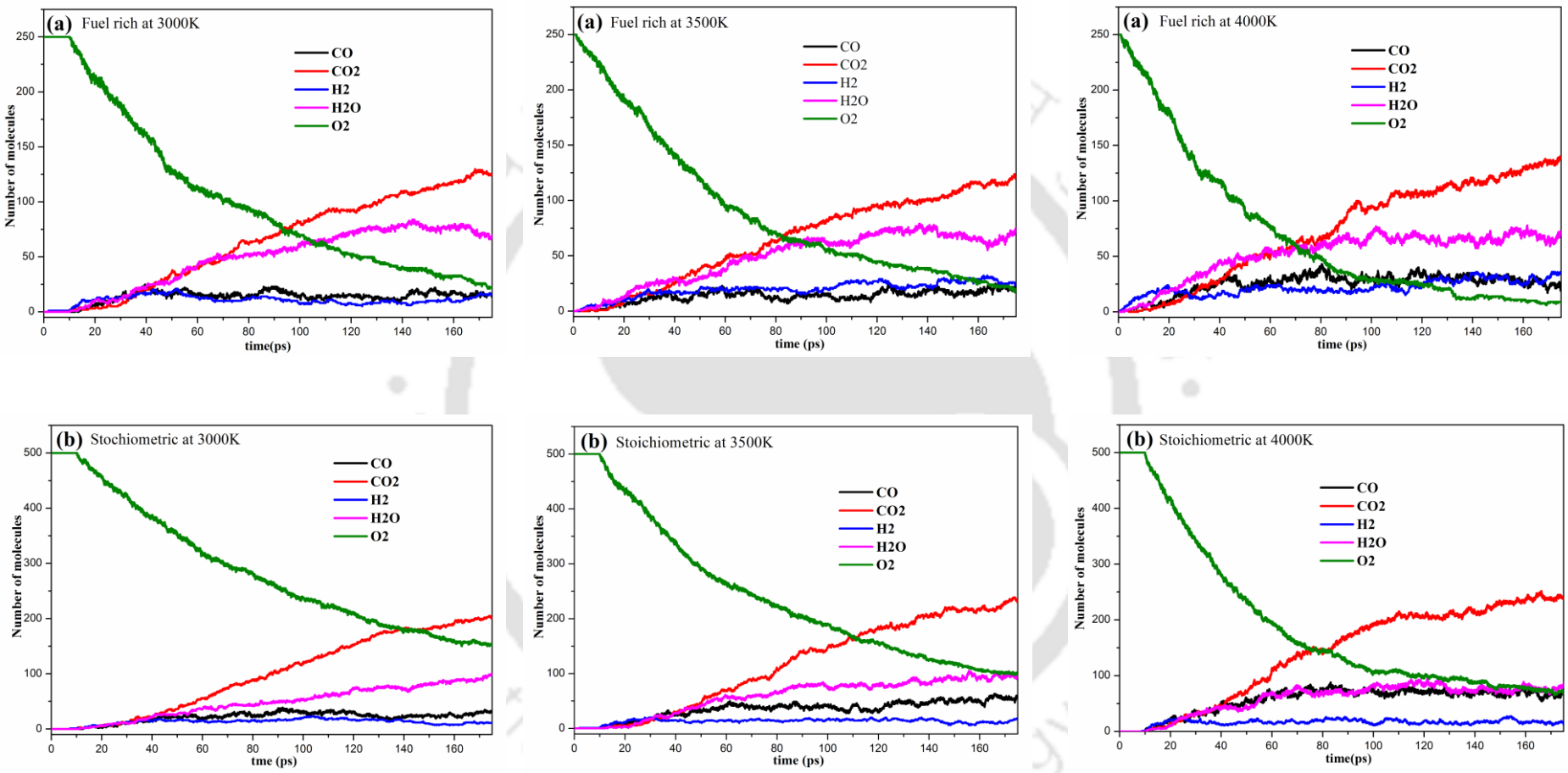
(a) Fuel rich at 3000K
(a) Fuel rich at 3500K
(a) Fuel rich at 4000K
(b) Stochiometric at 3000K
(b) Stoichiometric at 3500K
(b) Stoichiometric at 4000K
CO
CO2
H2
H2O
O2
Number of molecules
time(ps)
time (ps)
tme (ps)

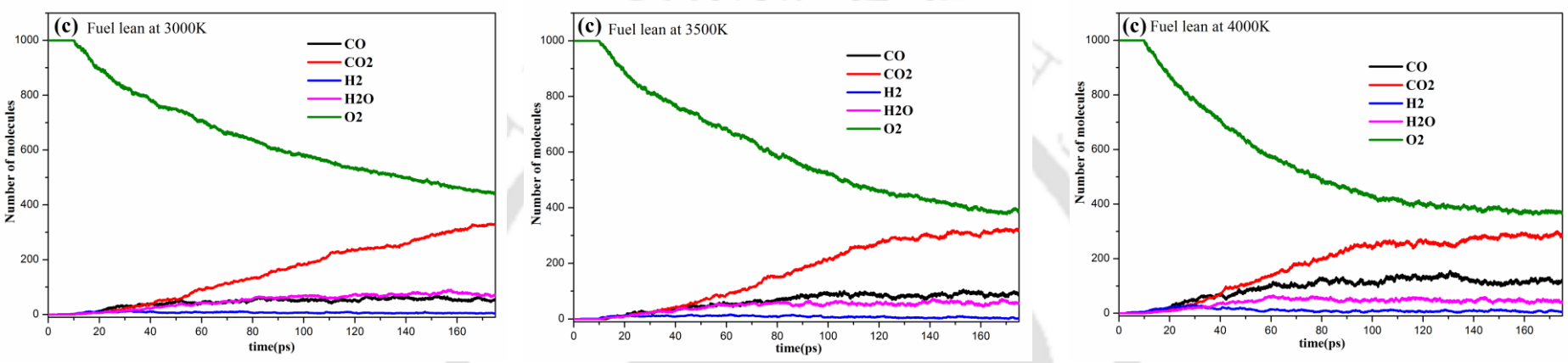

Fig. 2.4 Major products obtained from ReaxFF MD simulation during combustion of Brown coal at 3000-4000 K under (a) fuel rich, (b) stoichiometric, and (c) fuel lean condition

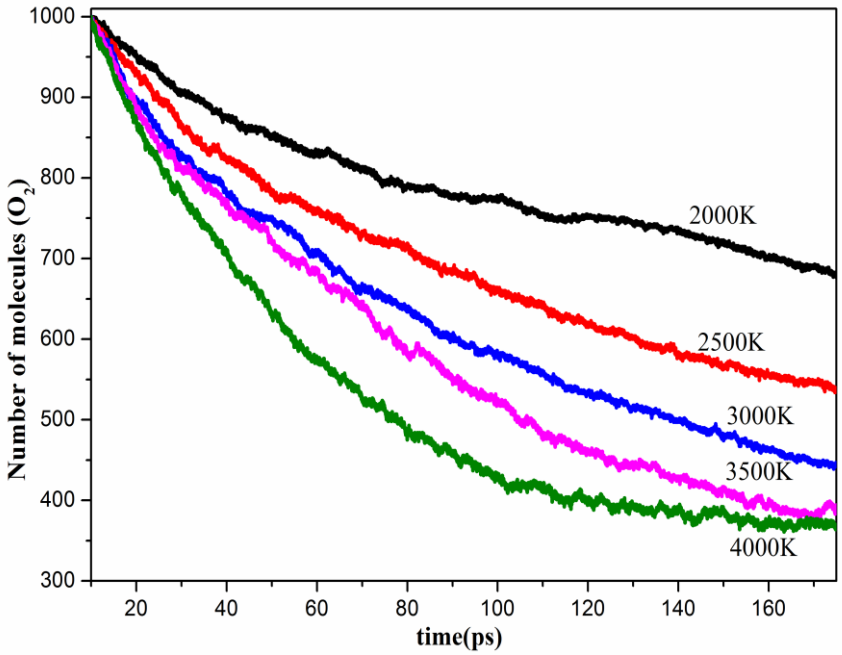

Fig. 2.5 Time evolution of O_2 molecules obtained from ReaxFF MD-simulation during combustion of Brown coal at different temperatures in fuel lean condition

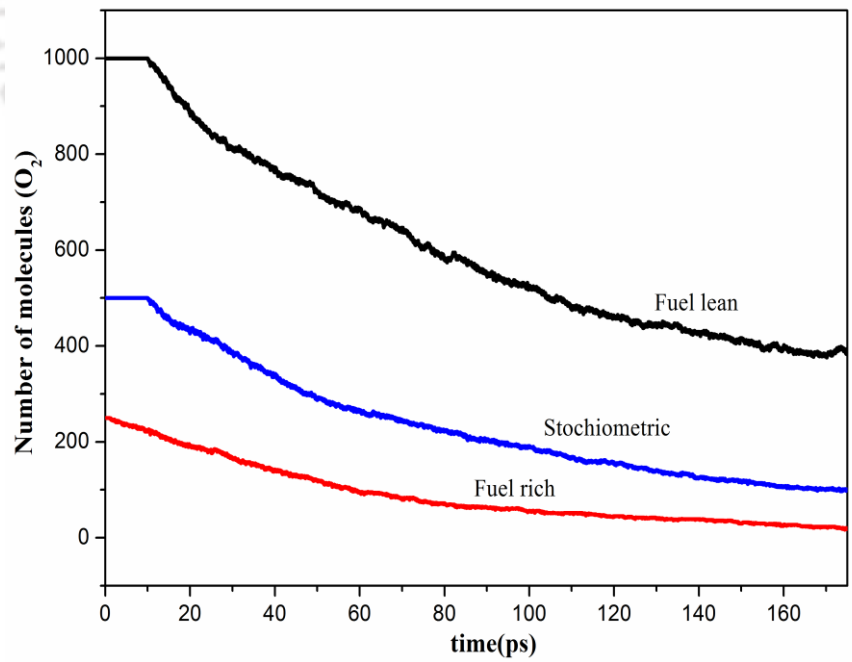

Fig. 2.6 Time evolution of O_2 molecules obtained from ReaxFF MD-simulation during combustion of Brown coal in fuel lean, stoichiometric, and fuel rich conditions

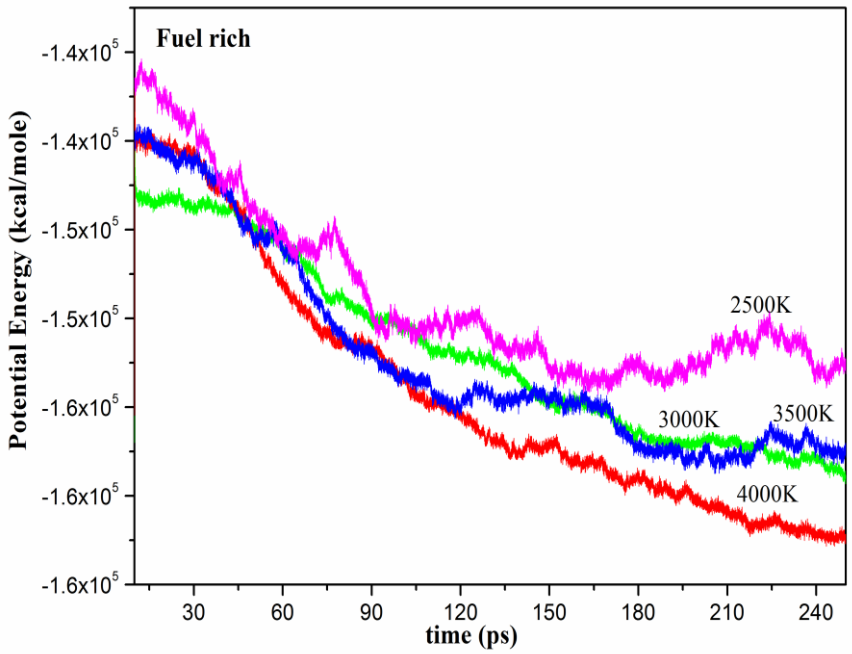

Fig. 2.7 Time evolution of potential energy during combustion of Brown coal at different temperatures in fuel rich condition

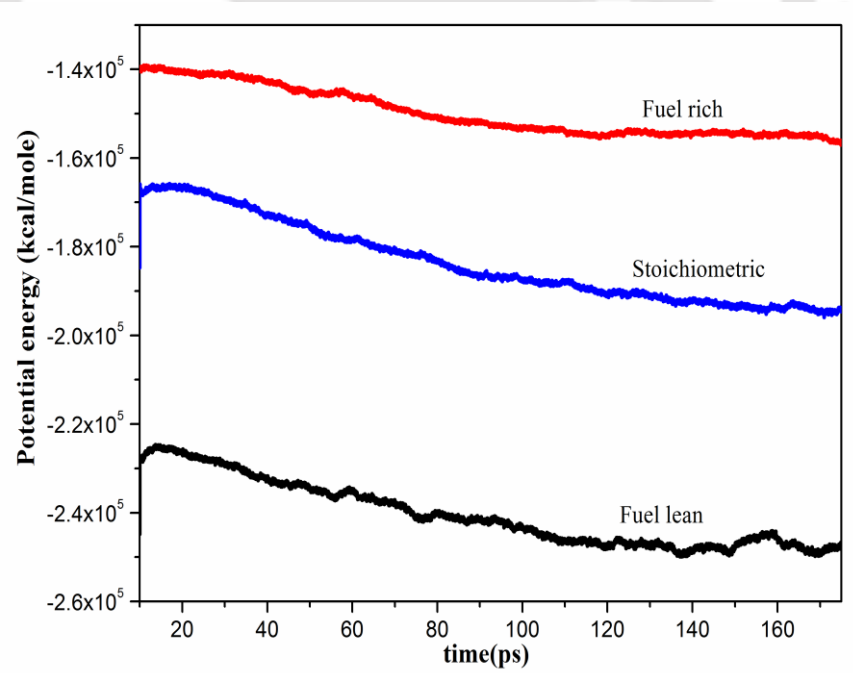

Fig. 2.8 Time evolution of potential energy during combustion of Brown coal in fuel lean, stoichiometric, and fuel rich conditions

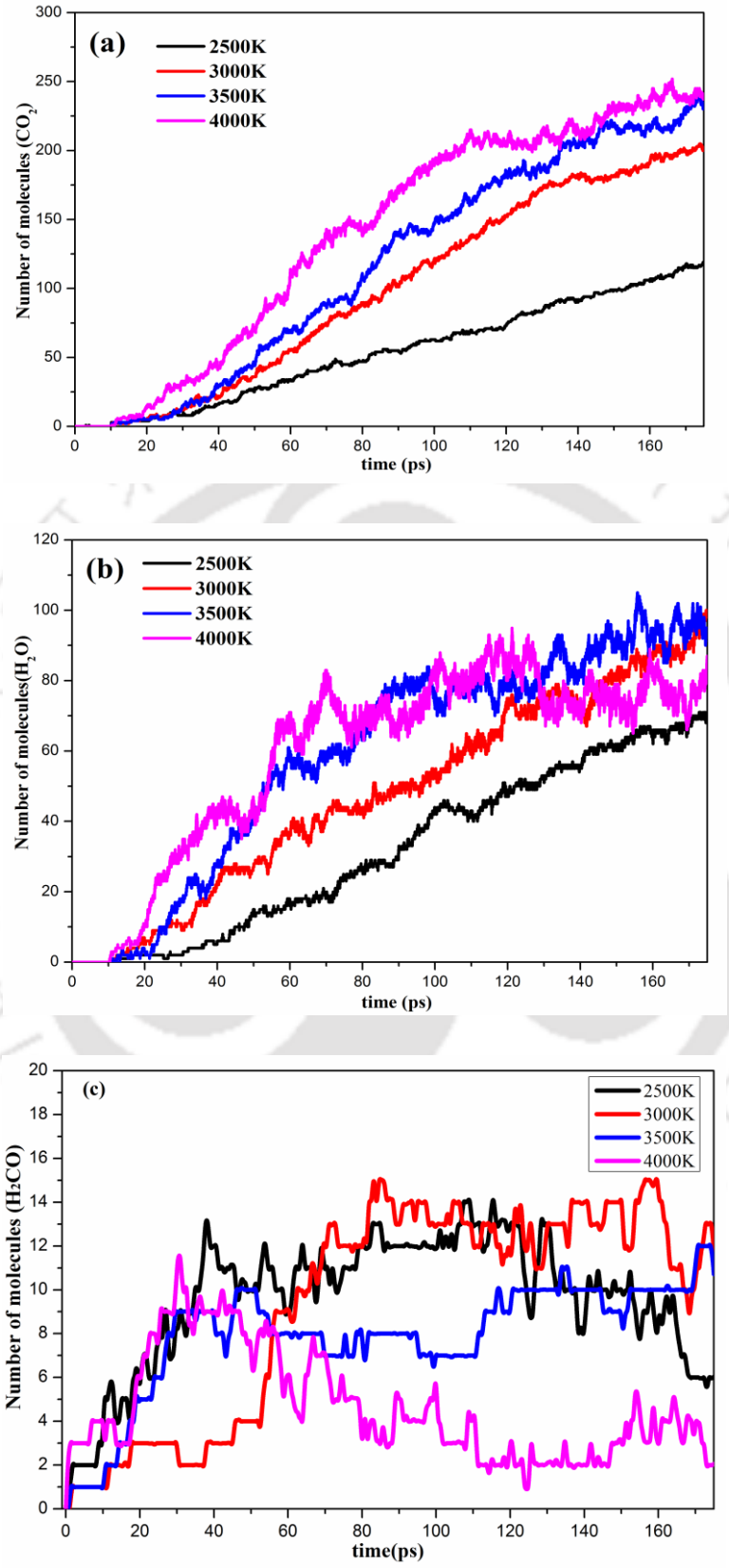

Fig. 2.9 Time evolution of (a) CO_2, (b) H_2O, and (c) H_2CO molecules during combustion of Brown coal using ReaxFF MD simulations at different temperatures

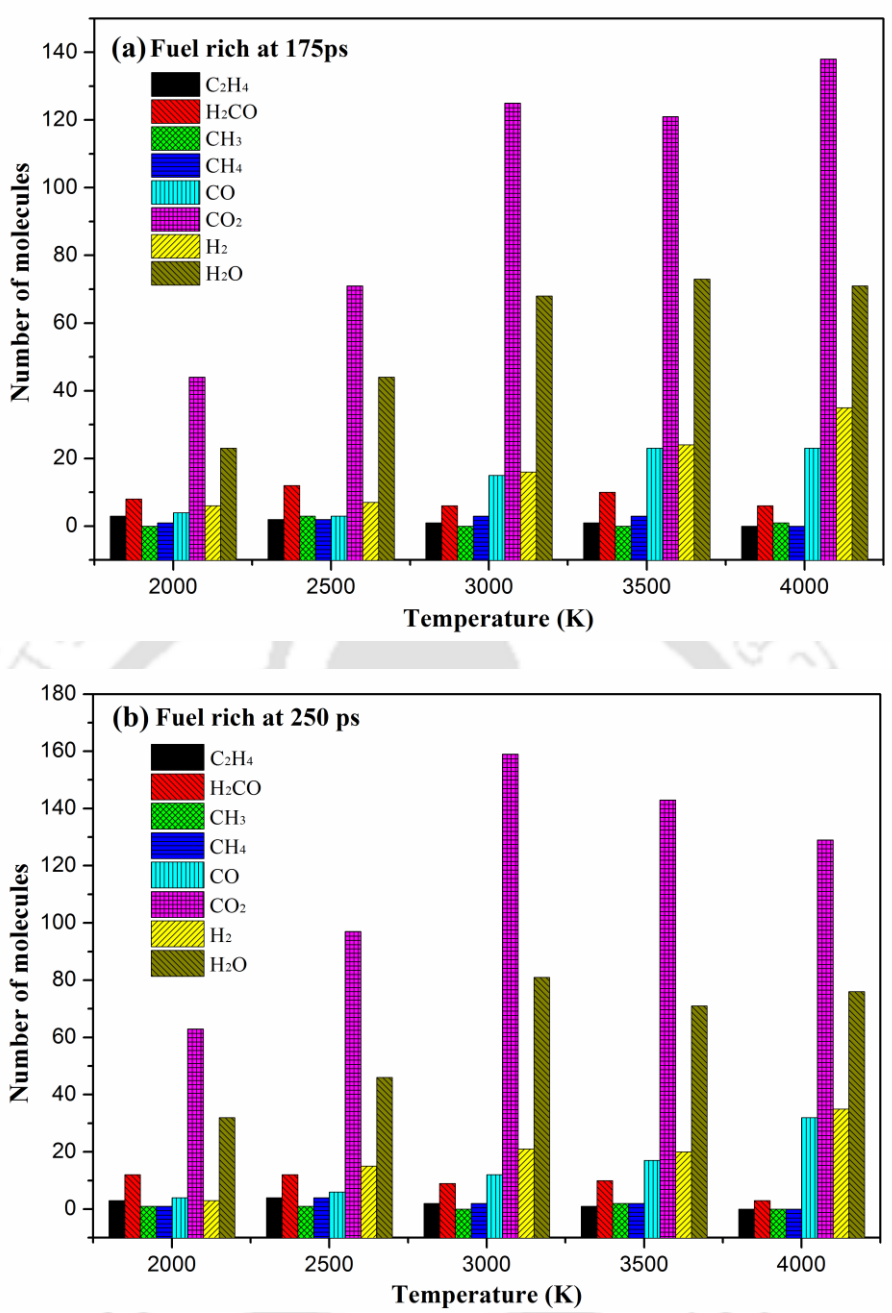

Fig. 2.10 Major products distribution sampling at (a) 175 ps and (b) 250 ps during combustion of Brown coal using ReaxFF-MD simulation

2.4.1.4 Pyrolysis of Brown Coal

When brown coal was pyrolysed at low temperature, higher molecular weight compounds were found to be very scarce. But in case of higher temperature, large number of valuable intermediates and gaseous products such as C_2H_4, CH_4, H_2CO, CO, CO_2, H_2O, and H_2 were generated during the pyrolysis of brown coal. Fig. 2.11 shows

the time evolution of major compounds obtained during the pyrolysis of brown coal using ReaxFF MD-simulation. It can be observed that a large amount of hydrogen molecules were released during the reaction due to thermal decomposition of brown coal. Irrespective of the system density, a large amount of hydrogen was released. Gaseous products like CO formed during the reaction were also large as compared to CO_2 molecules. This agrees with the experimental results reported earlier [36-38]. From experiments, it was found that the CO molecules produced were 2-3 times higher than the CO_2 molecules. From Fig. 2.11, at higher density, fewer amounts of molecule were generated during the thermal decomposition as compared to lower density. At lower density around 60-65 number of hydrogen molecules were released. Here 60-65 hydrogen molecules contribute to mole fraction of 0.466 or 46.6%. Thus, a pyrolysis process in coal contributes a major fraction of hydrogen.

Fig. 2.12 shows some valuable intermediates generated during the ReaxFF simulation at a constant temperature in three different densities (0.08, 0.1, 0.2 g/cm^3). From Fig. 2.12, it can be seen that increasing density leads to earlier initiation decomposition. Thus from Fig. 2.12, it was found that at lower density the number of intermediates increased as compared to higher densities which again agreed well with the experimental findings reported in the literature [39]. Large hydrocarbons formed were in very low weight fraction (~5%). These matches well with experiment study, where hydrocarbons like C_2H_4, H_2CO were generated in large quantity. Similarly, it was also found that a larger amount of hydrogen molecules were released at lower densities [40].

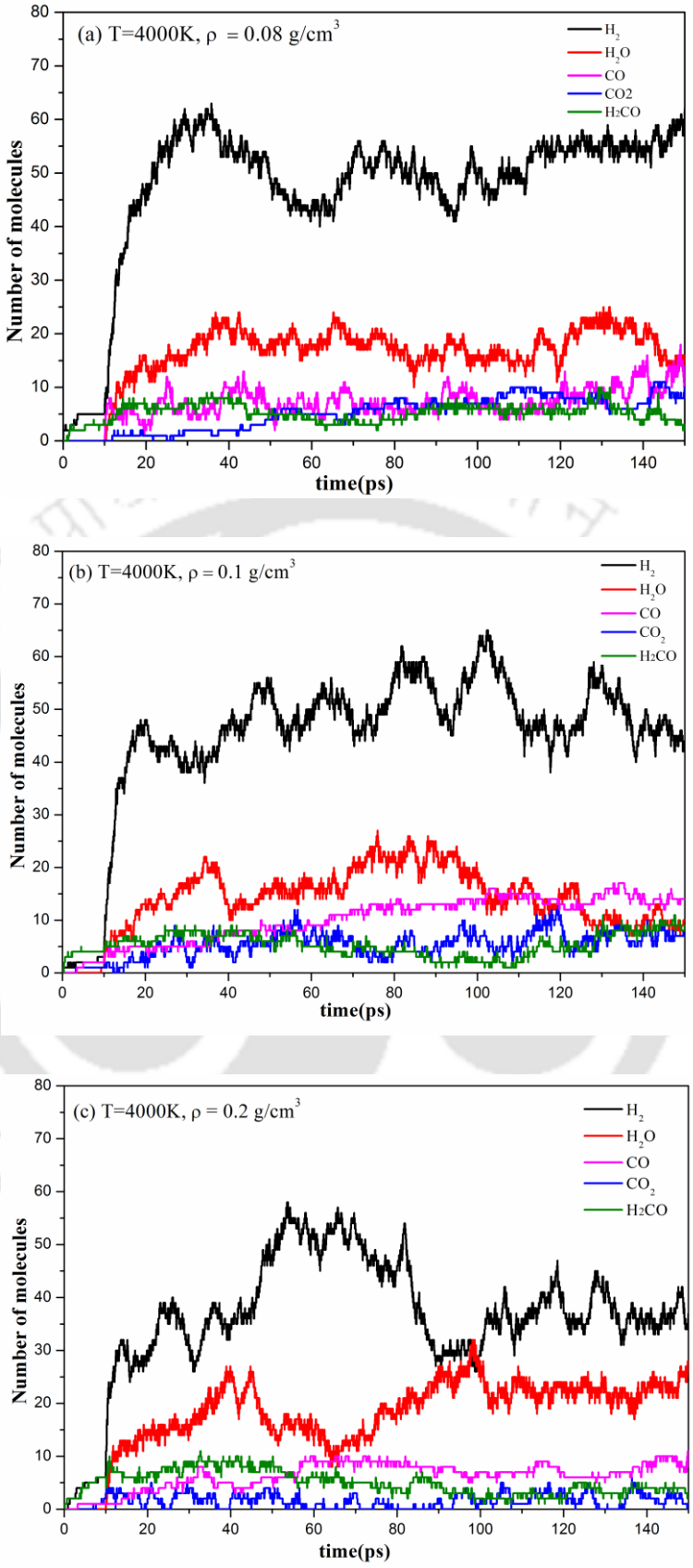

Fig. 2.11 Major products obtained from ReaxFF MD-simulation during pyrolysis of Brown coal at (a) 0.08 g/cm^3, (b) 0.1 g/cm^3, and (c) 0.2 g/cm^3

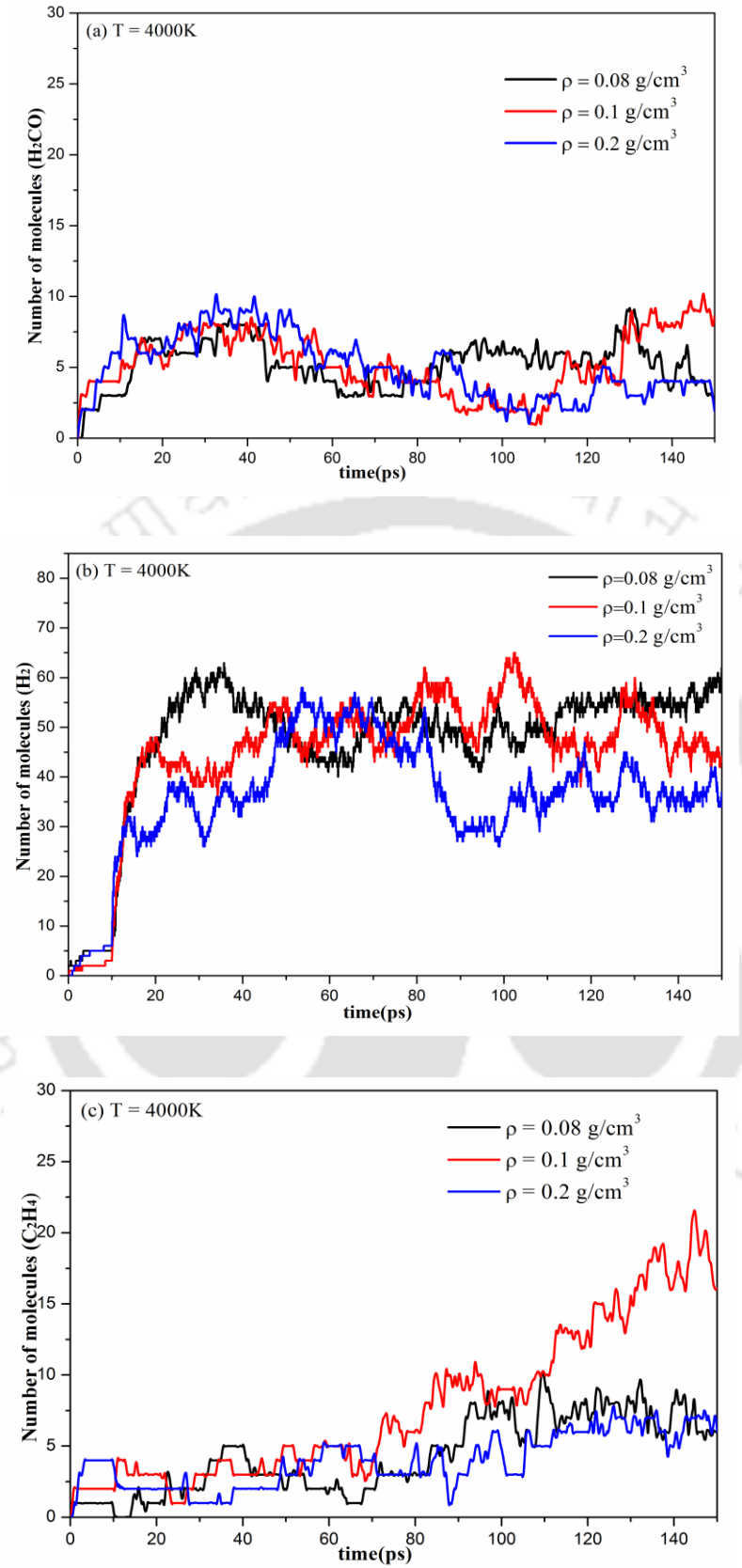

Fig. 2.12 Time evolution of (a) H_2CO, (b) H_2, and (c) C_2H_4 molecules during pyrolysis of Brown coal using ReaxFF MD-simulations at different densities

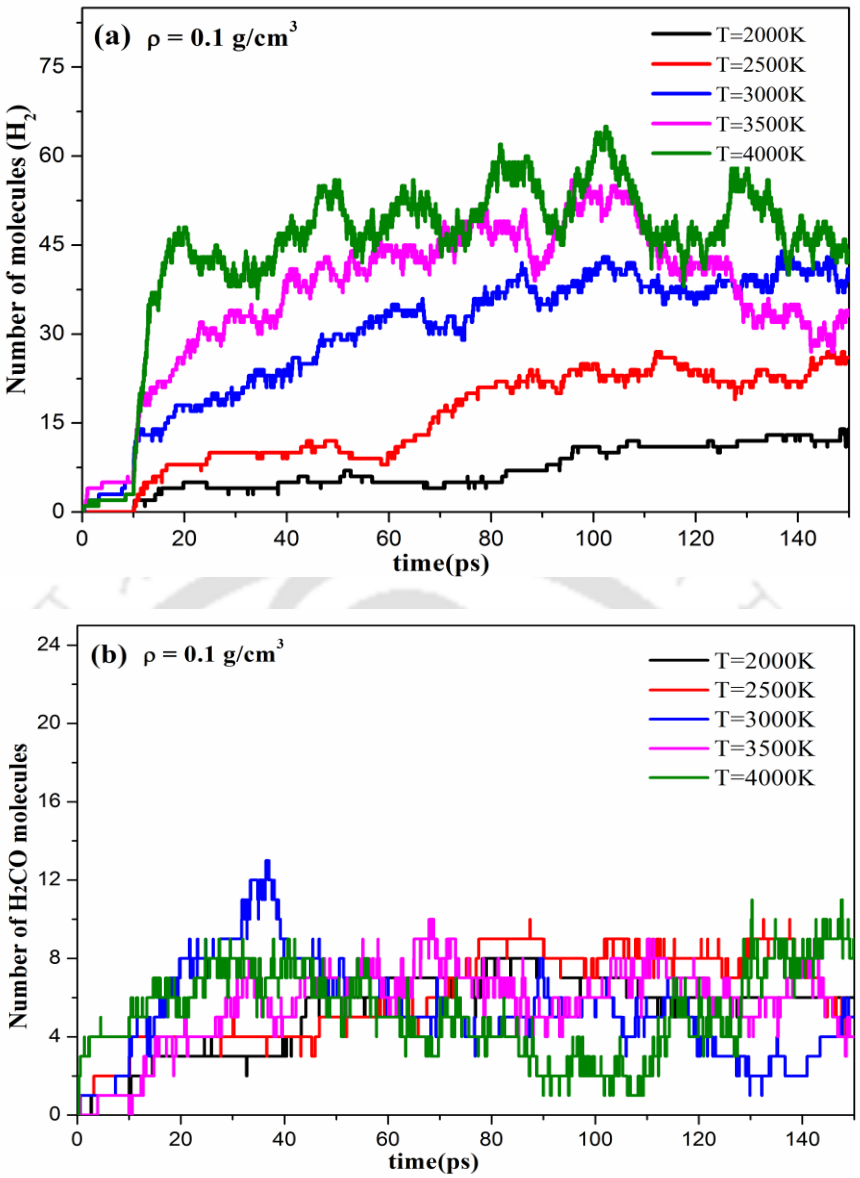

Fig. 2.13 Time evolution of (a) H_2 and (b) H_2CO molecules during pyrolysis of Brown coal using ReaxFF-MD simulations at different temperatures

2.4.1.5 Temperature Effects during Pyrolysis Process

Fig. 2.13 shows the time distribution of pyrolysis of brown coal at a temperature of 2000 K, 2500 K, 3000 K, 3500 K, and 4000 K respectively at constant density. The important intermediates generated during the thermal decomposition of brown coal which again matches qualitatively with the literature [36]. The hydrogen molecules present in brown coal were easily released at high temperature. Similarly, at high

temperature, H_2CO molecules were produced in a large quantity. Fig. 2.14 shows the time evolution of potential energy of pyrolysis of brown coal with different temperature. Here the coal molecules gain energy from the thermal decomposition process, thereafter with an increase in temperature, the potential energy of the system gradually increases with time, which shows that the process is an endothermic reaction. Fig. 2.15 shows the major product distribution at 150 ps. During the ReaxFF MD-simulation of brown coal, a large number of gaseous components (CO, CO_2, H_2, H_2O) and valuable intermediates (CH_3, CH_4, C_2H_4, H_2CO) were produced. Thus, a large amount of hydrogen molecule is released with an increase in temperature which is due to the large amount of hydrogen present in the coal molecules.

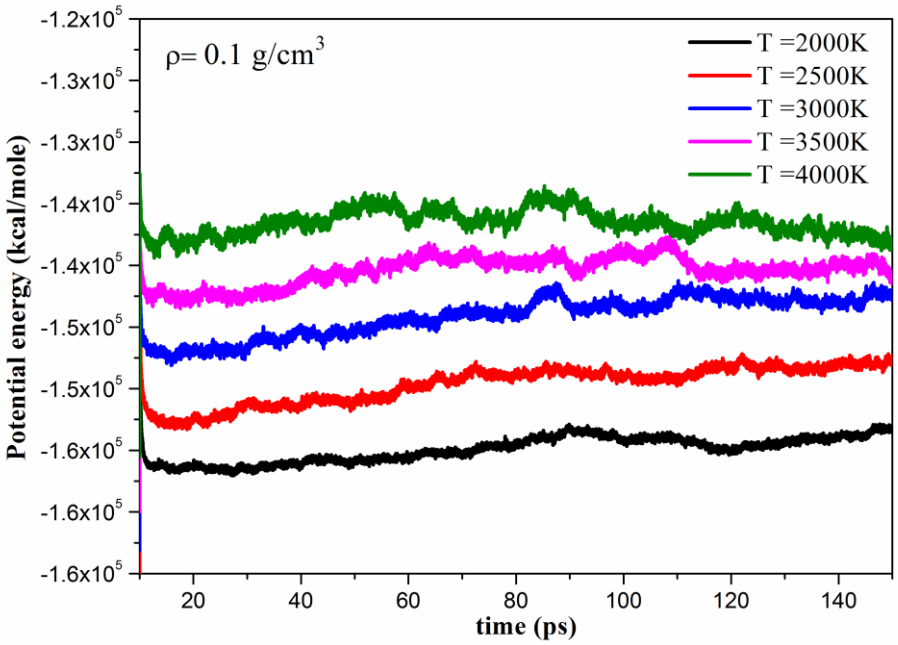

Fig. 2.14 Time evolution of potential energy during pyrolysis of Brown coal at different temperatures

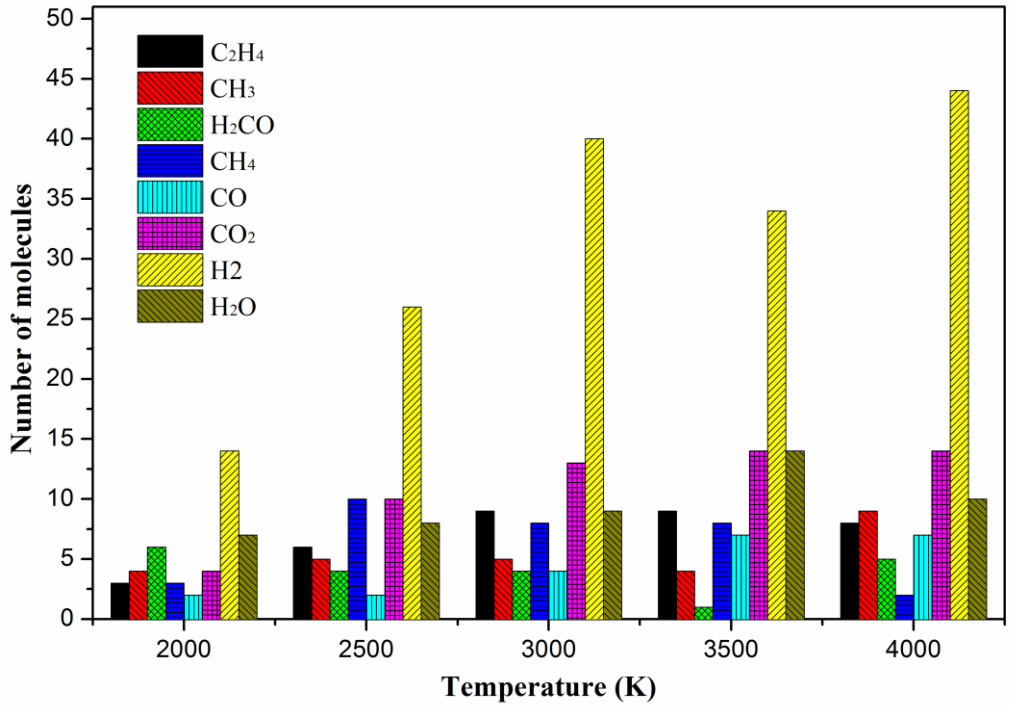

Fig. 2.15 Product distribution during sampling at 150 ps for Brown coal Pyrolysis using ReaxFF MD-simulation

2.4.2 Comparative Studies on Three Different Rank Coals

2.4.2.1 Formation of CO and CO_2 during Combustion Analysis

Fig. 2.16 shows the general trend for the CO and CO_2 formation during the combustion analysis. In the previous section 2.3.1 [10] with brown coal, we have obtained CO and CO_2 as the two major intermediates. The rate of reaction or formation is obtained by the following equation;

$$R_{CO} = \frac{C_{CO}}{W} \times \dot{m} \tag{2.13a}$$

$$R_{CO_2} = \frac{C_{CO_2}}{W} \times \dot{m} \tag{2.13b}$$

where C_{CO} and C_{CO_2} denotes CO and CO_2 concentration in a mole of CO/kg of coal and mole of CO_2/kg of coal respectively. W is the weight of coal sample in kg and $\dot{m}$ represents mass flow rates in kg of coal/ps respectively. The slope between concentration and time is usually written in chemical engineering terms as dC_A/dt. The rate of formation i.e. dC_{CO}/dt and dC_{CO_2}/dt with CO and CO_2 concentration were obtained graphically. From the slope, it was found that both the reactions followed a first order mechanism (equation (2.14a) and (2.14b)). The negative sign implies that both gases are consumed in the reaction.

$$-\frac{dC_{CO}}{dt} = k[CO] \tag{2.14a}$$

$$-\frac{dC_{CO_2}}{dt} = k[CO_2] \tag{2.14b}$$

Here 'k' represents the rate constant in ps^{-1} and takes the value 225.8 ps^{-1} and 184.8 ps^{-1} for CO and CO_2 respectively. This implies that the formation of CO is faster as compared to CO_2. This is further supplemented in Fig. 2.16, where it is observed that the rate of

formation of CO_2 is always higher than that of CO, which proves that CO_2 is the major intermediate gaseous product formed from the combustion of coal. This also agrees well with the previous experimental results [41-45].

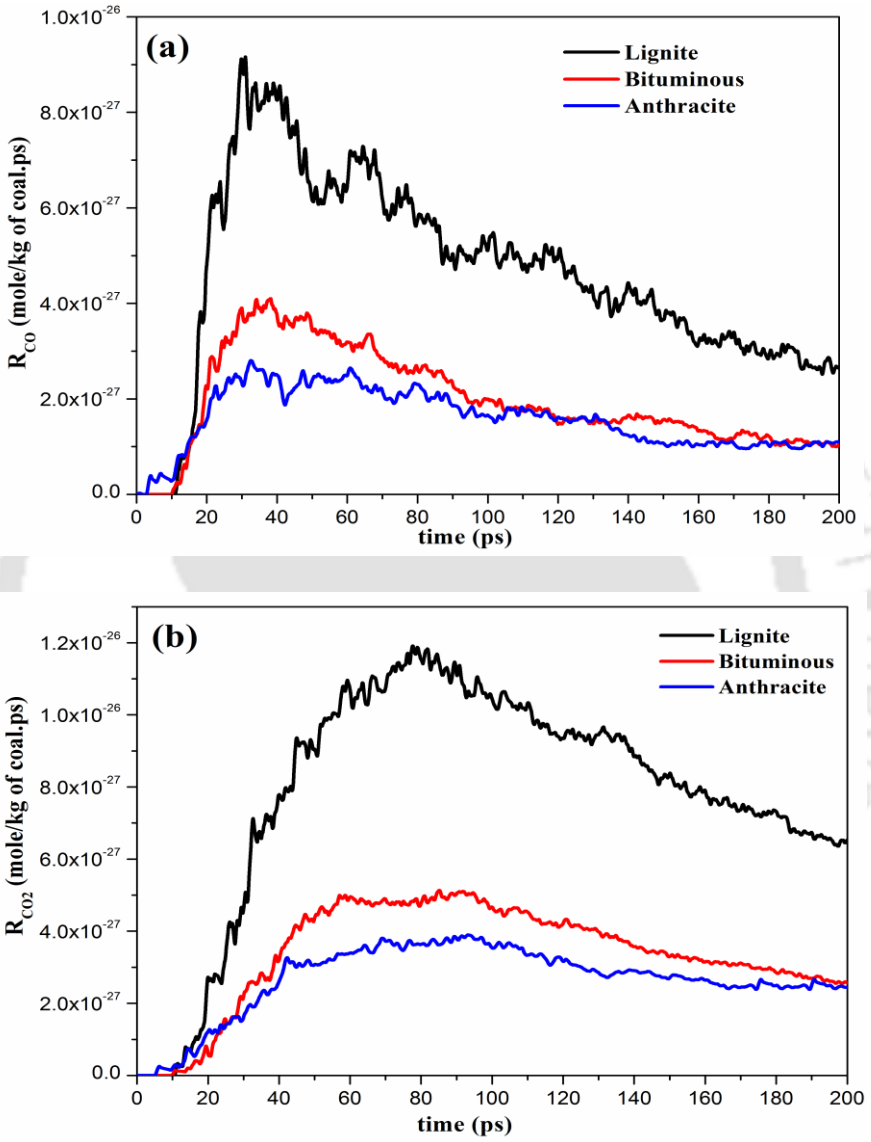

Fig. 2.16 Variation in the formation rate of (a) CO and (b) CO_2 for three different coals at 3500 K from ReaxFF simulation results

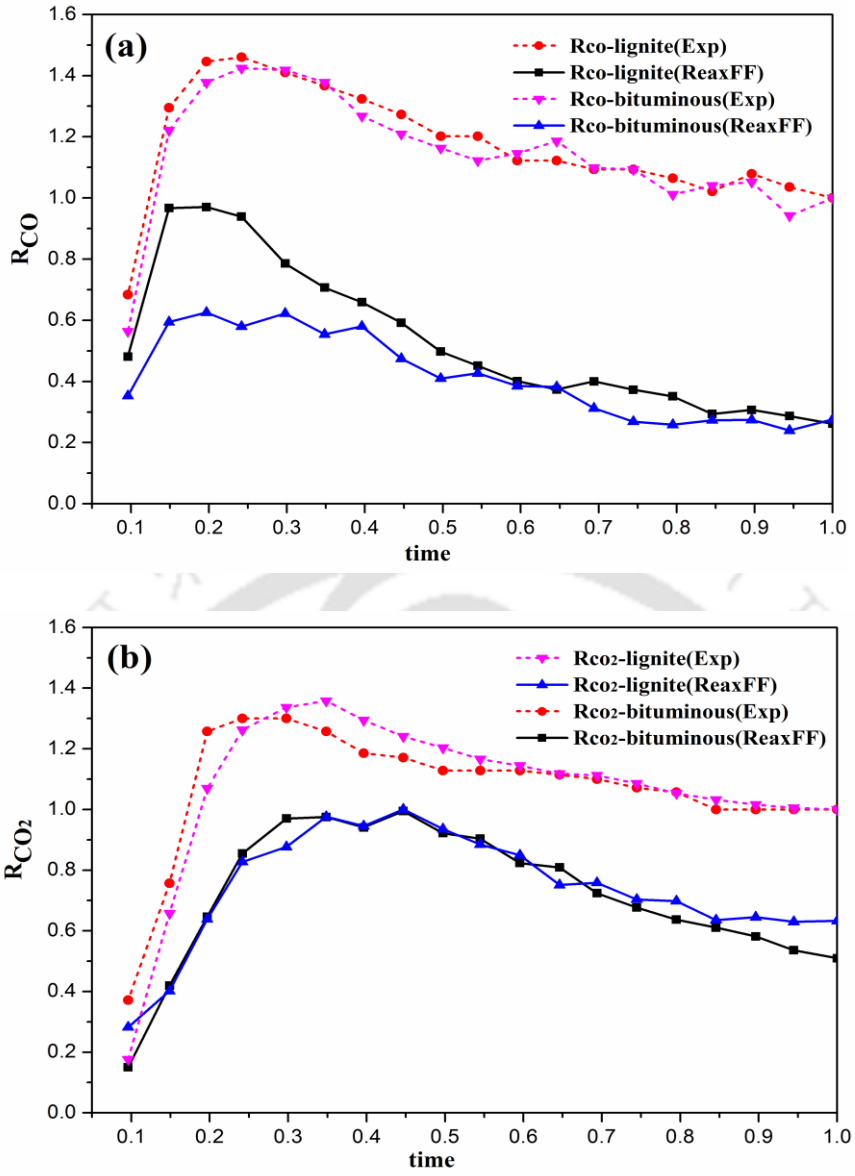

Fig. 2.17 Experimental [41, 42] and ReaxFF simulation results for formation rate of (a) CO and (b) CO_2 at 3500 K

The experimental and ReaxFF predicted rate of formation of CO and CO_2 is compared in Fig. 2.17(a) for CO and Fig. 2.17(b) for CO_2. While a qualitative match is found for CO, a quantitative agreement is found in CO_2. Here both the coordinates are represented in the dimensionless unit to simplify the graphical representation only. For chemical kinetic modelling, we usually adopt a closed homogeneous reactor with constraint volume and temperature in order to directly compare the results with ReaxFF. This has not been attempted in this work hence a qualitative trend was obtained in

Fig. 2.17. A similar behaviour was also observed with the combustion of *n*-dodecane where the likely molecule in ReaxFF and kinetic modelling was ethylene, even though the quantitative results show larger deviations [18]. Thus the studies on coal using ReaxFF is beneficial in predicting the emission rate of gases for the various rank of coal. In both the gases (CO and CO_2), the production rate reaches a maximum and then dies down gradually. Thus is due to the fact that initially the rate of formation of CO_2 and CO increases, thereafter it decreases as the oxygen concentration reaches its maximum value. Again it is observed that the rate of formation of CO_2 and CO is higher for lignite coal. This is primarily due to a large amount of oxygen present in the lignite version as compared to bituminous and anthracite coal [43]. Further, the magnitudes of formation rate of CO_2 and CO for lignite coal is higher than those of bituminous and anthracite coal.

Fig. 2.18 shows the variation of CO/CO_2 ratio for lignite, bituminous, and anthracite coals at a different temperature. It can be seen that for higher rank coal, the ratio of CO/CO_2 rapidly decreases with time which also agrees with experimental results [41, 42] irrespective of temperature. Thus they are oxidized rapidly while reaching an asymptotic value. The variation in the production rate of CO to CO_2 ratio is also compared with experimental values in Fig. 2.19(a) for lignite and Fig. 2.19(b) for anthracite. It is evident that production rate of CO_2 with respect to CO is enhanced with time and becomes constant which is a similar trend as per experimental studies [41, 42].

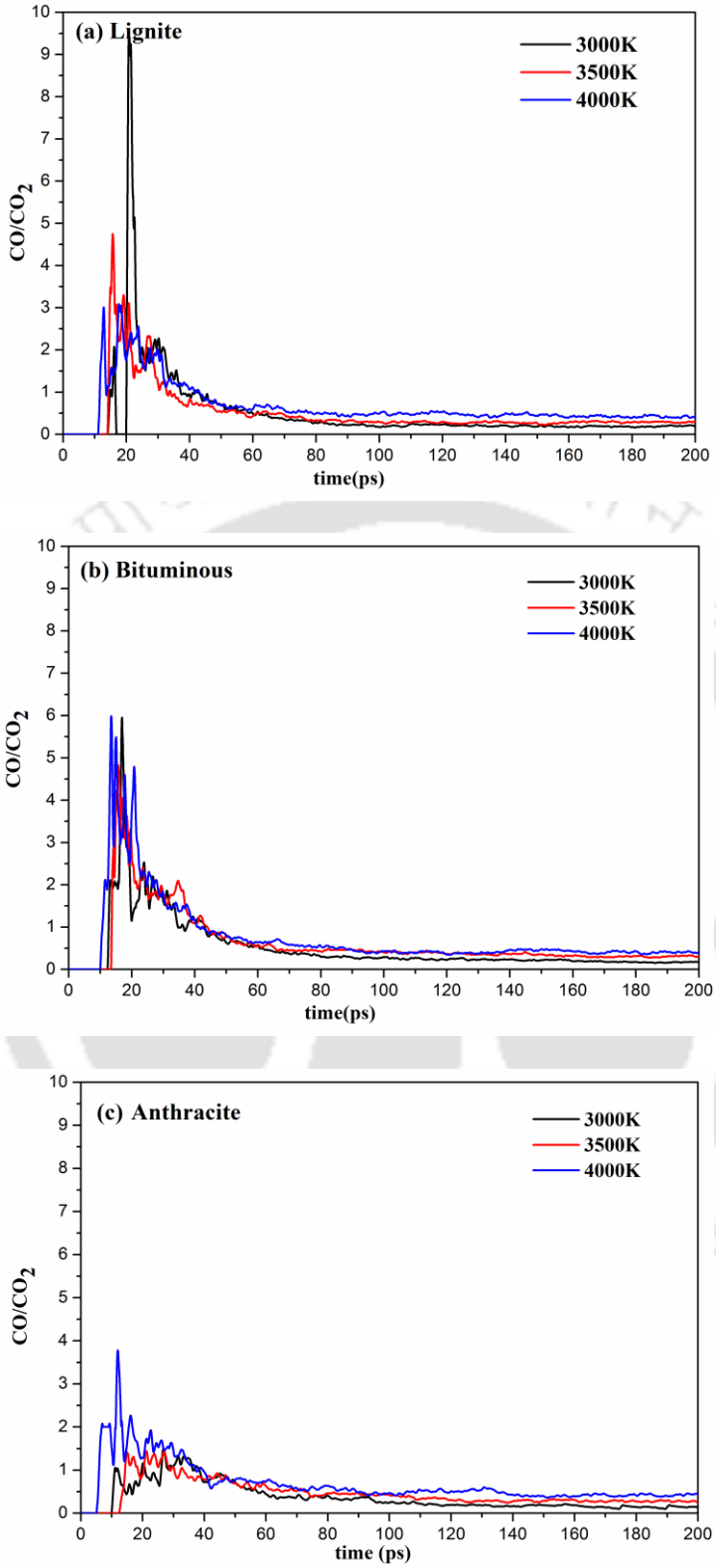

Fig. 2.18 Variation in CO/CO_2 ratio for (a) lignite, (b) bituminous, and (c) anthracite from ReaxFF simulation results

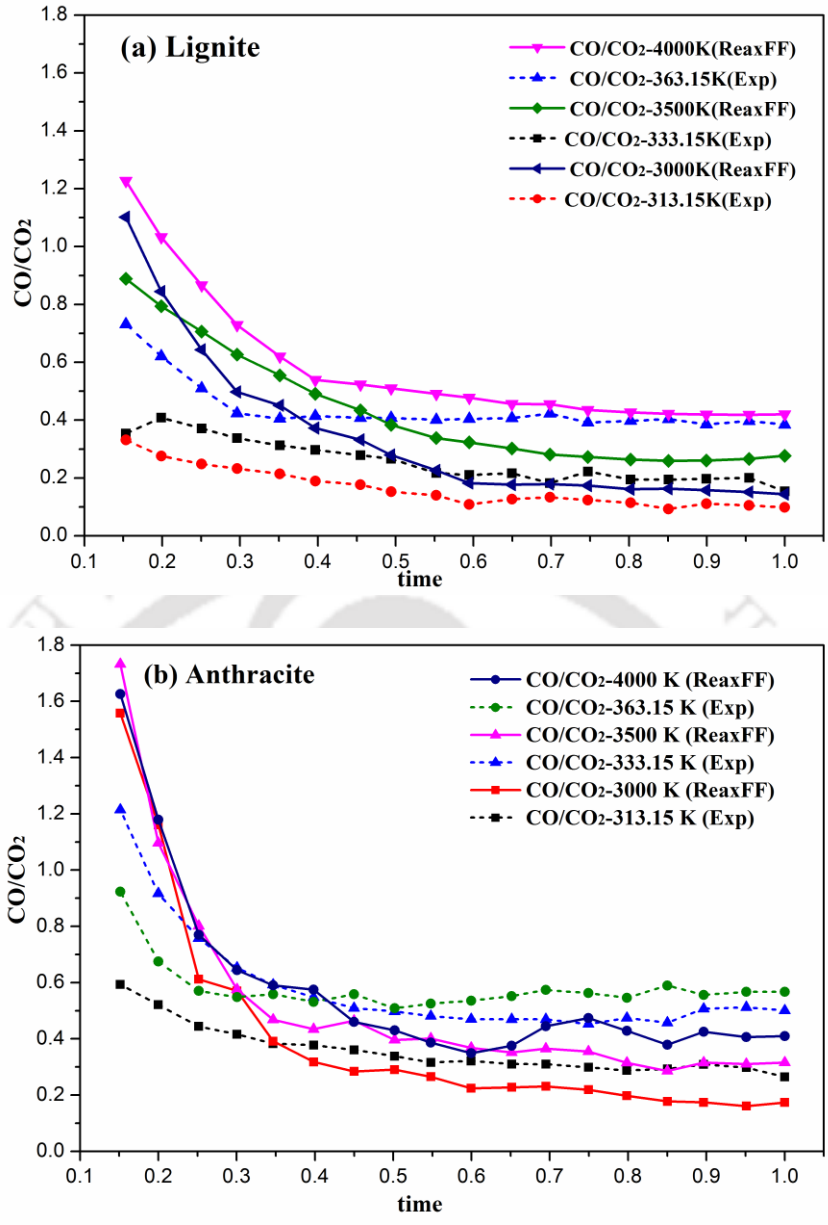

Fig. 2.19 Variation in CO/CO_2 ratio for (a) lignite and (b) anthracite for Experimental [41, 42] and ReaxFF results

2.4.2.2 Computation of Activation Energies for CO and CO_2

To benchmark our modelling approach, an attempt has been made to calculate the activation energies for both CO and CO_2 for all the three varieties of coal. Table 2.1 shows the activation energy of CO and CO_2 formation for all the three coals which is obtained from the Arrhenius plots. An important observation is a close match in the activation energies for both CO and CO_2. It is also proven that the formation of CO is

easier than CO_2 because of the lower activation energy. This also benchmarks our simulations against the reported data of Kaji et al. [43] and those obtained from the rate constants as given in equation (2.14a) and (2.14b). The smallest deviation in activation energies is observed for the bituminous coal. Table 2.2 discusses the formation of intermediates during the course of the reaction. Here it can be seen that the formation rate of CO is lower as compared to CO_2 molecules irrespective of temperature. However, this should not be confused by the activation energies as the data presented below is at a time step of 175 ps.

Table 2.1 Activation energy (*E*) of CO and CO_2 at 150 ps for combustion process

Types of coal	E_{CO} (kJ/mole) (ReaxFF)	E_{CO} (kJ/mole) (Experimental[43])	Ea_{CO_2} (kJ/mole) (ReaxFF)	E_{CO_2} (kJ/mole) (Experimental[43])
Lignite	46.1	51.5	56.4	56.1
Bituminous	52.1	54.4	60.5	59.4
Anthracite	59.2	58.2	64.4	59.4

Table 2.2 Formation of valuable intermediates of lignite coal at 175 ps

Temperature (K)	CO	CO_2	H_2	H_2O	H_2CO	CH_3	CH_4
2000	18	154	2	42	17	2	0
2500	29	272	2	63	18	0	1
3000	93	321	2	57	10	0	0
3500	93	321	2	57	6	1	1
4000	113	284	6	43	2	2	3

It should be noted that the CO molecules are formed at the start of the reaction (lower activation energies) and tend to decrease with time. For lignite coal, a large quantity of CO and CO_2 molecules were released at a higher temperature. A similar phenomenon was also observed for anthracite and bituminous coal. In general, a large portion of CO and CO_2 molecules are formed at a temperature range of 3000-4000 K due to the faster interaction between the carbon atoms (either from coal or from CO) and oxygen molecules. It is proposed that CO molecules are formed by the breakage of aromatic rings and subsequent incomplete reaction with oxygen molecules. Thereafter the CO molecules directly react with O_2 to form CO_2 molecules which are depicted in Fig. 2.20 and Fig. 2.21. Intermediates such as H_2, H_2O, H_2CO, CH_3, and CH_4 are also formed during the course of the reaction. We now proceed in determining a reaction mechanism for the simplest of the coal molecule i.e. lignite.

2.4.2.3 Reaction Mechanism for Lignite Combustion

Fig. 2.20 shows the reaction mechanism of ReaxFF simulation at a temperature of 3000 K in fuel rich condition. It starts with an equilibrated structure of coal molecule (5 ps). As the coal molecules start to interact with oxygen molecules, it starts to divide into two aromatics like ring structure at a time step of 5.55 ps. The aromatic rings open up to form straight carbon chain as 6.12 ps. Thus it is clear that the formation of CO is essentially due to the breakage of carbon-carbon (-C-C-) chain within the coal molecule. This also agrees with the lower activation energies as observed in a previous work [43] and our own comparison in Table 2.1. This is further supplemented in Fig. 2.21, where the production of CO starts earlier than CO_2 due to the breakage of -C-C- bond.

In the final stages, the carbon chain reacts with oxygen at a time step of 7.38 ps, where the first formation of CO is noticed. This is also accompanied by the release of the

radical $C_3OH^{\bullet}$. The radical $C_3OH^{\bullet}$ then reacts with an O_2 molecule to form the remaining CO molecules at 8.36 ps. Simultaneously this further releases the $C_2H^{\bullet}$ (unstable) radical. In the concluding part, the CO molecules tend to react with O_2 by forming the unstable form of carbon trioxide (CO_3) at 9.64 ps. This again reacts with O_2 and forms CO_2 at 13.44 ps with the abstraction of $O^{\bullet}$ radical. Some of the valuable intermediate such as H_2CO are formed after the reaction of CH_3 and O_2 molecules at the end of simulation i.e. 57.28 ps. In the whole process, the degradation of O_2 molecules starts at 1.013ps (Fig. 2.22). This is mainly due to the effect of higher temperature thereby facilitating more collisions.

2.4.2.4 Effect of Temperature in Combustion Analysis

Irrespective of the reaction mechanism, temperature and pressure only affect the reaction rates. In the previous section 2.4.1 [10], we have reported that the temperature highly affects the oxidation process i.e. large numbers of gaseous intermediates are generated during the reaction. In a similar manner, Fig. 2.23 shows that as temperature increases, the formation rate of CO and CO_2 increases for all coal variant namely anthracite, bituminous, and lignite. The formation rate of CO and CO_2 are found to be much higher at 4000 K as compared to lower temperature, which agrees with experimental observations [41, 42, 46]. It can be also observed that the production rate of CO and CO_2 for anthracite is much higher than that of bituminous and lignite. This is due to a large number of carbon i.e. 45 carbons in anthracite coal as compared to 18 carbon present in bituminous coal and 39 carbons present in lignite coal. Therefore when the oxygen molecules react with coal at high temperature, oxygen and carbon present in the coal react to form a large number of CO and CO_2 molecules. The formation rate of CO and CO_2 initially increases but then decreases at a faster rate at a higher temperature. This is due to the combustion process which proceeds at a faster rate at high temperature [47].

The experimental variation of the rate of formation of CO and CO_2 for lignite coal is also compared in Fig. 2.24(a) for CO and Fig. 2.24(b) for CO_2. The ReaxFF predicted rates are smooth when compared to the experimental rates. However, the trend and the order of magnitude do represent a similar trend i.e. the production of CO_2 picks up as the rate of formation declines for CO.

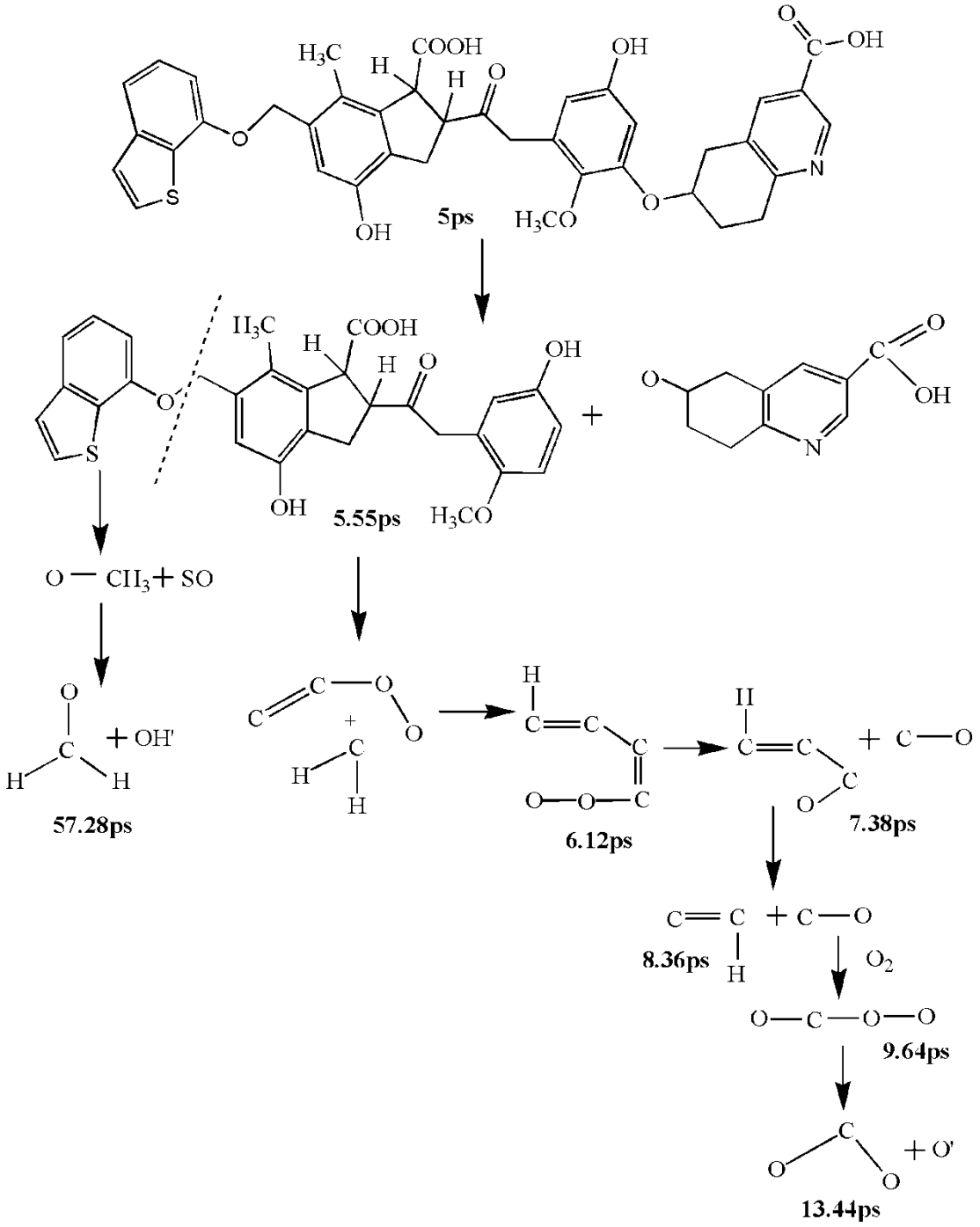

Fig. 2.20 Reaction Mechanism of lignite at 3000 K from ReaxFF-MD simulation

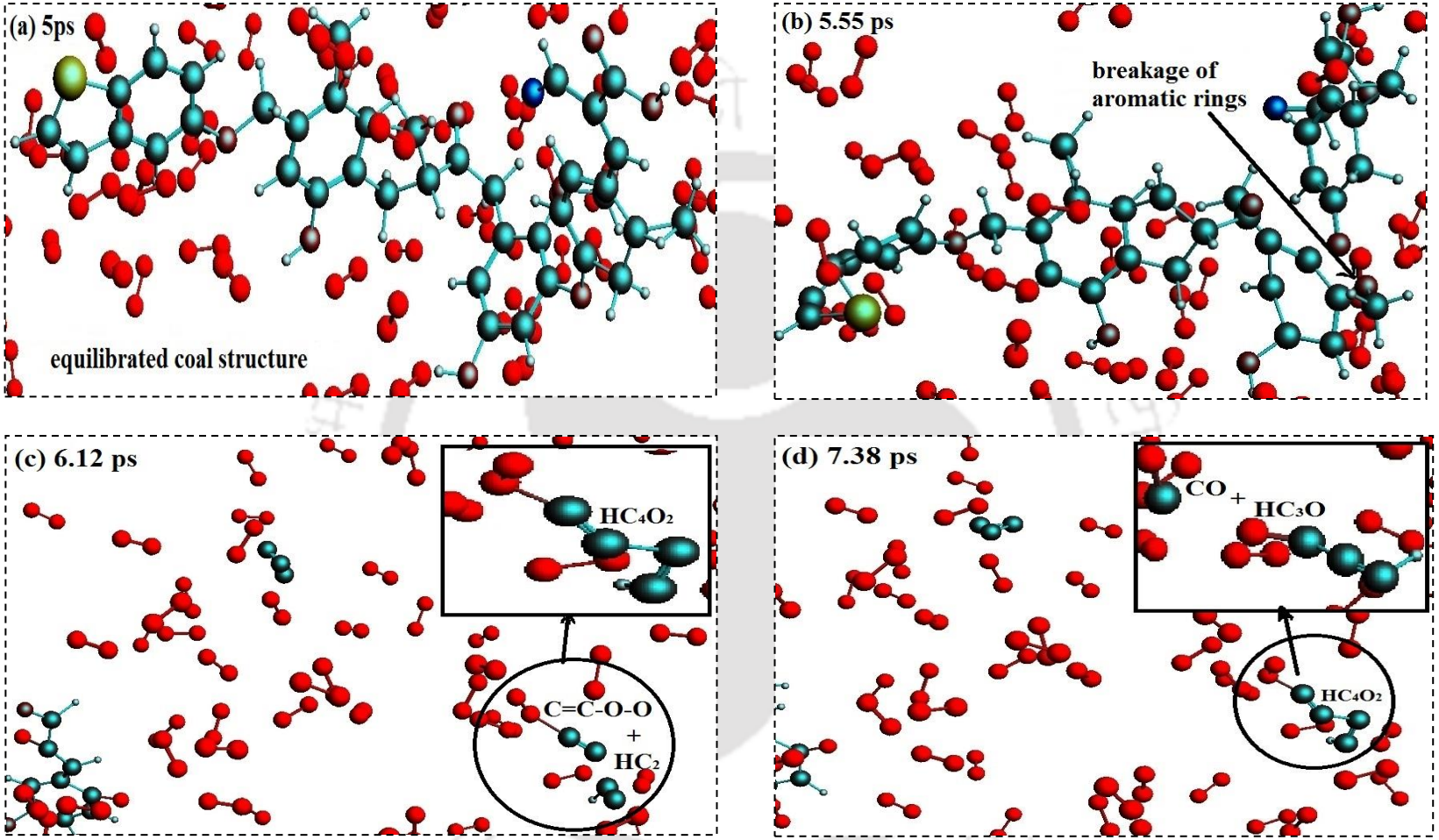
(a) 5ps
equilibrated coal structure
(b) 5.55 ps
breakage of
aromatic rings
(c) 6.12 ps
HC4O2
C=C-O-O
+
HC2
(d) 7.38 ps
CO
+
HC3O
HC4O2

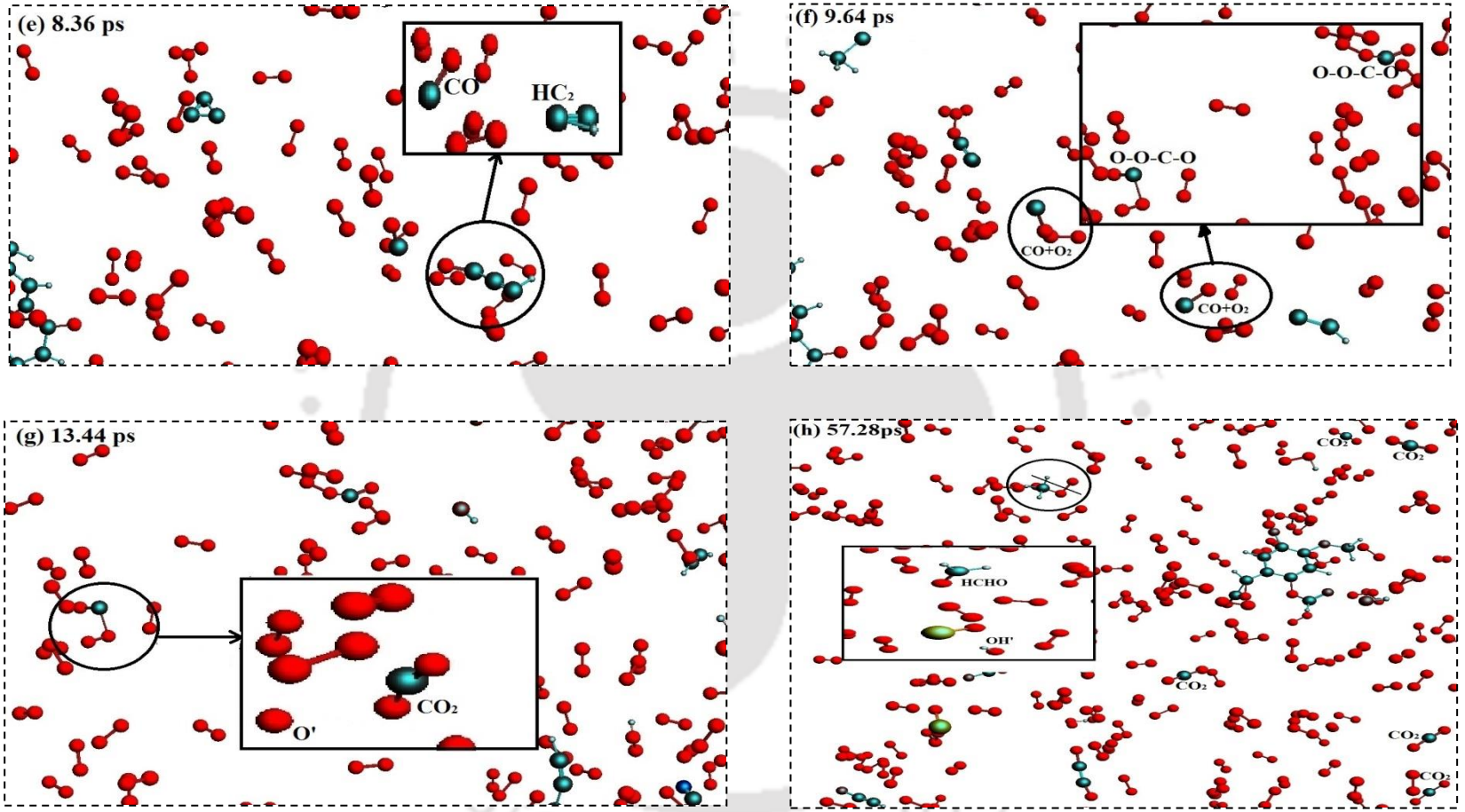

Fig. 2.21 Snapshot from ReaxFF MD simulation of (a) equilibrated system, (b) breakage of aromatic rings, (c-e) CO formation from C_2O_2, (f) carbon trioxide (CO_3) formation, (g) CO_2 formation, and (h) CO_2, H_2CO formation (Circle represents the reactant and rectangle represent the products formed after the reaction)

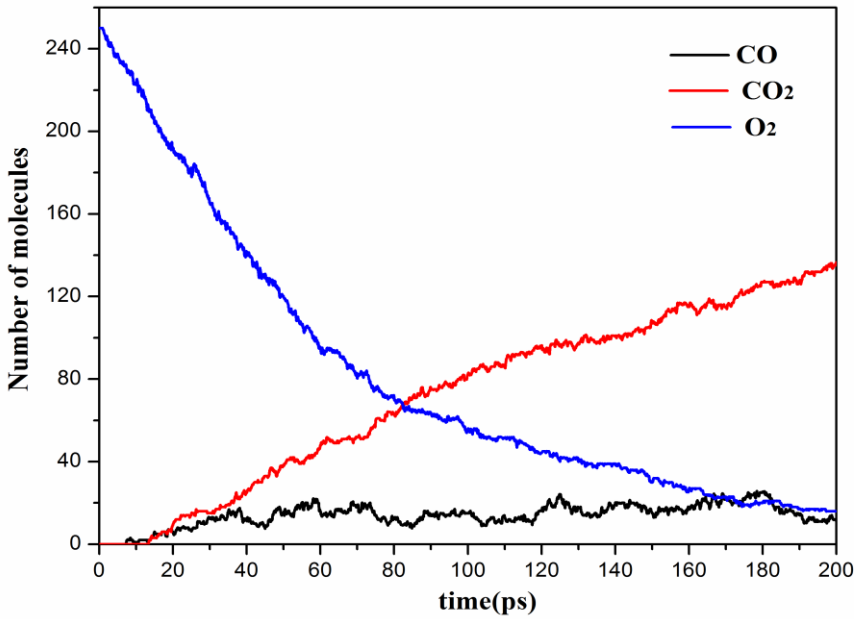

Fig. 2.22 Formation of CO and CO_2 molecules with time in ReaxFF simulation

2.4.2.5 Product Formation in Pyrolysis

In the pyrolysis process, a large amount of gaseous products and intermediates are obtained. A gaseous product like CO_2 is a major component which is also obtained in the combustion process [10]. However valuable products like CH_4, C_2H_4, and C_2H_6 are also evolved during the pyrolysis processes which agrees with the experimental findings [43]. Table 2.3 gives us an amount of gaseous products such as CH_4, C_2H_4, and C_2H_6 evolved during the pyrolysis analysis at 3000 K for three different coals i.e. anthracite, bituminous, and lignite. From Table 2.3, a larger amount of CH_4, C_2H_4, C_2H_6 are evolved in lignite and bituminous coals as compared to anthracite coal which agrees with the experimental trends [43]. Similarly, Table 2.4 shows the fraction of CO and CO_2 during the pyrolysis of anthracite, bituminous, and lignite coal at 3500 K. The oxygen containing groups present in the coal decomposes to produce CO and CO_2. Mole fractions of CO_2 and CO were found to be 7.26 and 14.52 mole% for lignite; similarly, 6.45 and 8.42 mole% for bituminous coal respectively. This is higher as compared to anthracite coal on account of higher oxygen content present in low-rank coals [43].

Hence as obvious during the decomposition, coal with higher oxygen content evolves more CO and CO_2.

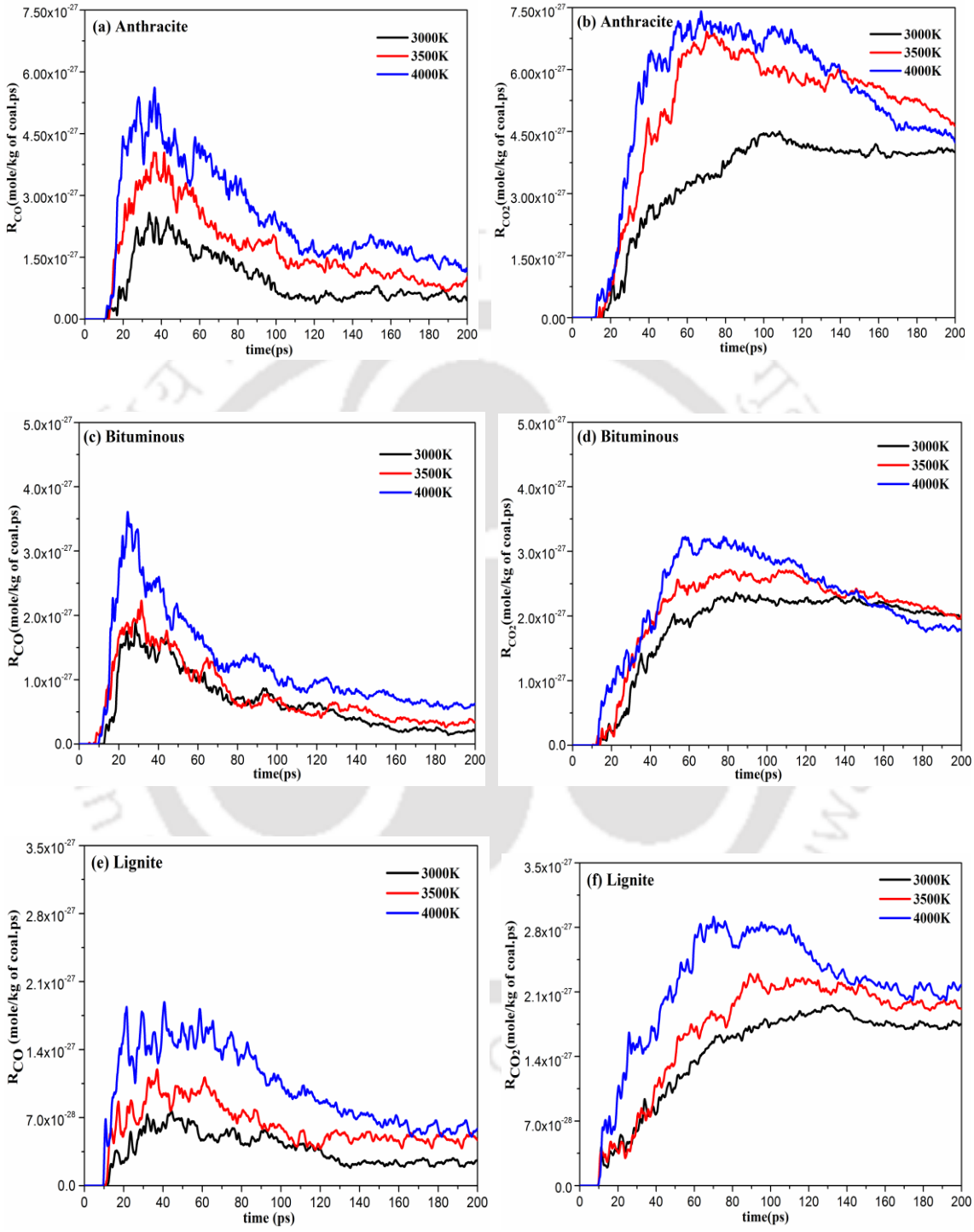

Fig. 2.23 The effect of temperature on the formation rate of CO, CO_2 for (a-b) anthracite, (c-d) bituminous, and (e-f) lignite from ReaxFF MD-simulation

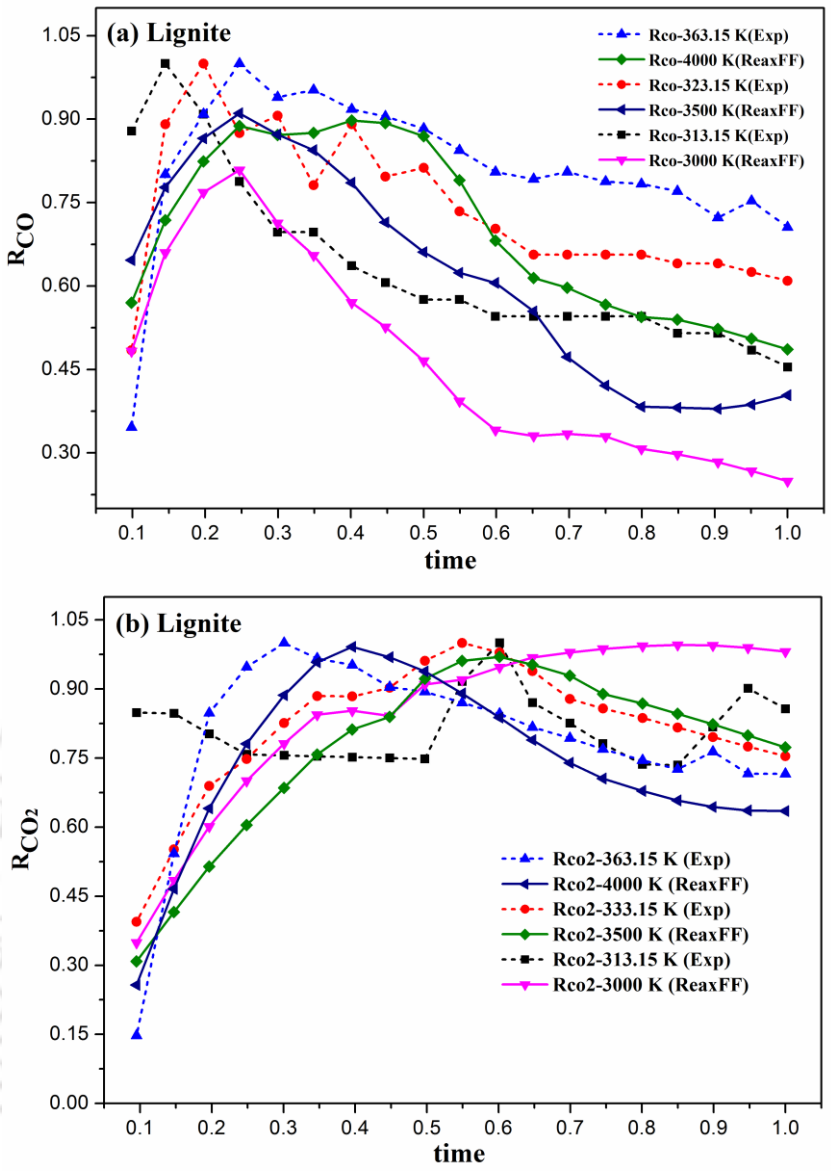

Fig. 2.24 Experimental and ReaxFF MD-simulation results for the effect of temperature on the formation rate of (a) CO, and (b) CO_2 for lignite

Table 2.3 Industrially relevant gas as evolved in pyrolysis at 3000 K

Types of coal	CH_4 (mole %)	C_2H_4 (mole %)	C_2H_6 (mole %)
Lignite	8.0645	22.5806	8.0645
Bituminous	6.4516	18.3140	6.4516
Anthracite	5.6451	11.2903	3.7058

Fig. 2.25 shows the amount of CO and CO_2 evolved during the pyrolysis at a different temperature. The van't Hoff's plot i.e. Fig. 2.25 shows a linear plot of CO and CO_2 with respect to temperature. As per experimental trend, a linear relation for CO evolution is found for all the coal samples [43]. It implies that the oxygen containing group easily decomposes when pyrolysed at 3500 K to produce CO_2. Table 2.4 gives the products of pyrolysis at 3500K which depicts that the coal releases a higher content of CO and CO_2 and it depends on the rank of the coal.

Table 2.4 Fraction of coal-O_2 evolved as CO_2 and CO on pyrolysis at 3500 K

Types of coal	CO_2 (mole %)	CO (mole %)
Lignite	7.258	14.516
Bituminous	6.452	8.419
Anthracite	5.645	1.613

Overall it is evident that the ReaxFF model (Fig. 2.20) points out to the fact that the functional groups decompose to produce light gas species such as CO, CO_2, H_2, CH_2, and CH_4. Both the aromatic and aliphatic portion of coal releases the radicals $H^{\bullet}$ and $OH^{\bullet}$ in order to form CH_2, CH_4, CO, and CO_2. The oxygenated coal molecules (CO, CO_2, and H_2O) and hydrocarbons (CH_3, CH_4, aliphatic) are hence the major intermediates formed during the reaction. In summary the coal molecules fragment to produce unsaturated molecules and hydrogen at a high temperature. This confirms the experimental reaction mechanism of Serio et al. [48], for the pyrolysis reaction which includes gas phase reaction between non-hydrocarbon species. Further, it also depicts the gas phase reaction involving hydrocarbon species (paraffin and olefins) and non-hydrocarbon species

(methane, CH_4). It also confirmed a gas-solid reaction involving char and non-hydrocarbon (CO, CO_2) which complements our ReaxFF MD-simulation results.

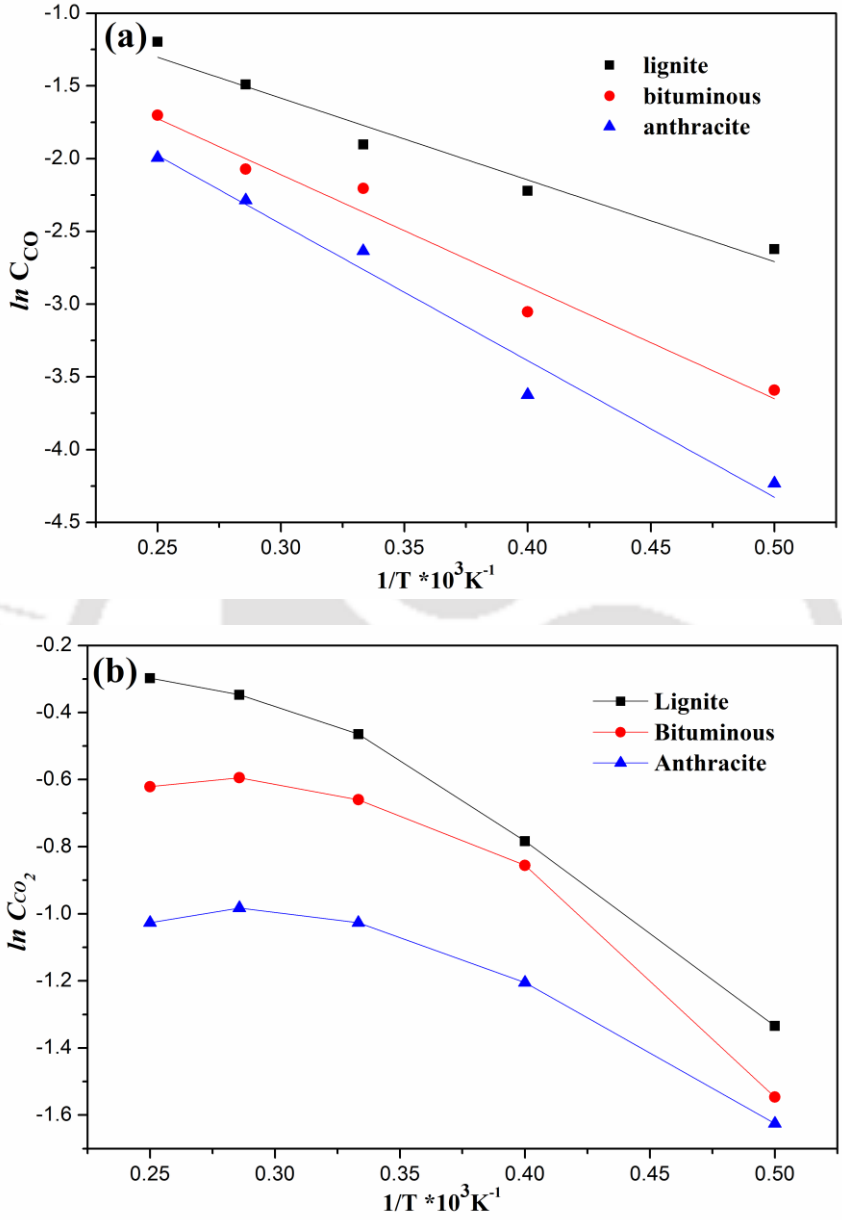

Fig. 2.25 Evolution of CO and CO_2 on pyrolysis of anthracite, bituminous, and lignite coals

References

[1] D. W. Krevelen, Coal--typology, physics, chemistry, constitution, Elsevier Science1993.

[2] L. Zeng-hua, W. Ya-li, S. Na, Y. Yong-liang, Y. Yu-jing, Experiment study of model compound oxidation on spontaneous combustion of coal, Procedia Earth and Planetary Science, 1 (2009) 123-129.

[3] A. A. Agroskin, Chemistry and technology of coal, Program for Scientific Translations [published for the US Department of the Interior and the National Science Foundation]1966.

[4] N. Vasilakos, Advances in coal chemistry, (1988).

[5] C. K. Westbrook, W. J. Pitz, O. Herbinet, H. J. Curran, E. J. Silke, A comprehensive detailed chemical kinetic reaction mechanism for combustion of n-alkane hydrocarbons from n-octane to n-hexadecane, Combustion and Flame, 156 (2009) 181-199.

[6] M. Hobbs, P. Radulovic, L. Smoot, Combustion and gasification of coals in fixed-beds, Progress in Energy and Combustion Science, 19 (1993) 505-586.

[7] G. Domazetis, J. Liesegang, B. James, Studies of inorganics added to low-rank coals for catalytic gasification, Fuel Processing Technology, 86 (2005) 463-486.

[8] G. Domazetis, B. D. James, J. Liesegang, Computer molecular models of low-rank coal and char containing inorganic complexes, Journal of Molecular Modeling, 14 (2008) 581-597.

[9] A. C. Van Duin, S. Dasgupta, F. Lorant, W. A. Goddard, ReaxFF: a reactive force field for hydrocarbons, The Journal of Physical Chemistry A, 105 (2001) 9396-9409.

[10] S. Bhoi, T. Banerjee, K. Mohanty, Molecular dynamic simulation of spontaneous combustion and pyrolysis of brown coal using ReaxFF, Fuel, 136 (2014) 326-333.

[11] M. R. Weismiller, A. C. v. Duin, J. Lee, R. A. Yetter, ReaxFF reactive force field development and applications for molecular dynamics simulations of ammonia borane dehydrogenation and combustion, The Journal of Physical Chemistry A, 114 (2010) 5485-5492.

[12] S. Bhoi, T. Banerjee, K. Mohanty, Insights on the combustion and pyrolysis behavior of three different ranks of coals using reactive molecular dynamics simulation, RSC Advances, 6 (2016) 2559-2570.

[13] S. J. Stuart, A. B. Tutein, J. A. Harrison, A reactive potential for hydrocarbons with intermolecular interactions, The Journal of Chemical Physics, 112 (2000) 6472-6486.

[14] A. C. Van Duin, A. Strachan, S. Stewman, Q. Zhang, X. Xu, W. A. Goddard, ReaxFFSiO reactive force field for silicon and silicon oxide systems, The Journal of Physical Chemistry A, 107 (2003) 3803-3811.

[15] K. Chenoweth, A. C. Van Duin, W. A. Goddard, ReaxFF reactive force field for molecular dynamics simulations of hydrocarbon oxidation, The Journal of Physical Chemistry A, 112 (2008) 1040-1053.

[16] S. Agrawalla, A. C. van Duin, Development and application of a ReaxFF reactive force field for hydrogen combustion, The Journal of Physical Chemistry A, 115 (2011) 960-972.

[17] E. Salmon, A. C. van Duin, F. Lorant, P.-M. Marquaire, W. A. Goddard, Early maturation processes in coal. Part 2: Reactive dynamics simulations using the ReaxFF reactive force field on Morwell Brown coal structures, Organic Geochemistry, 40 (2009) 1195-1209.

[18] Q.-D. Wang, J.-B. Wang, J.-Q. Li, N.-X. Tan, X.-Y. Li, Reactive molecular dynamics simulation and chemical kinetic modeling of pyrolysis and combustion of n-dodecane, Combustion and Flame, 158 (2011) 217-226.

[19] X. Liu, J.-H. Zhan, D. Lai, X. Liu, Z. Zhang, G. Xu, Initial pyrolysis mechanism of oil shale kerogen with reactive molecular dynamics simulation, Energy and Fuels, 29 (2015) 2987-2997.

[20] M. Zheng, X. Li, J. Liu, L. Guo, Initial chemical reaction simulation of coal pyrolysis via ReaxFF molecular dynamics, Energy and Fuels, 27 (2013) 2942-2951.

[21] Scientific Computing and Modelling (SCM), ADF; SCM, Theoretical Chemistry, Vrije Universiteit, Amsterdam, Netherlands, 2013.

[22] J. Tersoff, New empirical approach for the structure and energy of covalent systems, Physical Review B, 37 (1988) 6991.

[23] D. W. Brenner, Empirical potential for hydrocarbons for use in simulating the chemical vapor deposition of diamond films, Physical Review B, 42 (1990) 9458.

[24] T. P. Senftle, S. Hong, M. M. Islam, S. B. Kylasa, Y. Zheng, Y. K. Shin, C. Junkermeier, R. Engel-Herbert, M. J. Janik, H. M. Aktulga, The ReaxFF reactive force-field: development, applications and future directions, npj Computational Materials, 2 (2016) 15011.

[25] B. Arab, A. Shokuhfar, Molecular dynamics simulation of cross-linked urea-formaldehyde polymers for self-healing nanocomposites: prediction of mechanical properties and glass transition temperature, Journal of Molecular Modeling, 19 (2013) 5053-5062.

[26] J. P. Mathews, A. L. Chaffee, The molecular representations of coal–a review, Fuel, 96 (2012) 1-14.

[27] H. Kumagai, J. Hayashi, T. Chiba, K. Nakamura, Change in physical and chemical characteristics of brown coal along with a progress of moisture release, Abstracts of Papers of the American Chemical Society, American Chemical Society 1155 16th st, NW, Washington, DC 20036 USA, 1999, pp. U611-U611.

[28] M. R. Narkiewicz, J. P. Mathews, Improved low-volatile bituminous coal representation: incorporating the molecular-weight distribution, Energy and Fuels, 22 (2008) 3104-3111.

[29] I. Wender, Catalytic synthesis of chemicals from coal, Catalysis Reviews—Science and Engineering, 14 (1976) 97-129.

[30] F. Castro-Marcano, A. M. Kamat, M. F. Russo, A. C. van Duin, J. P. Mathews, Combustion of an Illinois No. 6 coal char simulated using an atomistic char representation and the ReaxFF reactive force field, Combustion and Flame, 159 (2012) 1272-1285.

[31] S. Niksa, G.-s. Liu, R. H. Hurt, Coal conversion submodels for design applications at elevated pressures. Part I. devolatilization and char oxidation, Progress in Energy and Combustion Science, 29 (2003) 425-477.

[32] G.-S. Liu, S. Niksa, Coal conversion submodels for design applications at elevated pressures. Part II. Char gasification, Progress in Energy and Combustion Science, 30 (2004) 679-717.

[33] N. M. Laurendeau, Heterogeneous kinetics of coal char gasification and combustion, Progress in Energy and Combustion Science, 4 (1978) 221-270.

[34] D.-e. Jiang, A. C. Van Duin, W. A. Goddard III, S. Dai, Simulating the initial stage of phenolic resin carbonization via the ReaxFF reactive force field, The Journal of Physical Chemistry A, 113 (2009) 6891-6894.

[35] K. Mae, H. Shindo, K. Miura, A new two-step oxidative degradation method for producing valuable chemicals from low rank coals under mild conditions, Energy and Fuels, 15 (2001) 611-617.

[36] P. F. Nelson, I. W. Smith, R. J. Tyler, J. C. Mackie, Pyrolysis of coal at high temperatures, Energy and Fuels, 2 (1988) 391-400.

[37] V. Kříž, Z. Brožová, Co-pyrolysis of coal/waste polymers mixtures, Acta Geodynamica et Geomaterialia, 4 (2007) 146.

[38] S. S. Tamhankar, J. T. Sears, Coal pyrolysis at high temperatures and pressures, Fuel, 63 (1984) 1230-1235.

[39] Y. Yun, G.-B. Lee, Effects of pressure in coal pyrolysis observed by high pressure TGA, Korean Journal of Chemical Engineering, 16 (1999) 798-803.

[40] J. Abichandani, C. Deradourian, R. Gannon, D. Stickler, J. Woodroffe, K. Neoh, Pressure effects on steam pyrolysis of coal, Fuel Processing Technology, 18 (1988) 133-146.

[41] K. Baris, S. Kizgut, V. Didari, Low-temperature oxidation of some Turkish coals, Fuel, 93 (2012) 423-432.

[42] K. Baris, H. Aydin, V. Didari, Statistical modeling of the effect of rank, temperature, and particle size on low-temperature oxidation of Turkish coals, Combustion Science and Technology, 183 (2010) 105-121.

[43] R. Kaji, Y. Hishinuma, Y. Nakamura, Low temperature oxidation of coals: Effects of pore structure and coal composition, Fuel, 64 (1985) 297-302.

[44] M. Itay, C. R. Hill, D. Glasser, A study of the low temperature oxidation of coal, Fuel Processing Technology, 21 (1989) 81-97.

[45] H. Wang, B. Z. Dlugogorski, E. M. Kennedy, Pathways for production of CO_2 and CO in low-temperature oxidation of coal, Energy and Fuels, 17 (2003) 150-158.

[46] D. Carpenter, D. Giddings, Initial stages of oxidation of coal with molecular oxygen I-effect of time temperature+coal rank on rate of oxygen consumption, Fuel, 43 (1964) 247-266.

[47] N. Marevich, A. Travin, Tendency toward spontaneous combustion of petrographic types of coal from Prokop'evsk deposits of Kuzbass, Izv. Akad. Nauk SSSR Otd. Tekh. Nauk, (1953) 1110-1117.

[48] M. A. Serio, D. G. Hamblen, J. R. Markham, P. R. Solomon, Kinetics of volatile product evolution in coal pyrolysis: experiment and theory, Energy and Fuels, 1 (1987) 138-152.

Chapter 3

Solid-Liquid Equilibria Predictions using COnductor like Screening MOdel for Real Solvent (COSMO-RS)

3.1 Introduction

Coal has traditionally been utilized as coal-to-liquid fuel and in particular coal-to-chemical industries. Most of the high and low-rank coals are reserves which make them a potential source for petrochemical industry [1-3]. For coal processing technology, the most important and fundamental understanding is its solvent swelling and solubility. The effect of swelling and solubility can be predicted from the interaction of coal and solvent which gives us an insight underlying the physical and chemical structure of coal. The solubilisation and swelling of coal molecules allow the fragments to interact with each other which ultimately lead to the formation of radicals [4, 5]. It is a well-known fact that the structure of coal is complex in nature due to a large number of carboxylate groups present in the low and medium rank coal. Hence the interaction of coal and solvent plays a vital role in the fragmentation of coal molecules [6, 7]. Some conventional solvents like methanol, tetraline, and N-methylpyrrolidione (NMP) form strong hydrogen bonds with coal particles. Therefore in such solvents, coal particles swell or solubilise in powder form which increases its surface area [8, 9].

With respect to Ionic Liquids (ILs), it has been pointed out that the fragmentation of coal in ILs depends on the cations particularly the length of the alkyl group associated with it. This is important as the correct choice of IL will help it in swelling and fragmenting the coal particle so as to increase its surface area. However, the choice of solvent and the quantification of a good contact are difficult to make as it has to disrupt the intra-hydrogen bonding network of coal. A possible way to do it through HOMO/LUMO or the highest occupied molecular orbital (HOMO) and lowest unoccupied molecular orbital (LUMO) interaction energy, which can be a useful indicator for CH–π bonding within compounds that

interact simultaneously. This has been well demonstrated for complexes with IL's [10, 11]. Thus, keeping the advantages in mind, the interaction between coal and IL's are investigated in this chapter through the HOMO-LUMO energy values and their corresponding energy gaps. An attempt has been made to recognize the stability and reactivity of chemical species with ILs. The coal considered in this work were of the following type: brown coal (lignite), anthracite and bituminous. They resemble the same structure as used in ReaxFF simulations (Chapter 2). The quantum chemical properties were computed for clusters containing the coal-IL mixture.

It should be noted that the HOMO-LUMO energy gap does not give us a complete picture for the coal-IL interaction, since the columbic (electrostatic) interaction force is also due to other factors such as charge distribution, molecular orbital, and electron density. In order to understand the macroscopic phenomena, COSMO (COnductor like Screening MOdel) methodology has been adopted which along with a statistical mechanical framework (i.e. RS or Real Solvents) computes the activity coefficient of a solute (coal) in the mixture (IL + Coal). The COSMO part predicts the screening charges when a solute is kept in the midst of a continuum with infinite dielectric constant. This is computed by solving the interaction between screening charge with itself, nuclei and solute electron density. The screening charges once obtained are then used to compute the restoring free energy (ΔG) by a statistical mechanical framework. This restoring free energy can then be converted to the chemical potential of a component in the mixture to predict the activity coefficient which is synonymous with classical thermodynamics. The details and methodology of such a model are given in section 3.2.2 and is used as a tool to predict the activity coefficient [12]. The model was first implemented as COSMO-RS (COnductor like Screening MOdel for Real

Solvent) [13-15] and then a further variant namely COSMO-SAC (COnductor like Screening MOdel for Segment Activity Coefficient) was also deduced [16]. Both COSMO-RS and COSMO-SAC obtain the activity coefficient of solutes in the mixture. With these activity coefficients, COSMO based methods can also predict the Infinite Dilution Activity Coefficient (IDAC) and solid-liquid-equilibrium (SLE). The IDAC value refers to the activity coefficient when the mole fraction of solute in mixture is close to zero. In summary, along with the HOMO-LUMO energies, the COSMO based predictions will help us in selecting the best cation and anion combinations among the 18 ILs studied in the current chapter. We shall first discuss the HOMO-LUMO interaction and then conclude the chapter with the COSMO based predictions.

3.2 HOMO-LUMO Interaction

Chattaraj et al. [17, 18] studied the electronic structure principles in quantum chemistry where seven basic parameters such as HOMO energy, LUMO energy, HOMO-LUMO band gap, chemical potential (μ), electronegativity (χ), chemical hardness (η), chemical softness (σ), and electrophilicity index (ω) were outlined. We shall discuss these with operational expression and orbital definition in the ensuing subsections.

3.2.1 HOMO and LUMO Orbital Energies

It is a well-known fact that the molecules possess both higher occupied molecular orbital energy (HOMO) and lower unoccupied molecular orbital energy (LUMO). LUMO energy is directly related to the electron affinity (EA) which has a capability to accept one electron from donor molecule and is influenced by the attack of nucleophiles [19]. This, in turn, affects the interacting system so as to make covalent or hydrogen bonding resulting in

the transfer of partial charges [20]. On the other side HOMO energy is directly related to the ionization potential (IP) which is influenced by the attack of electrophiles. The HOMO-LUMO [21-23] energy can be written as in the context of Density Functional Theory (DFT) as:

$$EA = -E_{LUMO} \tag{3.1}$$

$$IP = -E_{HOMO} \tag{3.2}$$

where E_{LUMO} and E_{HOMO} is Kohn-Sham [24] Eigen values associated with frontier molecular orbitals: LUMO and HOMO. Hard nucleophiles have low HOMO energy and hard electrophiles have high LUMO energy. If HOMO-LUMO band gap is more, the stability of the complex increases. This results in the easier transfer of partial charge between the molecules. In turn, it also affects its polarizability. Thus soft molecule having smaller HOMO-LUMO gap is more polarized than a hard molecule.

3.2.2 Electronegativity (χ) and Chemical potential (μ)

Electronegativity (χ) is a tendency of an atom to attract electron [21]. This can be represented by the average of HOMO and LUMO energy values. In terms of molecular orbital energy, electronegativity (χ) can be expressed as:

$$\chi = -\left(\frac{E_{HOMO} - E_{LUMO}}{2}\right) = \left(\frac{IP + EA}{2}\right) \tag{3.3}$$

Similarly, the chemical potential (μ) is a property of ground state which is simply the negative of electronegativity and mainly determines the escaping tendency of the electron [21]. In terms of molecular orbital energy, chemical potential (μ) can be expressed as:

$$\mu = \left(\frac{E_{HOMO} - E_{LUMO}}{2} \right) = -\left(\frac{IP + EA}{2} \right) \tag{3.4}$$

3.2.3 Global Hardness (η) and Global Softness (σ)

Pearson et al. [22] defined global hardness (η) and softness (σ) as the resistance of an atom, molecules or ions against deformation by mechanical forces. Global hardness measures charge transfer and stability of the interacting molecule. Softness is the reciprocal of Hardness which measures the extent of charge transfer. Global hardness and softness can also be measured by the HOMO/LUMO energy gap. Pearson et al. [22] defines the global hardness and global softness in terms of operational and orbital expression as given below.

$$\eta = E_{LUMO} - E_{HOMO} = \left(\frac{IP - EA}{2} \right) \tag{3.5}$$

$$\sigma = \left(\frac{1}{\eta} \right) = \left(\frac{2}{E_{LUMO} - E_{HOMO}} \right) = \left(\frac{2}{IP - EA} \right) \tag{3.6}$$

Large HOMO-LUMO gap implies the molecules are hard, hence the stability is higher and it opposes the charge transfer. On contrary, when molecules are soft, the HOMO-LUMO gap tends to be smaller. A smaller gap requires less amount of energy to transfer the molecules to a higher excited state. As a result, molecules are highly polarizable.

3.2.4 Electrophilicity Index (ω)

The capability of a substance to accept as electrons is termed as electrophilicity index (ω). From the previous report of Parr et al. [23], the electron affinity describes the capability of a substance to have only one electron from the surroundings. Electrophilicity index

mainly measures the lowering of energy as a result of electron flow between donor and acceptor.

$$\omega = \left(\frac{\mu^2}{2\eta}\right) = \left\{\frac{\left(\frac{E_{HOMO} - E_{LUMO}}{2}\right)^2}{E_{LUMO} - E_{HOMO}}\right\} = \left(\frac{\left(\frac{IP + EA}{2}\right)^2}{IP - EA}\right) \tag{3.7}$$

The schematic representation of HOMO/LUMO energy and band gap and other terms is given below (Fig. 3.1):

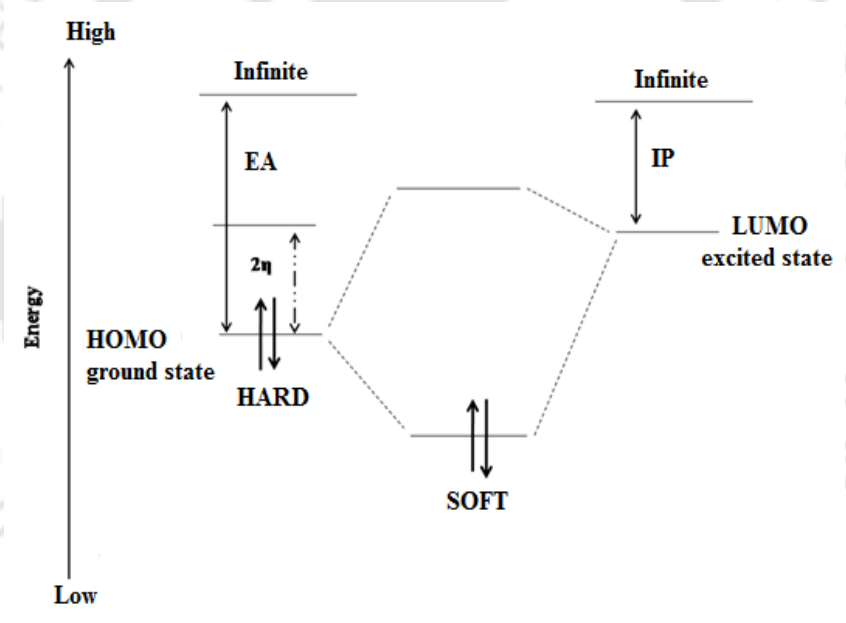

Fig. 3.1 Diagram of HOMO, LUMO and band gap

3.3 Computational Details

3.3.1 Geometry optimization

For the calculation, the structure of brown coal (lignite), bituminous, and anthracite were taken from literature [2, 25-27]. The initial structure of all the coals (Fig. 3.2) were

drawn by MOLDEN freeware [28]. Dummy atoms were used to add the cations, anions, and coal as proposed by Meng et al. [29]. Similarly, the cations and anions comprising 18 ILs were also drawn using a similar approach (Table 3.1). All the geometries were optimized using density function theory *B3LYP* [30] with the basis function of 6-31G*. The same level of theory was used to calculate the partial charges of coal molecules via *CHELPG* [31] scheme. A frequency optimization was done using the "*freq*" keyword in Gaussian 03 to detect the presence of any negative or imaginary frequencies. After the geometry optimization, the final structure was used to generate the COSMO file. All the calculations are done under vacuum and no packing effects within the liquids are assumed [7].

3.2.2 'COSMO' file Generation

A COnductor like Screening MOdel (COSMO) was proposed by Klamt [32]. In COSMO-RS [33, 34] surface properties are calculated by screening charge densities within the molecule. The screening charge is obtained when a molecule is placed in a perfect conductor which has infinite dielectric constant. In this way, the whole molecule is perfectly 'screened' by the continuum. Before inserting the molecule in the conductor, a cavity is formed within the continuum having spheres which have a radius 1.2 times of van der Waal (*vdW*) radii of the participating atoms of the molecule. Thus, the whole molecule is surrounded by *vdW* -like segmented surface or a polygon which is clearly visible in Fig. 3.3. In the segmented surface of molecules, the blue colour indicates a negative surface charge, which screens positive partial charges within the molecules, red colour indicates a positive surface charge which screens negative partial charges, while yellow and green colour represents close to neutral charges within the molecules. The number of segmented surfaces or polygons will vary based on the level of theory used and also with the size of the

molecules. This is usually performed at DFT level with *B3LYP* theory in *Turbomole 6.2* [35].

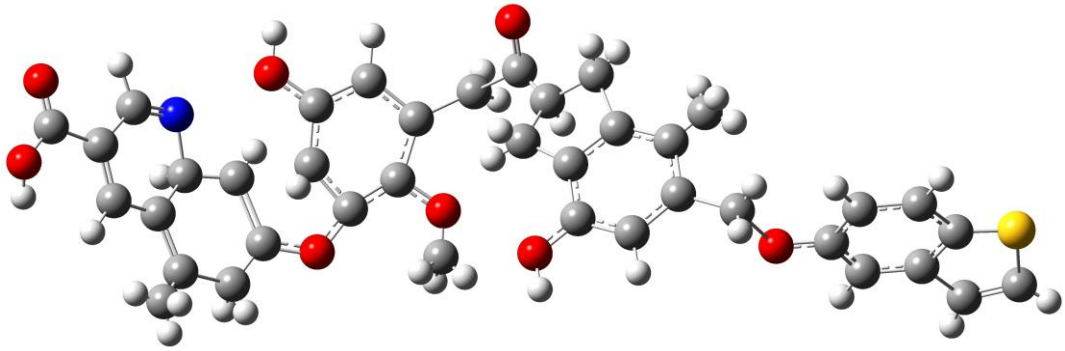

(a)

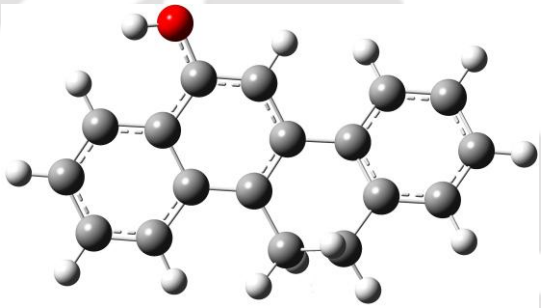

(b)

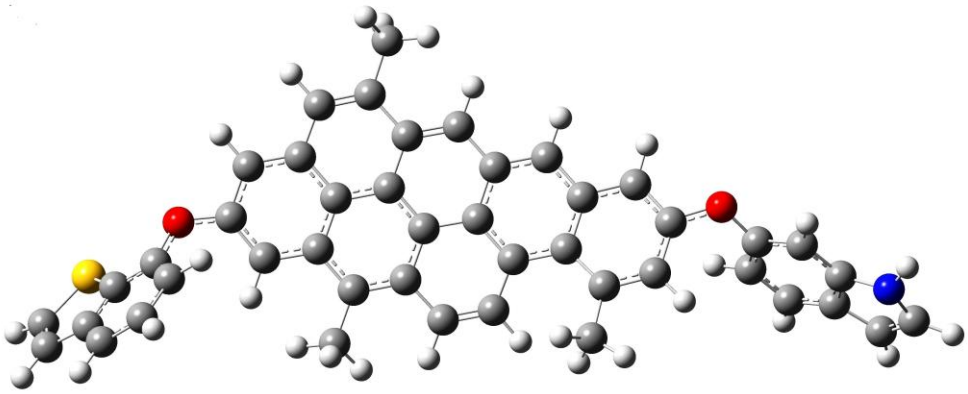

(c)

Fig. 3.2 Structure of (a) lignite ($C_{39}H_{35}O_{10}NS$), (b) bituminous ($C_{18}H_{14}O$), and (c) anthracite coals ($C_{45}H_{29}O_2NS$) (Colour represents the different atoms such as yellow: Sulphur, blue: Nitrogen, grey: Carbon, red: Oxygen, white: Hydrogen atoms respectively [2, 25-27])

Table 3.1 Ionic Liquids used in this study.

Name of the ionic liquid	Acronyms	Structures
1-butyl-2,3-dimethylimidazolium hexafluorophosphate	[BDMIM] [PF_6]	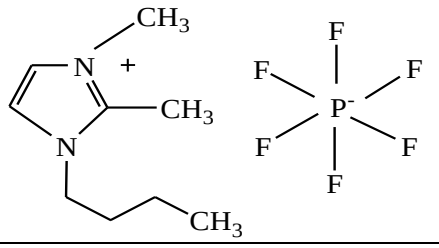
1-butyl-2,3-dimethylimidazolium tetrafluoroborate	[BDMIM] [BF_4]	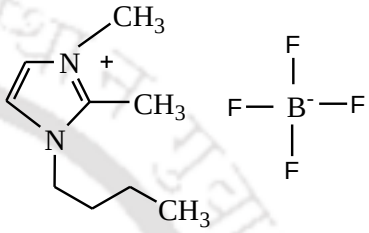
1-benzyl-3-methyleimidazolium tetrafluoroborate	[BYMIM] [BF_4]	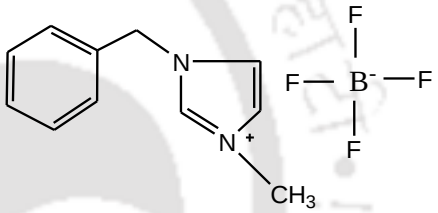
1-ethyl -3-methylimidazolium acetate	[EMIM] [$COOCH_3$]	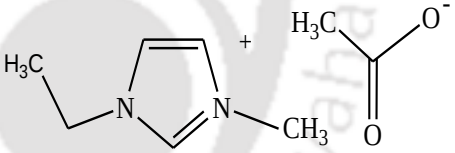
1-methyl -3-propylimidazolium methyl carbonate	[MPIM] [CH_3CO_3]	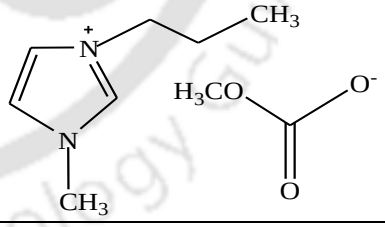
1-butyl-1-methylpyrrolidinium bis(trifluoromethylsulfonyl) imide	[BMPYR] [Tf_2N]	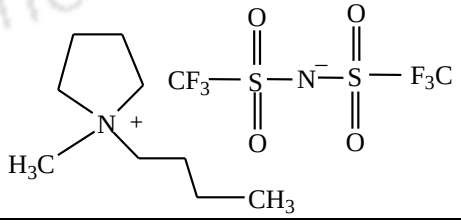
1-ethyl -3-dimethylimidazolium trifluoromethanesulfonate	[EMIM] [TfO]	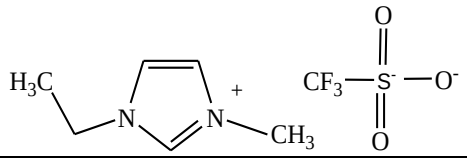

1,3-dihydroxy-2-methylimidazolium bis(trifluromethylsulfonyl) imide	[DHXMIM] [Tf_2N]	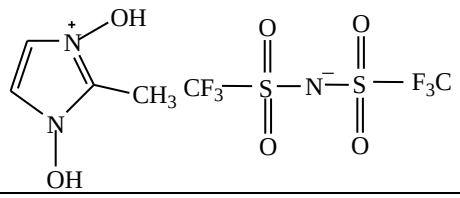
1,3-dimethoxyimidazolium bis(trifluromethylsulfonyl) imide	[DMXIM] [Tf_2N]	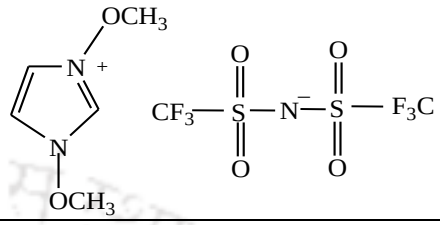
1,3-dimethoxy-2-methylimidazolium bis(trifluromethylsulfonyl) imide	[DMXMIM] [Tf_2N]	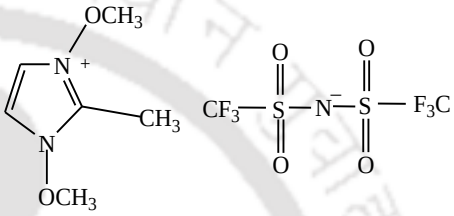
1-ethyl-3-methylimidazolium aminoacetate	[EMIM] [$C_2H_4NO_2$]	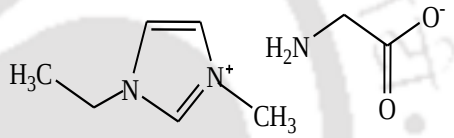
1,2-dimethyl-3-propylimidazolium bis(trifluoromethylsulfonyl) imide	[DMPIM] [Tf_2N]	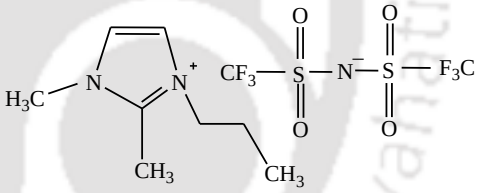
1-butyl-1-methylpyrrolidinium dicyanamide	[BMPYR] [$N(CN)_2$]	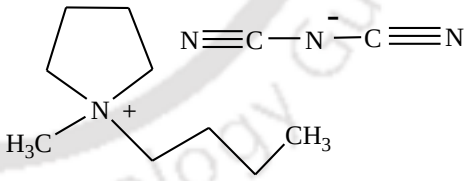
1-butyl-1-methyl pyrrolidinium methyl carbonate	[BMPYR] [CH_3CO_3]	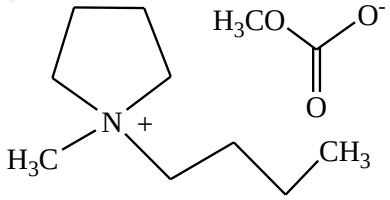

1-butyl-4-methylpyridinium tetrafluoroborate	[BMPY] [BF_4]	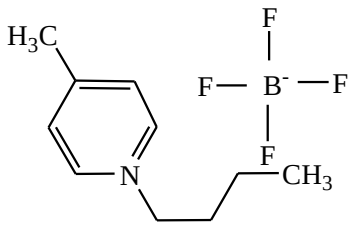
3-methyl-1-propylpyridinium bis(trifluromethylsulfonyl) imide	[MPPY] [Tf_2N]	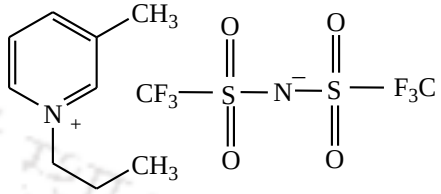
Tributylmethylammonium methylsulfate	[TMA] [$MeSO_4$]	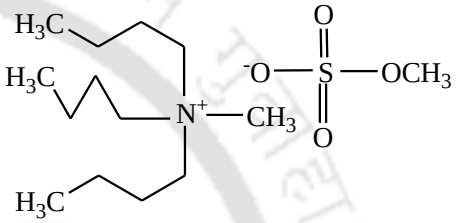
Tributylmethylphosphonium methylsulfate	[MTBP] [$MeSO_4$]	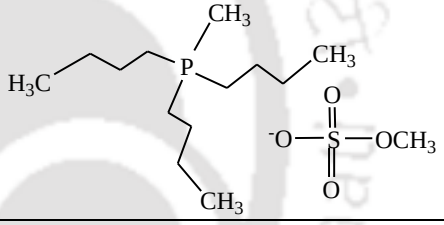

Thus, in this scheme, the steps namely geometry optimization of the molecule, construction of the segmented surface, and the calculation of the segment properties are performed. Due to the perfect screening by the conductor, charge densities are placed over the interface of solute and conductor. These charges are then divided into segments, each having a unique screening charge density value. Geometry optimization merely reflects the minimization of energy with respect to its nuclear coordinates. The segmented surface is then obtained by the union of all the vdW-spheres outlined around each atom. The segment properties is then calculated by defining the energy of solvation (E^{solv}) which solves the interaction of the segments with the solute nuclei (Z) (first term of equation (3.8)), solute electron density (second term of equation (3.8)), and interaction within the segments (third

term of equation (3.8)), as given below [35, 36]. q_α represents the screening charge of α^{th} segment [13].

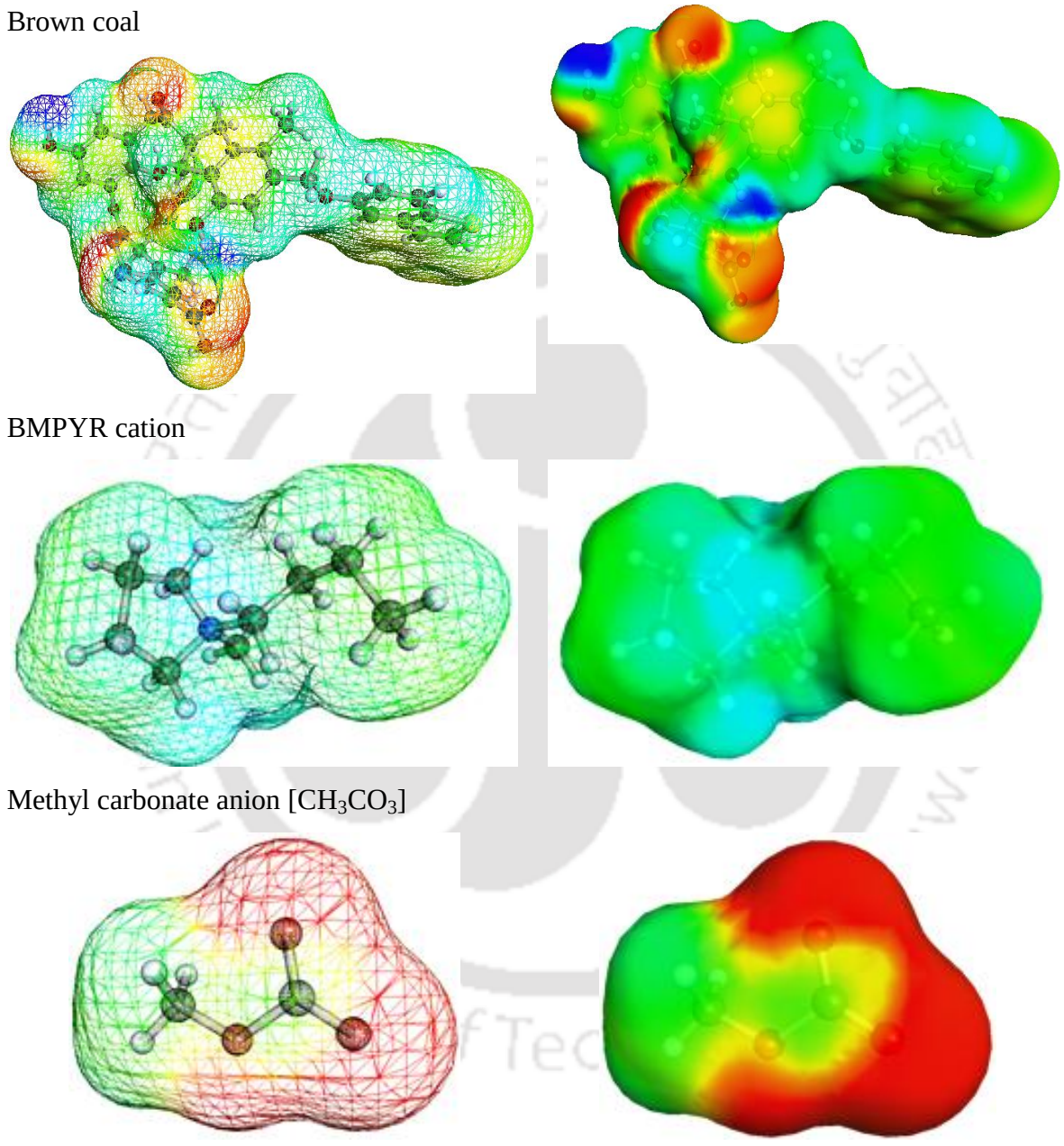

Fig. 3.3 Segmented surface and unimolecular solvation diagrams for brown coal, [BMPYR] cation, and [CH_3CO_3] anion (Colour represents the different segmented surface charges such as; red: positive charge, blue: negative charge, yellow and green: almost neutral charges).

$$4\pi\varepsilon_o E^{solv} = \sum_A \sum_\alpha Z_A q_\alpha B_{A\alpha} + \sum_\alpha q_\alpha C_\alpha + \frac{1}{2}\sum_\alpha \sum_\beta q_\alpha q_\beta D_{\alpha\beta} \tag{3.8}$$

The energy of solvation (E^{solv}) is then minimized with respect to the segments charges (q_α) as given below:

$$\left(\frac{dE^{solv}}{dq_\alpha}\right) = \sum_A Z_A B_{A\alpha} + C_\alpha + \sum_\beta q_\beta D_{\alpha\beta} = 0 \tag{3.9}$$

This process is called as "Self-Consistent Field (SCF)" or a "COSMO" calculation. After the solution of equation (3.9) [35, 36], each segment then possesses a certain charge and an area which in turn is divided to obtain the screening charge density $\sigma\left(q/A\right)$. In a pair-wise interacting surface segment, the surface segment of both molecules has net screening charge densities (SCD) σ and σ'. Thus an electrostatic interaction occurs between two molecules due to the change in shape and the specific interaction per unit area. This results in two form of energy namely, *misfit energy* and *hydrogen bonding energy*. The "misfit" of screening charge density and size of the molecule is defined as,

$$E_{misfit}(\sigma,\sigma') = a_{eff}\frac{\alpha'}{2}(\sigma+\sigma')^2 \tag{3.10}$$

where a_{eff} represents effective contact area between two surface segments, where α' is an adjustable parameter. If $\sigma=\sigma'$, the misfit energy of the surface contact will vanish. The hydrogen bonding (HB) can be described by two adjustable screening charge density, such as; (a) hydrogen-bonding donors which have strongly negative screening charge density (σ_{donor}), and (b) hydrogen-bonding acceptors associated with strongly positive screening

charge density ($\sigma_{acceptor}$). If two sufficiently polar pieces of surface of opposite polarity are in contact, then hydrogen bonding is represented as;

$$E_{HB} = a_{eff} C_{HB} \min\left\{0; \min\left(0; \sigma_{donor} + \sigma_{HB}\right) \max\left(0; \sigma_{acceptor} - \sigma_{HB}\right)\right\} \tag{3.11}$$

where $\sigma_{donor} = \min(\sigma, \sigma') < \sigma_{HB}$ and $\sigma_{acceptor} = \max(\sigma, \sigma') > \sigma_{HB}$. C_{HB} and σ_{HB} are two adjustable parameters. A van der Waals (*vdW*) interaction of the surface segments occurs when electrostatic misfit and hydrogen bonding interact.

$$E_{vdW} = a_{eff}\left(\tau_{vdW} + \tau'_{vdW}\right) \tag{3.12}$$

where τ_{vdW} and τ'_{vdW} are two element-specific adjustable parameters.

The charges are now stored in a file known as 'COSMO' file. The COSMO files stores the surface screening charge densities, optimized geometries, and energies. It is an important descriptor within the COSMO theory and a distribution of these charges (which usually lies within -0.03 to +0.03 e/ $Å^2$) are known as 'sigma profile' (σ-profile). The σ-profiles are merely the histograms of screening charge density which are later required to predict thermodynamic properties such as activity coefficient. The σ-profile for a mixture is the algebraic sum of σ-profiles of individual components as given below:

$$p^{IL}(\sigma) = p^{cation}(\sigma) + p^{anion}(\sigma) \tag{3.13}$$

where $p^{IL}(\sigma)$, $p^{cation}(\sigma)$, and $p^{anion}(\sigma)$ are the sigma profiles for ILs, cation, and anion respectively. The sigma profile of cation and anion obtained individually and then added via simple algebraic addition followed by normalization. This sigma profile (distribution of

screening charges) for each molecule is computed on the equilibrium geometry as obtained by density functional theory of PBV86 [37]. The ideal screening charges are then obtained by using the keyword *SCRF=COSMORS* at the same level of theory *[PBV86]* with the basis set of Triple Zeta Valence Potential (*TZVP*) [38] in combination with a density fitting basis set of *DGA1* [39].

3.2.3 COSMO-RS Theory

The 'RS' part is usually the statistical mechanical framework for predicting the Gibb's Free Energy of solvation given in terms of activity coefficient as (equation (3.14)) [33, 40, 41]:

$$\ln\left(x_{i/s}\gamma_{i/s}\right)=\frac{\Delta G_{i/S}^{solv}-\Delta G_{i/i}^{solv}}{kT}=\frac{\Delta G_{i/S}^{*solv}-\Delta G_{i/i}^{*solv}}{kT}+\ln\left(\frac{V_{i/i}}{V_{i/S}}\right) \tag{3.14}$$

where the subscripts '*i/s'* represents the solute (*i*) in a solvent (*S*), '*' indicates the pseudo-Gibbs energy of solvation, which is merely the non-translational contribution to ΔG and is measurable. The Gibb's Free energy of solvation (ΔG^{*solv}) mainly comprises the electrostatic (ES) and van der Waals (vdW) forces. The van der Waal's contribution is then computed using the London dispersion term $\Delta A_{i/S}^{*disp}$ and a cavity formation term $\Delta A_{i/S}^{*cav}$. The cavity formation term is the amount of work required to create a cavity for solute '*i'* in solvent '*S'* at constant volume and temperature. Here the constant volume arises from the vdW-radii of the atoms. Intramolecular vibration, rotation, and dipole-dipole interactions are neglected in this formalism. Thus equation (3.14) can be written as:

$$\Delta G_{i/S}^{*solv}=\Delta G_{i/S}^{*ES}+\Delta A_{i/S}^{*disp}+\Delta A_{i/S}^{*cav}-kT \tag{3.15}$$

Activity coefficients are then computed by obtaining the difference in the solvation Gibbs energies in the mixture and individual component respectively. In such calculations, the densities and dispersion energies between the two phases are assumed to be equal (equation (3.16)) [33, 40, 41],

$$\Delta G_{i/S}^{*solv} = \left(\frac{\Delta G_{i/S}^{*ES} - \Delta G_{i/i}^{*ES}}{kT} \right) + \ln\left(\gamma_{i/S}^{comb}\right) \tag{3.16}$$

The cavity formation term is now replaced with a combinatorial term $\ln\left(\gamma_{i/S}^{comb}\right)$ which is the same term as used in UNIQUAC (UNIversal QUAsiChemical) or UNIFAC (UNIvesral Functional group Activity Coefficient) models. The first term of equation (3.16) ($\Delta G_{i/S}^{*ES} - \Delta G_{i/i}^{*ES}$) is mainly the restoring free energy i.e. it becomes zero when the molecule is a perfect conductor. This occurs when it is immersed in a medium having infinite dielectric constant. So, any deviation from a perfect conductor is captured with the calculation of $\Delta G_{i/S}^{*ES}$. To make the calculation easier, the ensemble of molecules is assumed to be mimicked by an ensemble of independently-interacting segments. Here, the segments from each component molecules are mixed in proportion with the component mole fractions. For reducing the computational complexity, the segments are further divided into 61 histograms each having a width of 0.001 e/Å^2, i.e. -0.03 to +0.03 e/Å^2. The obtained interactions between histograms provide the amount of energy required to remove the pairwise segments from a fixed point in space. An analogy can be devised from a number of atoms *N*, at a fixed pressure *P* and temperature *T*, is also known as NPT-ensemble where a deduction of a particular molecule (mol_i) or a segment (Seg_α) (in this case histogram) gives a pathway for calculating the chemical potential of the particular molecule or a segment (histogram) respectively.

$$G\left(N-mol_i,P,T\right)=G\left(N,P,T\right)-\mu_{mol,i}$$
$$G\left(N-seg_\alpha,P,T\right)=G\left(N,P,T\right)-\mu_{seg,\alpha} \quad (3.17)$$

So, the total energy or the restoring free energy required will be equal to the sum of all segments (histograms) i.e. $\Delta G_{i/S}^{*ES}=\sum_{\alpha=1}^{N}\mu_{\alpha/S}$ in a mixture '*S*'. The detailed expressions for activity coefficient and methods are described in previous work [33, 40, 41].

3.4 Results and Discussion

3.4.1 HOMO-LUMO Interaction Studies of Coal and ILs

In this section six ionic liquids (IL's) such as; 1-butyl-1-methylpyrrolidinium methyl carbonate ([BMPYR][CH_3CO_3]), 1-butyl-1-methylpyrrolidinium dicyanamide ([BMPYR][$N(CN)_2$]), 1-butyl-1-methylpyrrolidinium bis(trifluromethanesulphonyl)imide ([BMPYR][Tf_2N]), 1-methyl-3-propylimidazolium methyl carbonate ([MPIM][CH_3CO_3]), Tributylmethylammonium methyl sulfate ([TMA][$MeSO_4$]), and Tributylmethylphosphonium methyl sulfate ([MTBP][$MeSO_4$]) were chosen for the interaction study (Table 3.1). In the subsequent sections we shall discuss briefly about the quantum descriptors and then explore its values with respect to the dissolution mechanism.

3.4.1.1 HOMO-LUMO Orbital Energies

The orbital energies of bituminous, anthracite, cations, and anions are shown in Fig. 3.4. A small difference is seen explicitly between the HOMO and LUMO energies of bituminous and anthracite coal respectively. While the HOMO energy of bituminous coal is -0.1934 eV, the HOMO energy of anthracite coal is -0.20125 eV. The corresponding values

of LUMO orbital for bituminous and anthracite coals are -0.04248 eV and -0.09785 eV respectively. LUMO is usually considered a location where other electrons may fill up its orbital. Thus, lower LUMO implies accommodation of a lesser number of electrons in its orbital. It indicates that no further electrons are available on the outer shell for transfer to another atom(s). This implies that the anthracite coal is more stable i.e. less reactive with a prospective solvent than bituminous coal because of its lower LUMO (higher negative) energy (Fig. 3.4). On the other hand, the cation has an electron donor tendency which is formed due to the external network or connectivity with other molecules via CH-π bond [42]. This is conventionally characterized by HOMO energy values.

The HOMO energy value for the cations follows the order: [MPIM] > [BMPYR] > [MTBP] > [TMA]. All the cation possesses negative HOMO energies i.e. -0.54841, -0.54719, -0.53241, -0.28751 eV and are found to be higher in magnitude than the corresponding LUMO energies. It should be noted that bituminous and anthracite coal requires electron acceptors because of a higher negative value of HOMO energy. Thus bituminous and anthracite coal can potentially interact with LUMO of the cation. In the ILs, the HOMO energy implies that the occupied state evolves from anion; while LUMO energy corresponds to that of the unoccupied state i.e. cation. On the other hand, among all the anions, the most stable anion is [Tf_2N] because of its lowest LUMO value. The LUMO (in eV) of anions is followed by: [CH_3CO_3] (0.28832) > [$MeSO_4$] (0.23126) > [$N(CN)_2$] (0.22796) > [Tf_2N] (0.14824). Thus based on the LUMO energy (eV) values the favourable ILs are as follows: [MPIM][CH_3CO_3] (-0.02719) > [MTBP][$MeSO_4$] (-0.02478) > [BMPYR][$N(CN)_2$] (-0.01764) > [TMA][$MeSO_4$] (-0.01433)> [BMPYR][Tf_2N] (-0.01419) > [BMPYR][CH_3CO_3] (-0.00149). Thus [MPIM][CH_3CO_3] possess lowest stability among

all the ILs due to the higher negative values of both HOMO and LUMO energies; whereas [BMPYR][CH_3CO_3] is more stable and a prospective solvent for coal due to its lower values of both HOMO and LUMO energies. This follows the expected trend on previous work [43].

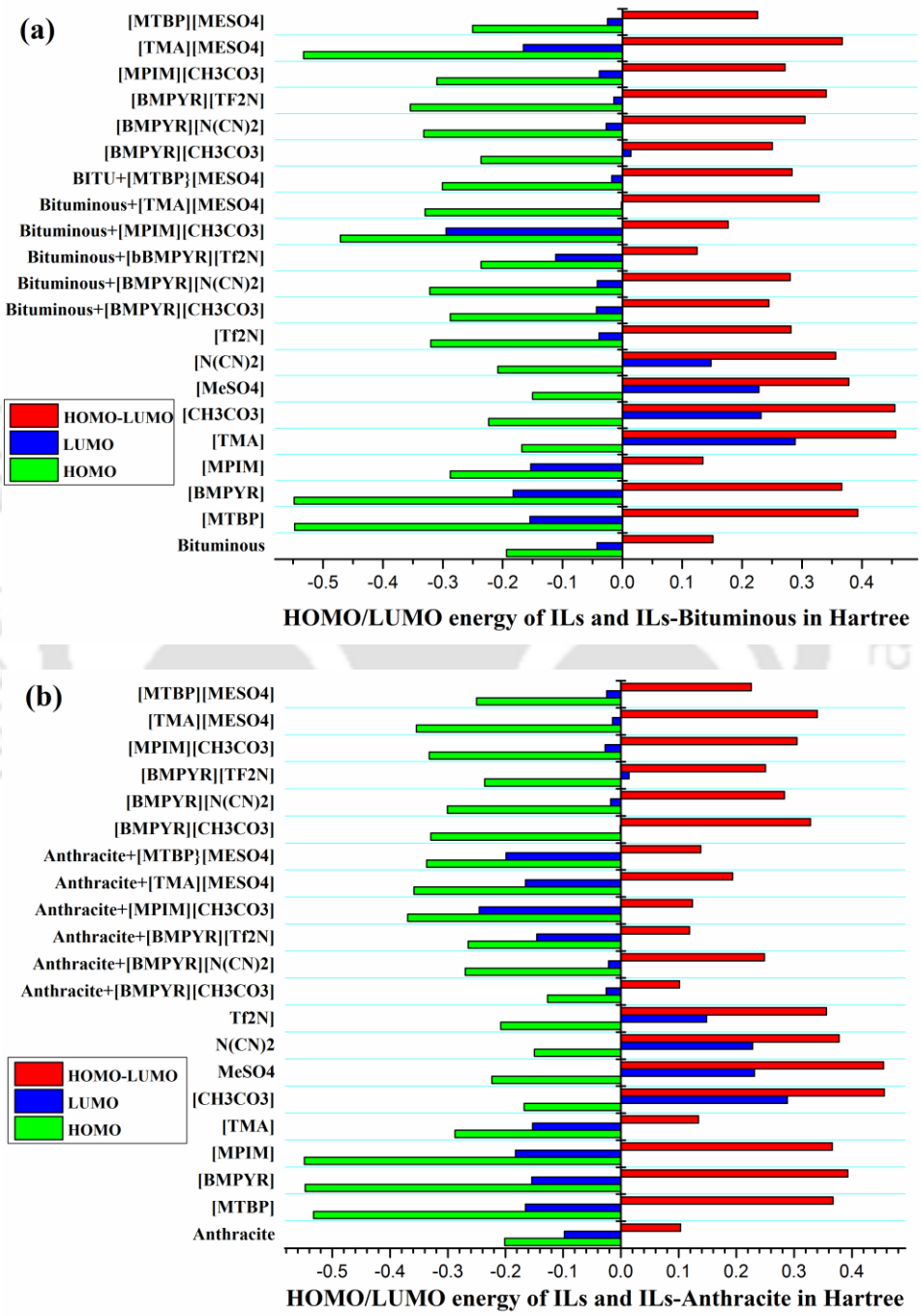

Fig. 3.4 HOMO/LUMO energy of cations, anions, ILs and their clusters with (a) Bituminous and (b) Anthracite coals

Till now we have discussed the orbital energies of individual IL. Let us explore if there is a correlation between the LUMO of IL and LUMO of IL-Coal complex. Thus for clusters of ILs with coal particles, LUMO energy is more important. The stability of ILs via LUMO and its external interacting network are more prominent for dissolving coal. Increase of the cation size lowers the positive charge of cation resulting in increasing polarizability and decreasing stability [42]. On the basis of higher LUMO (lower negative value) energies (eV), the most effective IL for bituminous coal are as follows: [TMA][$MeSO_4$] (-0.2945) > [BMPYR][$N(CN)_2$] (-0.0431) > [BMPYR][Tf_2N] (-0.04184) > [BMPYR][CH_3CO_3] (-0.03886) > [MTBP][$MeSO_4$] (-0.03851) > [MPIM][CH_3CO_3] (-0.01114). For anthracite coal (eV), it follows: [MPIM][CH_3CO_3] (-0.2458) > [MTBP][MeSO4] (-0.1988) > [TMA][$MeSO_4$] (-0.1654) > [BMPYR][Tf_2N] (-0.1458) > [BMPYR][$N(CN)_2$] (-0.02945) > [BMPYR][CH_3CO_3] (-0.0256). Therefore, for bituminous coal and anthracite coal taken together, [MPIM][CH_3CO_3] and [BMPYR][CH_3CO_3] are the potential ILs for dissolution. As a result, increasing the cation size and lowering of the positive charges of cation leads to a decrease in the stability.

The HOMO and LUMO energies are given in Table 3.2 along with the energy of highest (HOMO), second highest (HOMO-1), lowest (LUMO), and second lowest (LUMO+1) unoccupied orbital with their corresponding orbital energy gap. The pictorial view of the frontier molecular orbital and their respective positive and negative region are shown in Fig. 3.5 and Fig. 3.6. It should be noted that the combination of higher LUMO of ILs along with lower HOMO orbital values of bituminous and anthracite will invariably give the best IL.

Table 3.2 HOMO/LUMO Energies and HOMO-LUMO energy gap (eV) of pure molecule and their cluster with coal

SL. No	Name	HOMO (eV)	LUMO (eV)	HOMO-LUMO gap(eV)
1	Bituminous Coal	-0.19344	-0.04248	0.15096
2	Anthracite Coal	-0.20125	-0.09785	0.1034
3	[BMPYR]	-0.54719	-0.15429	0.3929
4	[MPIM]	-0.54841	-0.18247	0.36594
5	[MTBP]	-0.53241	-0.16524	0.36717
6	[TMA]	-0.28751	-0.15307	0.13444
7	$[CH_3CO_3]$	-0.16769	0.28832	0.45601
8	$[MeSO_4]$	-0.2234	0.23126	0.45466
9	$[N(CN)_2]$	-0.14982	0.22796	0.37778
10	$[Tf_2N]$	-0.20785	0.14824	0.35609
11	[BMPYR]$[CH_3CO_3]$	-0.32974	-0.00149	0.32825
12	[BMPYR][$N(CN)_2$]	-0.30069	-0.01764	0.28305
13	[BMPYR]$[Tf_2N]$	-0.23625	-0.01419	0.25044
14	[TMA]$[MeSO_4]$	-0.35437	-0.01433	0.34004
15	[MPIM]$[CH_3CO_3]$	-0.33209	-0.02719	0.3049
16	[MTBP]$[MeSO_4]$	-0.25037	-0.02478	0.225587
17	Bituminous+[BMPYR]$[CH_3CO_3]$	-0.32021	-0.03886	0.28135
18	Bituminous+[BMPYR]$[N(CN)_2]$	-0.28751	-0.0431	0.24441
19	Bituminous +[BMPYR]$[Tf_2N]$	-0.32179	-0.04184	0.27995
20	Bituminous+[MPIM]$[CH_3CO_3]$	-0.23625	-0.1114	0.12485
21	Bituminous+[TMA]$[MeSO_4]$	-0.4709	-0.2945	0.1764
22	Bituminous+[MTBP]$[MeSO_4]$	-0.3098	-0.03851	0.27129
23	Anthracite+[BMPYR]$[CH_3CO_3]$	-0.12697	-0.0256	0.10137
24	Anthracite+[BMPYR]$[N(CN)_2]$	-0.2698	-0.02145	0.24835
25	Anthracite+[BMPYR]$[Tf_2N]$	-0.26478	-0.1458	0.11898
26	Anthracite+[MPIM]$[CH_3CO_3]$	-0.3697	-0.2458	0.1239
27	Anthracite+[TMA]$[MeSO_4]$	-0.3587	-0.1654	0.1933
28	Anthracite+[MTBP]$[MeSO_4]$	-0.3369	-0.1987	0.1382

From Table 3.2, HOMO-LUMO band gap decreases as: [BMPYR][CH_3CO_3] > [BMPYR][Tf_2N] > [MTBP][$MeSO_4$] > [BMPYR][$N(CN)_2$] > [TMA][$MeSO_4$] > [MPIM][CH_3CO_3] for ILs-bituminous; and [BMPYR][$N(CN)_2$] > [TMA][$MeSO_4$] > [MTBP][$MeSO_4$] > [MPIM][CH_3CO_3] > [BMPYR][Tf_2N] > [BMPYR][CH_3CO_3] for ILs-anthracite. Here it can be observed that the trend is the same as with individual HOMO/LUMO energies of each IL. Thus, combining both the results, a lower band gap is seen for [MPIM][CH_3CO_3](0.12485 eV) and [BMPYR][CH_3CO_3](0.10137 eV) for bituminous and anthracite coal respectively. This means the ILs [MPIM][CH_3CO_3] and [BMPYR][CH_3CO_3] are more reactive, less stable and have a higher tendency for coal molecules.

3.4.1.2 Quantum Chemical Descriptors

The other descriptors namely, global hardness and global softness are calculated from HOMO/LUMO values and are shown for IL, IL-bituminous, and IL-anthracite in Fig. 3.7. Increasing softness and decreasing hardness are related to a lower HOMO-LUMO gap in IL-complex clusters. The high softness of cation helps in the CH-π interaction between clusters for e.g. overlap of LUMO of the cation with HOMO of coal molecule as previously discussed in sub-section 3.4.1.1. Following the same trend, [BMPYR][CH_3CO_3] and [MPIM][CH_3CO_3] have a high softness which exhibits a better dissolving power for anthracite coal and bituminous coal respectively. This statement agrees with the HOMO/LUMO energies as discussed in sub-section 3.4.1.1.

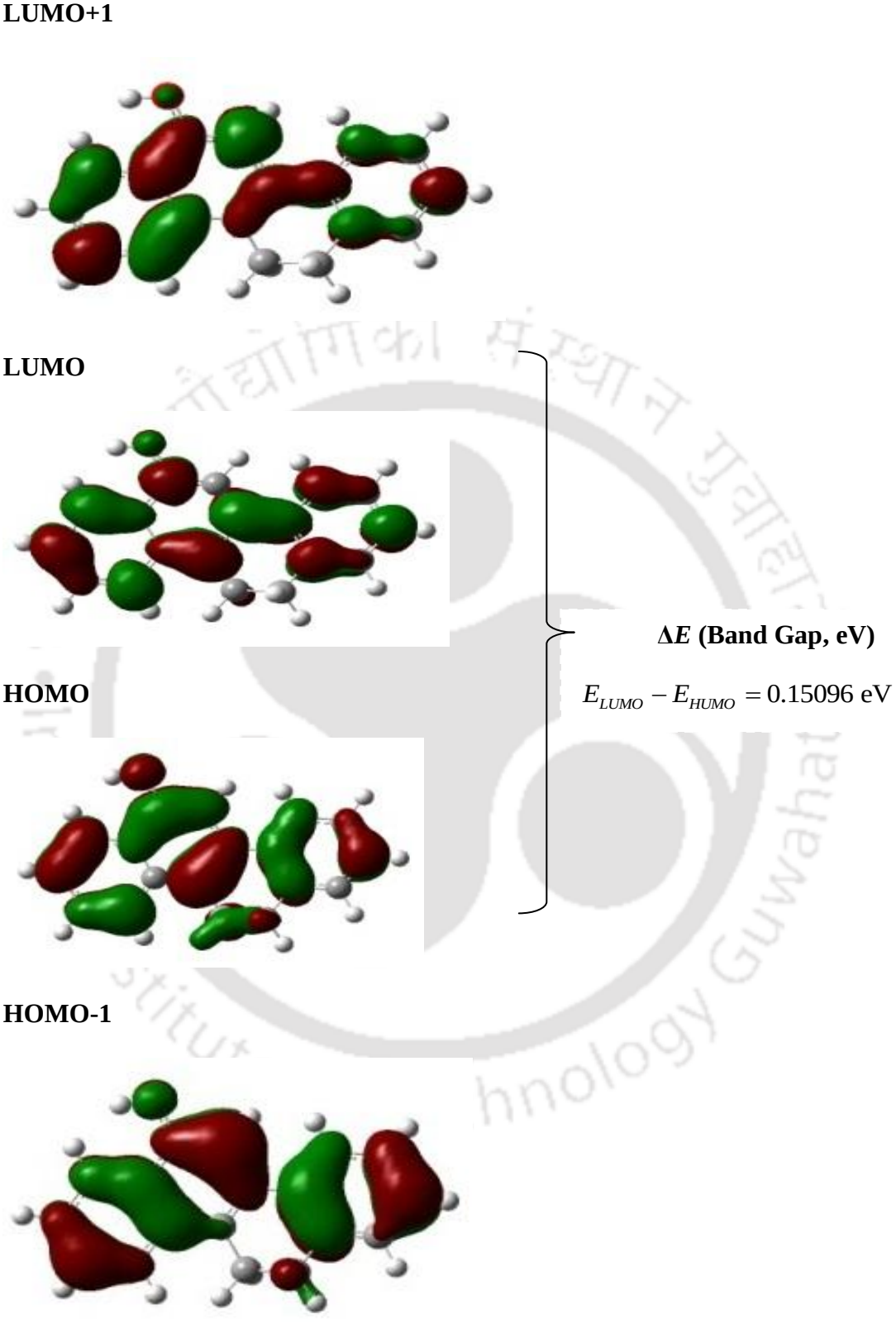

Fig. 3.5 Frontier Orbitals of Bituminous coal by B3LYP/6-31G* with band gap energy (eV)

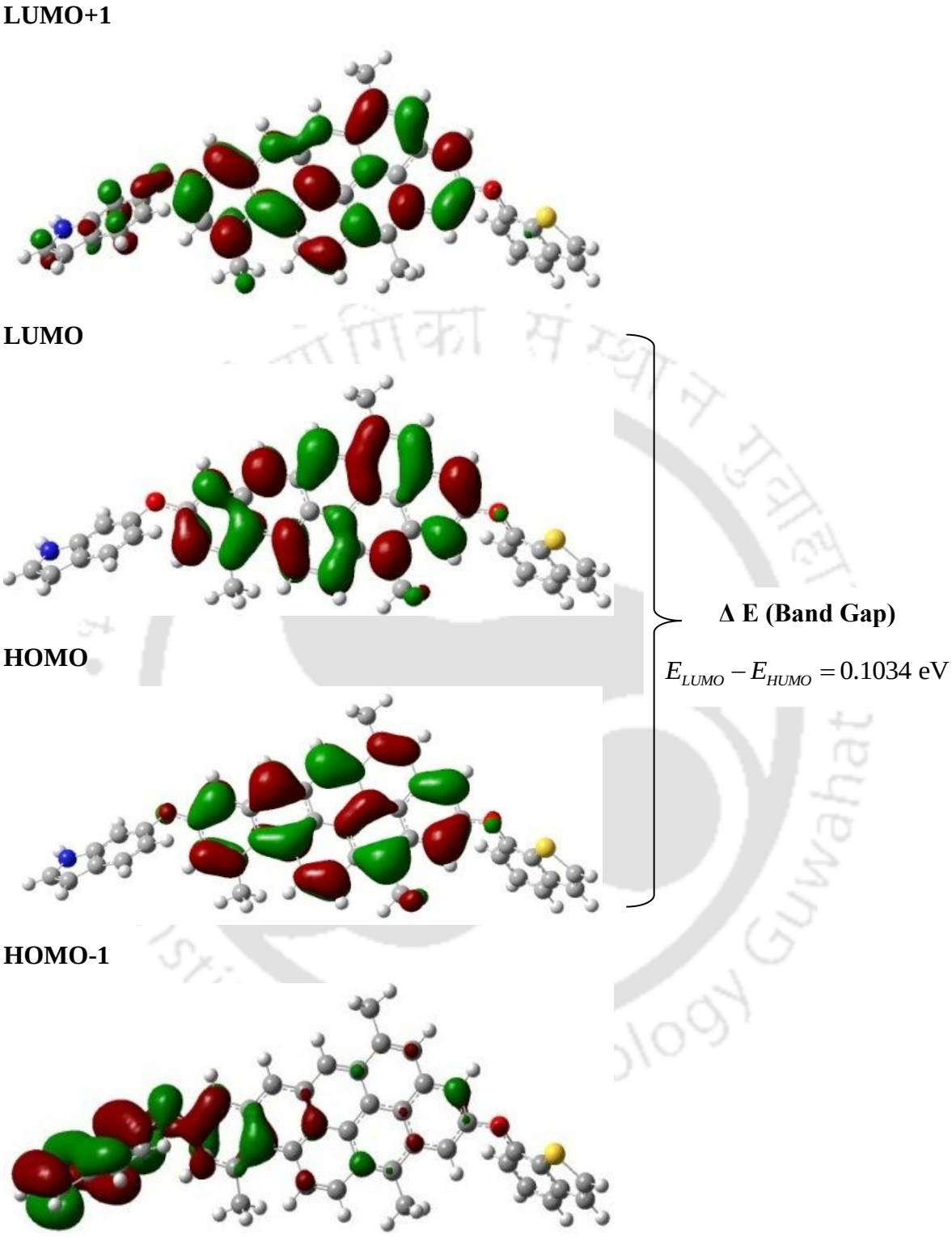

Fig. 3.6 Frontier Orbitals of Anthracite coal by B3LYP/6-31G* with band gap energy (eV)

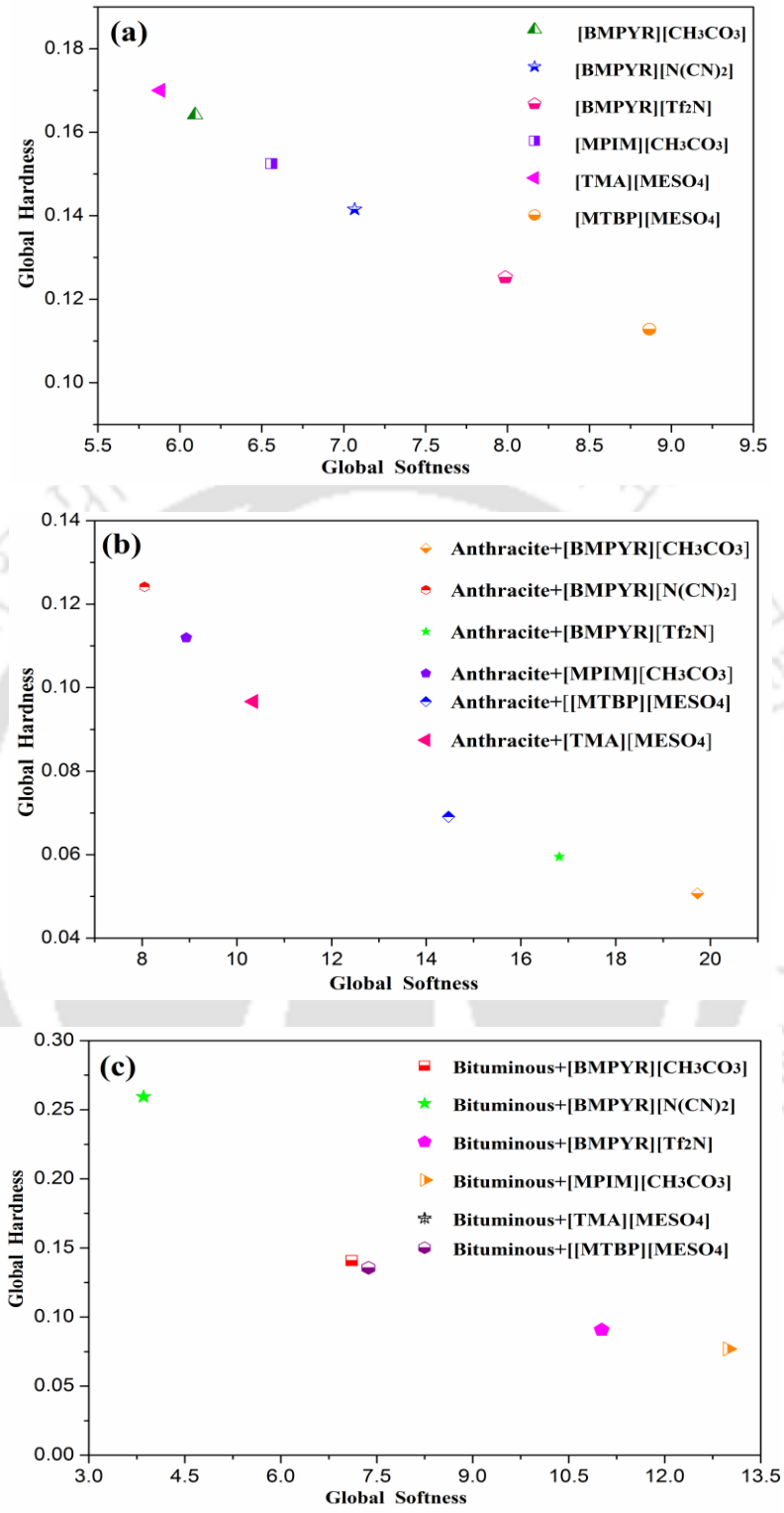

Fig. 3.7 Global hardness and Global softness of (a) ILs, (b) IL-Anthracite, and (c) IL-Bituminous Coals

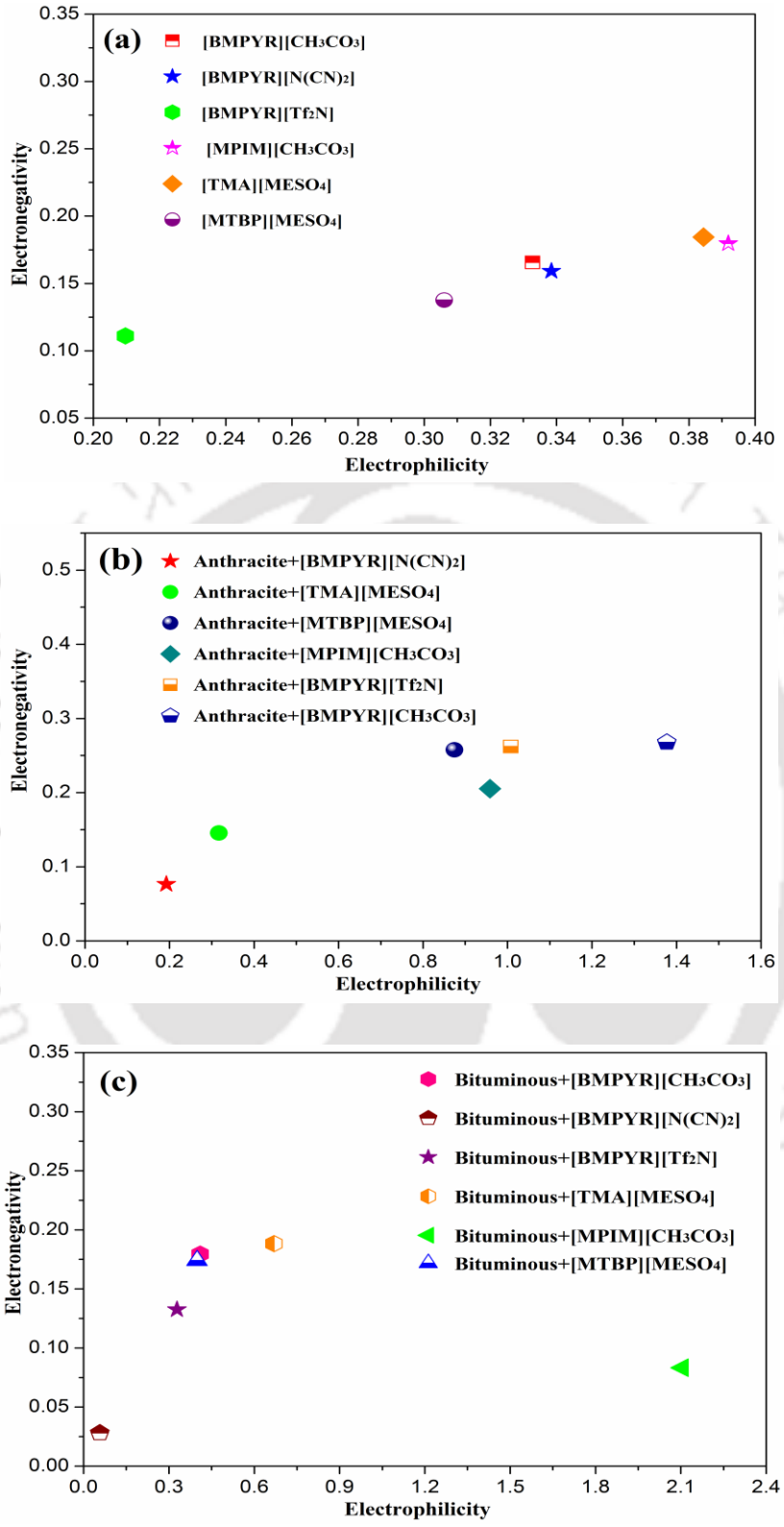

Fig. 3.8 Electrophilicity and electronegativity of (a) ILs, (b) IL-Anthracite, and (c) IL-Bituminous Coal

When comparing the electronegativity and electrophilicity index for the same clusters in Fig. 3.8, it can be seen that elctrophilicity increases with increasing electronegativity. This is due to the nucleophile which can donate the maximum number of electrons, while for the electrophile it is the opposite. IL's have both electrophilicity as well as electronegativity index. When IL's interact with coal molecules, electronegativity decreases as the inherent charge of anions contributes a strong electron affinity towards coal molecules. Thus a high electrophilicity index is favourable for strong interaction with ILs and compounds via CH-π bonding [42, 43]. In this case, similar result and trends were found for anthracite and bituminous coal. The decreasing order of electrophilicity for anthracite coal was: [BMPYR][CH_3CO_3] > [BMPYR][Tf_2N] > [MPIM][CH_3CO_3] > [TMA][$MeSO_4$] > [BMPYR][$N(CN)_2$] > [MTBP][$MeSO_4$] and for bituminous coal: [MPIM][$CH_3CO_{3]}$] > [TMA][$MeSO_4$] > [BMPYR][CH_3CO_3] > [MTBP][$MeSO_4$] > [BMPYR][Tf_2N] > [BMPYR][$N(CN)_2$]. So based on electrophilicity values, [BMPYR][CH_3CO_3] and [MPIM][$CH_3CO_{3]}$] are the best ILs for anthracite and bituminous coals respectively.

3.4.1.3 IDAC Prediction by COSMO-RS

Till now as discussed in previous sections namely 3.4.1.1 and 3.4.1.2, the HOMO-LUMO energies cannot be measured experimentally or described in the continuum. With the COSMO based modelling, the infinite dilution activity coefficient (IDAC) (γ_i^{∞}) provides us an important indicator which quantifies this very phenomenon as it is a measurable quantity and gives us the extent of the removal of a trace solute (coal) from solvent (IL). Lesser the IDAC values from unity, greater the tendency for the ILs to solubilize and remove coal species. We have successfully compared the IDAC's in the previous work [12] for ILs. However, we have again benchmarked the COSMO-RS model on structures which are

closely related to Coal such as Coumarin (Fig. 3.9). This follows a similar procedure as reported in the earlier work [34].

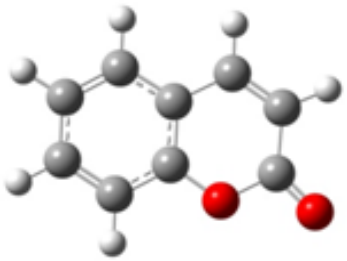

Fig. 3.9 Structures of benchmarking compounds (Coumarin) (red: Oxygen; grey: Carbon; white: Hydrogen atoms respectively) [44]

3.4.1.3.1 COSMO-RS benchmarking

For the validation of our COSMO-RS predicted results, we have conducted a benchmarking study on molecules which mimic a coal sample such as coumarin (Fig. 3.9) [44]. The experimental values of IDAC value are available in literature [44] with the following Ionic Liquids: 1-methylimidazolium trifluoromethanesulfonate [C_2MIM][TfO] and 1-butyl-3-methylimidazolium trifluoromethanesulfonate [C_4MIM][TfO]. The experimental and predicted IDAC values are listed in Tables 3.3. The predicted and experimental IDAC value is compared in order to validate our predictions. Therefore an absolute average deviation (AAD) of IDAC was calculated by following equation:

$$AAD = \frac{1}{N}\sum_{i=1}^{N}\left|x_i^{\exp} - x_i^{pred}\right| \qquad (3.18)$$

where $x_i^{\exp}$ and x_i^{pred} are experimental and predicted IDAC values and N is the number of data points. It can be seen that the experimental IDAC value matches reasonably well with the predicted IDAC value. An error (%) of 4.35 and 5.4% was obtained for IDAC

prediction of coumarin in [C_2MIM][TfO] and [C_4MIM][TfO] respectively. It may be due to the hydroxyl group which takes part in intramolecular hydrogen bonding. This interaction is not captured by the hydrogen bonding term as used in COSMO-RS.

Table 3.3 IDAC of Coumarin in ILs at Different Temperature

[C_2MIM][TfO]			[C_4MIM][TfO]		
Temperature (K)	COSMO-RS Value	Experimental Value [44]	Temperature (K)	COSMO-RS Value	Experimental Value [44]
262.23	0	0	290.10	0	0
275.51	2.12	2.69	278.38	1.44	1.43
287.63	1.93	1.82	292.36	1.37	1.21
300.83	1.68	1.64	304.12	1.29	1.16
310.00	1.50	1.44	315.13	1.20	1.08
318.83	1.32	1.27	322.71	1.13	1.04
326.92	1.17	1.19	331.17	1.06	1.04
333.56	1.06	1.12	337.47	1.01	1.01
338.77	1.01	1.05	341.68	1.00	1.00
341.68	1.00	1.00			

This with adequate benchmarking, we now move on with the actual coal molecules namely anthracite, bituminous and lignite.

3.4.1.4 COSMO-RS Predictions on Coal

As stated earlier, an important property namely energy of solvation (ΔG_i^{*sol}) at infinite dilution can be computed from COSMO-RS [12]. Gibb's free energy of solvation is defined as the energy change of a molecule from fixed position in ideal gas to a fixed position of solution and is related to the activity coefficient for phase equilibrium data as given below:

$$\Delta G_i^{*sol} = RT \ln \gamma_i^{\infty} \tag{3.19}$$

On the basis of IDAC value for anthracite coal, the ILs gave values of IDAC on decreasing values (higher solubility) as given below: [BMPYR][[CH_3CO_3] > [MTBP][$MESO_4$] > [BMPYR][Tf_2N] > [MPIM][CH_3CO_3] > [BMPYR][$N(CN)_2$] > [TMA][$MESO_4$] with corresponding Gibb's free energy of solvation (kJ/mol) at infinite dilution as (-7.6009 > -4.5776 > -2.5138 > -1.8799 > -0.6311 > 10.833). The corresponding trend for bituminous coal with the Gibb's free energy of solvation (kJ/mol) are as follows: [MPIM][CH_3CO_3] > [MTBP][$MESO_4$] > [BMPYR][Tf_2N] > [BMPYR][$N(CN)_2$] > [TMA][$MESO_4$] > [BMPYR][CH_3CO_3] (-8.517 > -6.437 > -4.892 > -4.5659 > -1.494 > 0.0028).

Now we have reached a position, where we can compare the predictions of HOMO-LUMO and COSMO-RS model qualitatively. Such a comparison is given in Table 3.4. This ranks the IL's based on the values of quantum chemical descriptors (LUMO, HOMO-LUMO gap, Electrophilicity Index, and Global Softness) and the COSMO based Gibb's free energy of solvation at infinite dilution. There are some common inferences that can be drawn from such an exercise. For e.g. a similar trend is observed for LUMO values and electrophilicity index (Table 3.4) for either coal. It should be noted that a lower negative value of LUMO indicates electrons can easily jump to the HOMO orbital. This also reflects in the HOMO-LUMO gap which gives a magnitude of this barrier. This same trend is again reflected in the global softness values, as higher values indicate easier polarizability. The comparisons of these trends (from their respective indicators) can be compared with those of Gibb's free energy of solvation values at infinite dilution (equation 3.19). This was required as the IDAC values are measurable using Gas-Liquid Chromatography. Although we did not perform actual experiments, but this methodology have been comprehensively validated in our earlier

work on ILs [42, 43]. A higher negative value is desirable as it implies an IDAC of less than unity. This provides higher solubility with coal particles. Thus the ILs, [BMPYR][CH_3CO_3] and [MPIM][CH_3CO_3] are the most preferable for anthracite and bituminous coal irrespective of the quantum descriptor (HOMO-LUMO or ΔG_i^{*sol}). Considering the average ranking for all the descriptors in the subset of ILs, the preference for anthracite coal follows as: [BMPYR][CH_3CO_3] > [MTBP][$MeSO_4$] > [BMPYR][Tf_2N] > [MPIM][CH_3CO_3] > [BMPYR][$N(CN)_2$] > [TMA][$MeSO_4$]. The subsequent trend for bituminous coal is: [MPIM][CH_3CO_3] > [MTBP][$MeSO_4$] > [BMPYR][Tf_2N] > [BMPYR][$N(CN)_2$] > [TMA][$MeSO_4$] > [BMPYR][CH_3CO_3]. In summary, the ILs [BMPYR][CH_3CO_3] and [MPIM][CH_3CO_3] are recommended for the dissolution of anthracite and bituminous respectively.

3.4.1.5 Effect of Sigma Profile on IL's and Coal

The preceding section gives us an idea about the scale and rank of interaction using both HOMO-LUMO and COSMO-RS based predictions. We now move on to further study this interaction through another COSMO based descriptor known as Sigma Profile analysis. Sigma profile is a descriptor which tells us about the extent of hydrogen bond donors and acceptors within a molecule. Screening charge densities (σ) possess both positive (right) and negative (left) values. If the profile is lying on the left side of a cut-off value of -0.0082 e/Å^2, then it has a high ability to donate hydrogen bond (or accept electron). On the contrary, the right side of +0.0082 e/Å^2 side states a high accepting ability of hydrogen bond (or donating electron). Anions lie on the positive side because of their inherent negative partial charges and cations lie on the negative side due to the positive partial charges inside the aromatic ring.

Table 3.4 Comparative study of IL-Anthracite and IL-Bituminous based on scalar quantities

Constraints	Objectives	Rank (Selection of ILs)					
		1 (most preferable)	2	3	4	5	6 (least preferable)
ILs-Anthracite Coal							
Based on HOMO/LUMO energy values	More LUMO (lower negative)	[BMPYR][CH_3CO_3]	[BMPYR][$N(CN)_2$]	[BMPYR][Tf_2N]	[TMA][$MeSO_4$]	[MTBP][$MeSO_4$]	[MPIM][CH_3CO_3]
Based on HOMO–LUMO energy gap	Small Gap	[BMPYR][CH_3CO_3]	[BMPYR][Tf_2N]	[MPIM][CH_3CO_3]	[MTBP][$MeSO_4$]	[TMA][$MeSO_4$]	[BMPYR][$N(CN)_2$]
Based on Global softness	Higher Global Softness	[BMPYR][CH_3CO_3]	[BMPYR][Tf_2N]	[MTBP][$MeSO_4$]	[TMA][$MeSO_4$]	[MPIM][CH_3CO_3]	[BMPYR][$N(CN)_2$]
Based on Electrophilicity	Higher Electrophilicity	[BMPYR][CH_3CO_3]	[BMPYR][Tf_2N]	[MPIM][CH_3CO_3]	[TMA][$MeSO_4$]	[BMPYR] [$N(CN)_2$]	[MTBP][$MeSO_4$]
Overall Rank		[BMPYR][CH_3CO_3]	[BMPYR][Tf_2N]	[MPIM][CH_3CO_3]	[TMA][$MeSO_4$]	[MTBP][$MeSO_4$]	[BMPYR][$N(CN)_2$]
(ΔG_i^{*sol}) COSMO-RS Predictions in kJ/mol (Eq. 3.19)		-7.6009	-2.5133	-1.8799	10.833	-4.5776	-0.6311
Rank based on COSMO-RS		[BMPYR][CH_3CO_3]	[MTBP][$MeSO_4$]	[BMPYR][Tf_2N]	[MPIM][CH_3CO_3]	[BMPYR][$N(CN)_2$]	[TMA][$MeSO_4$]
ILs-Bituminous Coal							
Based on HOMO/LUMO energy values	More LUMO (lower negative)	[MPIM][CH_3CO_3]	[MTBP][$MeSO_4$]	[BMPYR][CH_3CO_3]	[BMPYR][Tf_2N]	[BMPYR][$N(CN)_2$]	[TMA][$MeSO_4$]
Based on HOMO–LUMO energy gap	Small Gap	[MPIM][CH_3CO_3]	[TMA][$MeSO_4$]	[BMPYR][$N(CN)_2$]	[MTBP][$MeSO_4$]	[BMPYR][Tf_2N]	[BMPYR][CH_3CO_3]
Based on Global softness	Higher Global Softness	[MPIM][CH_3CO_3]	[TMA][$MeSO_4$]	[BMPYR][Tf_2N]	[MTBP][$MeSO_4$]	[BMPYR][CH_3CO_3]	[BMPYR][$N(CN)_2$]
Based on Electrophilicity	Higher Electrophilicity	[MPIM][CH_3CO_3]	[TMA][$MeSO_4$]	[BMPYR][CH_3CO_3]	[MTBP][$MeSO_4$]	[BMPYR][Tf_2N]	[BMPYR][$N(CN)_2$]
Overall Rank		[MPIM][CH_3CO_3]	[TMA][$MeSO_4$]	[BMPYR][CH_3CO_3]	[MTBP][$MeSO_4$]	[BMPYR][Tf_2N]	[BMPYR][$N(CN)_2$]
(ΔG_i^{*sol}) COSMO-RS Predictions in kJ/mol (Eq. 3.19)		-8.517	-1.499	0.0028	-6.437	-4.892	-4.5659
Rank based on COSMO-RS		[MPIM][CH_3CO_3]	[MTBP][$MeSO_4$]	[BMPYR][Tf_2N]	[BMPYR][$N(CN)_2$]	[TMA][$MeSO_4$]	[BMPYR][CH_3CO_3]

This section discusses the sigma profile (Fig. 3.10) analysis of ILs and coal particle taken together on a same dimensionless reference scale. The two proposed ILs namely [BMPYR][CH_3CO_3] and [MPIM][CH_3CO_3] as obtained from the earlier section are used a benchmark for sigma profile analysis. From Fig. 3.10, it is clear that the bituminous and anthracite coal have both positive and negative charges. For ILs the profile lying to the negative side is due to the large cation; while the positive side is due to the anion. From both the plots, it is evident that the sigma profile of ILs and coal are complimentary in nature [42]. This indicates high solubility which is true as per our results as discussed in section 3.4.1.1 to 3.4.1.3.

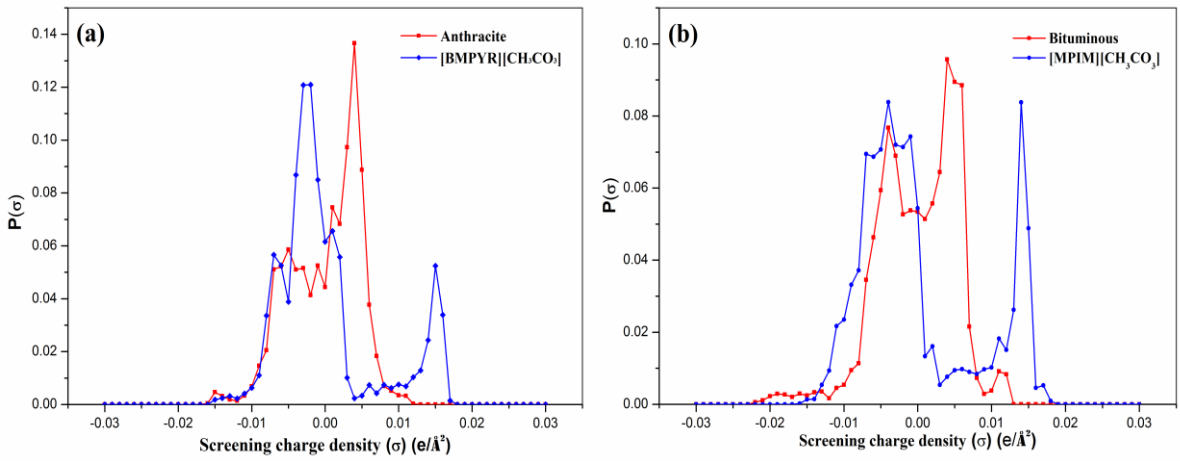

Fig. 3.10 Sigma profile of (a) Anthracite coal in [BMPYR][CH_3CO_3] and (b) Bituminous coal in [MPIM][CH_3CO_3]

We now move ahead and compute the phase equilibria diagrams which chemical engineers usually encounter and use it for designing the process operation in industries. This can be ascertained by the Solid-Liquid Equilibria (SLE) diagrams of coal (solid) in IL (liquid) at different temperatures.

3.4.2 COSMO-RS based Screening of Ionic Liquids for Dissolution and Dispersion of Coal

3.4.2.1 Solid-Liquid-Equilibrium Prediction using COSMO-RS

The solid state of a compound is related to the liquid state by its heat of crystallization (or Gibb's free energy of fusion, ΔG) [14]. Here, in this work, Gibbs free energy of solvation (ΔG_i^{*sol}) is used for SLE prediction. Gibb's free energy of solvation is defined as the change in Gibbs free energy associated with moving a molecule '*i*' from a fixed position in an ideal gas to a fixed position in a solution [45, 46]. The COSMO solvation model gives the electrostatic contribution to the solvation free energy. The activity coefficient and Henry's law constant using a group contribution solvation model were earlier calculated by Lin and Sandler [16]. In the case of solid compounds, a negative value of ΔG_i^{*sol} implies a highly soluble, favourable, and spontaneous dissolution process. A positive ΔG_i^{*sol} indicates that energy is necessary to break the intermolecular bond within the crystal lattice of coal molecule [47]. The Gibb's free energy of solvation is represented by equation (3.19) in section 3.4.1. The solid-liquid equilibrium [48-50] can be written as,

$$\ln(X_{solute}^{L}\gamma_{solute}^{L}) = \frac{\Delta H_{fus}}{R}\left(\frac{1}{T_m}-\frac{1}{T}\right)+\frac{\Delta C_p}{R}\left(\frac{T_m-T}{T}\right)+\frac{\Delta C_p}{R}\ln\left(\frac{T_m}{T}\right) \qquad (3.20)$$

where X_{solute}^{L} is the mole fraction of solute in the liquid phase, γ_{solute}^{L} is the activity coefficient of solute in liquid phase, ΔH_{fus} is enthalpy of fusion, T_m is melting point temperature and ΔC_p is difference between the specific heat of solute in the solid and liquid phase [34]. The enthalpy of fusion ΔH_{fus} is assumed to be temperature independent, whereas the activity

coefficient γ^{L}_{solute} is temperature and concentration dependent. Here, it was assumed that ΔC_p is constant over the temperature T and T_m. Further, the right hand side of the equation (3.20) i.e. second and third terms are assumed to be nearly very close, so that the two terms cancels out. Thus, the simplified form of the equation (3.20) can be written as,

$$\ln(X^{L}_{solute}\gamma^{L}_{solute}) = \frac{\Delta H_{fus}}{R}\left(\frac{1}{T_m} - \frac{1}{T}\right) \tag{3.21}$$

With the help of the activity coefficients predicted from COSMO-RS, (equation (3.21)) one can predict the SLE behaviour [49, 51]. For this, the mole fraction of solute in the ideal case (i.e. activity coefficient of the solute in the liquid phase is unity i.e., γ^{L}_{solute} =1) is computed which is given below in equation (3.22).

$$\ln(X^{L}_{solute}) = \frac{\Delta H_{fus}}{R}\left(\frac{1}{T_m} - \frac{1}{T}\right) \tag{3.22}$$

In this work, SLE has been predicted for the binary system using 18 ILs listed in Table 3.1. To predict the SLE of a new compound the estimation of the melting point temperature (T_m) and latent heat of fusion (H_{fus}) is necessary. Due to the complex structure of a given solute (brown coal), multiple melting point temperatures or latent heats of fusion may exist with similar values. There are several group and non-group-contribution methods to calculate the melting point temperature (T_m) and latent heat of fusion (H_{fus}). Here we have used the *Joback method* [52, 53] for estimating the melting point temperature (T_m) and latent heat of fusion (H_{fus}). The Joback method is a group contribution method which includes non-ring group, ring group, halogen group, oxygen group, nitrogen group, and

sulphur group as listed in Table 3.5. Equation (3.23) [52, 53] defines the melting point temperature (T_m) and equation (3.24) [52, 53] defines the heat of fusion (H_{fus}) as given below,

$$T_m = 122.5 + \sum T_{m,i} \tag{3.23}$$

$$\Delta H_{fus} = -0.88 + \sum \Delta H_{fus,i} \tag{3.24}$$

Table 3.5 Joback Method for Computing Enthalpy of Fusion (H_{fus}) and Melting point Temperature (T_m)

Group	Non-ring groups		Ring groups				
	$-CH_3$	$-CH_2-$	$-CH_2-$	>CH-	=CH-	=C<	
T_m	-5.1	11.27	7.75	19.88	8.13	37.02	
H_{fus}	0.908	2.59	0.49	3.243	1.101	2.394	
Group	Oxygen groups					Nitrogen groups	Sulphur groups
	-OH (alcohol)	-OH (phenol)	-O- (NR)	>C=O (NR)	-COOH	=N- (R)	-S- (R)
T_m	44.45	82.83	22.23	61.2	155.5	68.4	79.93
H_{fus}	2.406	4.49	1.188	4.189	11.051	3.649	1.557

From this work, T_m and ΔH_{fus} were found to 1514.07 K and 107 kJ/mole respectively. The values closely matched with the experimental data reported by Ikeda et al [54]. Once the ideal solubility (i.e. mole fraction) is known, the activity coefficient is predicted by the COSMO-RS theory [33, 40, 41]. The activity coefficient value is again substituted in equation (3.21) to get the actual mole fraction in solution, which is the predicted solubility. The predicted solubility is then compared with the experimental

solubility in order to compare our predictions. Thereafter the absolute average deviation (*AAD*) in mole fraction in liquid phase was calculated by equation (3.18) in section 3.4.1.

3.4.2.2 Validation of SLE using Pseudo Coal and Ionic Liquid

Before attempting to predict the SLE of coal containing systems, we shall try to benchmark the SLE prediction on known systems resembling the coal structure. Some part of our validation is already available with solutes such as benzothiophene (solid) in 1-ethyl-3-methylimidazolium ethyl sulphate ([EMIM][$EtSO_4$]) and 1-ethyl-3-methylimidazolium acetate ([EMIM][CH_3COO]) [41]. Further, the SLE for the binary systems of (IL (solid) + thiophene) consisting of the ILs: *n*-butyl-4-methylpyridinium tosylate [BM_4PY][TOS], *n*-butyl-3-methylpyridinium tosylate [BM_3PY][TOS], *n*-hexyl-3-methylpyridinium tosylate [HM_3PY][TOS], and 1,4-dimethylpyridinium tosylate [$M_{1,4}PY$][TOS] were also predicted successfully using COSMO-RS [50]. Thus, in our earlier work, both cases i.e. IL as a solid and liquid has been used to predict the SLE [41, 49].

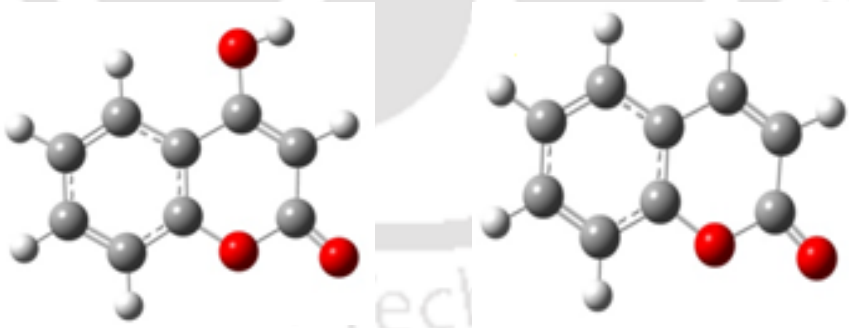

(a) 4-Hydroxycoumarin **(b)** Coumarin

Fig. 3.11 Structures of benchmarking compounds (red: Oxygen atom; grey: Carbon; white: Hydrogen) [44]

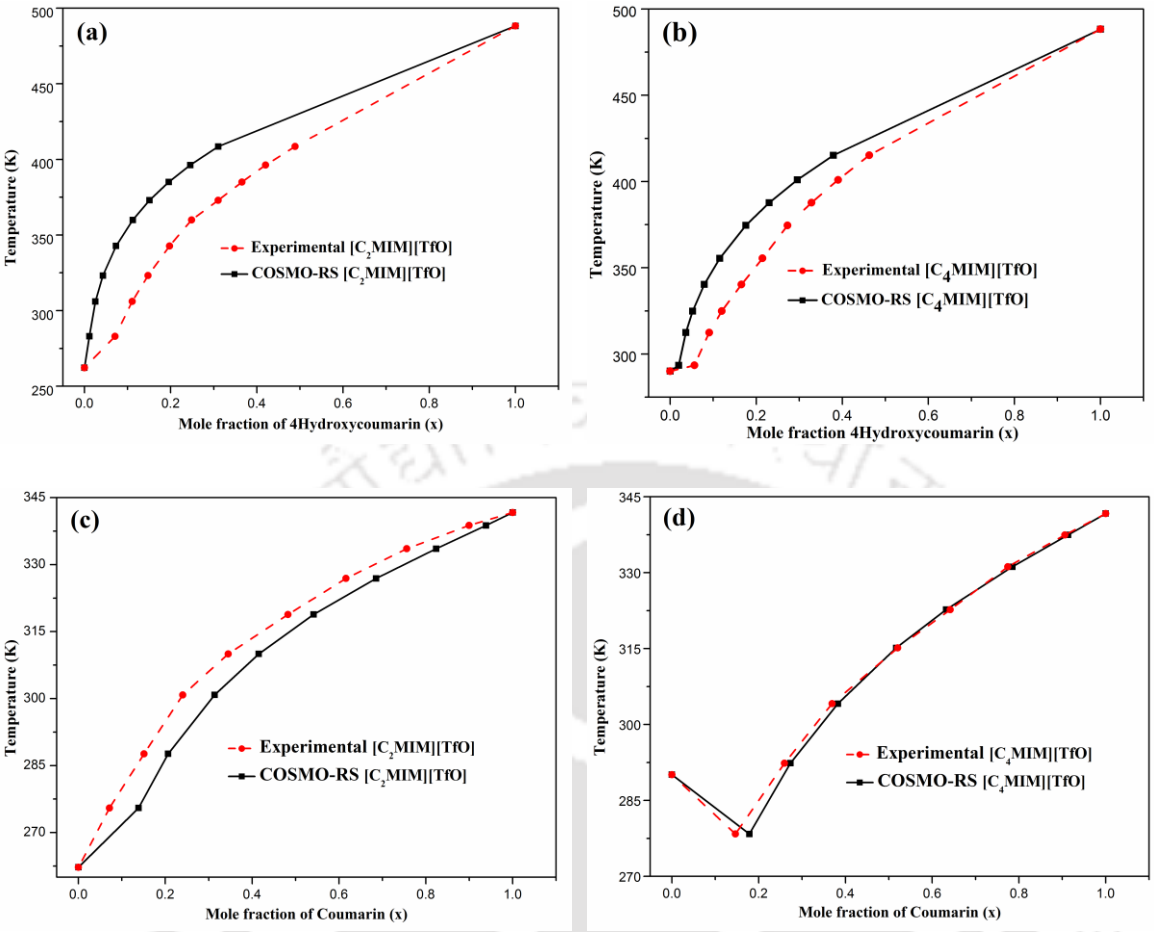

Fig. 3.12 Experimental [44] and predicted solubility of [C_2MIM][TfO] and [C_4MIM][TfO] in (a-b) 4-Hydroxycoumarin and (c-d) coumarin

However, to ensure that the prediction using COSMO-RS model is consistent with our study, we have conducted benchmarking studies on molecules which mimic the brown coal sample such as coumarin and 4-hydroxycoumarin (Fig. 3.11). The SLE experimental data for the compounds in the following Ionic Liquids: 1-methylimidazolium trifluoromethanesulfonate [C_2MIM][TfO] and 1-butyl-3-methylimidazolium trifluoromethanesulfonate [C_4MIM][TfO] are available in literature (Fig. 3.12) [44]. Fig. 3.12d shows a eutectic point at a constant temperature. The eutectic composition can be calculated from the intersection of the two solubility curves. This represents the maximum value of molar enthalpy at eutectic point. The eutectic point present in curve shows that the

components are immiscible with the solid phase. However, it can be seen that the experimental and predicted SLE matches reasonably well considering the method to be a-priori. A Root Mean Square Error (%) of 5.6% and 1.3% was obtained for SLE prediction of coumarin in [C_2MIM][TfO] and [C_4MIM][TfO] respectively. The corresponding values for 4-hydroxycoumarin were a bit higher i.e. 12.5% and 14% respectively. It may be due to the hydroxyl group tends to be as controlling factor in intramolecular hydrogen bonding. This interaction is not captured by the hydrogen bonding term as used in COSMO-RS. It should be noted that we have used the methodology and COSMO-RS parameters as used in our earlier work [34].

3.4.2.3 Prediction of Gibb's free energy of Solvation at Infinite Dilution

After the successful benchmarking of the COSMO-RS model, Gibb's free energy of solvation was predicted at infinite dilution for all the 18 ILs having various combinations of cations and anions as reported in Table 3.1. ΔG_i^{*sol} plays an important role in selecting the best combination for the dissolution of coal. This has been calculated using equation (3.19) as discussed earlier. Fig. 3.13 shows the variation of ΔG_i^{*sol} with temperature for the ILs listed in Table 3.1. Some of the results have already been discussed in Table 3.4 while comparing HOMO-LUMO and COSMO-RS predictions.

The comparative values of ΔG_i^{*sol} gives an idea about the tendency of the IL in dissolving brown coal particle. A higher negative value is preferable as it indicates that the process is favourable and spontaneous. IL's such as [BDMIM][PF_6], [BYMIM][BF_4], [BDMIM][BF_4], and [BMPY][BF_4] possess a positive value of Gibb's free energy of solvation implying that the process becomes unfavourable and immiscible in nature. Thus,

more amount of external energy is required to make the process feasible. ILs such as [MPPY][Tf_2N], [BMPYR][Tf_2N], [DMXMIM][Tf_2N], [EMIM][TfO], [EMIM][$N(CN)_2$], [BMPYR][$N(CN)_2$], and [EMIM][$C_2H_4NO_2$] high value of negative Gibb's free energy are supposed to be highly miscible in brown coal.

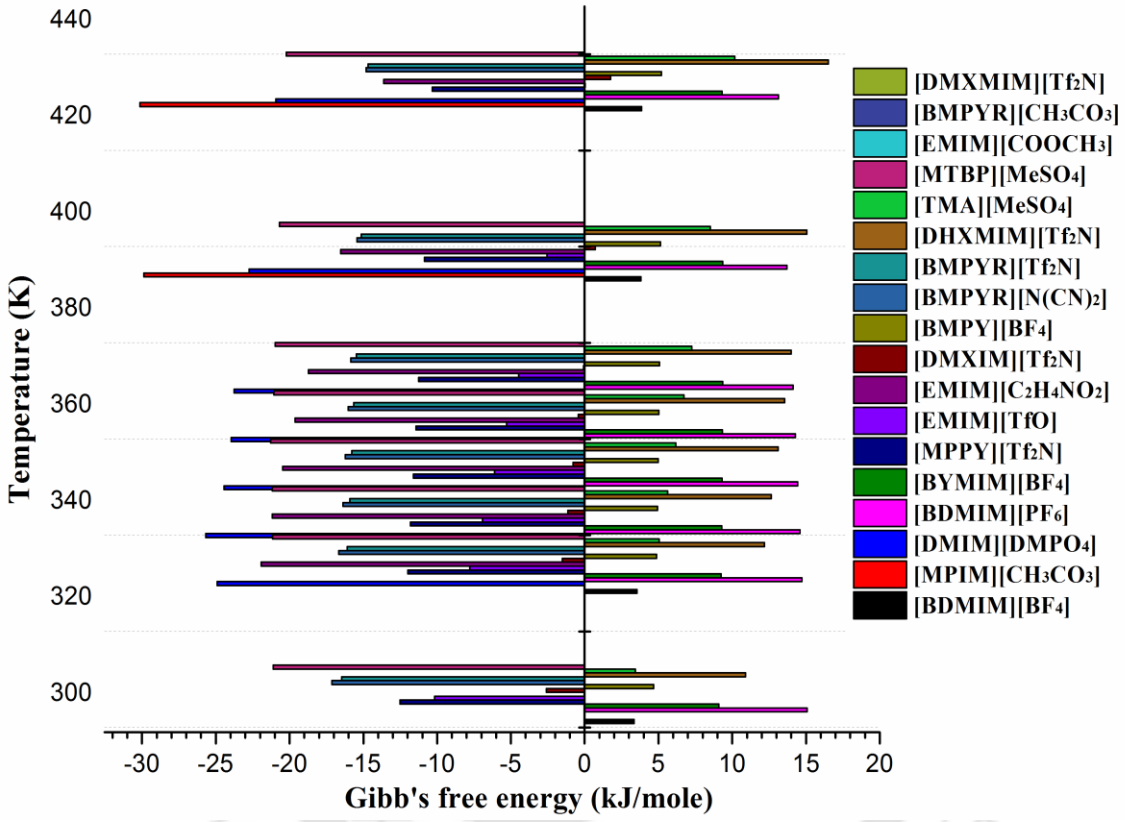

Fig. 3.13 Gibb's free energy (ΔG_i^{∞}) of solvation with temperature

In the next section, the effect of SLE of the IL and brown coal was reported and a relation between Gibb's free energy of solvation at infinite dilution and SLE was obtained. A word of caution should be taken for fluorine based anions, since at high temperature; these tend to form HF which causes corrosion of the reactor vessel. Hence they should be avoided. On the contrary, even though they are expensive, attention needs to be paid to sulfate, acetate, phosphate, and nitrogen containing ILs.

3.4.2.4 SLE of Ionic Liquid and Coal system

Fig. 3.14 to Fig. 3.17 displays the mole fraction with temperature of brown coal in ionic liquids (ILs). From the figures it can be seen that the solubility of brown coal in ILs increases with increase in temperature. Here reduced temperature (T_r) is used in the figures to simplify the values of y-axis within a range of 0 to 1. It is expressed as the ratio of actual temperature (T) to melting point temperatures (T_m) of a sample. The increasing order of solubility of brown coal in IL's for different types of cations are as follows:

Imidazolium based: [EMIM][$COOCH_3$] > [EMIM][$C_2H_4NO_2$] > [DMXIM][Tf_2N] > [DMPIM][Tf_2N] > [EMIM][TfO] > [DMXMIM][Tf_2N] > [BDMIM][BF_4] > [BYMIM][BF_4] > [BDMIM][PF_6] > [MPIM][CH_3CO_3] > [DHXMIM][Tf_2N]

Pyrrolidinium based: [BMPYR][CH_3CO_3] > [BMPYR][Tf_2N] > [BMPYR][$N(CN)_2$]

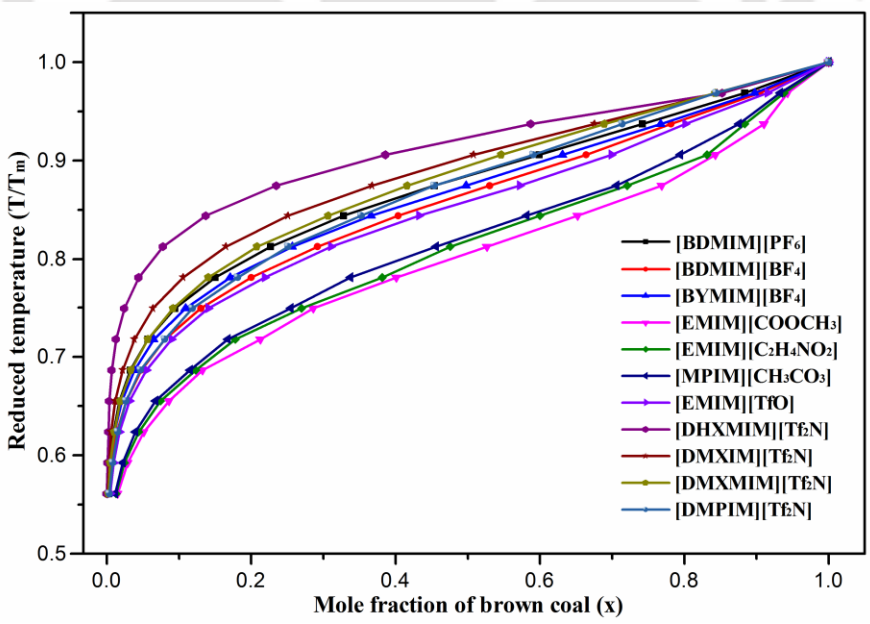

Fig. 3.14 Solubility of brown coal in imidazolium based ILs (T_m =1514.07 K)

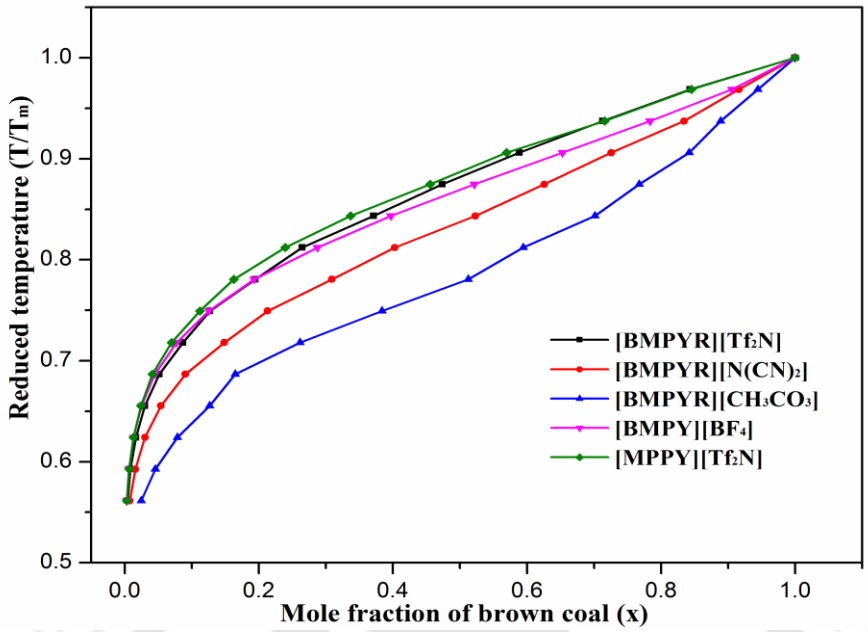

Fig. 3.15 Solubility of brown coal in pyridinium and pyrrolidinium based ILs (T_m =1514.07 K)

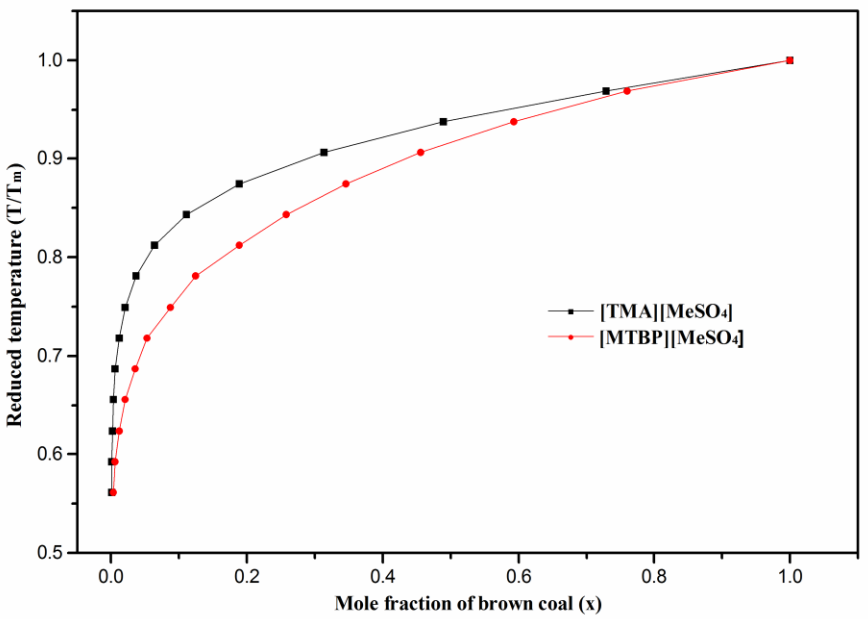

Fig. 3.16 Solubility of brown coal in ammonium and phosphonium based ILs (T_m =1514.07 K)

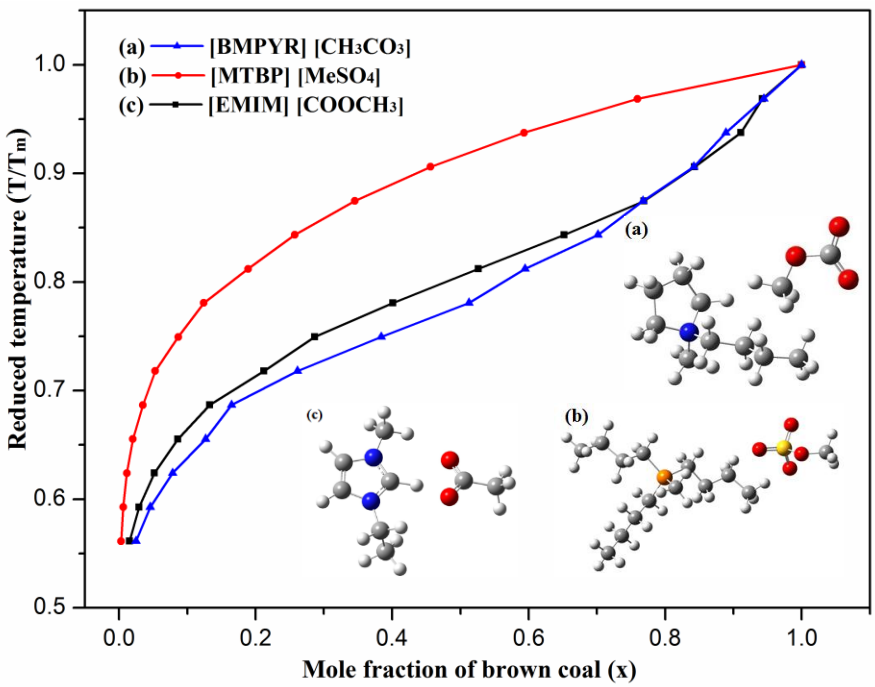

Fig. 3.17 Comparison of solubility of brown coal in imidazolium, phosphonium and pyrrolidinium based ILs (T_m =1514.07 K)

Within the IL's the solubility of brown coal in IL was found to be in the order of [BMPYR][CH_3CO_3] > [EMIM][$COOCH_3$] > [MTBP][$MeSO_4$]. Therefore, the pyrrolidinium based cations possess higher solubility when compared to other cations such as imidazolium and phosphonium. Further for a particular temperature, it is seen that the predicted COSMO-RS solubility decreases with increase in the length of the carbon chain. As a result, 1-butyl-1-methylpyrrolidinium methyl carbonate [BMPYR][CH_3CO_3] was found to possess the highest miscibility with brown coal.

3.4.2.5 Sigma Profile of IL and coal

Now let us observe the sigma profile of [BMPYR][CH_3CO_3] and brown coal together. Fig. 3.18 displays the sigma profile of brown coal and [BMPYR][CH_3CO_3]. As before, the two vertical dashed lines indicate the cut-off region for hydrogen bond donor

($\sigma_{HB} < -0.0082$ e/Å^2) and hydrogen bond acceptor ($\sigma_{HB} > +0.0082$ e/Å^2) [34]. This means that the profile lying on the left side of σ_{HB} will have the ability to participate in a high or fraction of hydrogen bonding and profile lying in the right side of σ_{HB} will have the ability to accept hydrogen bonds. [CH_3CO_3] is positioned on the positive side of the profile, which was due to the negative charge on its core. The negative screening charge of [BMPYR] was due to the positive charge residing inside the aromatic ring of the pyrrolidinium cation. From Fig. 3.18 it is clear that the brown coal has both positive and negative charges, therefore, the peaks of the brown coal lie in between -0.0082 e/Å^2 to +0.0082 e/Å^2 i.e.; the neutral region, hence the brown coal from its pseudo structure is non-polar in nature. Continuing with a similar trend as observed in Fig. 3.10, Fig. 3.18 also confirms that the sigma profile of [BMPYR][CH_3CO_3] and brown-coal are complementary in nature which indicates that the brown coal and [BMPYR][CH_3CO_3] are highly miscible.

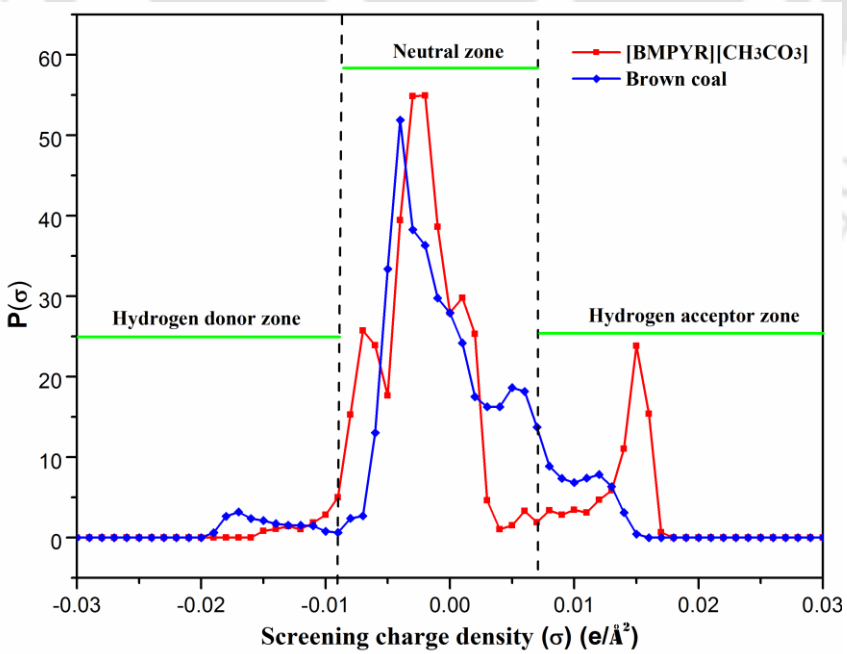

Fig. 3.18 Sigma profile of Brown coal in [BMPYR][CH_3CO_3]

References

[1] J. G. Speight, Handbook of coal analysis, John Wiley & Sons2015.

[2] J. P. Mathews, A. L. Chaffee, The molecular representations of coal–A review, Fuel, 96 (2012) 1-14.

[3] M. W. Haenel, Recent progress in coal structure research, Fuel, 71 (1992) 1211-1223.

[4] M. W. Haenel, J. Narangerel, U. B. Richter, A. Rufińska, The first liquefaction of high-rank bituminous coals by preceding hydrogenation with homogeneous borane or iodine catalysts, Angewandte Chemie International Edition, 45 (2006) 1061-1066.

[5] I. Mochida, K. Takeshita, Coal Liquefaction Fundamentals, by D. Duayne Whitehurst, ACS Symposium Series, 1980, pp. 259.

[6] M. D. Abràmoff, P. J. Magalhães, S. J. Ram, Image processing with ImageJ, Biophotonics International, 11 (2004) 36-42.

[7] F. P. Miknis, D. A. Netzel, T. F. Turner, J. C. Wallace, C. H. Butcher, Effect of different drying methods on coal structure and reactivity toward liquefaction, Energy and Fuels, 10 (1996) 631-640.

[8] M. Fujiwara, H. Ohsuga, T. Takanohashi, M. Iino, Swelling of the extracts and residues from carbon disulfide-N-methyl-2-pyrrolidinone mixed solvent extraction, Energy and Fuels, 6 (1992) 859-862.

[9] T. Ishizuka, T. Takanohashi, O. Ito, Effects of additives and oxygen on extraction yield with CS_2-NMP mixed solvent for argonne premium coal samples, Fuel, 72 (1993) 579-580.

[10] P. A. Hunt, B. Kirchner, T. Welton, Characterising the electronic structure of ionic liquids: An examination of the 1-butyl-3-methylimidazolium chloride ion pair, Chemistry–A European Journal, 12 (2006) 6762-6775.

[11] P. Hunt, The simulation of imidazolium-based ionic liquids†, Molecular Simulation, 32 (2006) 1-10.

[12] T. Banerjee, A. Khanna, Infinite dilution activity coefficients for trihexyltetradecyl phosphonium ionic liquids: measurements and COSMO-RS prediction, Journal of Chemical and Engineering Data, 51 (2006) 2170-2177.

[13] A. Klamt, COnductor-like Screening MOdel for Real Solvents: A new approach to the quantitative calculation of solvation phenomena, The Journal of Physical Chemistry, 99 (1995) 2224-2235.

[14] F. Eckert, A. Klamt, Fast solvent screening via quantum chemistry: COSMO-RS approach, AIChE Journal, 48 (2002) 369-385.

[15] A. Klamt, F. Eckert, COSMO-RS: a novel and efficient method for the a priori prediction of thermophysical data of liquids, Fluid Phase Equilibria, 172 (2000) 43-72.

[16] S.-T. Lin, S. I. Sandler, A priori phase equilibrium prediction from a segment contribution solvation model, Industrial and Engineering Chemistry Research, 41 (2002) 899-913.

[17] P. K. Chattaraj, H. Lee, R. G. Parr, HSAB principle, Journal of the American Chemical Society, 113 (1991) 1855-1856.

[18] P. K. Chattaraj, U. Sarkar, D. R. Roy, Electrophilicity index, Chemical reviews, 106 (2006) 2065-2091.

[19] M. Karelson, V. S. Lobanov, A. R. Katritzky, Quantum-chemical descriptors in QSAR/QSPR studies, Chemical Reviews, 96 (1996) 1027-1044.

[20] P. Thanikaivelan, V. Subramanian, J. R. Rao, B. U. Nair, Application of quantum chemical descriptor in quantitative structure activity and structure property relationship, Chemical Physics Letters, 323 (2000) 59-70.

[21] L. Pauling, The nature of the chemical bond and the structure of molecules and crystals: an introduction to modern structural chemistry, Cornell University Press1960.

[22] R. G. Pearson, W. E. Palke, Support for a principle of maximum hardness, The Journal of Physical Chemistry, 96 (1992) 3283-3285.

[23] R. G. Parr, L. v. Szentpaly, S. Liu, Electrophilicity index, Journal of the American Chemical Society, 121 (1999) 1922-1924.

[24] W. Kohn, L. J. Sham, Self-consistent equations including exchange and correlation effects, Physical Review, 140 (1965) A1133.

[25] H. Kumagai, J. Hayashi, T. Chiba, K. Nakamura, Change in physical and chemical characteristics of brown coal along with a progress of moisture release, Abstracts of Papers of the American Chemical Society, American Chemical Society 1155 16th st, NW, Washington, DC 20036 USA, 1999, pp. U611-U611.

[26] M. R. Narkiewicz, J. P. Mathews, Improved low-volatile bituminous coal representation: incorporating the molecular-weight distribution, Energy and Fuels, 22 (2008) 3104-3111.

[27] I. Wender, Catalytic synthesis of chemicals from coal, Catalysis Reviews—Science and Engineering, 14 (1976) 97-129.

[28] G. Schaftenaar, J. H. Noordik, Molden: A pre-and post-processing program for molecular and electronic structures, Journal of Computer-Aided Molecular Design, 14 (2000) 123-134.

[29] Z. Meng, A. Dölle, W. R. Carper, Gas phase model of an ionic liquid: semi-empirical and ab initio bonding and molecular structure, Journal of Molecular Structure: THEOCHEM, 585 (2002) 119-128.

[30] A. D. Becke, Density functional calculations of molecular bond energies, The Journal of Chemical Physics, 84 (1986) 4524-4529.

[31] C. M. Breneman, K. B. Wiberg, Determining atom-centered monopoles from molecular electrostatic potentials. The need for high sampling density in formamide conformational analysis, Journal of Computational Chemistry, 11 (1990) 361-373.

[32] A. Klamt, G. Schüürmann, COSMO: a new approach to dielectric screening in solvents with explicit expressions for the screening energy and its gradient, Journal of the Chemical Society, Perkin Transactions 2, (1993) 799-805.

[33] T. Banerjee, M. K. Singh, A. Khanna, Prediction of binary VLE for imidazolium based ionic liquid systems using COSMO-RS, Industrial and Engineering Chemistry Research, 45 (2006) 3207-3219.

[34] T. Banerjee, K. K. Verma, A. Khanna, Liquid–liquid equilibrium for ionic liquid systems using COSMO-RS: Effect of cation and anion dissociation, AIChE journal, 54 (2008) 1874-1885.

[35] O. Treutler, R. Ahlrichs, Efficient molecular numerical integration schemes, The Journal of Chemical Physics, 102 (1995) 346-354.

[36] R. I. Burnett, Predicting liquid-phase thermodynamic properties using COSMO-SAC, 2012.

[37] J. P. Perdew, Density-functional approximation for the correlation energy of the inhomogeneous electron gas, Physical Review B, 33 (1986) 8822.

[38] A. Schäfer, C. Huber, R. Ahlrichs, Fully optimized contracted Gaussian basis sets of triple zeta valence quality for atoms Li to Kr, The Journal of Chemical Physics, 100 (1994) 5829-5835.

[39] C. Sosa, J. Andzelm, B. C. Elkin, E. Wimmer, K. D. Dobbs, D. A. Dixon, A local density functional study of the structure and vibrational frequencies of molecular transition-metal compounds, The Journal of Physical Chemistry, 96 (1992) 6630-6636.

[40] T. Banerjee, R. K. Sahoo, S. S. Rath, R. Kumar, A. Khanna, Multicomponent liquid-liquid equilibria prediction for aromatic extraction systems using COSMO-RS, Industrial and Engineering Chemistry Research, 46 (2007) 1292-1304.

[41] N. R. Varma, A. Ramalingam, T. Banerjee, Experiments, correlations and COSMO-RS predictions for the extraction of benzothiophene from n-hexane using imidazolium-based ionic liquids, Chemical Engineering Journal, 166 (2011) 30-39.

[42] S. R. Pilli, T. Banerjee, K. Mohanty, HOMO–LUMO energy interactions between endocrine disrupting chemicals and ionic liquids using the density functional theory: Evaluation and comparison, Journal of Molecular Liquids, 207 (2015) 112-124.

[43] T. Banerjee, A. Ramalingam, Desulphurization and denitrification of diesel oil using ionic liquids: Experiments and quantum chemical predictions, Elsevier2015.

[44] A. D. dos Santos, A. R. Morais, C. Melo, R. Bogel-Łukasik, E. Bogel-Łukasik, Solubility of pharmaceutical compounds in ionic liquids, Fluid Phase Equilibria, 356 (2013) 18-29.

[45] V. S. Bryantsev, M. S. Diallo, W. A. Goddard Iii, Calculation of solvation free energies of charged solutes using mixed cluster/continuum models, The Journal of Physical Chemistry B, 112 (2008) 9709-9719.

[46] E. Mullins, Y. Liu, A. Ghaderi, S. D. Fast, Sigma profile database for predicting solid solubility in pure and mixed solvent mixtures for organic pharmacological compounds with COSMO-based thermodynamic methods, Industrial and Engineering Chemistry Research, 47 (2008) 1707-1725.

[47] Y. A. Kholod, E. N. Muratov, L. G. Gorb, F. C. Hill, A. G. Artemenko, V. E. Kuz'min, M. Qasim, J. Leszczynski, Application of quantum chemical approximations to environmental problems: prediction of water solubility for nitro compounds, Environmental Science and Technology, 43 (2009) 9208-9215.

[48] J. M. Prausnitz, R. N. Lichtenthaler, E. G. de Azevedo, Molecular thermodynamics of fluid-phase equilibria, Pearson Education1998.

[49] N. R. Verma, G. Gopal, R. Anantharaj, T. Banerjee, (Solid+ liquid) equilibria predictions of ionic liquid containing systems using COSMO-RS, The Journal of Chemical Thermodynamics, 48 (2012) 246-253.

[50] B. Bouillot, S. b. Teychené, B. a. Biscans, An evaluation of COSMO-SAC model and its evolutions for the prediction of drug-like molecule solubility: part 1, Industrial and Engineering Chemistry Research, 52 (2013) 9276-9284.

[51] M. Kick, P. Keil, A. König, Solid–liquid phase diagram of the two Ionic Liquids EMIMCl and BMIMCl, Fluid Phase Equilibria, 338 (2013) 172-178.

[52] K. G. Joback, R. C. Reid, Estimation of pure-component properties from group-contributions, Chemical Engineering Communications, 57 (1987) 233-243.

[53] K. G. Joback, A unified approach to physical property estimation using multivariate statistical techniques, Massachusetts Institute of Technology, 1984.

[54] E. Ikeda, J. C. Mackie, Thermal decomposition of two coal model compounds-pyridine and 2-picoline. Kinetics and product distributions, Journal of analytical and applied pyrolysis, 34 (1995) 47-63.

Chapter 4

Experimental Dissolution and Dispersion of Coal in Ionic Liquids

4.1 Introduction

In view of the various advantages of IL's as a solvent [1-26], it was decided to choose the best IL by screening various combinations of cations and anions. From the previous chapter, we have screened the potential IL's with COnductor like Screening MOdel for Real Solvents (COSMO-RS) by computing the Solid-Liquid Equilibrium of these 18 ILs (Table 3.1) in coal. Activity coefficients of coal in IL's were also considered to predict the Solid-Liquid-Equilibrium (SLE) in Chapter 3 [27]. The recommended IL's were the ones which possessed high solubility in IL.

Based on Chapter 3, the following ILs were selected for experiments: 1-butyl-3-methylimidazolium hexafluorophosphate [BMIM][PF_6], 1-butyl-1-methylpyrrolidinium methyl carbonate [BMPYR][CH_3CO_3], 1-butyl-4-methylpyridinium tetrafluoroborate [BMPY][BF_4], tributylmethylphosponium methyl sulfate [MTBP][$MeSO_4$] and tributylmethylammonium methyl sulfate [TMA][$MeSO_4$].

4.2 Experimental Analysis

4.2.1 Materials

Indian coals with four different ranks were collected from Dugda Mines, Jharia Mines, Hingula Mines, and Dakra Mines and were coded as coal-1, coal-2, coal-3 and coal-4 respectively. The sizes of all coal samples were obtained by sieving the coal samples using –500 mesh sieve shaker. The ultimate analysis was conducted by CHNS elemental analyzer (*Variel CUBE*, Germany), while the proximate analysis was carried out by American Society for Testing of Materials (ASTM D 3173-3187, ASTM D 3175-3189) standards [28, 29]. The

proximate and ultimate analysis data are given in Table 4.1. Our aim is to compare the carbon content of these coals before and after pretreatment. An increase in the carbon content signifies higher calorific value together with lesser ash content. All the IL's used in this study were purchased from the *Sigma-Aldrich* and were used as received. The structures of ILs are given in Table 4.2.

4.2.2 Methods

Coal sample preparation: The coals were dried for 24 h at 50 ºC. To reduce the effect of mineral matter for quantitative analysis, coal samples were washed with 0.1N HCl for 4 h. The HCl treated coal samples were again washed with ionized water till neutral pH is attained. Thereafter they were dried for 48 h at 60 ºC in a vacuum drying oven.

IL-treated coal sample preparation: The HCl-treated coal samples were mixed with IL (1 g: 2 mL), and immersed in an oil bath at 100 ºC for 4 h. The detailed experimental procedure is shown in Fig. 4.1. The samples were washed with ionized water until a neutral pH was recorded. In a similar manner, the IL-treated coal samples were dried in a vacuum oven for 48 h at 60ºC for quantitative analysis. All the IL-treated coal sample, sizes, and shapes were determined before and after thermal treatment using an optical microscope (Leica DM750M).

Estimation of Ash Yield and Moisture content: After weighing the empty crucible, 1g of coal was gradually transferred to the crucible and the weight of the crucible with coal sample was again noted. The sample was then spread gently onto the crucible for even distribution. Thereafter the coal sample was inserted in a hot air oven (Optic Technology, ISO 9001:2008 certified) at a temperature of 105 ºC for 1 h. The samples were again

weighed after sufficient cooling in a desiccator. The moisture content (wt.%) was then calculated by measuring the loss in mass of water to its original mass [28]. The mineral matter (wt.%) was obtained at a temperature of 750 ºC for 1 h, while the volatile matter (wt.%) was obtained at a temperature of 925 ºC for 7 min [29] in a muffle furnace (1200AC BOX Muffle Furnace, VB Ceramic Consultant). The mineral matter is merely the residue remaining after the complete combustion at 750 ºC.

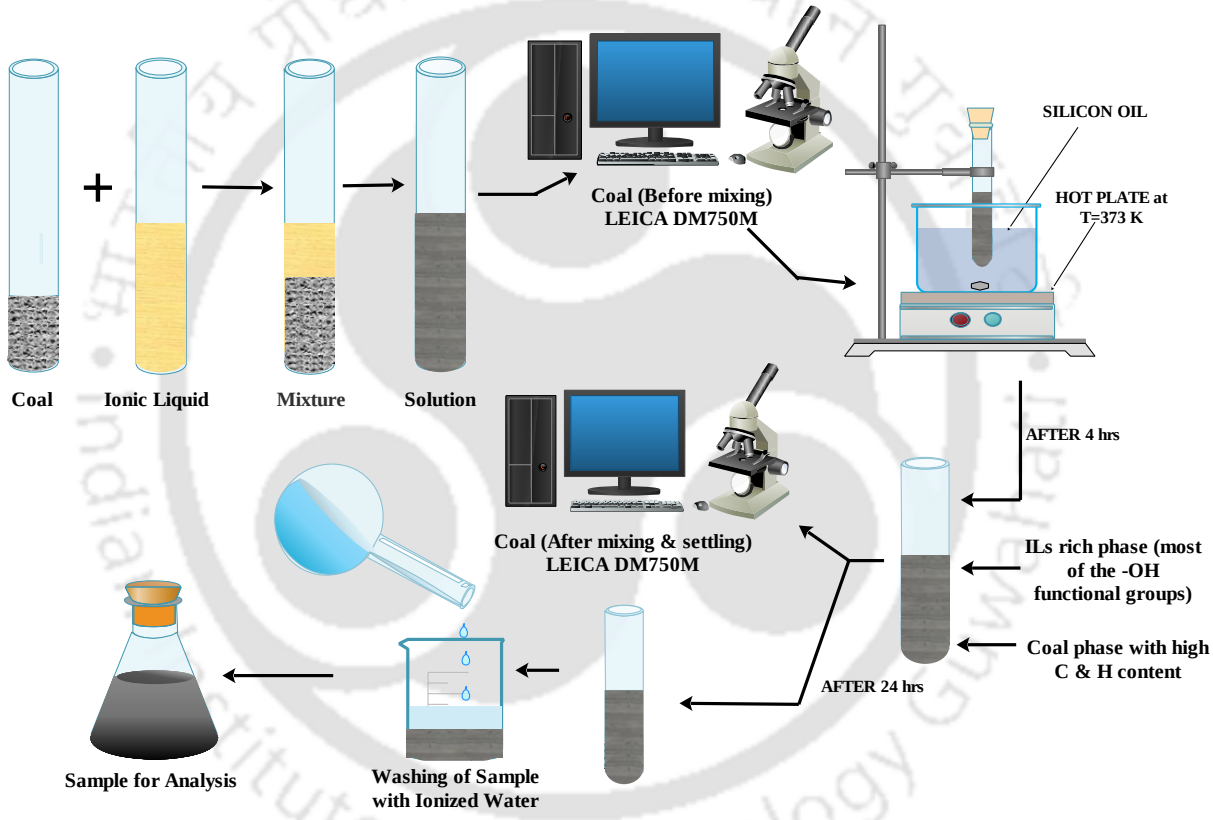

Fig. 4.1 Schematic representation of experimental setup and methodology

Swelling Studies: The swelling ratio (Q) [30] is measured by the fraction of the change in the volume of the coal solution. Initially, a measured quantity of coal and IL (1 g: 2 mL) were taken for centrifugation. Thereafter the coal-IL mixture was mixed and the initial volume was measured (v_1). The mixture was then heated for 4 h at a temperature of

100 ºC in an oil bath (Fig. 4.1). After its heating, the solution was kept for 24 h so as to attain equilibration. The equilibrate solution was again centrifuged for 5 min and the swollen volume is then recorded as v_2. Swelling ratio (Q) [30] was then defined as the ratio of the swollen volume (v_2) to the initial volume (v_1) of the coal-IL, which is expressed in equation (4.1).

$$Swelling\ ratio\,(Q) = \frac{Swollen\ volume\,(v_2)}{Initial\ volume\,(v_1)} \tag{4.1}$$

Table 4.1 Proximate and Ultimate analysis of Raw coal Samples

Coal Samples	Coal 1	Coal 2	Coal 3	Coal 4
Proximate Analysis (wt.%)				
Moisture	1.60	2.96	7.12	5.07
Ash	33.73	51.29	26.56	43.88
Volatile matter	25.40	22.71	47.29	30.33
Fixed carbon	39.27	23.03	19.06	20.73
Ultimate Analysis (wt.%)				
Carbon	56.92	57.64	54.60	32.39
Hydrogen	3.07	2.96	3.81	2.24
Nitrogen	1.87	1.76	1.98	1.28
Oxygen	38.15	37.64	39.61	64.10

Extraction Yield of Coal in ILs: The extraction yield was conducted by mixing coal in IL at a temperature of 100 ºC for 4 h. After the heat treatment, a dark black solution was observed. A soluble portion appeared on the upper surface of the centrifuge tube. The mixture of solid/liquid was separated by using a centrifugal separator. The soluble materials were then extracted and the residues were collected via multiple deionized washing for

removing the ILs. The residue was then dried for 24 h in a vacuum drying oven and the extract yield was calculated by using the following equation,

$$Extract\ Yield(\%) = \frac{Mass\ of\ [coal\ sample - residue]}{Mass\ of\ coal\ sample} \times 100 \qquad (4.2)$$

Table 4.2 Ionic Liquids used in this Study

Name of the ionic liquid	Acronyms	Structures
1-butyl-3-methylimidazolium hexafluorophosphate	[BMIM][PF_6]	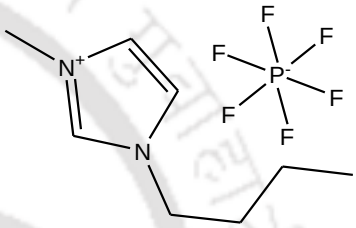
1-butyl-1-methylpyrrolidinium methyl carbonate	[BMPYR][CH_3CO_3]	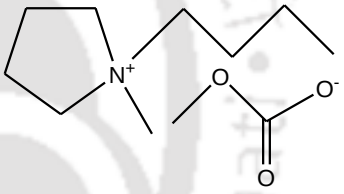
1-butyl-4-methylpyridinium tetrafluoroborate	[BMPY][BF_4]	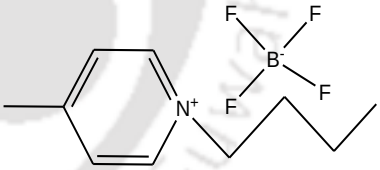
Tributylmethylammonium methyl sulfate	[TMA][$MeSO_4$]	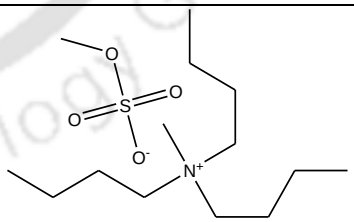
Tributylmethylphosphonium methyl sulfate	[MTBP][$MeSO_4$]	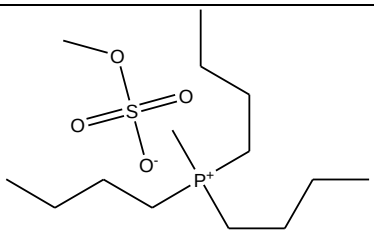

Characterization: It is a cumbersome process to estimate the amount of coal material dissolved and dispersed in ILs. Therefore, the use of an optical microscope (Leica DM 750M) for microscopic observation (200X magnifications) can help us to predict the particle size and shape of pretreated and untreated coals. Similarly, Fourier Transform Infrared Spectroscopy (FTIR) technique [31] was used to quantify the oxygen-containing groups in both the raw coal and IL-treated coal. This was performed by analyzing the wave numbers which were in the range of 4000-450 cm^{-1} at a scan rate of 40 along with a spectral resolution of 4 cm^{-1}. Potassium bromide (KBr) pellet method was used to obtain the FTIR spectra. KBr pellets were made by pressing a mixture of coal samples and moisture free KBr at a ratio of 1:100. However, it should be noted that the FTIR spectra only gives us a qualitative idea of functional groups in coal. Therefore, for quantitative analysis, of raw coal and IL-treated coal, the peak height method is used. The peak height method used for the quantitative analysis was obtained by the curve fitting method using *Origin 8.5* software.

4.3 Results and Discussions

All the IL's selected from COSMO-RS screening were liquid at room temperature. Based on the proximate and ultimate analysis data (Table 4.1), coals 1-3 are designated as bituminous variety, while coal 4 as 'lignite', as it possesses a high percentage ash. Coal samples (coal 1-4) with each of the IL's listed in Table 4.2 were placed in a centrifuge tube (Fig. 4.2). From Fig. 4.2, it can be observed that at room temperature (upper row) the ILs show good contact with coal 1. After heating till 100 ºC (middle row) for 4 h, a black, dense and dispersed solution was observed. It remained a dark black solution (lower row) even after cooling at room temperature for 24 h. The only ILs which did not follow this trend

were [BMIM][PF_6] and [TMA][$MeSO_4$]. Interestingly both these ILs are hydrophobic, unlike the remaining ones which are hydrophilic.

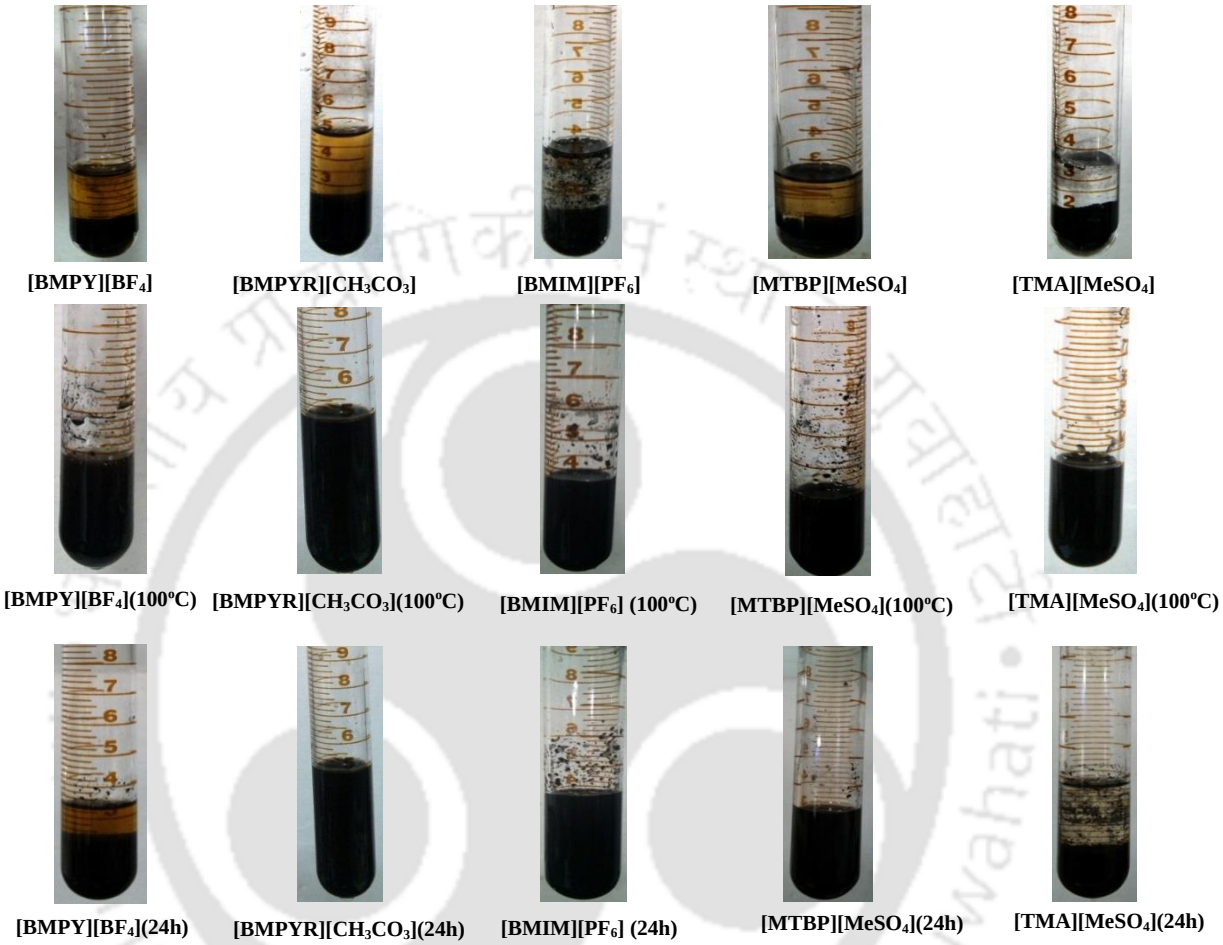

Fig. 4.2 Appearance of coal 1 and five different IL's before (upper row); and after heating till 100 ºC (middle row) and cooling for 24h (lower row)

4.3.1 Morphology of Raw Coal and Five Different IL-Pretreated Coals

Fig. 4.3a shows the optical micrograph of raw coal 1 which is smeared in water for 4 h. The average particle sizes of the coal samples were measured by *ImageJ software package* [32-34]. The average particle size for the raw coal 1 was found to be ~500 µm. The subsequent particle size of coal particles in [BMIM][PF_6] (Fig. 4.3b), [BMPY][BF_4] (Fig.

4.3c), and [TMA][$MeSO_4$] (Fig. 4.3d) were fractionated within a range of 200-300 µm. From Fig. 4.3c it is clear that the swelling or the fragmentation is more pronounced for the IL: [BMPY][BF_4]. Similarly, a finer and uniform size of the coal is prevalent from Fig. 4.3e and Fig. 4.3f. It is clear that with coal-1, the IL's namely [BMIM][PF_6], [BMPY][BF_4], and [TMA][$MeSO_4$] gave an irregular and non-uniform particle size distribution.

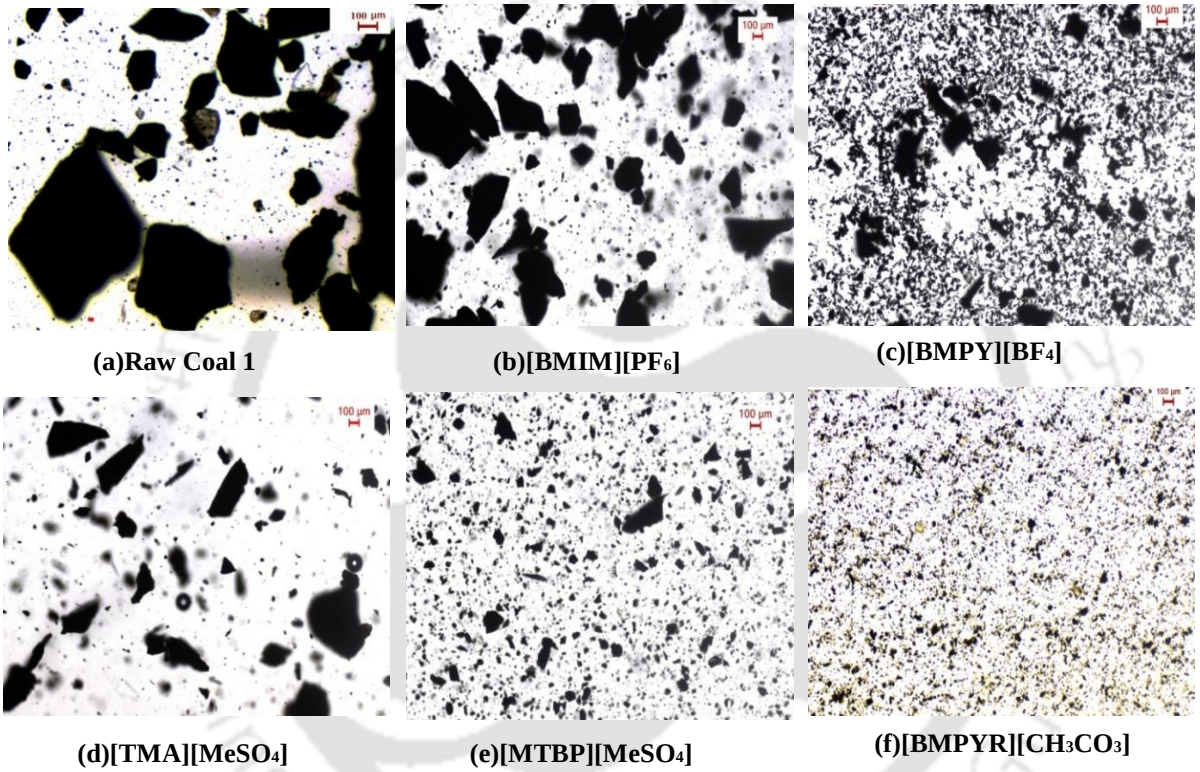

Fig. 4.3 Optical micrograph (200x) of coal 1 suspended in (a) water and after heating at 100ºC with ILs (b) [BMIM][PF_6] (c) [BMPY][BF_4] (d) [TMA][$MeSO_4$] (e) [MTBP][$MeSO_4$], and (f) [BMPYR][CH_3CO_3]

A contrary trend was observed for [MTBP][$MeSO_4$] and [BMPYR][CH_3CO_3], where it had a powder like texture (10-20 µm). The IL [BMPYR][CH_3CO_3] (Fig. 4.3e), gave the most uniform dispersed particles as a result of which the particle size reduced to a range of 10-50 µm. This is mainly attributed to the π-π stacking, π-cation interaction and electrostatic

interaction which allows [BMPYR][CH_3CO_3] to considerably modify the cross-linked network of coal 1 molecules [35, 36].

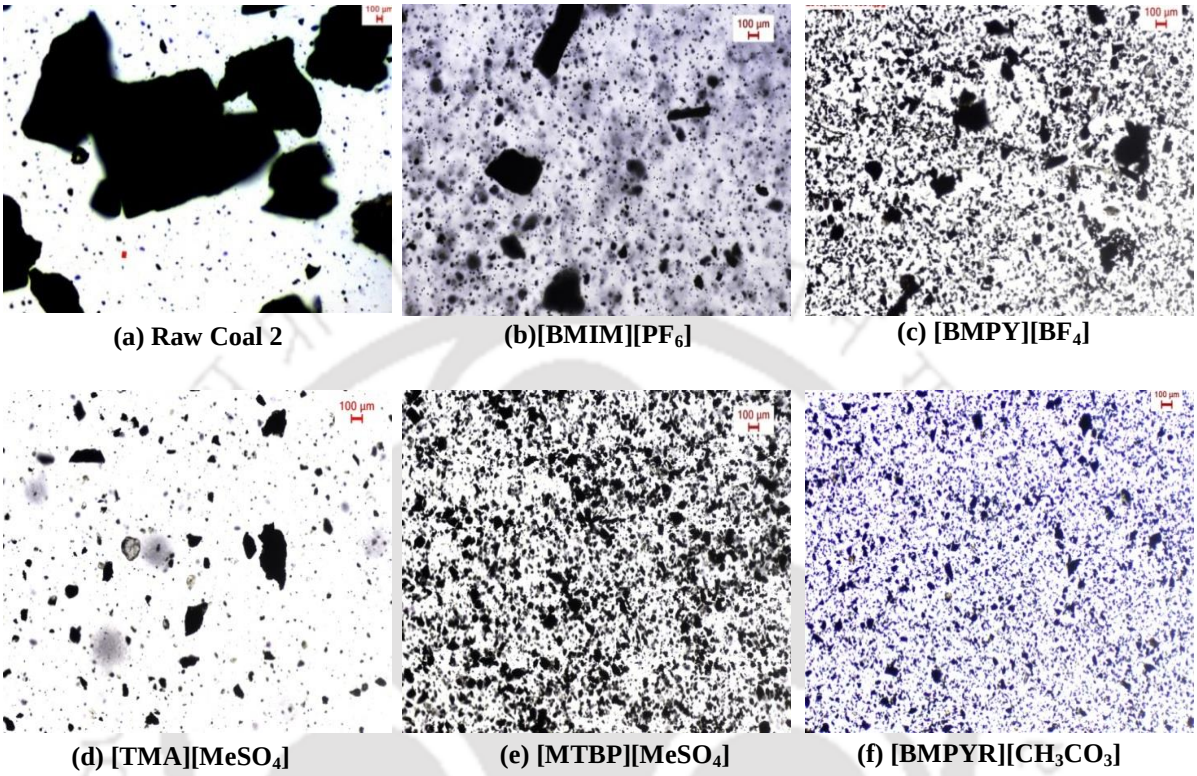

Fig. 4.4 Optical micrograph (200x) of coal 2 suspended in (a) water and after heating at 100ºC with ILs (b) [BMIM][PF_6] (c) [BMPY][BF_4] (d) [TMA][$MeSO_4$] (e) [MTBP][$MeSO_4$], and (f) [BMPYR][CH_3CO_3]

From Fig. 4.4, it can be seen that coal 2 shows a similar morphological change. Here the average particle size for raw coal are also in the range ~500 µm. Coal 2 dispersed in [BMIM][PF_6], [BMPY][BF_4], and [TMA][$MeSO_4$] had finer texture (10-50 µm). The formation of cross-linked structure can be due to the dispersive interaction between coal and ILs [15]. [MTBP][$MeSO_4$] and [BMPYR][CH_3CO_3] reduced the coal particles to a size <10 µm. This is particularly beneficial for coal processing application such as coal liquefaction process, where the catalyst needs to be in contact with a larger surface area [6].

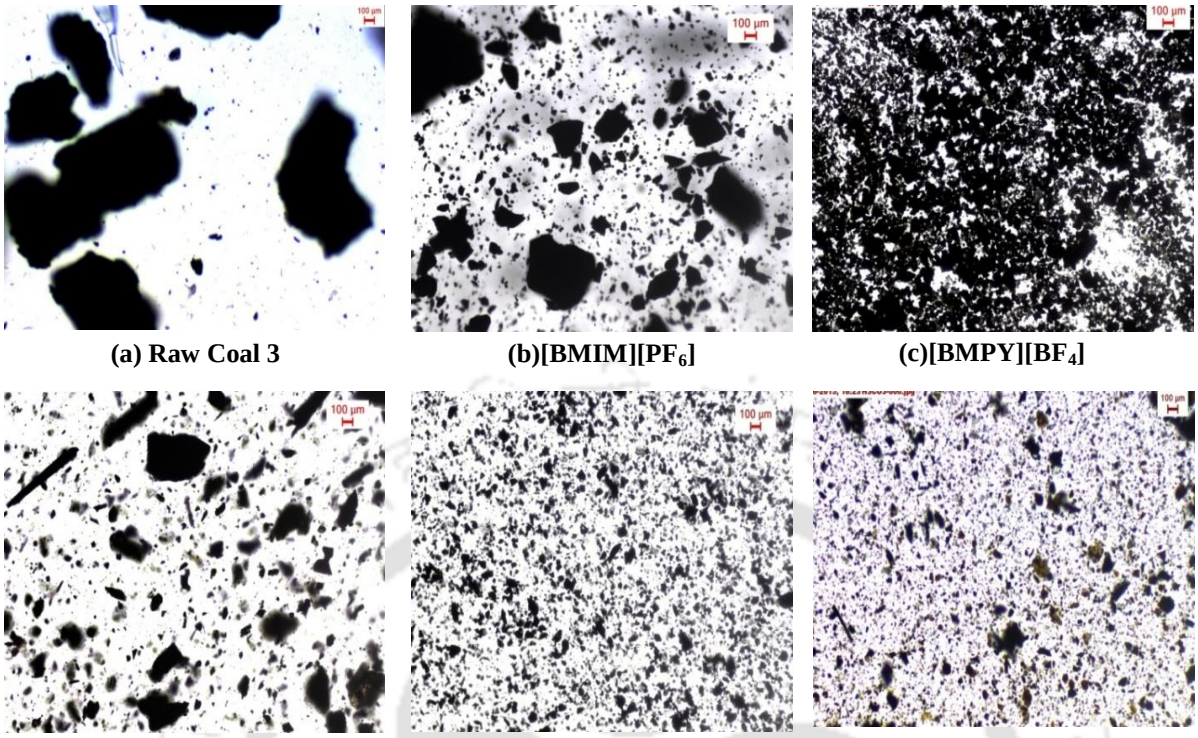

(a) Raw Coal 3 **(b)[BMIM][PF_6]** **(c)[BMPY][BF_4]**

(d) [TMA][$MeSO_4$] **(e) [MTBP][$MeSO_4$]** **(f) [BMPYR][CH_3CO_3]**

Fig. 4.5 Optical micrograph (200x) of coal 3 suspended in (a) water and after heating at 100ºC with ILs (b) [BMIM][PF_6] (c) [BMPY][BF_4] (d) [TMA][$MeSO_4$] (e) [MTBP][$MeSO_4$] and (f) [BMPYR][CH_3CO_3]

Fig. 4.5 shows the optical micrograph of raw coal 3 with their respective dispersed ILs. It was observed that [BMIM][PF_6] and [TMA][$MeSO_4$] gave a higher dispersed particle size. This was also in contrary to what was obtained for [BMPY][BF_4] and [MTBP][$MeSO_4$] where the intermolecular interaction between the coal and ILs was higher. Fig. 4.5f clearly indicates that the cross-linked structure of coal is fragmented and dispersed efficiently by [BMPYR][CH_3CO_3], as some of the particles appear to be translucent. This might be due to the some of the coal particles which appears to be thin and small [25]. Similarly for coal 4, the ILs [BMIM][PF_6] (Fig. 4.6b) and [TMA][$MeSO_4$] (Fig. 4.6d) did not swell appreciably. For the remaining ILs (Fig. 4.6), the swelling was particularly high for the IL's

[MTBP][$MeSO_4$] (Fig. 4.6e) and [BMPYR][CH_3CO_3] (Fig. 4.6f) where they were able to fracture and fragment the coal to an average size of <10 µm.

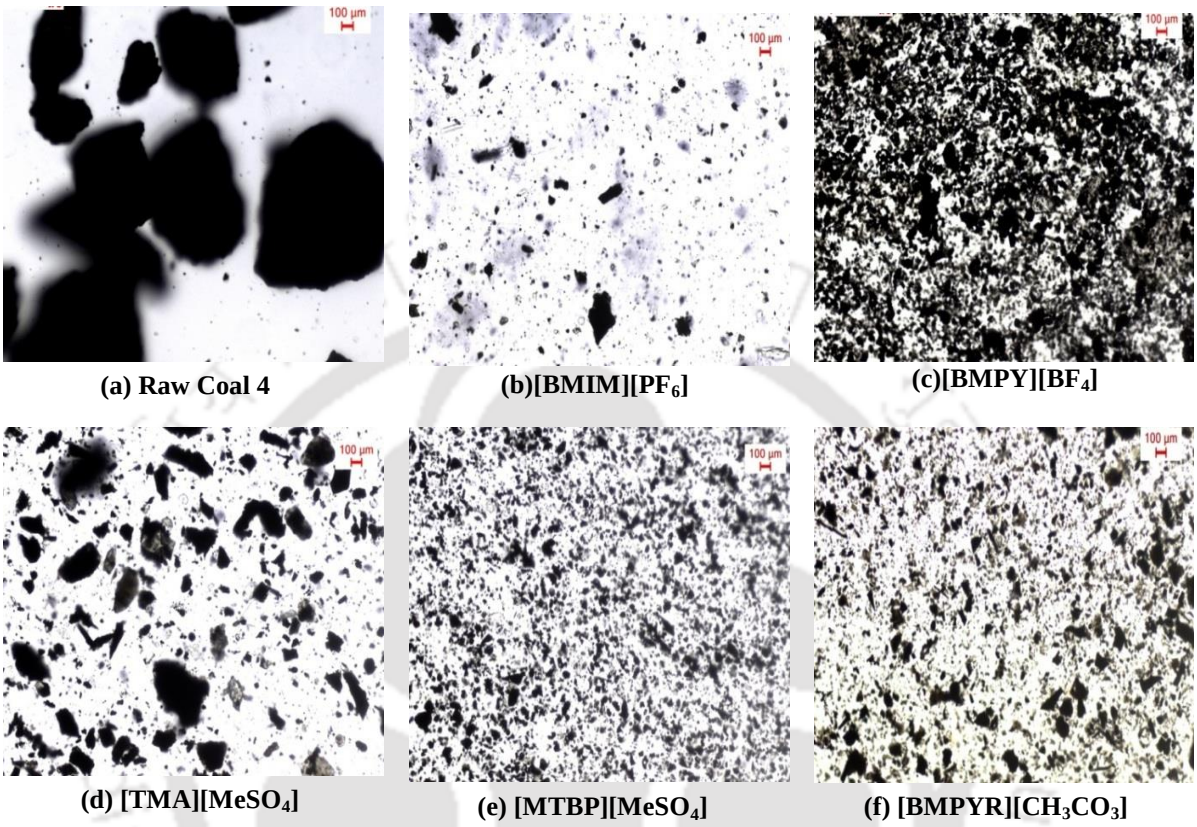

Fig. 4.6 Optical micrograph (200x) of coal 4 suspended in (a) water and after heating at 100ºC with ILs (b) [BMIM][PF_6] (c) [BMPY][BF_4] (d) [TMA][$MeSO_4$] (e) [MTBP][$MeSO_4$] and (f) [BMPYR][CH_3CO_3]

The fractionation of macromolecular structure mainly occurs due to the breakage of the hydrogen bond donor groups present in coal. Generally, in low and medium rank coals, non-covalent interaction in the cross-linked structure of coal molecules play a vital role [15]. This interaction is due to the hydrogen bonding and ionic bonding of aromatic groups present in the coal molecules. The cross-linked structure of coal molecules here gets disrupted due to the fractionation of non-covalent bonding. The ILs here merely allows the π-π stacking, π-cation interaction, electrostatic interaction, and hydrogen bonding to interact

with the macromolecular structure of coal molecules. However, quantifying their effect is very difficult as numerous intermediates are known to form during fractionation. This interaction causes an increase of swelling ratio because of the formation of other inclusive compounds [26]. Hence interaction of coal and ILs was performed by using both Reactive Molecular Dynamics [37] and COSMO-RS [27] simulations as already discussed earlier. In the next section, the measurement of swelling ratios was carried out to confirm this observation.

4.3.2 Swelling Behavior of Coal/ILs Mixtures

Table 4.3 shows the swelling behavior of four different Indian coals in ILs. It can be observed that the swelling ratio depends on both the rank and the type of the solvent used. The IL's are known to disrupt mainly hydroxyl group (phenolic and free) from its macromolecular structure. This is reflected in a higher swelling ratio for all the ILs. It should be noted that the swelling enhances the coal porosity and improve the dispersion of the coal structure [38-40]. Due to the ILs; weaker bond within the coal network tends to break leading to the formation of macro-pores. This eventually increases the coal porosity and hence ensures easy dispersion of catalyst onto the coal structure. This is evident in the previous studies [38-40], where the dispersion of the hydrogen-bond donor within the solvent was found with coal. From Table 4.3, swelling ratio's (Q) for IL's are as follows: [BMPYR][CH_3CO_3](Q=1.52), [BMPY][BF_4](Q=1.22), [BMIM][PF_6](Q=1.26), [TMA][$MeSO_4$](Q=1.02), and [MTBP][$MeSO_4$](Q=1.103). It can be observed that coal 4 (lignite coal) interacts strongly with IL [BMPYR][CH_3CO_3], thereby giving a higher magnitude of swelling ratio. A similar ratio is not visible for the ILs [TMA][$MeSO_4$] and [MTBP][$MeSO_4$]. Therefore, it is recommended that the ILs having a small cation chain can

significantly swell the coal macromolecular structure as compared to larger alkyl chain length [41].

Table 4.3 Swelling ratio for Four Different Coal

Coal/ILs	[BMPYR] [CH_3CO_3]	[BMPY] [BF_4]	[BMIM] [PF_6]	[TMA] [$MeSO_4$]	[MTBP] [$MeSO_4$]
Coal 1	1.43	1.14	1.12	1.02	1.01
Coal 2	1.31	1.13	1.23	1.01	1.03
Coal 3	1.27	1.14	1.14	1.01	1.07
Coal 4	1.52	1.22	1.26	1.01	1.10

Table 4.4 Characteristic Peaks and Functional Groups [7-10]

Wave number, (cm^{-1})	Functional groups
780	C-H bonded aromatic ring
915	C-H bonded aromatic ring
1032	C-O-H deformation
1108	Phenolic, C-O stretch
1329	symmetric aliphatic C-H bending of methyl groups
1420	asymmetric aliphatic C-H deformation of methylene and methoxyl
1637	aromatic ring C=C in stretching-methoxyl substitute benzene or phenol
2866	aliphatic C-H stretch vibration-methyl CH_2
2954	symmetric aliphatic C-H stretch vibration-methyl CH_3
3465	OH stretching vibration of hydrogen-bonded hydroxyl group

4.3.3 FTIR Spectra for Raw and IL-pretreated Coal

FTIR spectra of the raw coals (coal 1-4) and benificiated coal with the three ILs namely, [BMPYR][CH_3CO_3], [BMPY][BF_4], and [BMIM][PF_6] are shown in Fig. 4.7-4.10. Table 4.4 shows the details of characteristic peaks and their functional groups used in this work [7-10]. The prime objective concerning the dissolution and swelling of the coal particles are due to the breakage of the hydrogen bonding network as outlined in the earlier section. This is mainly due to the reduction of the –OH containing functional groups such as phenolic and carboxylic groups [7-10]. We have computed this reduction by comparing the strength of the –OH groups from FTIR spectra.

4.3.3.1 Oxygen-Containing Functional Groups

In general, the functional groups cannot be derived directly from the position and shape of the spectral peak. However, quantitative results can be indirectly used to analyze the groups. The peak height, as well as the peak area, are thus considered for the quantitative analysis[16, 42]. These will be used to analyze and compare the content of main functional groups such as –OH stretching and functional groups consisting of hydrogen bonds. Table 4.5 shows the peak area of a typical transmittance peak for all the coal samples (with and without IL-pretreatment). The transmittance peak area of O–H stretch, hydrogen-bonded alcohol, and phenols at 3465 cm^{-1} get reduced in all the coal samples when treated particularly with the IL: [BMPYR][CH_3CO_3] [7-10]. The area of hydrogen-bonded alcohol, O–H stretch and –OH phenolic group for coal 2-[BMIM][PF_6] mixture was 22.6% higher as compared to the raw coal. Similarly, the carbonyl and C=O stretching (carboxylic acid) for coal 4-[BMIM][PF_6] was found to be 23.54% higher when compared to raw coal 4 i.e.

lignite. The corresponding values in [BMPY][BF_4] and [BMPYR][CH_3CO_3] were found to be 33.9% and 51.5% lower when compared to lignite.

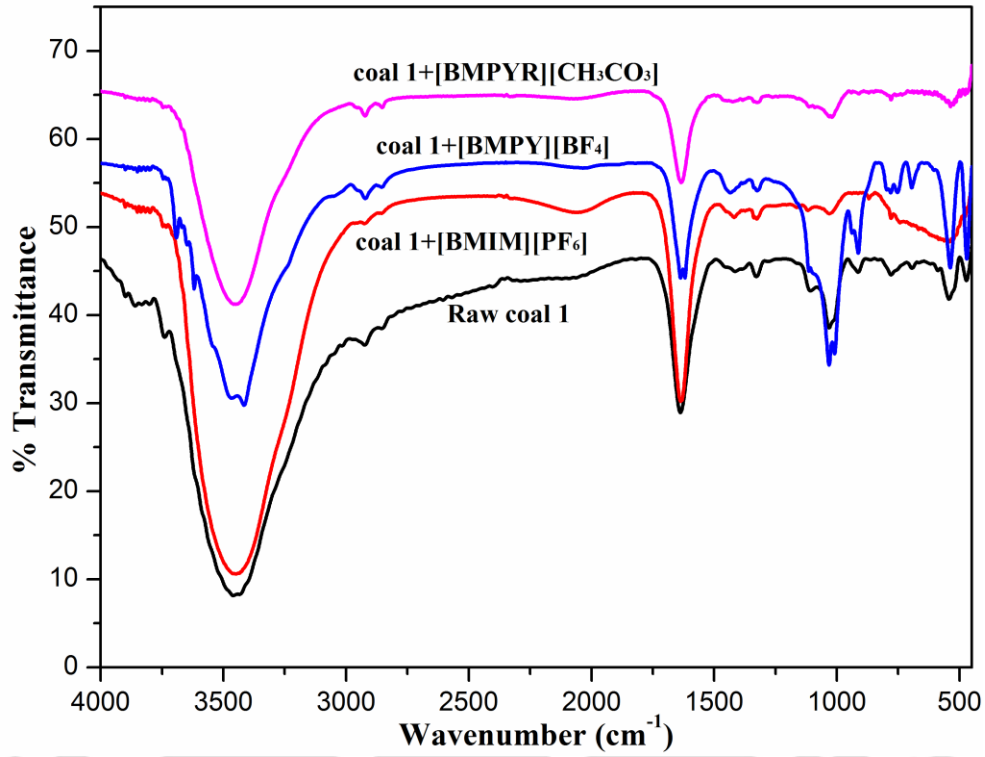

Fig. 4.7 Comparative FTIR spectra of raw coal 1 and three different IL-pretreated coal 1

The overall effect of dissolution with respect to all the hydroxyl groups across the coal samples are summarized in Table 4.5. The hydroxyl group is said to appear in the range of 3600-3200 cm^{-1} for all the coal samples [31]. A characteristic peak at ~3465 cm^{-1} indicates the long winding of phenol hydroxyl group in the samples. The transmittance peak of phenolic C–O appears at 1108 cm^{-1}, while the corresponding transmittance peak of C–O–H is found at 1032 cm^{-1} [7-10]. Both the values were used to quantify the phenolic and carboxylic groups present in the raw and pretreated coal. From Fig. 4.7-4.10, the position of the functional groups remains the same for raw and pretreated coal. It implies there is no shift in the respective peak position. Thus, the ILs does not have any influence on functional

group in coal; it merely reduces the intensity of free hydroxyl group in the pretreated coal samples.

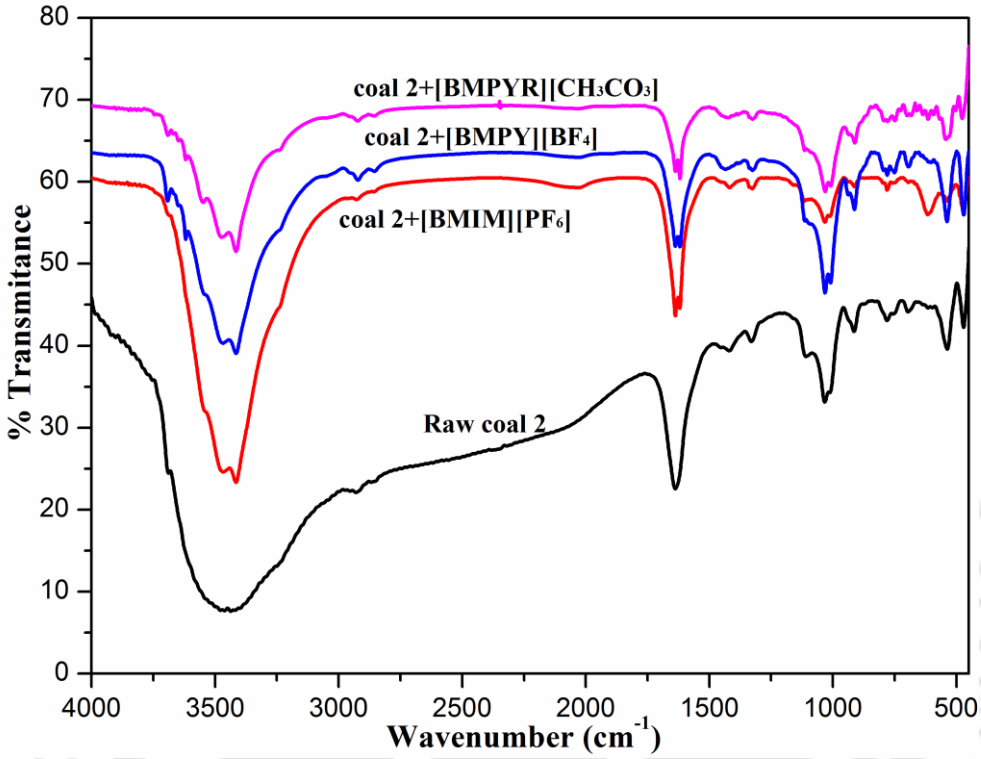

Fig. 4.8 Comparative FTIR spectra of raw coal 2 and three different IL-pretreated coal 2

From a quantitative approach (Table 4.5), an overall 47.6%, 55.6% and 68.1% reduction was achieved in the peak area of free hydroxyl group (3465 cm^{-1}) for the ILs [BMIM][PF_6], [BMPY][BF_4], and [BMPYR][CH_3CO_3] with coal 1 (bituminous coal) respectively. Similarly, an average size of 10-50 µm and a reduction in particle size close to 35.4%, 34.2%, and 68.1% were seen for coal 2, coal 3, and coal 4 respectively with the IL: [BMPYR][CH_3CO_3]. It can also be seen that the intensities of the stretching band due to hydrogen bonding –OH decreased by ~60% when compared to the raw coal. This decrease was due to the fact that the –OH functional groups are now extracted into the Ionic Liquid rich phase.

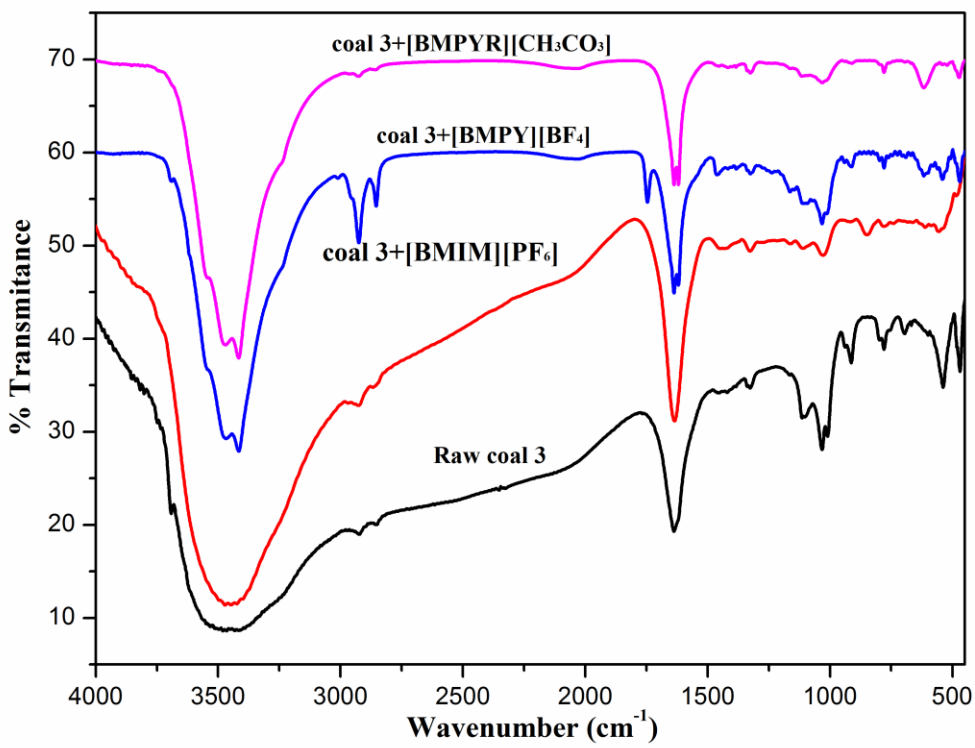

Fig. 4.9 Comparative FTIR spectra of raw coal 3 and three different IL-pretreated coal 3

The transmittance peak intensity of alcoholic, phenolic free hydroxyl, and self-association hydroxyl hydrogen bond in [BMIM][PF_6] are greater than that of raw coal 2. While they are seen to diminish in both [BMPY][BF_4] and [BMPYR][CH_3CO_3]. For the remaining coal samples, the corresponding transmittance peaks are found to be lower irrespective of the type of ILs. Thus, IL [BMPYR][CH_3CO_3] has a better destructive effect on hydroxyl group for coal 1 and coal 4. As a result, deformation of coal 1 and coal 4 gave a value of 68.14% and 68.15% peak areas with pretreated [BMPYR][CH_3CO_3]. This is similar to the FTIR measurements performed earlier by Hu et al. [16] on imidazolium-based cations. This is also confirmed from both the FTIR spectra and the swelling characteristics (section 4.3.2).

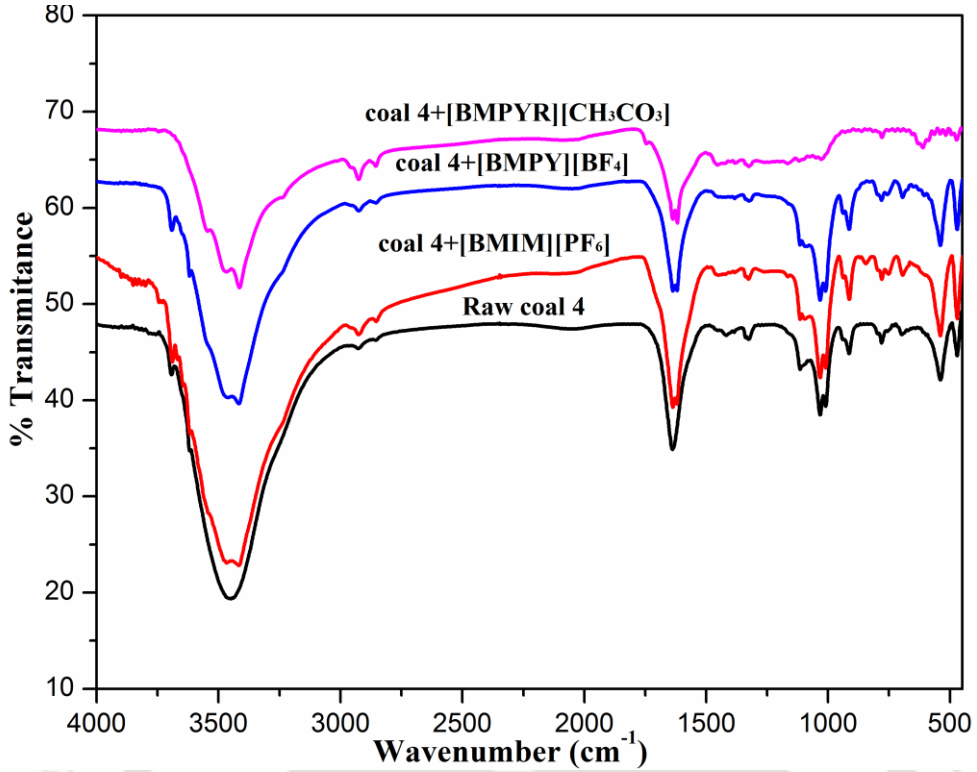

Fig. 4.10 Comparative FTIR spectra of raw coal 4 and three different IL-pretreated coal 4

4.3.3.2 Aromatic hydrocarbon groups

Even though a reduction of these groups are not necessary since they reduce the carbon content and the calorific value of coal, still a study is required to observe the change in the peak positions of pre- and post-dissolution with ILs. The spectral intensity of aromatic rings C=C (1637 cm^{-1}) (Fig. 4.7-4.10) and C-H at (915 cm^{-1}) respectively indicate aromatic like structures in the raw coal. An overall 21.3%, 23.3%, and 24.9% reduction in the peak area for aromatic –CH (780 cm^{-1}) was noticed for the ILs [BMIM][PF_6], [BMPY][BF_4], and [BMPYR][CH_3CO_3] with coal 4 (lignite coal) respectively. The spectral intensity of aromatic rings –C=C at 1637 cm^{-1} in [BMPYR][CH_3CO_3] and [BMPY][BF_4] treated coal are lower for coal samples 1, 2 and 4. A reduction of 19.56% and 32.58% for coal 1 and coal 4 treated with [BMPYR][CH_3CO_3] indicates that IL's can destruct aromatic structure partly

which agrees with the observation of Hu et al. [16]. This mechanism of interaction is indeed very difficult to predict. This is further complicated by the formation of number of intermediate components making determination very cumbersome. An alternative way is to obtain meaningful and accurate data based on Reactive Force Field simulations. From the previous chapter 3 [37] we have depicted the reaction mechanism using ReaxFF simulation at a temperature of 3000 K in fuel rich condition. From the simulations, it was confirmed that the formation of CO is essentially due to the breakage of carbon-carbon (-C-C-) chain within the coal molecule. It was proposed that CO molecules are formed by the breakage of aromatic rings and subsequent incomplete reaction with oxygen molecules [43]. Destruction of aromatic rings are also complemented by Speight [44] which reports the partial fracture of an aromatic component within coal at high temperature.

4.3.3.3 Aliphatic hydrocarbon groups

The intensity peak for the symmetric stretch vibration of $–CH_3$, the aliphatic stretch vibration of $–CH_3$ can be located at 2954 cm^{-1} and 2866 cm^{-1} respectively. For asymmetric $–CH_3$ and symmetric aliphatic vibration of C–H (methoxy group), the peaks can be attributed at 1420 cm^{-1}, and 1329 cm^{-1} respectively [7-10]. From Fig. 4.7-4.10, quantitatively these groups are reduced by ~36.54 % as compared to the phenolic and free hydroxyl groups (Table 4.5). For coal 4 with [BMIM][PF_6], [BMPY][BF_4], and [BMPYR][CH_3CO_3], an overall 30.6%, 38.7%, and 41.8% reduction in the peak area of aliphatic C-H (1329 cm^{-1}) was observed from Table 4.5. Similarly, aliphatic –CH stretching was found to decrease on an average by ~40% when compared to raw coal 1 and 4. This is due to the proposed interaction of IL which eventually breaks the C–H bond.

Table 4.5 FTIR Peak area of Typical Transmittance Peaks

Peak structure classification	Aromatic hydrocarbon			Aliphatic hydrocarbon				Oxygen containing functional group		
Peak position, cm^{-1}	780	915	1637	1329	1420	2866	2954	1032	1108	3465
Functional group	C-H	C-H	C=C	C-H (Methyl)	C-H (Methylene & Methoxy)	C-H (Methyl-CH_2)	C-H (Methyl-CH_3)	C-O-H	C=O	O-H (hydrogen bonded hydroxyl)
raw coal 1	6.03	7.07	8.69	5.59	4.43	1.20	0.72	15.53	3.94	39.01
coal 1+[BMIM][PF_6]	4.07	6.27	9.01	3.76	5.98	1.26	1.23	8.31	2.77	20.44
coal 1+[BMPY][BF_4]	3.18	3.72	6.81	3.92	5.03	0.87	1.29	6.27	2.35	17.30
coal 1+[BMPYR][CH_3CO_3]	2.41	2.84	6.99	2.88	4.99	1.13	1.27	6.53	0.88	12.43
raw coal 2	1.28	3.54	7.00	2.01	1.40	6.17	1.41	9.21	1.61	22.90
coal 2+[BMIM][PF_6]	2.13	5.35	8.05	2.12	3.01	1.15	1.28	3.63	1.06	29.63
coal 2+[BMPY][BF_4]	3.28	6.54	7.32	4.66	4.31	1.17	1.37	12.15	1.65	17.66
coal 2+[BMPYR][CH_3CO_3]	2.69	3.50	5.13	3.94	3.53	2.88	2.11	6.12	1.07	14.79
raw coal 3	3.37	3.31	7.77	1.96	1.35	1.75	1.14	4.65	9.72	21.79
coal 3+[BMIM][PF_6]	2.37	4.99	6.82	1.03	2.76	1.93	1.92	2.48	1.26	21.67
coal 3+[BMPY][BF_4]	4.76	3.81	9.78	2.15	6.67	6.55	8.76	7.42	4.17	28.51
coal 3+[BMPYR][CH_3CO_3]	3.58	9.89	8.46	0.087	4.64	0.79	0.45	3.91	3.93	14.32
raw coal 4	4.82	7.13	8.81	4.68	2.44	1.01	1.38	8.13	2.81	32.15
coal 4+[BMIM][PF_6]	3.79	6.09	8.99	3.25	1.41	1.42	1.67	5.72	4.53	29.53
coal 4+[BMPY][BF_4]	3.69	7.41	6.24	2.86	0.65	1.09	1.75	3.86	4.17	21.38
coal 4+[BMPYR][CH_3CO_3]	3.62	0	5.94	2.72	0.74	0.85	1.93	1.25	1.74	10.24

On the contrary for methyl $–CH_3$, an 80% and 30% rise of the transmittance peak is seen for raw coal 1 and 4 respectively. It should be noted that due to the partial dissolution effect of ILs on aliphatic hydrocarbons, the transmittance peak area of methyl $–CH_3$ asymmetric deformation vibration at 2954 cm^{-1} was found to decrease only for [BMPYR][CH_3CO_3] in coal 3. For the remaining ILs, the area of methyl $–CH_3$ in [BMIM][PF_6], [BMPYR][CH_3CO_3], and [BMPY][BF_4] treated coals were higher than that of raw coal, the only anomaly being coal 3.

For methyl –CH vibration, the transmittance peak area of at 1329 cm^{-1} were found to decrease for all the coal samples in [BMPYR][CH_3CO_3]. It is also observed that reduction in methyl –CH are 48.48% and 41.88% respectively for coal 1 and coal 4 for the same IL. Thus, it indicates that [BMPYR][CH_3CO_3] has a better destructive effect on methyl –CH bond when compared to methyl $–CH_3$. This agrees with the experimental studies on imidazolium based cations by Hu et al.[16]. Hence, in summary, the decrease in –C=C peaks are directly proportional to transmittance peak areas of –OH and –CH while inversely proportional to methyl $–CH_3$.

4.3.4 Proximate and Ultimate Analysis of ILs-pretreated Coal Sample

The recommended IL namely [BMPYR][CH_3CO_3] was then used to determine the proximate and ultimate analysis (Table 4.6) of all the variants of coal. This will help us to determine the final carbon content in all the coal samples. As compared to the raw coal (Table 4.1) it was observed that there is a significant reduction in ash yields (wt. %) in all the coal samples. The volatile matter too showed a remarkable decrease across the coal samples. From the proximate analysis, the fixed carbon content was found to increase by an average

amount of 1/3rd as compared to the raw coal. The oxygen content as measured by difference also provided a sharp decrease as observed from swelling and FTIR spectra. This decrease may be attributed to the reduction of the free and phenolic hydroxyl groups. The result will hence help in the partial utilization of low grade or non-coking coal. This process is quite suitable for a country such as India, which does not have sufficient reserves of good coking coal. It will further reduce the harmful substances exhausted into the atmosphere from the byproduct type coke oven plant. An estimated amount of 700 g/ton of dust particles are said to be released per 3000 m^3/ton from the volume of exhaust product [45]. It will further reduce the dust emissions, improve the working climate, and recover the sensible heat of the coke.

Table 4.6 Proximate and Ultimate analysis of IL-pretreated coal samples

ILs-pretreated Coal Samples	Coal 1+ [BMPYR] [CH_3CO_3]	Coal 2+ [BMPYR] [CH_3CO_3]	Coal 3+ [BMPYR] [CH_3CO_3]	Coal 4+ [BMPYR] [CH_3CO_3]
Proximate Analysis (wt.%)				
Moisture	3.65	2.45	6.30	4.22
Ash	25.77	42.34	19.84	36.92
Volatile Matter	21.32	19.05	42.31	27.62
Fixed Carbon	49.25	36.15	31.55	31.24
Ultimate Analysis (wt.%)				
Carbon	59.55	56.18	63.77	38.22
Hydrogen	3.01	4.15	5.29	2.42
Nitrogen	1.67	1.81	2.39	1.15
Oxygen	35.86	37.86	28.55	58.21

4.3.5 Recovery of Ionic Liquids

Recovery of ILs is considered an important operation for reducing the operating costs. After the dissolution experiments, the IL's were washed with ionized water and then stored in stoppered vials. Thereafter, the IL's were recovered by heating till 70 ºC in an oil bath so as to initiate the evaporation of the volatile organic compounds present in coal. This will also include a slow vaporization of the moisture content. Thereafter the sample mixture was placed in a hot air oven (Optic Technology, ISO 9001:2008 certified) for more than 24 h in order to remove the remaining moisture content [46]. The amount of collected samples recovered is given in Table 4.7. It can be observed that the recovery of hydrophilic ILs namely, [BMPYR][CH_3CO_3] (87.98 wt.%), [BMIM][PF_6] (93.63 wt.%), and [BMPY][BF_4] (95.23 wt.%) were less as compared to hydrophobic ILs such as [TMA][$MeSO_4$] (96.52 wt.%), and [MTBP][$MeSO_4$] (96.51 wt.%). This is due to the fact that some amount of the hydrophilic IL gets washed out with the ionized water itself. The highest recovery was reported for [TMA][$MeSO_4$] (96.52%).

Table 4.7 Moisture content of recovered Ionic Liquids

Ionic Liquids	Recovered Ionic Liquids (wt.%)	Moisture content (wt.%)
[BMIM][PF_6]	93.63	2.67
[BMPYR][CH_3CO_3]	87.98	15.05
[BMPY][BF_4]	95.23	2.29
[TMA][$MeSO_4$]	96.52	1.95
[MTBP][$MeSO_4$]	96.51	2.13

Additionally, the moisture content in recovered IL's were also confirmed by a Karl-Fisher Titrator (787 KF Titrino, Metrohm, USA) as given in Table 4.7. [BMPYR][CH_3CO_3] possessed the highest amount of moisture (15.05 wt.%) after recovery. It should be noted that the carbon content and swelling was the highest with the same IL pretreated coal. This indicates from an economic point of view, the use of [BMPYR][CH_3CO_3] may not be beneficial as it increases the recovery cost in coal beneficiation.

4.3.6 Yield Extraction of Coal in ILs

The extract yield was calculated by equation 4.1 for different coals and reported in Table 4.8. The extracted yield follows the order: [BMPYR][CH_3CO_3] > [BMPY][BF_4] > [BMIM][PF_6]. This is due to the IL-[BMPYR][CH_3CO_3] having anion with a larger charge density [$CH_3CO_3^-$] which easily interacts with the polar entities of coal. The charge densities of all the anions in decreasing order of magnitude are: [CH_3CO_3](0.002), [BF_4](0.00176), and [PF_6](0.00152). From the results, IL-[BMPYR][CH_3CO_3] gave a total yield of 27.41 wt.% for coal 2 (bituminous); and 35.13 wt.% for coal 4 (lignite) respectively. All the extract yields for four different coals in ILs were listed in Table 4.8. Painter et al. [6, 15] used the IL [BMIM][Cl] to dissolve a significant portion of Illinois No. 6 coal, Powder River Basin, and Upper Freeport coal. Their results gave high extract yield >22.5, >19.2, and >14.4 wt.% which are complementary with our IL namely [BMPYR][CH_3CO_3].

Table 4.8 Extract Yield (wt.%) obtained after heating to 100ºC for 4 h

Coal Types	**Extract Yield (wt. %)**			
	[BMI] $[PF_6]$	[BMPY] $[BF_4]$	[BMPYR] $[CH_3CO_3]$	[BMIM] [Cl][6, 15]
Coal 1	16.35	21.63	24.76	-
Coal 2	18.05	24.02	27.41	-
Coal 3	14.73	19.27	23.03	-
Coal 4	20.29	23.31	35.13	-
Illinois No. 6 coal [6, 15]	-	-	-	>22.5
Powder River Basin [6, 15]	-	-	-	>19.2
Upper Freeport [6, 15]	-	-	-	>14.4

References

[1] K. Mae, T. Maki, H. Okutsu, K. Miura, Examination of relationship between coal structure and pyrolysis yields using oxidized brown coals having different macromolecular networks, Fuel, 79 (2000) 417-425.

[2] L. M. Lucht, N. A. Peppas, Macromolecular structure of coals: 2. Molecular weight between crosslinks from pyridine swelling experiments, Fuel, 66 (1987) 803-809.

[3] J. W. Larsen, T. K. Green, J. Kovac, The nature of the macromolecular network structure of bituminous coals, The Journal of Organic Chemistry, 50 (1985) 4729-4735.

[4] G. Pitt, G. R. Millward, Coal and modern coal processing: An introduction, Academic Press1979.

[5] J. P. Mathews, A. L. Chaffee, The molecular representations of coal–A review, Fuel, 96 (2012) 1-14.

[6] P. Painter, R. Cetiner, N. Pulati, M. Sobkowiak, J. Mathews, Dispersion of liquefaction catalysts in coal using ionic liquids, Energy and Fuels, 24 (2010) 3086-3092.

[7] D. Smook, Removal of mineral material from solvent-refined coal by solvent extractions, Fuel Processing Technology, 88 (2007) 795-798.

[8] J. Ibarra, E. Munoz, R. Moliner, FTIR study of the evolution of coal structure during the coalification process, Organic Geochemistry, 24 (1996) 725-735.

[9] M. Sobkowiak, P. Painter, Determination of the aliphatic and aromatic CH contents of coals by FT-ir: studies of coal extracts, Fuel, 71 (1992) 1105-1125.

[10] I. K. Oikonomopoulos, M. Perraki, N. Tougiannidis, T. Perraki, M. J. Frey, P. Antoniadis, W. Ricken, A comparative study on structural differences of xylite and matrix

lignite lithotypes by means of FT-IR, XRD, SEM and TGA analyses: An example from the Neogene Greek lignite deposits, International Journal of Coal Geology, 115 (2013) 1-12.

[11] K. Miura, K. Mae, W. Li, T. Kusakawa, F. Morozumi, A. Kumano, Estimation of hydrogen bond distribution in coal through the analysis of OH stretching bands in diffuse reflectance infrared spectrum measured by in-situ technique, Energy and Fuels, 15 (2001) 599-610.

[12] H. Weingärtner, Understanding ionic liquids at the molecular level: Facts, problems, and controversies, Angewandte Chemie International Edition, 47 (2008) 654-670.

[13] N. V. Plechkova, K. R. Seddon, Applications of ionic liquids in the chemical industry, Chemical Society Reviews, 37 (2008) 123-150.

[14] J. S. Wilkes, A short history of ionic liquids—from molten salts to neoteric solvents, Green Chemistry, 4 (2002) 73-80.

[15] P. Painter, N. Pulati, R. Cetiner, M. Sobkowiak, G. Mitchell, J. Mathews, Dissolution and dispersion of coal in ionic liquids, Energy and Fuels, 24 (2010) 1848-1853.

[16] C. Hu, S. Jiang, Z. Wu, M. Miao, Influence of ionic liquids on the species and content of coal functional group, Electronic Journal of Geotechnical Engineering, 19 (2014) 1365-1375.

[17] O. O. Sonibare, T. Haeger, S. F. Foley, Structural characterization of Nigerian coals by X-ray diffraction, Raman and FTIR spectroscopy, Energy, 35 (2010) 5347-5353.

[18] L. Wang, Y. Xu, S. Jiang, M. Yu, T. Chu, W. Zhang, Z. Wu, L. Kou, Imidazolium based ionic liquids affecting functional groups and oxidation properties of bituminous coal, Safety Science, 50 (2012) 1528-1534.

[19] X. Li, J.-i. Hayashi, C.-Z. Li, FT-Raman spectroscopic study of the evolution of char structure during the pyrolysis of a Victorian brown coal, Fuel, 85 (2006) 1700-1707.

[20] T. Jawhari, A. Roid, J. Casado, Raman spectroscopic characterization of some commercially available carbon black materials, Carbon, 33 (1995) 1561-1565.

[21] P. R. Solomon, R. M. Carangelo, FT-ir analysis of coal: 2. Aliphatic and aromatic hydrogen concentration, Fuel, 67 (1988) 949-959.

[22] S. Maity, X-ray structural parameters of some Indian coals, Current Science, 91 (2006) 337-340.

[23] G. S. F. Tianbo, L. Yunyi, Application of ionic liquid [BMIm]BF_4 in swelling pretreatment of Shenhua coal [J], Coal Conversion, 2 (2010) 008.

[24] C. Min, G. Xiaohu, Z. Aiyun, M. Man, Swelling capacity of coal sample in ionic liquid, Coal Conversion, 32 (2009) 58-60.

[25] J. W. Kim, D. Kim, C. S. Ra, G. B. Han, N.-K. Park, T. J. Lee, M. Kang, Synthesis of ionic liquids based on alkylimidazolium salts and their coal dissolution and dispersion properties, Journal of Industrial and Engineering Chemistry, 20 (2014) 372-378.

[26] J. Cummings, K. Shah, R. Atkin, B. Moghtaderi, Physicochemical interactions of ionic liquids with coal; the viability of ionic liquids for pre-treatments in coal liquefaction, Fuel, 143 (2015) 244-252.

[27] S. Bhoi, D. Dey, T. Banerjee, K. Mohanty, Solid–liquid equilibria predictions for the dissolution of brown coal in ionic liquids using a continuum solvation model, Fuel Processing Technology, 126 (2014) 112-121.

[28] D. ASTM, 3173-87: Standard test method for moisture in the analysis sample of coal and coke, Gaseous Fuels Coal Coke, 5 (1989) 300.

[29] D. ASTM, 3175-89: Standard test method for moisture in the analysis sample of coal and coke, Gaseous Fuels Coal Coke, 5 (1989) 305.

[30] T. K. Green, J. Kovac, J. W. Larsen, A rapid and convenient method for measuring the swelling of coals by solvents, Fuel, 63 (1984) 935-938.

[31] J. Coates, Interpretation of infrared spectra, a practical approach, Encyclopedia of Analytical Chemistry, (2000).

[32] W. Rasband, ImageJ. US National Institutes of Health, Bethesda, MD, 1997.

[33] T. Ferreira, W. Rasband, ImageJ user guide, IJ1. 46r. Natl. Inst. Health, Bethesda, MD. http://rsb.info.nih.gov/ij/docs/guide/user-guide.pdf, (2012).

[34] M. D. Abràmoff, P. J. Magalhães, S. J. Ram, Image processing with ImageJ, Biophotonics International, 11 (2004) 36-42.

[35] P. Painter, P. Opaprakasit, A. Scaroni, Ionomers and the structure of coal, Energy and Fuels, 14 (2000) 1115-1118.

[36] P. Opaprakasit, A. W. Scaroni, P. C. Painter, Ionomer-like structures and π-cation interactions in Argonne Premium coals, Energy and Fuels, 16 (2002) 543-551.

[37] S. Bhoi, T. Banerjee, K. Mohanty, Insights on the combustion and pyrolysis behavior of three different ranks of coals using reactive molecular dynamics simulation, RSC Advances, 6 (2016) 2559-2570.

[38] H. Hu, G. Sha, G. Chen, Effect of solvent swelling on liquefaction of Xinglong coal at less severe conditions, Fuel Processing Technology, 68 (2000) 33-43.

[39] F. Pinto, I. Gulyurtlu, L. Lobo, I. Cabrita, Effect of coal pre-treatment with swelling solvents on coal liquefaction, Fuel, 78 (1999) 629-634.

[40] F. P. Miknis, D. A. Netzel, T. F. Turner, J. C. Wallace, C. H. Butcher, Effect of different drying methods on coal structure and reactivity toward liquefaction, Energy and Fuels, 10 (1996) 631-640.

[41] P. J. Hall, H. Marsh, K. M. Thomas, Solvent induced swelling of coals to study macromolecular structure, Fuel, 67 (1988) 863-866.

[42] W. Zhang, F.-g. Zeng, FTIR analysis of hydrogen bond in middle maturate coals, Journal-Taiyuan University of Technology, 36 (2005) 545.

[43] R. Kaji, Y. Hishinuma, Y. Nakamura, Low temperature oxidation of coals: Effects of pore structure and coal composition, Fuel, 64 (1985) 297-302.

[44] J. G. Speight, The Chemistry and Technology of coal, CRC Press2012.

[45] Technical Guidelines Manuals in Coke Oven Plants, Ministry of Environment Government of India, August 2010.

[46] R. P. Swatloski, S. K. Spear, J. D. Holbrey, R. D. Rogers, Dissolution of cellose with ionic liquids, Journal of the American Chemical Society, 124 (2002) 4974-4975.

5.1 Introduction

The kinetic model is an important tool to understand and predict the combustion properties of fuels as thermal degradation and kinetic studies are two important factors during the initial steps of coal conversion. A large number of pyrolytic reactions take place during the coal combustion; hence it is very difficult to analyze its kinetics. Thermal stability can be observed by using a simultaneous Thermogravimetric Analyzer (TGA). During thermal analysis, kinetic parameters such as activation energy (E_a), and pre-exponential factor (A) can be predicted by TGA method. Researchers assumed that the first order reaction following an Arrhenius-type equation is the simplest method to describe the thermal degradation of coal [1, 2].

The pyrolysis of coal mainly takes place in three different stages, namely (a) first stage: low temperature for the removal of moisture, (b) devolatilisation: the removal of volatile and mineral matters, and (c) slowest process: liberate gaseous molecules and char formation [3]. Heydari et al. [4] reported a kinetic study of Canadian coal by using the Thermogravimetric Analyzer. From their analysis, the interactions of coal/ILs failed to alter the thermal and physical properties of coal. Some of the IL's were found to effectively destroy the more active groups of coal and hence improve the exothermic oxidation. The chapter mainly focuses on the effects of ionic liquids (ILs) and mixed solvents (IL + solvent) on the coal oxidation process and its associated morphological changes observed before and after thermal treatment. Two important kinetic parameters such as; activation energy (E_a) and pre-exponential factor (A) were considered for the thermal degradation study of untreated, IL-pre-treated, and a mixed solvent (IL + solvent) treated coal.

5.2 Experimental Analysis

The preparation methods for IL-pre-treated coals were briefly described in the previous chapter 4 in section 4.2 [5], hence it is not discussed here. The proximate and elemental analysis data of raw coal is available in Table 4.1 (Chapter 4). In this study, three ionic liquids (ILs) namely: 1-butyl-3-methylimidazolium hexafluorophosphate [BMIM][PF_6], 1-butyl-1-methylpyrrolidinium methyl carbonate [BMPYR][CH_3CO_3], and 1-butyl-4-methylpyridinium tetrafluoroborate [BMPY][BF_4], along with one conventional solvent i.e. pyridine were used as mixed solvents (Table 5.1). The proximate and elemental analysis of [BMPYR][CH_3CO_3] + pyridine beneficiated coal given in Table 5.2.

Table 5.1 Ionic Liquids and Conventional Solvent used in this Study

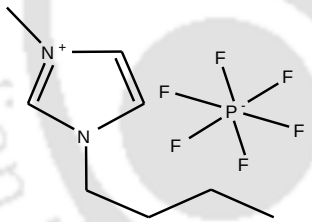 1-butyl-3-methylimidazolium hexafluorophosphate, [BMIM][PF_6]	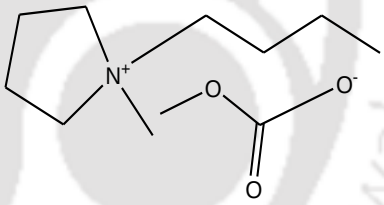 1-butyl-1-methylpyrrolidinium methyl carbonate, [BMPYR][CH_3CO_3]
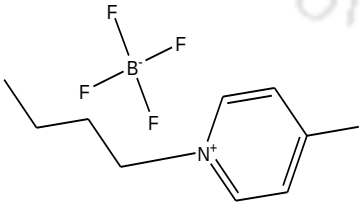 1-butyl-4-methylpyridinium tetrafluoroborate, [BMPY][BF_4]	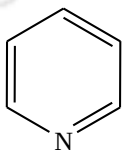 Pyridine [C_5H_5N]

Table 5.2 Proximate and Ultimate Analysis of Mixed Solvent pre-treated Coal Samples

[BMPYR][CH_3CO_3]+ pyridine pre-treated Coal Samples	Coal 1+ mixed solvent	Coal 2+ mixed solvent	Coal 3+ mixed solvent
Proximate Analysis (wt.%)			
Moisture	3.20	3.15	5.61
Ash	25.62	41.22	19.23
Volatile Matter	20.86	19.76	41.01
Fixed Carbon	50.32	35.87	34.15
Ultimate Analysis (wt.%)			
Carbon	60.13	57.18	63.73
Hydrogen	2.86	4.02	5.21
Nitrogen	1.28	1.63	2.22
Oxygen	35.73	37.17	28.84

5.2.1 Experimental Methods

The coal samples were initially dried at a temperature of 50 °C for 24 h. The dried coal samples and ILs were mixed at a ratio of 1g: 2mL. The mixture was then immersed in an oil bath for 4 h at a temperature of 100 °C. On a similar manner, the mixture of coal + IL + pyridine was also prepared at a respective ratio of 1g: 2mL: 2mL and immersed in the oil bath at the identical condition. The experiments with pyridine were conducted to observe the effect of co-solvents with IL's. The samples were then washed several times with deionized water for the removal of ILs from the coal surface. The coal samples were then washed and dried in a vacuum drying oven for 72 h at 60 ºC. The morphology studies were conducted prior and after the thermal treatment of coal and mixed solvents (IL + pyridine) by an optical

microscope (Leica DM750M). The microscopic view (200X magnifications) will eventually determine the difference between shape and size of raw and mixed solvents pre-treated coals.

Swelling ratio (Q) is another important descriptor for the dissolution study, which is exemplified as the ratio of final volume to the initial volume of the mixture [6]. For the swelling study, a particular ratio of coal and solvent were taken in a centrifuge tube. The initial volume (v_1) was measured by mixing the coal/solvent solution. The final volume (v_2) was then measured by centrifuging the equilibrate mixture solution for 5-10 min. A swollen part of coal was observed at the top of the surface. The mixture solution was then separated using a centrifugal separator. After the separation, the residue was collected and multiple washing was performed. The residue was then dried in a vacuum drying oven for further analysis. The extract yield was calculated by equation (5.1).

$$Extract\,Yield\,(wt.\%) = \frac{Mass\,of\,[coal\,sample - residue](g)}{Mass\,of\,coal\,sample\,(g)} \times 100 \qquad (5.1)$$

Thermal analyses were carried out using a Thermogravimetric Analyzer (TGA) (*Mettler Toledo, Switzerland; TGA851e/LF/1100)*. Around <10 mg coal powder (~500 µm) were placed in an alumina crucible. The samples were exposed to a nitrogen atmosphere at a flow rate of 60 ml/min. The non-isothermal thermogravimetric analyses were then recorded. All the experiments were performed at a temperature range of 303-1123 K with a heating rate of 10 K/min. The heating rates of coal and the inert environment were set based on the previous studies [4, 7]. The mass loss rate was measured by TG curve; whereas, the derivative of mass change was calculated by DTG curve [2]. To obtain an accurate result, all the experiments were repeated three times.

5.2.2 Kinetic Study

The pyrolysis of coal can be described by the Arrhenius expression which correlates the mass loss (TGA) and its derivative (DTG) with respect to temperature. By using Arrhenius equation and assuming that the reaction is of the first order; kinetic parameters such as activation energy (E_a) and pre-exponential factor (A) can be calculated. Arrhenius equation is written as:

$$k(T) = Ae^{-\frac{E_a}{RT}} \tag{5.2}$$

where $k(T)$, A, E_a, R, and T are temperature dependent reaction rate constant, pre-exponential factor (min^{-1}), activation energy (kJ/mol), universal gas constant (kJ/mol. K), and temperature (K) respectively. The general expression for a solid compound is:

$$\frac{d\alpha}{dt} = k(T)\, f(\alpha) \tag{5.3}$$

where $d\alpha/dt$ is non-isothermal reaction rate, α is the loss of mass fraction or mass loss ratio. $f(\alpha)$ is a function of α which depends on the reaction mechanism. Conversion of α in terms of change of mass of coal can be represented by:

$$\alpha = \frac{m_i - m_t}{m_i - m_f} \tag{5.4}$$

where m_i, m_f, and m_t are the initial mass, final mass, and mass at time t for the coal sample after thermogravimetric analysis. Equation (5.3) can be rewritten as;

$$\frac{d\alpha}{dt} = Ae^{-\frac{E_a}{RT}} f(\alpha) \tag{5.5}$$

For the coal pyrolysis, the conversion function can be written as $f(\alpha) = (1-\alpha)^n$, where *n* is the order of reaction. Now equation (5.5) can be written as;

$$\frac{d\alpha}{dt} = Ae^{-\frac{E_a}{RT}} (1-\alpha)^n \tag{5.6}$$

The kinetic studies for solid compounds are usually conducted under non-isothermal condition at constant heating rate due to the scarcity of experimental data when compared to isothermal conditions. Equation (5.6) hence takes the form:

$$\frac{d\alpha}{dT}.\frac{dT}{dt} = Ae^{-\frac{E_a}{RT}} (1-\alpha)^n \tag{5.7}$$

$$\frac{d\alpha}{dT} = \frac{A}{\beta} e^{-\frac{E_a}{RT}} (1-\alpha)^n \tag{5.8}$$

where $\beta \left({}^{dT}\!/_{dt} \right)$ is the heating rate constant. Now, integrating equation (5.8) using Coats-Redfern method [8], we get:

$$\int_0^{\alpha} \frac{d\alpha}{(1-\alpha)^n} = \int_{T_0}^{T} \frac{A}{\beta} e^{-\frac{E_a}{RT}} dT \tag{5.9}$$

$$\ln\left[-\ln(1-\alpha)/T^2 \right] = \ln\left[{}^{AR}\!/_{\beta E_a (1-2RT/E_a)} \right] - {}^{E_a}\!/_{RT} \tag{5.10}$$

The term $\ln\left[AR/\beta E_a\left(1-2RT/E_a\right)\right]$ is a constant and the plot of $\ln\left[-\ln\left(1-\alpha\right)/T^2\right]$ vs. $1/T$ should give a straight line, from which the values of E_a and A can be calculated [9].

5.3 Results and Discussions

5.3.1 Yield Extraction and Swelling Studies

Swelling ratio and extract yield of three different coals are shown in Fig. 5.1. It is observed that [BMPYR][CH_3CO_3]-pre-treated coal gave a swelling ratio (Q) of 1.43, 1.31, and 1.27 for coal-1, coal-2, and coal-3 respectively. For coal-1 the swelling ratio of [BMPYR][CH_3CO_3] (Q=1.43) pre-treated coal is higher than [BMIM][PF_6] (Q=1.14) and [BMPY][BF_4] (Q=1.1.12). Hence [BMPYR][CH_3CO_3] has the highest magnitude of coal/ILs interactions. This is true as higher the interaction, weaker the strength of the bonds within the coal particles [10].

For IL + pyridine, swelling ratio is found to be higher when compared to IL-pre-treated coal. The swelling ratio results for the mixed solvent is then compared with ILs and shown in Fig. 5.1. The increment of swelling ratio for mixed solvents might be due to the additional interaction between the mixed solvent and coal macromolecular network. Therefore, the coal-coal macromolecular interactions are further weakened resulting in the improvement of swelling ratio. This is inline with the studies concerning the enhancement of coal macro-pores and dispersion characteristics from previous experiments [11, 12]. As reported for individual IL, the swelling ratio of coal-1 is the highest for mixed solvent [BMPYR][CH_3CO_3] + pyridine.

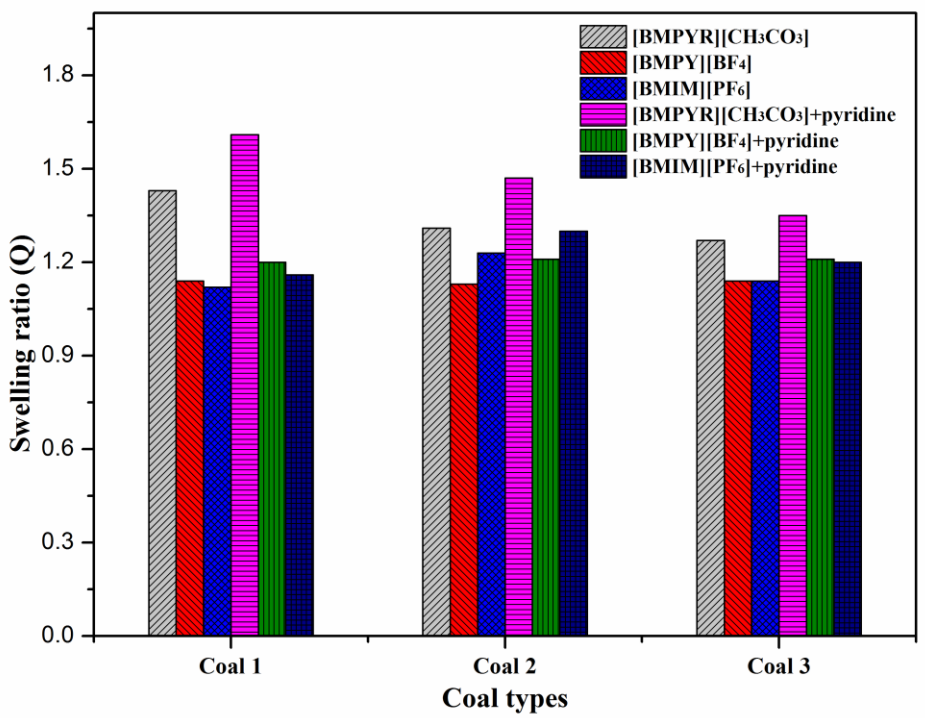

Fig. 5.1 Swelling ratios (Q) of mixed solvent and IL-pre-treated coal 1-3

Extract yields of IL-pre-treated and mixed solvent pre-treated coals are shown in Fig. 5.2. It is observed from Fig. 5.2 that the extraction yield of mixed solvent is higher when compared to individual IL-pre-treated coal. Painter et al. [13] reported mixed solvent such as; [BMIM][Cl]+NMP and [BMIM][Cl]+pyridine which gave a higher extract yield as compared to ILs and conventional solvents. The [BMPYR][CH_3CO_3]-pre-treated coals gave an extract yield of 24.76, 27.41, and 23.03 wt.% for coal-1, coal-2, and coal-3 respectively. The mixed solvent, [BMPYR][CH_3CO_3] + pyridine pre-treated coal gave an extract yield of 29.16, 32.31, and 25.05 wt.% for coal-1, coal-2, and coal-3 respectively. This is higher as compared to explicit IL-pre-treated coal. The mixed solvents followed the order: [BMPYR][CH_3CO_3] > [BMPY][BF_4] > [BMIM][PF_6]. From these studies, it is envisaged that the IL [BMPYR][CH_3CO_3] gave a high extract yield due to a large charge density of its

anion [CH_3CO_3] being able to favourably interact with the reactive site of coal macromolecular networks [14].

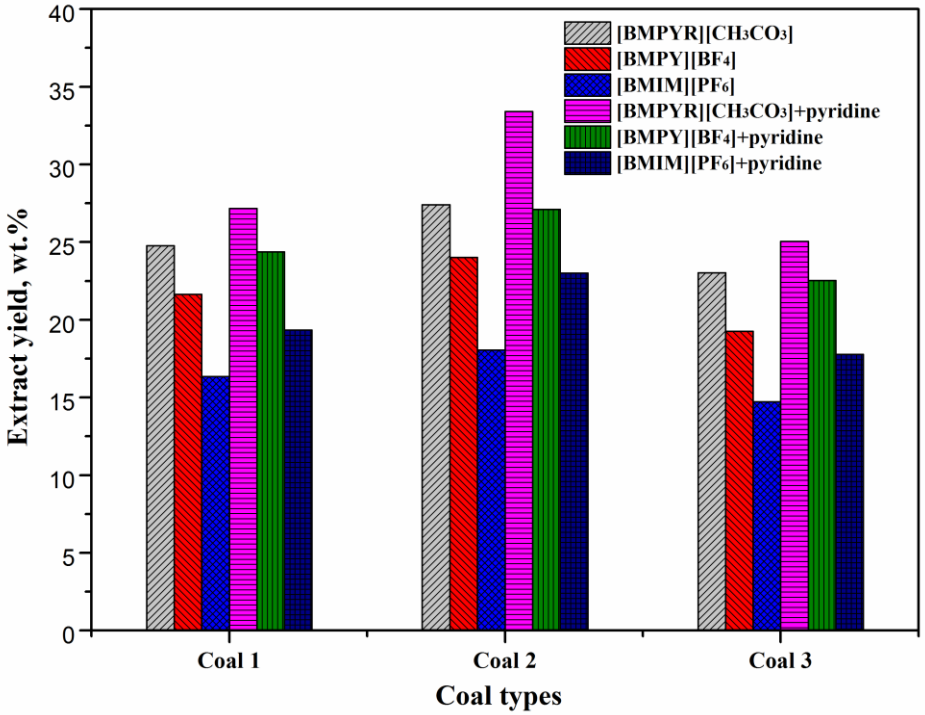

Fig. 5.2 Extract yield (wt.%) of mixed solvent and IL-pre-treated coal 1-3

5.3.2 Thermal Degradation Study

Fig. 5.3 to Fig. 5.5 shows a representative plot of TG/DTG curves. From the DTG curve, it is observed that initially moisture is removed within a range 30-200 °C. Similar peaks are also observed in ILs and mixed solvent pre-treated coal. The IL-pre-treated coal samples (coal-2 and coal-3) then displays the presence of evolution peaks within a temperature range of 200-350 °C due to the liberation of light molecular weight hydrocarbons [15], whereas; in the case of untreated coal, these peaks were absent. Similarly, IL-pre-treated coal samples displayed peaks within a temperature range of 350-650 °C that is due to the release of heavy hydrocarbons and volatile matter [15]. Hence, this observation confirms that during pyrolysis, coal samples releases both low and high

molecular weight hydrocarbons as well as valuable intermediates. This also agrees well with Reactive Force Field Simulations as outlined in chapter 2 [16, 17]. From this observation, mixed solvent, as well as IL-pre-treated coal would possibly increase the liquefaction performance by the swelling and fracture of coal.

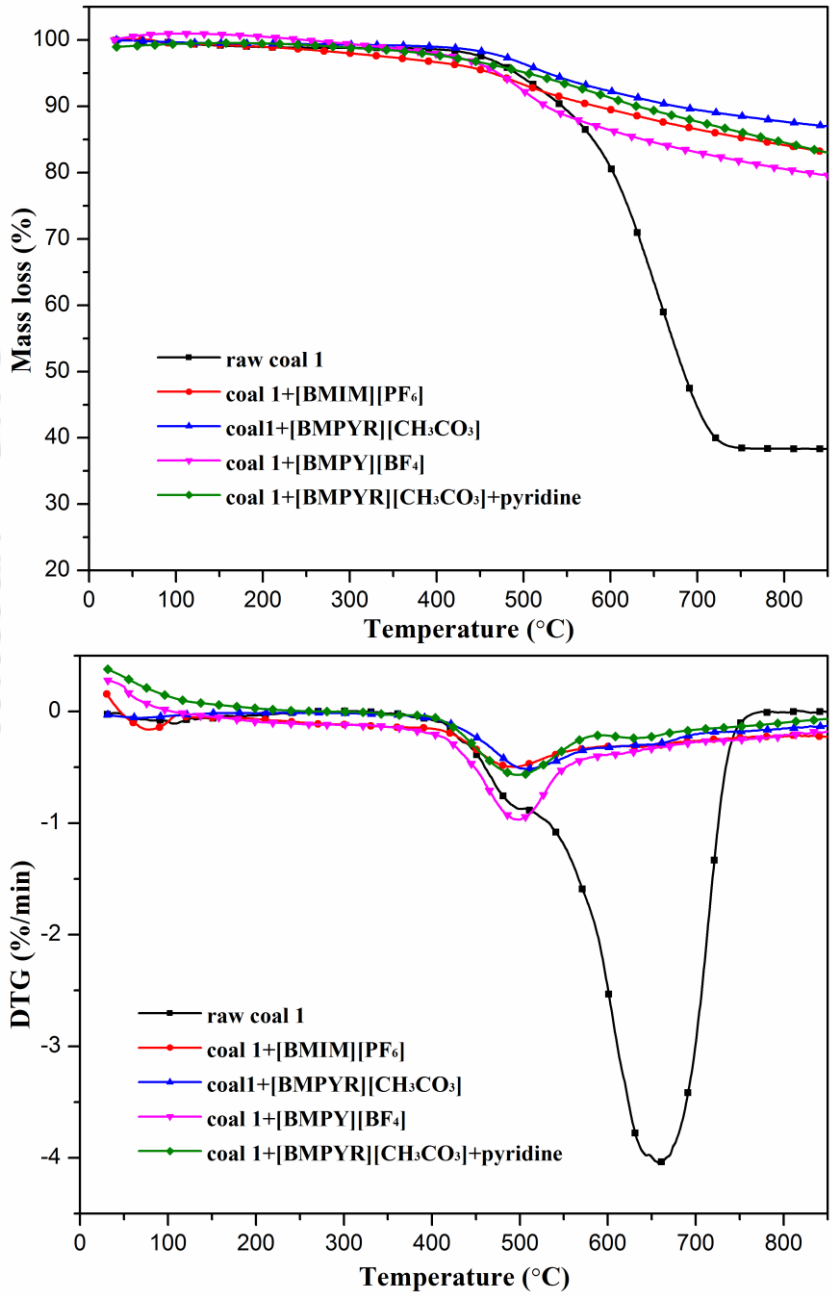

Fig. 5.3 TG/DTG plot of raw coal, mixed solvent and IL-pretreated coal-1

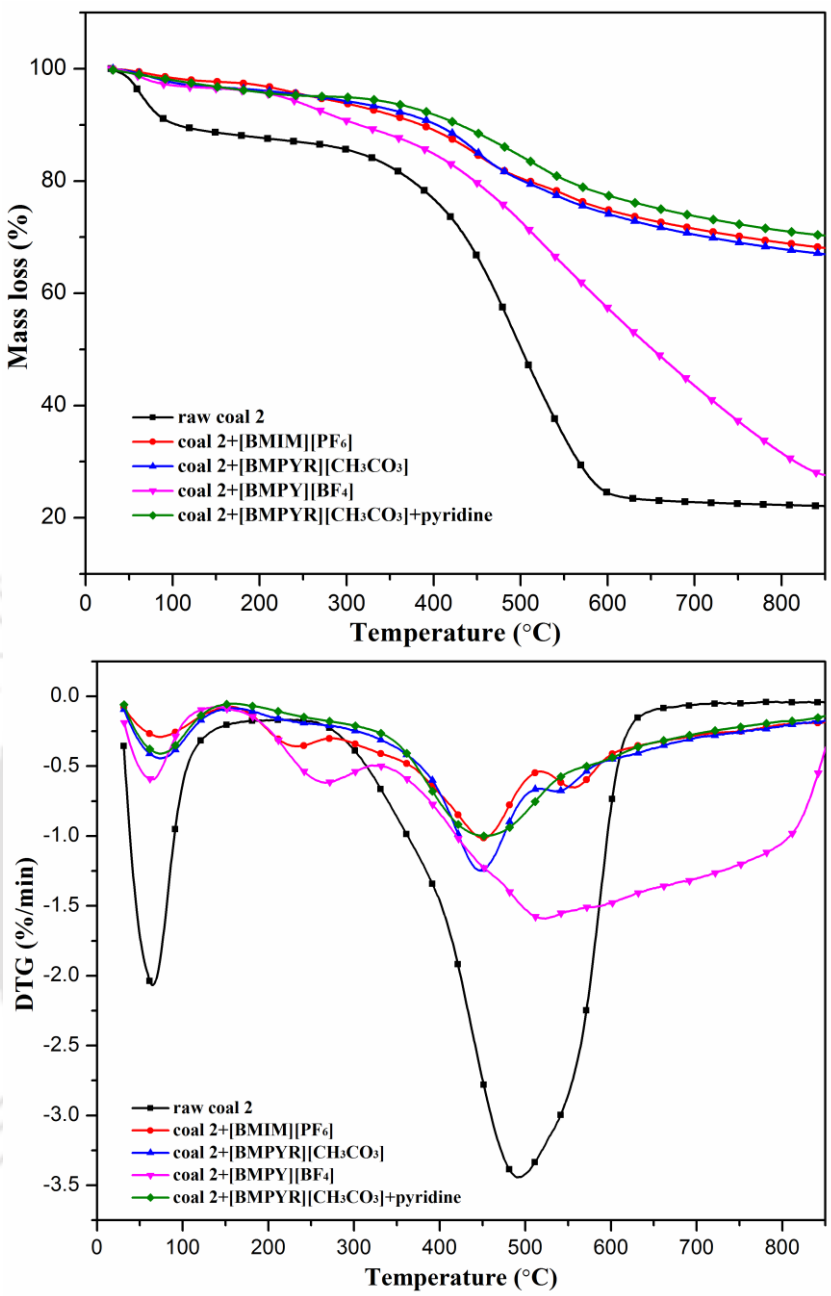

Fig. 5.4 TG/DTG plot of raw coal, mixed solvent and IL-pretreated coal-2

TGA curves show a firm decline in the mass loss with respect to temperature. An extensive amount of weight loss occurs in the raw coal which is around 59.02, 58.03, and 56.50 % for coal-1, coal-2, and coal-3 respectively at a temperature range of around 350-730°C. This is due to the presence of groups such as hydroxyls, carboxyl, and phenol based in the raw coal molecules [7]. However, lower mass is lost for both mixed solvent and IL-

pretreated coal (Table 5.3). The TGA/DTG plots show that the mass loss of both mixed solvent and IL pre-treated coal sample is approximately linear. The proximate analysis results also confirm the same (Table 5.2). The proximate and ultimate analyses data for ionic liquids (Table 4.6) are reported in the previous chapter 4 [5].

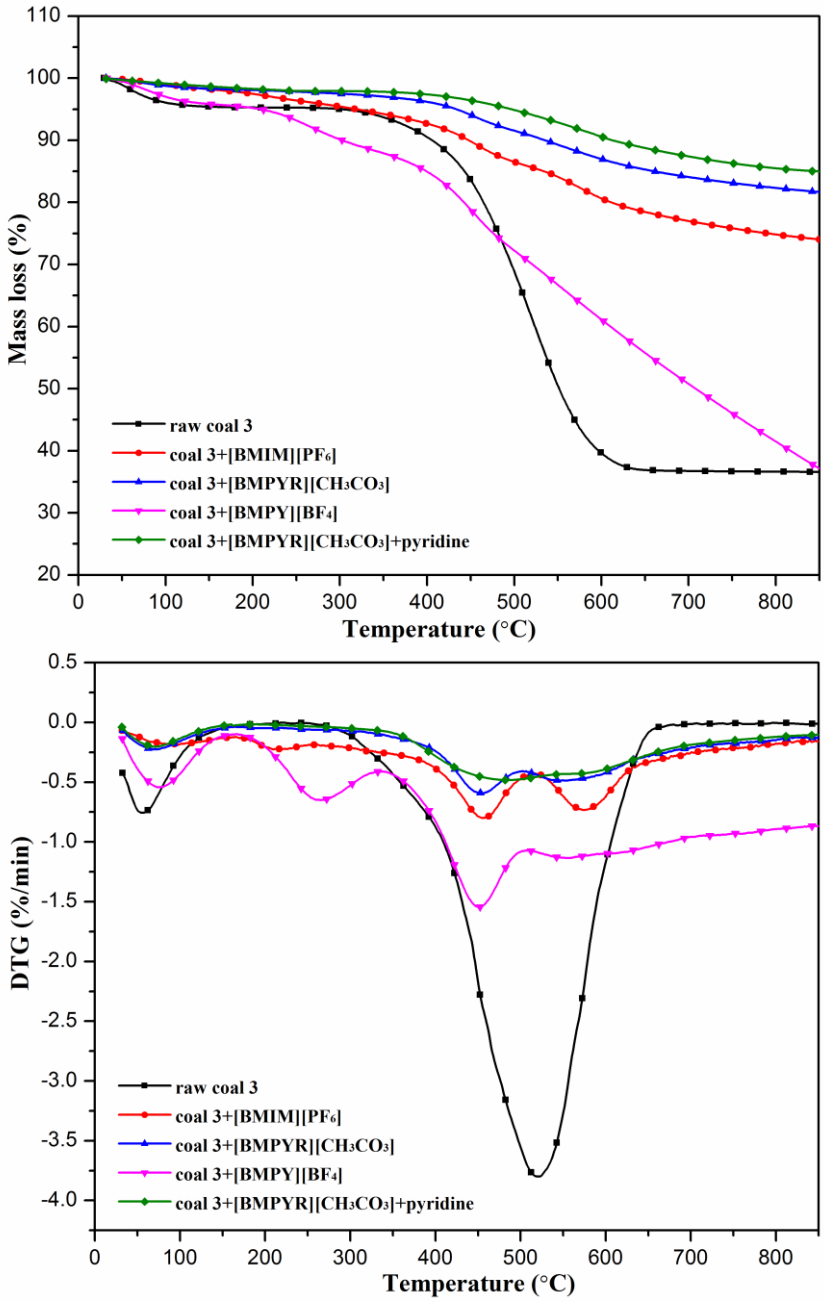

Fig. 5.5 TG/DTG plot of raw coal, mixed solvent and IL-pretreated coal-3

Thus, in summary, the idea for such an exercise was to confirm that in comparison with IL-pretreated coals, raw coal contains a lesser amount of carbon and a high proportion of oxygen and hydrogen (Table 5.1 and Table 5.2). This causes the reduction of heating or calorific value due to the lesser energy present in C–O, and C–H bonds as compared to C–C bonds [18]. As a result, coal-1 pretreated with [BMPY][BF_4], [BMIM][PF_6], [BMPYR][CH_3CO_3], and [BMPYR][CH_3CO_3] + pyridine gave a mass loss of 14.85, 10.25, 9.75, and 10.19 % of mass respectively.

Table 5.3 Mass Loss (%) Analysis of Three Different Coals

Coal Sample/Temperature (°C)	31-350	350-430	430-730
raw coal 1	1.18	0.68	59.01
coal 1+[BMPY][BF_4]	1.26	1.47	14.86
coal 1+[BMIM][PF_6]	2.64	1.24	10.25
coal 1+[BMPYR][CH_3CO_3]	1.18	0.06	9.75
coal 1+[BMPYR][CH_3CO_3]+pyridine	0.24	1.61	10.19
Temperature (°C)	31-200	200-350	350-600
raw coal 2	11.87	5.43	58.03
coal 2+[BMPY][BF_4]	3.65	8.17	30.64
coal 2+[BMIM][PF_6]	2.74	5.43	16.64
coal 2+[BMPYR][CH_3CO_3]	3.65	3.3	18.77
coal 2+[BMPYR][CH_3CO_3]+pyridine	3.59	2.39	16.73
Temperature (°C)	31-200	200-350	350-630
raw coal 3	4.59	1.65	56.49
coal 3+[BMPY][BF_4]	4.59	7.42	30.12
coal 3+[BMIM][PF_6]	2.39	3.29	15.01
coal 3+[BMPYR][CH_3CO_3]	1.84	1.09	11.16
coal 3+[BMPYR][CH_3CO_3]+pyridine	1.48	0.57	8.45

Fig. 5.3 to Fig. 5.5 also shows the TG/DTG plot of coal-1, coal-2, and coal-3 respectively. A drastic mass loss is seen to occur from the temperature range of 430-730 ºC. This is the temperature where devolatilization takes place in the respective coal. The shift in temperature for mixed solvent and IL-pretreated coal indicates that IL's and IL + pyridine are indeed successful in disintegrating the cross-linked network of coal [13, 19, 20]. From the TG results, the lowest weight loss was observed for both [BMPYR][CH_3CO_3] and [BMPYR][CH_3CO_3] + pyridine pre-treated coal. It implies that a mixture of pyridine with ILs might be additionally effective toward the removal of coal containing functional groups even though this is not experimentally confirmed.

5.3.3 Morphological Studies

Fig. 5.6 to Fig. 5.8 provides the microscopic images for coal 1-3 before and after pre-treatment with mixed solvents (IL + pyridine). From Fig. 5.6 (coal-1), it is observed that a fairly large fraction of coal molecules fragments after the IL + pyridine pre-treatment. This is also briefly described in Chapter 4 for coal/ILs [5] where we have analysed the same with dissolution using Ionic Liquids. Raw coal-1 (Fig. 5.6a) is seen to possess an average particle size of 500 μm. This implies that the particles sizes remain unchanged after coal particles are smeared into water. However, this size gets reduced with IL + solvent. Fig. 5.6b illustrates a reduction to 100-200 μm after the coal are treated with [BMIM][PF_6] + pyridine. [BMPY][BF_4] + pyridine and [BMPYR][CH_3CO_3] + pyridine are seen to fragment the coal particles to a larger extent and sizes up to 50-100 μm are obtained. In summary, the dispersion of mixed solvent pretreated coal is higher as compared to IL-pretreated coal [5]. The fragmentation is mainly due to the additional interaction of mixed solvents with coal-

coal network along with the weakening of the hydrogen bonding networks. As a result, an increase in the surface area of coal makes the surface appear with a finer texture [13].

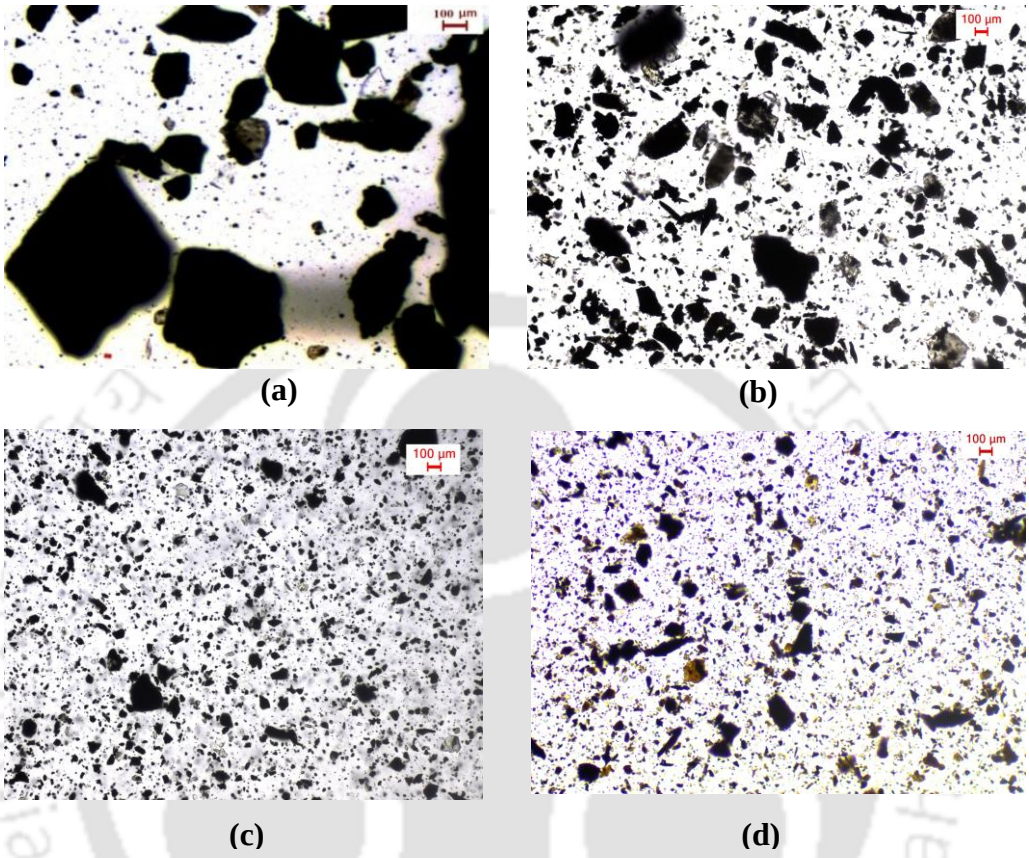

Fig. 5.6 Optical micrograph (200X) of coal 1 smeared in (a) water and after heating at 100^{o}C with (b) [BMIM][PF_6]+pyridine (c) [BMPY][BF_4]+pyridine (d)[BMPYR][CH_3CO_3]+pyridine

It is evident that [BMIM][PF_6] + pyridine and [BMPY][BF_4] + pyridine treated coal gets fractured till a particle size of 10-50 µm (Fig. 5.7b and Fig. 5.7c). [BMPYR][CH_3CO_3] + pyridine treated coal (Fig. 5.7c) gave a uniform particle size (~5-10 µm) with finer texture. Similarly, Fig. 5.8 exhibits the microscopic images for coal-3 before and after thermal treatment. A huge fragmentation is perceived after [BMPYR][CH_3CO_3] + pyridine pre-treatment. The size of coal particles is seen to reduce to around <10 µm. A similar

insight on coal morphology with IL is also reported by other researchers [13, 21], as well as from our previous chapter 4 [5].

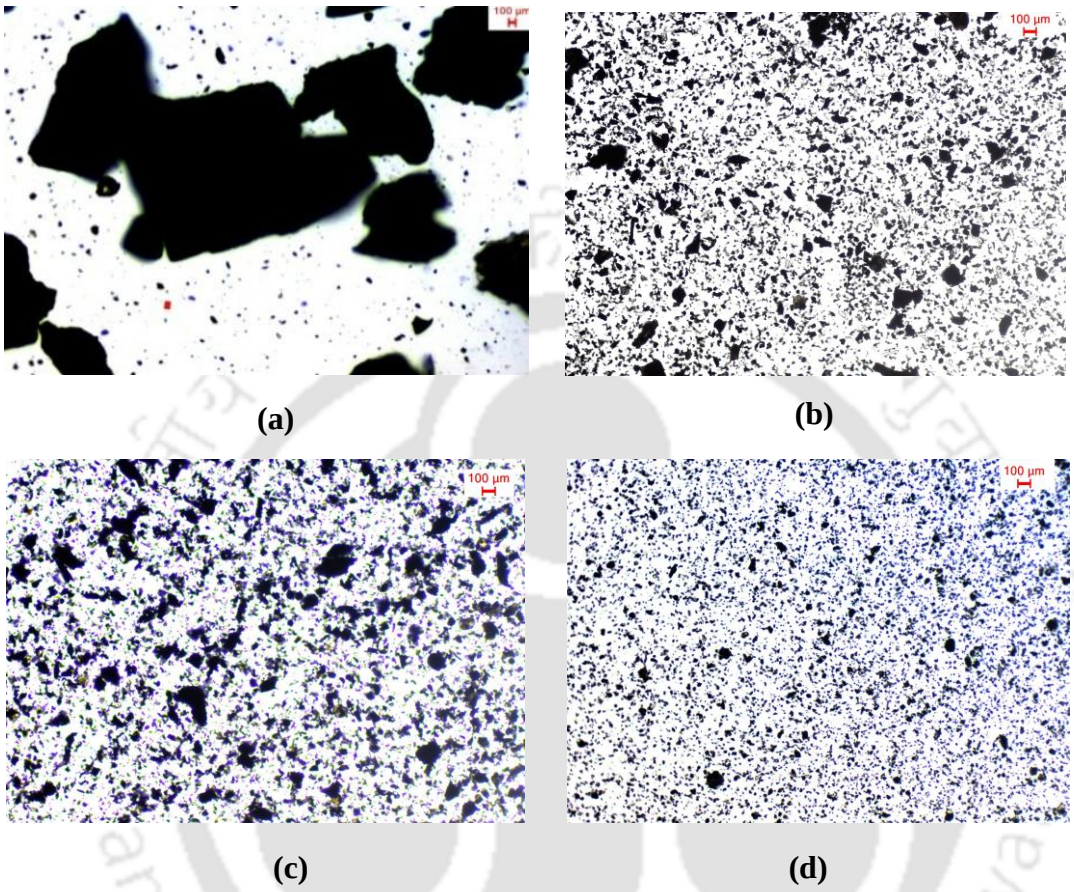

Fig. 5.7 Optical micrograph (200X) of coal 2 smeared in (a) water and after heating at 100^{o}C with (b) [BMIM][PF_6]+pyridine (c) [BMPY][BF_4]+pyridine (d)[BMPYR][CH_3CO_3]+pyridine

5.3.4 Kinetic Parameters

From the TGA analysis, kinetic parameters for untreated, mixed solvents, and IL-pretreated coal were calculated using equation (5.10). The plot between $\ln\left[-\ln\left(1-\alpha\right)/T^2\right]$ and $1/T$ gave a straight line, which is evident from Fig. 5.9 to Fig.

5.11. The activation energy (E_a) and pre-exponential factor (A) are listed in Table 5.5. The correlation coefficient (R^2) value indicate that the equations are linear.

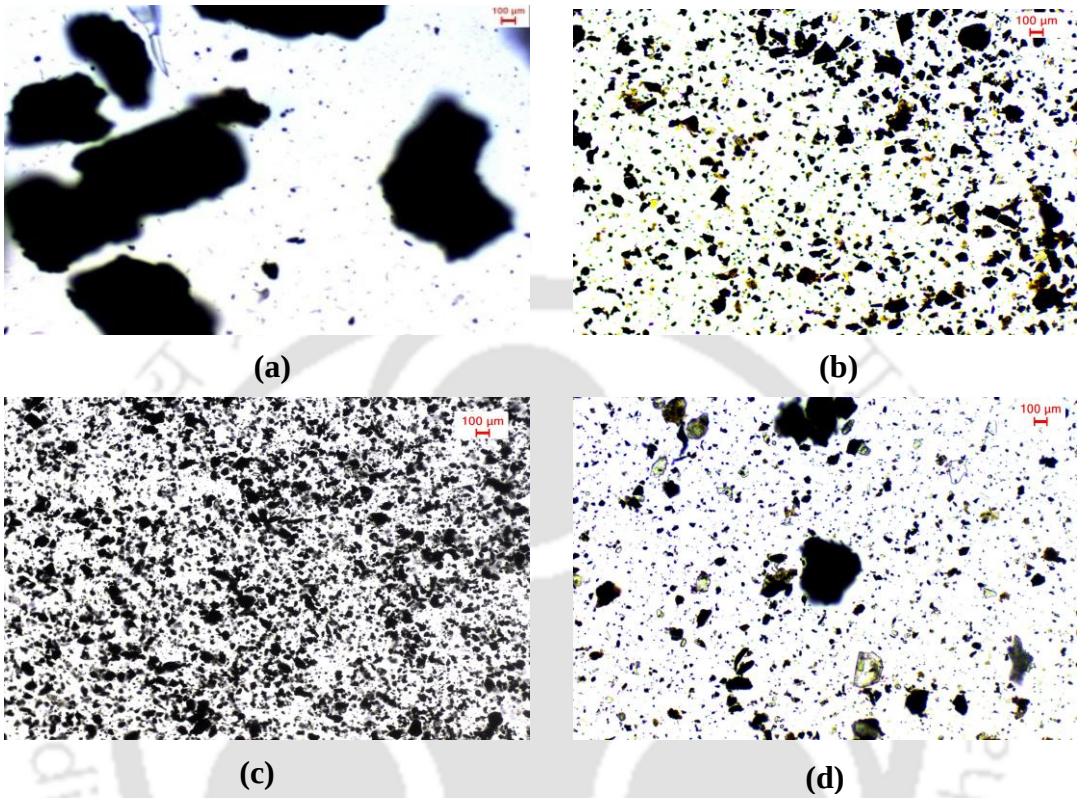

Fig. 5.8 Optical micrograph (200X) of coal 3 smeared in (a) water and after heating at 100°C with (b) [BMIM][PF_6]+pyridine (c) [BMPY][BF_4]+pyridine (d)[BMPYR][CH_3CO_3]+pyridine

The kinetic parameters listed in Table 5.4 shows that the values of activation energy are higher for the untreated coal as compared to that of mixed solvent or IL-pretreated coal. The values of activation energy for untreated coal 1-3 are 40.71, 42.25, and 67.78 kJ/mol, respectively, whereas for IL-pretreated coal, the activation energy is within a range of 12.14-39.34 kJ/mol. Similarly, an activation energy of 20.674, 17.761, and 15.468 kJ/mol were found for coal 1-3 treated with mixed solvent ([BMPYR][CH_3CO_3] + pyridine). Following a similar trend, untreated coal requires high activation energy to fragment the coal

macromolecular structure. Dameng et al. [22] also reported a higher activation energy for a low-rank coal (less carbon) when compared to high-rank coal. This is due to the fact that a low-rank coal requires higher energy to activate the atoms and molecules so as to undergo a chemical reaction. Table 5.2 (CHNS analysis) also confirms a similar trend where we observe an increase in the fixed carbon content with mixed solvent pre-treated coal.

Table 5.4 Kinetic Parameters of Three Different Coals

Coal Sample	E_a (kJ/mole)	Correlation coefficient R^2	A(min^{-1})
raw coal 1	67.78	0.992	1.8E+07
coal 1+[BMPY][BF_4]	36.40	0.928	2.6E+09
coal 1+[BMIM][PF_6]	29.47	0.858	3.2E+09
coal 1+[BMPYR][CH_3CO_3]	15.98	0.923	3E+10
coal 1+[BMPYR][CH_3CO_3]+pyridine	20.67	0.996	2E+10
raw coal 2	42.25	0.958	4.7E+07
coal 2+[BMPY][BF_4]	19.32	0.991	3.4E+09
coal 2+[BMIM][PF_6]	12.86	0.939	2.9E+10
coal 2+[BMPYR][CH_3CO_3]	17.84	0.942	7E+09
coal 2+[BMPYR][CH_3CO_3]+pyridine	17.76	0.997	2E+10
raw coal 3	40.71	0.964	1.5E+08
coal 3+[BMPY][BF_4]	17.34	0.966	1.8E+10
coal 3+[BMIM][PF_6]	12.14	0.976	7.1E+10
coal 3+[BMPYR][CH_3CO_3]	14.79	0.972	8.6E+09
coal 3+[BMPYR][CH_3CO_3]+pyridine	15.47	0.909	2E+10

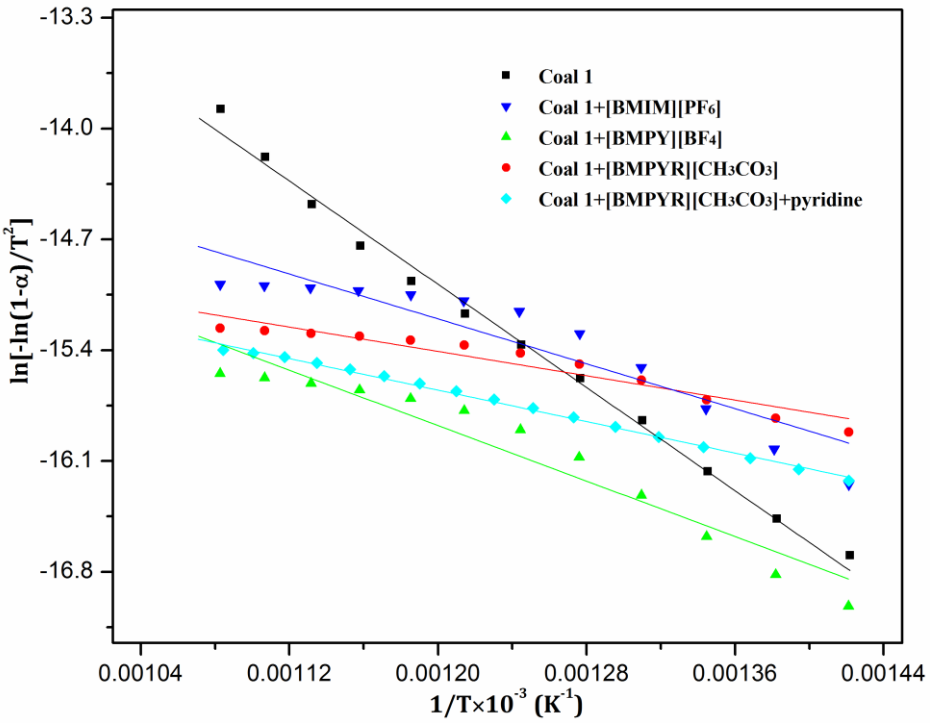

Fig. 5.9 Arrhenius plot of raw coal, mixed solvent and IL-pretreated coal-1

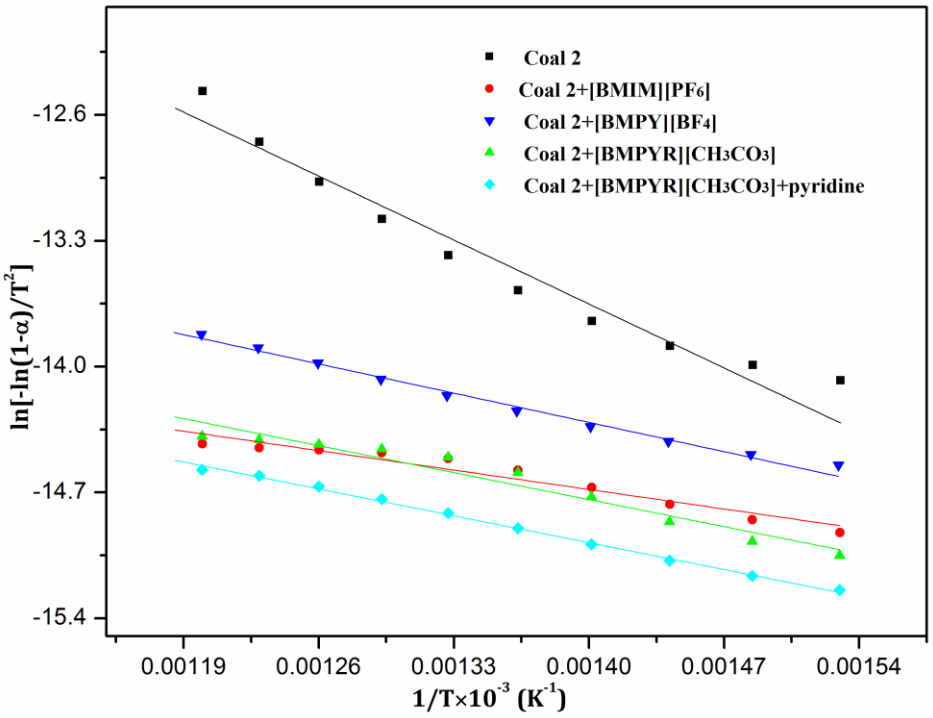

Fig. 5.10 Arrhenius plot of raw coal, mixed solvent and IL-pretreated coal-2

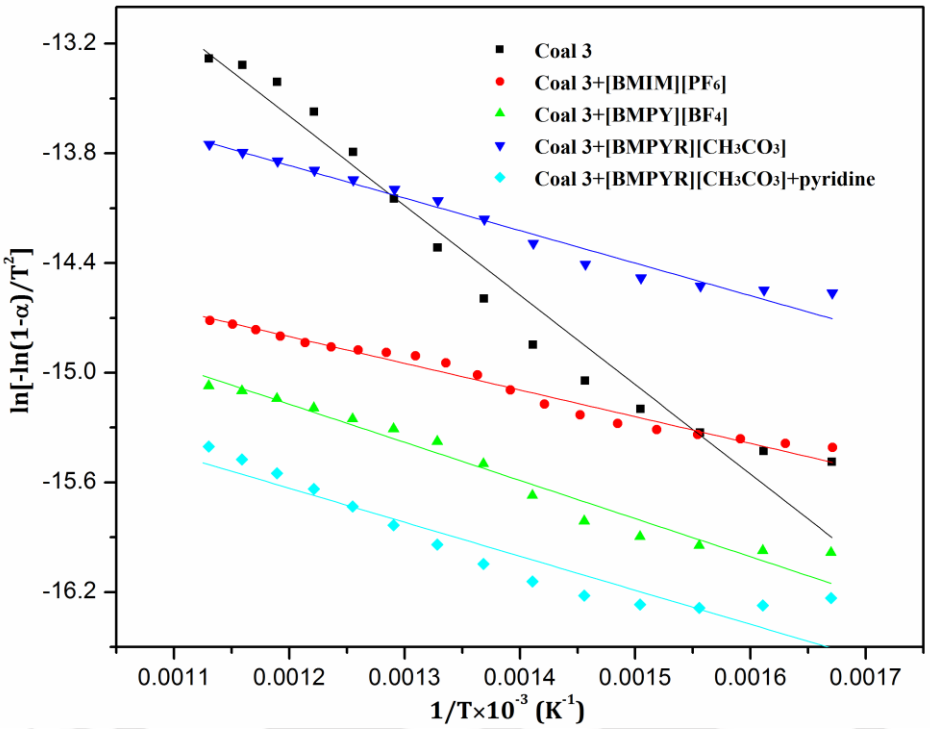

Fig. 5.11 Arrhenius plot of raw coal, mixed solvent and IL-pretreated coal-3

It is also observed that a high swelling ratio of coal exhibits a lower energy for the fragmentation of the coal molecules. This may be due to the fact that a coal with large pore size requires a lower energy barrier to fragment and swell coal structure [23, 24]. From Fig. 5.1, it is observed that the swelling ratio is the highest for [BMPYR][CH_3CO_3] and [BMPYR][CH_3CO_3] + pyridine pretreated coals and this, in turn, exhibits lower activation energy (Table 5.5). Bradley et al. [25] also reported a similar trend for the IL-treated coal samples. In summary, the mixed solvent does affect the swelling properties and the solvent extraction. On the contrary, the thermal property of coal gets marginally affected by the addition of pyridine. Therefore, the mixed solvents can be recommended as a part of beneficiation strategy towards ashless coal.

References

[1] M. Otero, L. Calvo, M. Gil, A. García, A. Morán, Co-combustion of different sewage sludge and coal: a non-isothermal thermogravimetric kinetic analysis, Bioresource Technology, 99 (2008) 6311-6319.

[2] D. K. Seo, S. S. Park, Y. T. Kim, J. Hwang, T.-U. Yu, Study of coal pyrolysis by thermo-gravimetric analysis (TGA) and concentration measurements of the evolved species, Journal of Analytical and Applied Pyrolysis, 92 (2011) 209-216.

[3] M. Varol, A. Atimtay, B. Bay, H. Olgun, Investigation of co-combustion characteristics of low quality lignite coals and biomass with thermogravimetric analysis, Thermochimica Acta, 510 (2010) 195-201.

[4] M. Heydari, M. Rahman, R. Gupta, Kinetic study and thermal decomposition behavior of lignite coal, International Journal of Chemical Engineering, 2015 (2015).

[5] S. Bhoi, T. Banerjee, K. Mohanty, Beneficiation of Indian coals using Ionic Liquids, Fuel Processing Technology, 151 (2016) 1-10.

[6] T. K. Green, J. Kovac, J. W. Larsen, A rapid and convenient method for measuring the swelling of coals by solvents, Fuel, 63 (1984) 935-938.

[7] W. Lan-yun, J. Shu-guang, X. Yong-liang, Z. Wei-qing, K. Li-wen, W. Zheng-yan, C. Ting-xiang, Effect of imidazolium based ionic liquids on coal exothermic oxidation by thermal analysis experiments, Procedia Engineering, 26 (2011) 647-651.

[8] A. Coats, J. Redfern, Kinetic parameters from thermogravimetric data, (1964).

[9] L. Zhou, Y. Wang, Q. Huang, J. Cai, Thermogravimetric characteristics and kinetic of plastic and biomass blends co-pyrolysis, Fuel Processing Technology, 87 (2006) 963-969.

[10] M. F. Abdullah, M. A. M. Ishak, K. Ismail, Pyrolysis and liquefaction of acetone and mixed acetone/tetralin swelled mukah balingian malaysian sub-bituminous coal–the effect on coal conversion and oil yield, Malaysian Journal of Analytical Sciences, 12 (2008) 118-122.

[11] H. Hu, G. Sha, G. Chen, Effect of solvent swelling on liquefaction of Xinglong coal at less severe conditions, Fuel Processing Technology, 68 (2000) 33-43.

[12] F. Pinto, I. Gulyurtlu, L. Lobo, I. Cabrita, Effect of coal pre-treatment with swelling solvents on coal liquefaction, Fuel, 78 (1999) 629-634.

[13] P. Painter, N. Pulati, R. Cetiner, M. Sobkowiak, G. Mitchell, J. Mathews, Dissolution and dispersion of coal in ionic liquids, Energy and Fuels, 24 (2010) 1848-1853.

[14] J. Cummings, K. Shah, R. Atkin, B. Moghtaderi, Physicochemical interactions of ionic liquids with coal; the viability of ionic liquids for pre-treatments in coal liquefaction, Fuel, 143 (2015) 244-252.

[15] R. Probstein, R. Hicks, Synthetic fuels, international student edition, McGraw-Hill Inc, 1982.

[16] S. Bhoi, T. Banerjee, K. Mohanty, Molecular dynamic simulation of spontaneous combustion and pyrolysis of brown coal using ReaxFF, Fuel, 136 (2014) 326-333.

[17] S. Bhoi, T. Banerjee, K. Mohanty, Insights on the combustion and pyrolysis behavior of three different ranks of coals using reactive molecular dynamics simulation, RSC Advances, 6 (2016) 2559-2570.

[18] S. Munir, S. Daood, W. Nimmo, A. Cunliffe, B. Gibbs, Thermal analysis and devolatilization kinetics of cotton stalk, sugar cane bagasse and shea meal under nitrogen and air atmospheres, Bioresource Technology, 100 (2009) 1413-1418.

[19] N. Meine, F. Benedito, R. Rinaldi, Thermal stability of ionic liquids assessed by potentiometric titration, Green Chemistry, 12 (2010) 1711-1714.

[20] N. Pulati, M. Sobkowiak, J. P. Mathews, P. Painter, Low-temperature treatment of Illinois No. 6 coal in ionic liquids, Energy and Fuels, 26 (2012) 3548-3552.

[21] P. Painter, R. Cetiner, N. Pulati, M. Sobkowiak, J. Mathews, Dispersion of liquefaction catalysts in coal using ionic liquids, Energy and Fuels, 24 (2010) 3086-3092.

[22] L. Dameng, Y. Qi, T. Dazhen, Reaction kinetics of coalification in the Ordos Basin, China, Geology of Fossil Fuels: Coal, 18 (1997) 147-159.

[23] F. E. Ndaji, K. M. Thomas, Effect of solvent basicity on the kinetics of solvent swelling of coal, Fuel, 72 (1993) 1531-1535.

[24] Y. Otake, E. M. Suuberg, Temperature dependence of solvent swelling and diffusion processes in coals, Energy and Fuels, 11 (1997) 1155-1164.

[25] L. C. Bradley, S. F. Miller, B. G. Miller, D. A. Tillman, A study on the relationship between fuel composition and pyrolysis kinetics, Energy and Fuels, 25 (2011) 1989-1995.

भारतीय प्रौद्योगिकी संस्थान गुवाहाटी
Indian Institute of Technology Guwahati

Chapter 5

Effect of Mixed Solvents on Thermal Degradation of Coal

Chapter 6

Conclusions and Future Scope

6.1 Conclusions

The entire thesis fell under three categories namely ReaxFF simulations of raw coal, COSMO-RS predictions on IL-coal interaction, and beneficiation experiments with selected Ionic Liquids. In the initial part, ReaxFF reactive MD-simulation was used to investigate the combustion and pyrolysis of brown coal (lignite), bituminous, and anthracite coal. The combustion simulation of coal was done under three different conditions, namely fuel lean, fuel rich, and stoichiometric ratio at a temperature range from 2000-4000 K. The investigations of the combustion process and product distribution of various intermediates were also carried out. The coal combustion analysis showed that coal combustion was initialized by thermal decomposition to produce smaller fragments. The fragments were then oxidized and some of the hydrogen radicals reacted with oxygen to produce H_2O molecules. The major gaseous components such as CO, CO_2, H_2, CH_2 and CH_4 were produced with an increase in temperature during the reaction. This was verified by the experimental studies reported in the literature.

The density and temperature effect on the pyrolysis of brown coal was investigated and it was found that the density does not affect the pyrolysis process as much as temperature. Thereafter the combustion and pyrolysis results were compared with the experimental data and it was observed that ReaxFF results matches with the experimental findings in terms of rate of formation of CO and CO_2. This rate was higher for the lignite (brown coal) and bituminous coals as compared to anthracite coal. The activation energy for anthracite coal was found to be 59.2 kJ/mole for CO and 64.4 kJ/mole for CO_2. Similarly, the production rate of CH_4, C_2H_4 and C_2H_6 was also higher for lignite as compared to bituminous and anthracite coal.

After successful structural analysis of coal molecules, a simultaneous interacting system such as coal and Ionic Liquids (ILs) were studied using DFT. The effect of various cations: pyrrolidinium, imidazolium, ammonium, and phosphonium were studied with the coal species. Based on HOMO/LUMO energy, [BMPYR][CH_3CO_3], and [MPIM][CH_3CO_3] were found to be the less stable or more reactive with anthracite and bituminous coals respectively. The related quantum chemical descriptors namely global softness, global hardness, electrophilicity, electronegativity gave the same trend for the respective ILs.

Solid-Liquid Equilibrium (SLE) prediction of brown coal in ILs was also predicted using COSMO-RS model. As the temperature increased, the solubility of brown coal in IL was found to increase. From the SLE prediction, [BMPYR][CH_3CO_3] has the highest solubility in brown coal. It was observed that the brown coal is highly miscible with smaller cationic structures which do not have aromatic rings. The sigma profiles of brown coal and [BMPYR][CH_3CO_3] were found to be complementary to each other indicating higher miscibility. Gibb's free energy of solvation at infinite dilution also showed similar complementary results.

To validate the above theoretical predictions, experiments were conducted with actual coal samples as received from the coal mine. In this regard, the dissolution of five selected Ionic liquids and four Indian Coals were studied by morphological and FTIR spectroscopy. From the microscopic observation, it was observed that ILs [MTBP][$MeSO_4$] and [BMPYR][CH_3CO_3] can significantly fracture the coal molecules, as the average particles size of coal molecules was reduced to a range of 10-20 µm. For the confirmation of the microscopic observation of coal structure, FTIR analysis was conducted for the study of species containing oxygen functional groups. From FTIR analysis, it can be confirmed that

the aromatic hydrocarbon, aliphatic hydrocarbon, and oxygen containing functional groups present in the coal molecules gets reduced to an appreciable extent in these ILs. The IL [BMPYR][CH_3CO_3] gave the best result for the fragmentation of coal molecules with respect to both qualitative as well as quantitative trend. A better extraction yield was observed with the IL, [BMPYR][CH_3CO_3]. Overall, from the quantitative analysis, the peak areas of oxygen-containing functional groups in all the four coal samples were found to decrease by pre-treatment with IL.

In continuation, an experimental investigation was also performed to study the effects of ILs and mixed solvent on pre-treated coal. For this, Ionic liquids (ILs) based on different cations were chosen for the dispersion and dissolution of coal at a temperature of 100 °C. The bituminous variant was found to interact favourably with [BMPYR][CH_3CO_3] + pyridine giving a higher extract yield and swelling ratio as compared to other solvents. Thermal studies of IL-pretreated and mixed solvent pretreated coal were then conducted using a Thermogravimetric Analyzer (TGA). During pyrolysis, a higher mass loss was observed for raw coal when compared to mixed solvents and IL- pretreated coal. The kinetic study shows that the activation energy was lower for IL-pretreated coal as compared to untreated coal. This implies that the IL-pretreated coal required less energy to activate the atoms and molecules to undergo a chemical reaction. The interaction of ILs and mixed solvents were found were to be mostly coal specific. This study proved that the coal pre-treatment with co-solvents are beneficial towards coal liquefaction process.

6.2 Future Scope

6.2. 1 Use of Low-Cost Deep Eutectic Solvents

IL's are usually highly viscous, making its recyclability difficult. One of the approaches to avoid such an event is to use mixed solvents such as those we have discussed in Chapter 5. Further due to the restrictive cost of Ionic Liquids, alternative low-cost solvents such as Deep Eutectic Solvents (DESs) are desired and needs to be explored for coal beneficiation study. Deep Eutectic Solvents (DES) are a combination of Hydrogen Bond Acceptor (HBA) such as inorganic salt and a Hydrogen bond donor (HBD) giving rise to a new solvent having an eutectic point. This is mainly due to the hydrogen bond interactions with each other making it a liquid at the desired temperature, with a melting point lower than that of each individual component. Due to the eventual advantages of DESs such as low cost of components, easy to prepare, tunable physicochemical properties and negligible vapour pressure makes them promising solvents for coal processing.

6.2 Ionic Liquid based Direct Coal Liquefaction

The ability of the Ionic Liquids to fragment the coal particle has been demonstrated aptly in the thesis. One of the concluding outcomes of this work can be its contact with commercially available dissolution catalysts. One such catalyst namely Molybdenum disulphide (MoS_2) is well known for coal liquefaction. A single stage liquefaction can be validated and performed at coal liquefaction conditions by the use of a hydrogen-donor solvent such as tetralin. The IL recovery can then be further demonstrated so that these solvents can be commercially explored for direct coal liquefaction.

List of Publications

Referred Journals:

[1] **Sanjukta Bhoi**, Debanjan Dey, Tamal Banerjee, Kaustubha Mohanty. Solid-Liquid Equilibria Predictions for the Dissolution of Brown Coal in Ionic Liquids using a Continuum Solvation Model, ***Fuel Processing Technology***. 126(2014), 112-121.

[2] **Sanjukta Bhoi**, Tamal Banerjee, Kaustubha Mohanty. Molecular dynamic simulation of spontaneous combustion and pyrolysis of brown coal using ReaxFF, ***Fuel***, 136(2014), 326-333.

[3] **Sanjukta Bhoi**, Tamal Banerjee, Kaustubha Mohanty. Insights on the combustion and pyrolysis behaviour of three different ranks of coals using reactive molecular dynamics simulation. ***RSC Advances***, 6(2016), 2559-2570.

[4] **Sanjukta Bhoi**, Tamal Banerjee, Kaustubha Mohanty. Beneficiation of Indian coals using Ionic Liquids. ***Fuel Processing Technology***, 151(2016), 1-10.

[5] **Sanjukta Bhoi**, Kaustubha Mohanty, Tamal Banerjee. Quantum Chemical Insights and Continuum Solvation Predictions on the Dissolution of Bituminous and Anthracite Coal in Ionic Liquid. ***Journal of Molecular Liquids*** 221(2016), 919-929.

[6] **Sanjukta Bhoi**, Tamal Banerjee, Kaustubha Mohanty. Effects of Ionic Liquids on Thermal Degradation and Kinetic Studies of Coals by Thermogravimetric Analysis. (submitted to *Mineral Engineering*)

International/National Conferences:

[1] **Sanjukta Bhoi**, Tamal Banerjee, Kaustubha Mohanty. Experimental Studies on the Dissolution and Dispersion of Four Indian Coals. ***Iberoamerican Meeting on Ionic Liquids 2015***, 2-3 July 2015, Madrid, Spain.

[2] **Sanjukta Bhoi**, Tamal Banerjee, Kaustubha Mohanty. Ionic Liquids: A Potential Solvent for Yield Extraction of Indian Coal. ***26th EUCHEM on Molten Salts and Ionic Liquids***, 3-8 July 2016, Vienna, Austria.

[3] **Sanjukta Bhoi**, Tamal Banerjee, Kaustubha Mohanty. Insight in the swelling behavior of Indian Coals in a pyrrolidinium based ionic liquid. Sixth National Level

Annual Research Symposium of Chemical Engineering Research scholars, ***ChEmference***, 5-6th Dec 2015, IIT Hyderabad, India.

[4] **Sanjukta Bhoi**, Tamal Banerjee, Kaustubha Mohanty. Quantum chemical based screening of ionic liquids for dissolution of brown coal. 68th Annual Session of Indian Institute of Chemical Engineers, ***CHEMCON 2015***, Indian Chemical Engineers Congress, Dec 27-30th, 2015, IIT Guwahati, India.

[5] **Sanjukta Bhoi**, Tamal Banerjee, Kaustubha Mohanty. An experimental investigation on effect of ionic liquids on Indian Coal oxidation by Thermogravimetry Analysis. ***6th World Petrocoal Congress, International Conference and Exhibition***, 15-17th Feb 2016, NDCC New Delhi, India.

[6] **Sanjukta Bhoi**, Tamal Banerjee, Kaustubha Mohanty. Behavioral study of three Indian bituminous coal extraction using ionic liquids. ***7th DAE-BRNS Biennial Symposium on Emerging Trends in Separation Science and Technology - SESTEC 2016***, 17-20th May 2016, IIT, Guwahati, India.

[7] Tooba Fatma, **Sanjukta Bhoi**, Tamal Banerjee. Molecular Dynamic Simulation of Spontaneous Combustion of Brown Coal using ReaxFF. ***National Conference on Challenges in Environmental Research-2016***. 4-5th June, 2016, Centre for the Environment, IIT Guwahati, India.